



**FRIEDRICH-SCHILLER-  
UNIVERSITÄT  
JENA**

# **High-frequency light-matter interaction in atoms and molecules**

**Dissertation**  
(kumulativ)

zur Erlangung des akademischen Grades doctor rerum naturalium  
(Dr. rer. nat)

vorgelegt dem Rat der Chemisch-Geowissenschaftlichen Fakultät der  
Friedrich-Schiller-Universität Jena

von Karl Michael Ziems, M. Sc.  
geboren am 27.10.1993 in Selb

**Gutachter:**

1. Prof. Dr. Stefanie Gräfe, Friedrich-Schiller-Universität Jena
2. Prof. Dr. Volker Engel, Julius-Maximilians-Universität Würzburg
3. Prof. Dr. Timo Jacob, Universität Ulm

Tag der öffentlichen Verteidigung: 07. September 2023

*To*  
*Marie Therese Ziems*  
*and*  
*Tara Sallis*





# Contents

<b>List of Abbreviations</b>	<b>iii</b>
<b>Publication list</b>	<b>iv</b>
<b>1. Introduction</b>	<b>1</b>
<b>2. Theory</b>	<b>5</b>
2.1. Quantum dynamics . . . . .	5
2.1.1. State vector and operator . . . . .	5
2.1.2. Time evolution . . . . .	7
2.1.3. Dirac picture and perturbation theory . . . . .	8
2.1.4. Time-independent Schrödinger equation . . . . .	9
2.2. Light-matter interaction . . . . .	10
2.2.1. Light-matter interaction Hamiltonian . . . . .	10
2.2.2. Dipole approximation and gauge transformation . . . . .	12
2.2.3. Light pulses and chirps . . . . .	14
2.3. Molecular systems . . . . .	19
2.3.1. Molecular Hamiltonian . . . . .	19
2.3.2. Quantum chemistry . . . . .	20
2.3.3. Molecular excited-state dynamics . . . . .	21
<b>3. Numerical methods</b>	<b>23</b>
3.1. Quantum mechanics on a grid . . . . .	23
3.2. Split operator method . . . . .	25
3.3. Imaginary time propagation . . . . .	26
<b>4. Results</b>	<b>29</b>
4.1. Correlation dynamics in molecular XUV ionisation . . . . .	30
4.1.1. The extended Shin-Metiu model system . . . . .	31
4.1.2. Electron-electron correlation and time delays . . . . .	33
4.1.3. Nuclear-electron correlation and photoelectron imprints . . . . .	35
4.2. Attosecond ionisation dynamics of modulated, few-cycle XUV pulses . . . . .	39
4.3. Non-adiabatic relaxation dynamics of furan - theoretically addressed for attosecond x-ray absorption . . . . .	43
4.4. The contribution of ionisation to static and ultrafast x-ray scattering . . . . .	49

<b>5. Summary and Outlook</b>	<b>55</b>
<b>Bibliography</b>	<b>63</b>
<b>A. Acknowledgement</b>	<b>75</b>
<b>B. Documentation of authorship</b>	<b>77</b>
<b>C. Declaration of authorship</b>	<b>79</b>
<b>D. Publications</b>	<b>81</b>
D.1. F.G. Fröbel*, <u>K.M. Ziems</u> *, U. Peschel, S. Gräfe, A. Schubert, The impact of electron-electron correlation in ultrafast attosecond single ionization dynamics, <i>J. Phys. B.: At. Mol. Opt. Phys.</i> , <b>2020</b> , <i>53</i> , 144005 . . . . .	82
D.2. <u>K.M. Ziems</u> , J. Bruhnke, V. Engel, S. Gräfe, Nuclear-electron correlation effects and their photoelectron imprint in molecular XUV ionisation, <i>Front. Chem.</i> , <b>2022</b> , <i>10</i> , 942633 . . . . .	95
D.3. <u>K.M. Ziems</u> , M. Wollenhaupt, S. Gräfe, A. Schubert, Attosecond ionization dynamics of modulated, few-cycle XUV pulses, <i>J. Phys. B.: At. Mol. Opt. Phys.</i> , <b>2023</b> , <i>56</i> , 105602 . . . . .	107
D.4. S. Severino*, <u>K.M. Ziems</u> *, M. Reduzzi, A. Summers, H.-W. Sun, Y.-H. Chien, S. Gräfe, J. Biegert, Non-adiabatic electronic and vibrational ring-opening dynamics resolved with attosecond core-level spectroscopy, <i>Nature</i> , <b>2023</b> (submitted) . . . . .	123
D.5. <u>K.M. Ziems</u> , M. Simmermacher, S. Gräfe, A. Kirrander, The contribution of Compton ionization to ultrafast x-ray scattering, <i>J. Chem. Phys.</i> , <b>2023</b> , <i>159</i> , 044108 . . . . .	179

# List of Abbreviations

<b>AES</b>	Auger Electron Spectroscopy
<b>CEP</b>	Carrier-envelope Phase
<b>CI</b>	Conical Intersection
<b>cm</b>	Coherent Mixed
<b>EXAFS</b>	Extended X-ray Absorption Fine Structure
<b>FC</b>	Franck-Condon
<b>FT</b>	Fourier Transform
<b>FWHM</b>	Full Width At Half Maximum
<b>HHG</b>	High Harmonic Generation
<b>IAM</b>	Independent Atom Model
<b>IAP</b>	Isolated Attosecond Pulse
<b>NIR</b>	Near-infrared
<b>RO</b>	Ring-opening
<b>ROCI</b>	Ring-opening Conical Intersection
<b>RP</b>	Ring-puckering
<b>RPCI</b>	Ring-puckering Conical Intersection
<b>SVEA</b>	Slowly Varying Envelope Approximation
<b>SXR</b>	Soft X-ray
<b>TDSE</b>	Time-dependent Schrödinger Equation
<b>TISE</b>	Time-independent Schrödinger Equation
<b>UV</b>	Ultraviolet
<b>XAFS</b>	X-ray Absorption Fine Structure
<b>XANES</b>	X-ray Absorption Near-edge Structure
<b>XAS</b>	X-ray Absorption Spectroscopy
<b>XES</b>	X-ray Emission Spectroscopy
<b>XFEL</b>	X-ray Free-Electron Laser
<b>XPS</b>	X-ray Photoelectron Spectroscopy
<b>XUV</b>	Extreme Ultraviolet

**The following publications are part of this thesis:**

- 1) F.G. Fröbel\*, K.M. Ziems\*, U. Peschel, S. Gräfe, A. Schubert, The impact of electron-electron correlation in ultrafast attosecond single ionization dynamics, *J. Phys. B.: At. Mol. Opt. Phys.*, **2020**, *53*, 144005
- 2) K.M. Ziems, J. Bruhnke, V. Engel, S. Gräfe, Nuclear-electron correlation effects and their photoelectron imprint in molecular XUV ionisation, *Front. Chem.*, **2022**, *10*, 942633
- 3) K.M. Ziems, M. Wollenhaupt, S. Gräfe, A. Schubert, Attosecond ionization dynamics of modulated, few-cycle XUV pulses, *J. Phys. B.: At. Mol. Opt. Phys.*, **2023**, *56*, 105602
- 4) S. Severino\*, K.M. Ziems\*, M. Reduzzi, A. Summers, H.-W. Sun, Y.-H. Chien, S. Gräfe, J. Biegert, Non-adiabatic electronic and vibrational ring-opening dynamics resolved with attosecond core-level spectroscopy, *Nature*, **2023** (submitted)
- 5) K.M. Ziems, M. Simmermacher, S. Gräfe, A. Kirrander, The contribution of Compton ionization to ultrafast x-ray scattering, *J. Chem. Phys.*, **2023**, *159*, 044108

Asterisks indicate equally contributing authors.

# 1. Introduction

The study of electron and nuclear dynamics is a central focus in atomic and chemical physics and is motivated by the desire to understand the behaviour of atoms and molecules on a fundamental level. Within the framework of quantum mechanics, we describe atoms and molecules by stationary eigenstates. If we superpose these states coherently, we create a wave packet that evolves dynamically on a timescale determined by the states' energy difference. Thus, the superposition of rotational, vibrational and electronic states, leads to, respectively, rotational dynamics on the picosecond ( $1 \text{ ps} = 10^{-12} \text{ s}$ ), vibrational dynamics on the femtosecond ( $1 \text{ fs} = 10^{-15} \text{ s}$ ), and electron dynamics on the attosecond ( $1 \text{ as} = 10^{-18} \text{ s}$ ) timescale. One way to create these wave packets and, thus, initiate dynamics is via light-matter interaction. For example, electronic excitation creates a nuclear wave packet in an excited electronic state, or sudden ionisation leads to an electron wave packet in the cation. Hence, the interplay of light-matter interaction with electron and nuclear dynamics is a fundamental question in atomic and chemical physics.

In addition, unravelling electron and nuclear dynamics has implications beyond the fundamental interest since the motion of electrons and nuclei is at the heart of light-induced processes in chemistry and biology. Understanding them better is essential to explore processes, such as photosynthesis, radiation damage, and vitamin D formation, and to make progress in important industrial and medical areas, such as photocatalysis, solar energy harvesting, and photodynamic therapy<sup>[1–6]</sup>.

The first step to observing dynamics is the development of light technologies with pulse durations capable of resolving the intrinsic time scale of molecular particles. Historically, the first such light technology came in the second half of the 20th century with the discovery of the laser that, subsequently, allowed the generation of femtosecond light pulses in the ultraviolet (UV) (100 nm–400 nm) to near-infrared (NIR) (700 nm–2500 nm). These light pulses can be used in time-resolved pump-probe experiments. Here, the pump pulse excites the system and a second delayed probe pulse detects the pump-induced dynamics. Such setups have been used to resolve the nuclear motion on the femtosecond timescale and gave rise to the now well-established femtochemistry research field<sup>[7,8]</sup>. At the advent of the 21st century, the construction of X-ray Free-Electron Laser (XFEL) facilities<sup>[9–12]</sup> extended the spectral range of femtosecond pulses, opening up the extreme ultraviolet (XUV) (10 nm–124 nm or 10 eV–124 eV) to hard x-ray (0.01 nm–0.25 nm or 5 keV–100 keV) regime. Consequently, new methods, such as non-resonant x-ray scattering, could be used to track nuclear dynamics<sup>[13]</sup>. At the same time, major scientific discoveries and tech-

nological advances, such as chirped pulse amplification<sup>[14]</sup>, pulse compression and spectral broadening via self-phase modulation<sup>[15,16]</sup>, carrier-envelope phase stabilisation<sup>[17]</sup>, and chirped multilayer coatings<sup>[18]</sup>, culminated in the creation of isolated attosecond light pulses via high harmonic generation (HHG)<sup>[19,20]</sup> in the XUV to soft x-ray (SXR) (124 eV–5 keV) spectral region<sup>[21,22]</sup>. Additionally to resolving nuclear dynamics, the investigation of electron motion on its natural timescale of attoseconds was now in reach and created the new research field of attosecond science<sup>[23–25]</sup>. In the future, x-ray pulses from XFELs are poised to enter the attosecond time duration, expanding the methods capable of tracking electron dynamics<sup>[26–30]</sup>.

Applying the aforementioned light technologies specifically to ultrafast electron dynamics in molecules is often summarized under the term attosecond chemistry or short attochemistry<sup>[1,2,31]</sup>. Here, attosecond electron dynamics plays a crucial role in understanding the early stages of light-induced processes. Moreover, correlation processes, i.e. the coupling between the particles in molecules, become pivotal. The initial light interaction leads to electron dynamics governed by the interaction and correlation of all electrons in the system. Subsequently, the rearrangement of electrons triggers nuclear motion on the femtosecond timescale, which in turn can influence electron dynamics and can lead to coupled electron and nuclear motion. Of particular interest are conical intersections (CIs), nuclear geometry points where electronic states cross and strong nuclear-electron coupling occurs<sup>[32]</sup>. These are ubiquitous drivers of light-induced chemistry and biology, seen in processes like the retinal isomerisation of the vision process and the photostability of DNA bases<sup>[33,34]</sup>. Therefore, the long-term goal of attochemistry is to understand and subsequently manipulate electron dynamics in molecules to steer nuclear dynamics and photochemical processes. This could open opportunities for the rational design of new molecules with specific properties and reactivity.

While such attosecond quantum control schemes are yet out of reach and necessitate substantial technological and theoretical advances, current research focuses on developing experimental tools to monitor electron and nuclear dynamics, and on understanding the fundamentals behind coupled electron and nuclear motion. Experimental techniques can be broadly divided into two approaches: *(i)* attosecond measurements without attosecond pulses and *(ii)* attosecond pump-probe spectroscopy. In *(i)*, techniques known from strong-field physics<sup>[35]</sup> are employed, such as laser-induced electron diffraction<sup>[36–38]</sup>, holography<sup>[39,40]</sup>, attoclock<sup>[41,42]</sup>, or high-harmonic spectroscopy<sup>[43–45]</sup>. These methods are based on the recollision process upon ionisation by intense NIR pulses<sup>[20]</sup>. While these light pulses have a duration of tens of femtoseconds, the ionisation process is highly non-linear and sensitive to the instantaneous value of the electric field. This allows a sub-cycle time resolution on the attosecond timescale. However, the non-linearity of strong light pulses leads to complex, non-perturbative dynamics that are difficult to simulate and analyse. Moreover, competing processes, such as ionisation from deeper-lying molecular orbitals, have to be considered<sup>[43,44]</sup>. Attosecond pump-probe spectroscopy *(ii)* is based

---

on the analogy with femtochemistry pump-probe spectroscopy. Instead of isolated femtosecond pulses, isolated attosecond pulses (IAPs) are employed to obtain an attosecond time resolution. Naturally, light pulses in the XUV to x-ray spectral region can facilitate attosecond pulse duration and are obtained experimentally either via HHG or at XFELs. Crucially, IAPs with high intensity and photon flux are needed due to the low cross section of high-frequency light-matter interactions. However, attosecond pulses by HHG lack intensity and photon flux for attosecond pump, attosecond probe experiments, and pulses from XFELs are just about to enter attosecond time duration. Therefore, instead of a sequence of two IAPs, most attosecond pump-probe experiments use one IAP and one few-cycle NIR pulse. Depending on the setup and the measured observable, either pulse can serve as a pump or probe. The specific combination of XUV pump and NIR probe is termed attosecond streaking. It is a regularly employed technique in attosecond science, e.g. to characterise attosecond pulses or to measure photoionisation time delays<sup>[23,46]</sup>.

The first pump-probe experiment with attosecond temporal resolution was performed by Sansone et al. in 2010<sup>[47]</sup>. They used an XUV IAP and a time-delayed few-cycle NIR pulse to ionise molecular hydrogen. Detecting the asymmetry in the formation of charged atomic fragments revealed electron localisation between the two protons in  $\text{H}_2^+$  with sub-fs resolution. Subsequent experiments have targeted electron and nuclear dynamics in diatomic and small polyatomic molecules, such as  $\text{O}_2$ ,  $\text{N}_2$ ,  $\text{CO}$ ,  $\text{CO}_2$ , and  $\text{C}_2\text{H}_4$ <sup>[48–54]</sup>. Larger systems have also been investigated, most prominently in 2014, when Calegari et al. observed charge migration in the amino acid phenylalanine<sup>[55]</sup>. Charge migration is initiated by an ionising attosecond pump pulse that creates a superposition of hole states, i.e. an electronic wave packet, that manifests as attosecond modulation of the electron density<sup>[56]</sup>. Calegari’s experimental approach used a NIR pulse to probe the intrinsic charge migration initiated by the pump by measuring the quantum yield of a particular molecular fragment with attosecond resolution. Motivated by these early results, several pioneering experiments have followed that investigated various attosecond phenomena. Apart from charge migration, experiments looked into correlation dynamics trying to understand the exact nature of the photoionisation processes under the influence of coupled particles<sup>[57]</sup>, photoionisation time delays aiming at measuring the intrinsic time needed to liberate an electron from a molecule<sup>[46]</sup>, the effect of chirality and non-dipole interactions on the dynamics<sup>[58,59]</sup>, and autoionisation decays<sup>[52,60]</sup>.

While these studies were experimental milestones facilitated by novel light technologies, they also relied strongly on theoretical and computational insight to analyse and understand the experimental observables. Therefore, apart from the discussed developments in light technologies and experimental approaches, advancements in theory are pivotal for understanding dynamics and attochemistry. The accurate theoretical description of attosecond processes that combines light-matter interactions with coupled electron and nuclear dynamics represents a formidable challenge and is still in its early stages. As outlined in the beginning, the processes induced by attosecond pulses require a description

of electron-electron and nuclear-electron correlation in multi-particle molecular systems. Crucially, these correlations occur not only in bound states but also in the continuum that must be included in simulations. Additionally, the light pulses of pump-probe experiments must be incorporated explicitly. In the case of NIR pulses or high-intensity XUV pulses, non-perturbative treatments are needed. Currently, a complete description of these processes is only possible for  $\text{H}_2$ . Thus, common theoretical approaches have to rely on approximations. For example, in the single active electron approximation, only one electron interacts with the light pulse and is described quantum dynamically, the frozen nuclei approximation disregards the nuclear degrees of freedom, and the sudden approximation and first-order perturbation theory limit the exact nature of the light pulse interaction in the ionisation process. Consequently, significant efforts are underway to derive new approximated methods to model electron dynamics in bound and continuum states with coupling to nuclear degrees of freedom<sup>[2]</sup>.

In this work, a different approach is chosen. Instead of applying approximated methods, we employ a reduced-dimensionality molecular quantum model system. This allows for numerically exact electron-electron and nuclear-electron correlation, an explicit light-molecule interaction and a grid-based continuum. The model is applied to current problems in attochemistry and gives qualitative conclusions beyond any of the aforementioned theoretical approximations. In this context, we study molecular correlation dynamics, photoionisation time delays, and post-ionisation dynamics, which are light-induced processes that strongly rely on particle correlation. Furthermore, we investigate few-cycle, high-intensity effects beyond first-order perturbation treatments.

Since attosecond science is a fast-evolving research field, new technology developments are poised to spark new methods and experiments. In this regard, we look into core-level spectroscopy and transient absorption in the attosecond regime<sup>[61]</sup> as a novel experimental tool that allows the observation of attosecond dynamics in neutral molecules. This is an important milestone for translating attochemistry to biologically relevant systems since, so far, most experiments rely on an initial photoionisation step and track cationic dynamics. Furthermore, with XFELs coming ever closer to attosecond pulses in the hard x-ray regime, time-resolved x-ray scattering could combine the extreme temporal resolution of attosecond pulses with picometer spatial resolution<sup>[62,63]</sup>. We contribute to understanding how x-ray scattering can be used in the future for attosecond experiments and evaluate the role of ionising transitions in the scattering signal.



## 2. Theory

This chapter covers the theoretical background and methods used for the research in chapter 4. First, a brief summary of quantum dynamics is given involving state vectors, operators, and different ways to treat the time evolution of a quantum system. Moreover, we introduce perturbation theory and the spectral representation in the basis of time-independent solutions. Second, semi-classical light-matter interaction is presented. Maxwell's equations, gauge transformations, dipole approximation and pulse chirping are discussed in this context. Third, the molecular Hamiltonian is introduced, and common concepts of quantum chemistry and molecular excited-state dynamics referenced. Throughout this chapter - unless stated otherwise - atomic units are used. Vectors in three-dimensional space are indicated in bold.

### 2.1. Quantum dynamics

The following section introduces some of the fundamental aspects of quantum dynamics. For more details and a general overview of (time-dependent) quantum mechanics, we refer to established literature<sup>[64-67]</sup>, which is also the basis of this section.

The dynamics of a quantum system is governed by the time-dependent Schrödinger equation (TDSE),

$$i \frac{\partial}{\partial t} |\Psi(t)\rangle = \hat{H}(t) |\Psi(t)\rangle. \quad (2.1)$$

Here,  $i$  is the imaginary unit,  $\hat{H}(t)$  the system's Hamiltonian, and  $|\Psi(t)\rangle$  a time-dependent state vector in Hilbert space - a complex and linear vector space with an inner product - that completely describes the system.

The Hamiltonian is the quantum mechanical analogue to the classical Hamiltonian function and contains expressions for the system's energy and possible (time-dependent) interactions. For now, we keep its form general and focus on time evolution before discussing the Hamiltonian for light-matter interaction and the molecular Hamiltonian in section 2.2 and section 2.3, respectively.

#### 2.1.1. State vector and operator

The state vector,  $|\Psi(t)\rangle$ , can be expanded in any basis of eigenstates. A common expansion is in terms of position and momentum eigenstates,  $\{|\mathbf{x}\rangle\}$  and  $\{|\mathbf{p}\rangle\}$ , and gives for a single

particle in three dimensions

$$|\Psi(t)\rangle = \int d^3x |\mathbf{x}\rangle \langle \mathbf{x} | \Psi(t)\rangle = \int d^3x \Psi(\mathbf{x}, t) |\mathbf{x}\rangle \quad (2.2)$$

$$|\Psi(t)\rangle = \int d^3p |\mathbf{p}\rangle \langle \mathbf{p} | \Psi(t)\rangle = \int d^3p \Psi(\mathbf{p}, t) |\mathbf{p}\rangle. \quad (2.3)$$

This yields, respectively, the position and momentum wave function,

$$\Psi(\mathbf{x}, t) = \langle \mathbf{x} | \Psi(t)\rangle \quad (2.4)$$

$$\Psi(\mathbf{p}, t) = \langle \mathbf{p} | \Psi(t)\rangle. \quad (2.5)$$

These are related by Fourier transform (FT) as evident by inserting, respectively, unity in momentum and position space:

$$\Psi(\mathbf{x}, t) = \int d^3p \langle \mathbf{x} | \mathbf{p}\rangle \langle \mathbf{p} | \Psi(t)\rangle = (2\pi)^{3/2} \int d^3p e^{+ip\mathbf{x}} \Psi(\mathbf{p}, t), \quad (2.6)$$

$$\Psi(\mathbf{p}, t) = \int d^3x \langle \mathbf{p} | \mathbf{x}\rangle \langle \mathbf{x} | \Psi(t)\rangle = (2\pi)^{3/2} \int d^3x e^{-ip\mathbf{x}} \Psi(\mathbf{x}, t). \quad (2.7)$$

Here, we use the position eigenstate in momentum representation,  $\langle \mathbf{p} | \mathbf{x}\rangle = (2\pi)^{3/2} e^{-ip\mathbf{x}}$ , and the momentum eigenstates in position representation,  $\langle \mathbf{x} | \mathbf{p}\rangle = (2\pi)^{3/2} e^{+ip\mathbf{x}}$ . These representations and their relation prove useful for numerical implementations and are discussed further in chapter 3.

While the state vector contains all information about the system, its interpretation is not straightforward. The established approach to the abstract vector is the Born interpretation<sup>[68]</sup>. It defines the probability density as

$$P(\mathbf{x}, t) = |\Psi(\mathbf{x}, t)|^2 \quad (2.8)$$

and states that the probability of finding a particle in the volume element  $d^3x$ , centred at point  $\mathbf{x}$  and at time  $t$  is proportional to  $P(\mathbf{x}, t)d^3x$ . This frames the probabilistic approach to quantum mechanics where - contrary to classical mechanics - only statements about the probabilities of results are possible.

A general way to extract information from a state vector is by applying an operator,  $\hat{O}$ , and calculating the expectation value,

$$\langle \hat{O}(t)\rangle = \langle \Psi(t) | \hat{O} | \Psi(t)\rangle. \quad (2.9)$$

Experimentally measurable quantities, i.e. observables, are real-valued and represented by Hermitian operators<sup>[69]</sup>. These are defined as operators that are equal to their conjugate transpose (or adjoint),

$$\hat{O}_H = \hat{O}_H^\dagger. \quad (2.10)$$

It can be shown that the eigenvalues,  $\{w_\alpha\}$ , of a Hermitian operator,  $\hat{O}_H$ , are real and its

eigenstates,  $\{|\phi_\alpha\rangle\}$ , with different eigenvalues,  $w_\alpha \neq w_\beta$ , are orthogonal, i.e.  $\langle\phi_\alpha|\phi_\beta\rangle = 0$ . If the system,  $|\Psi(t)\rangle$ , is in an eigenstate of a Hermitian operator, i.e.  $|\Psi(t)\rangle = |\phi_\alpha\rangle$ , the probability of measuring the corresponding real eigenvalue,  $w_\alpha$ , equals one. If the system is in a superposition of eigenstates, i.e.  $|\Psi(t)\rangle = \sum_i c_i(t) |\phi_i\rangle$ , the average value is given by the sum of all eigenvalues,  $w_i$ , weighted by corresponding probabilities,  $|c_i(t)|^2$ ,

$$\langle\hat{O}_H(t)\rangle = \langle\Psi(t)|\hat{O}_H|\Psi(t)\rangle \quad (2.11)$$

$$= \sum_i c_i^*(t) \sum_{j=0}^{\infty} c_j(t) \langle\phi_i|\hat{O}_H|\phi_j\rangle \quad (2.12)$$

$$= \sum_i |c_i(t)|^2 w_i. \quad (2.13)$$

A system's Hamiltonian,  $\hat{H}(t)$ , is an example for a Hermitian operator.

### 2.1.2. Time evolution

The time evolution of a quantum system is determined by its equation of motion as presented in Eq. 2.1. A formal solution for an initial state,  $|\Psi(t_0)\rangle$ , can be obtained as

$$|\Psi(t)\rangle = \hat{U}(t, t_0) |\Psi(t_0)\rangle \quad (2.14)$$

by using the time-evolution operator or propagator,  $\hat{U}(t, t_0)$ , as defined in the Schrödinger picture of quantum mechanics<sup>[70]</sup>. This operator is defined by its

- i) unitarity:  $\hat{U} = \hat{U}^{-1}$ ,
- ii) identity:  $\hat{U}(t, t) = 1$ , and
- iii) closure:  $\hat{U}(t, t_0) = \hat{U}(t, t_1)\hat{U}(t_1, t_0)$ .

Inserting Eq. 2.14 into Eq. 2.1 yields

$$i \frac{\partial}{\partial t} \hat{U}(t, t_0) |\Psi(t_0)\rangle = \hat{H}(t) \hat{U}(t, t_0) |\Psi(t_0)\rangle, \quad (2.15)$$

which holds for any state  $|\Psi(t_0)\rangle$  giving, subsequently, the operator relation

$$i \frac{\partial}{\partial t} \hat{U}(t, t_0) = \hat{H}(t) \hat{U}(t, t_0). \quad (2.16)$$

For the trivial case of a time-independent Hamiltonian,  $\hat{H}_0$ , the differential equation is solved by

$$\hat{U}(t, t_0) = e^{-i\hat{H}_0(t-t_0)}. \quad (2.17)$$

Otherwise, integration over time from  $t_0$  to  $t$  and using the identity condition results in

$$\hat{U}(t, t_0) = 1 - i \int_{t_0}^t dt_1 \hat{H}(t_1) \hat{U}(t_1, t_0). \quad (2.18)$$

This integral equation is solved iteratively by subsequent integrations,

$$\hat{U}(t, t_0) = 1 + \sum_{n=1}^{\infty} (-i)^n \int_{t_0}^t dt_1 \hat{H}(t_1) \int_{t_0}^{t_1} dt_2 \hat{H}(t_2) \dots \int_{t_0}^{t_{n-1}} dt_n \hat{H}(t_n). \quad (2.19)$$

Note that the integrals are time-ordered, i.e.  $t_1 > t_2 > \dots > t_n$ . The Dyson series is found by introducing the time-ordering operator,  $\hat{T}$ , together with symmetry considerations,

$$\hat{U}(t, t_0) = 1 + \sum_{n=1}^{\infty} \frac{(-i)^n}{n!} \int_{t_0}^t dt_1 \int_{t_0}^{t_1} dt_2 \dots \int_{t_0}^{t_{n-1}} dt_n \hat{T} [\hat{H}(t_1) \hat{H}(t_2) \dots \hat{H}(t_n)] \quad (2.20)$$

$$= \hat{T} e^{-i \int_{t_0}^t \hat{H}(\tau) d\tau}. \quad (2.21)$$

If the Hamiltonian commutes with itself at different times, i.e.  $[\hat{H}(t_i), \hat{H}(t_j)] = 0$ , the time-ordering can be dropped,

$$\hat{U}(t, t_0) = e^{-i \int_{t_0}^t \hat{H}(\tau) d\tau}. \quad (2.22)$$

However, this is not the case for most problems and especially not for the light-matter interactions investigated in this work. Analytical solutions are, thus, rare and the time evolution has to be solved numerically. This is explained in section 3.1 by means of the short-time propagator. In conclusion, inserting Eq. 2.17, 2.21, 2.22 in Eq. 2.14 gives the time evolution of the state vector for a

$$\text{time-independent Hamiltonian: } |\Psi(t)\rangle = e^{-i\hat{H}_0(t-t_0)} |\Psi(t_0)\rangle, \quad (2.23)$$

$$\text{commuting time-dependent Hamiltonian: } |\Psi(t)\rangle = e^{-i \int_{t_0}^t \hat{H}(\tau) d\tau} |\Psi(t_0)\rangle, \quad (2.24)$$

$$\text{general time-dependent Hamiltonian: } |\Psi(t)\rangle = \hat{T} e^{-i \int_{t_0}^t \hat{H}(\tau) d\tau} |\Psi(t_0)\rangle. \quad (2.25)$$

### 2.1.3. Dirac picture and perturbation theory

The above approach can be used to obtain expressions for time-dependent perturbation theory in the interaction (or Dirac) picture<sup>[71]</sup>. In brief, the time-dependent Hamiltonian is split into a time-independent contribution,  $\hat{H}_0$ , and a time-dependent interaction,  $\hat{W}(t)$ ,

$$\hat{H}(t) = \hat{H}_0 + \hat{W}(t). \quad (2.26)$$

Within the Dirac picture, we define the interaction state vector and the interaction operator as

$$|\Psi_I(t)\rangle = e^{i\hat{H}_0 t} |\Psi(t)\rangle \quad (2.27)$$

$$\hat{W}_I(t) = e^{i\hat{H}_0 t} \hat{W}(t) e^{-i\hat{H}_0 t}. \quad (2.28)$$

Insertion into the TDSE yields the time evolution of the interaction state vector similar to Eq. 2.25,

$$|\Psi_I(t)\rangle = \hat{T} e^{-i \int_{t_0}^t \hat{W}_I(\tau) d\tau} |\Psi_I(t_0)\rangle. \quad (2.29)$$

Going back to the Schrödinger picture (via Eq. 2.27) gives the state vector

$$|\Psi(t)\rangle = e^{-i\hat{H}_0 t} \hat{T} e^{-i \int_{t_0}^t \hat{W}_I(\tau) d\tau} e^{i\hat{H}_0 t_0} |\Psi(t_0)\rangle \quad (2.30)$$

$$= e^{-i\hat{H}_0(t-t_0)} |\Psi(t_0)\rangle \quad (2.31)$$

$$+ \sum_{n=1}^{\infty} \frac{(-i)^n}{n!} e^{-i\hat{H}_0 t} \int_{t_0}^t dt_1 \int_{t_0}^{t_1} dt_2 \dots \int_{t_0}^{t_{n-1}} dt_n \hat{T} [\hat{W}_I(t_1) \hat{W}_I(t_2) \dots \hat{W}_I(t_n)] e^{i\hat{H}_0 t_0} |\Psi(t_0)\rangle. \quad (2.32)$$

Truncating the infinite sum in Eq. 2.32 at order  $k$  results in an approximated state vector expressed in terms of  $k$  (time-ordered) interactions and is the basis of time-dependent perturbation theory,

$$|\Psi^{(k)}(t)\rangle = \sum_{n=0}^k |\psi^{(n)}(t)\rangle \quad (2.33)$$

$$|\psi^{(n)}(t)\rangle = \frac{(-i)^n}{n!} e^{-i\hat{H}_0 t} \int_{t_0}^t dt_1 \int_{t_0}^{t_1} dt_2 \dots \int_{t_0}^{t_{n-1}} dt_n \hat{T} [\hat{W}_I(t_1) \hat{W}_I(t_2) \dots \hat{W}_I(t_n)] e^{i\hat{H}_0 t_0} |\Psi(t_0)\rangle. \quad (2.34)$$

Here,  $|\Psi^{(k)}(t)\rangle$  is the state vector up to  $k$ -th order perturbation, while  $|\psi^{(n)}(t)\rangle$  is the state vector describing a contribution of  $n$ -th order. Since the interaction operator terms are strictly time-ordered, perturbation theory is used in light-matter interaction to describe consecutive perturbative events to a ground state  $|\Psi(t_0)\rangle$ , e.g.  $n$ -th order perturbation theory is used to describe the interaction of a system with  $n$  photons.

#### 2.1.4. Time-independent Schrödinger equation

If the Hamiltonian describing the system is time-independent, the state vector can be written as a product state of a time-independent state vector and a time-dependent phase,

$$|\Psi(t)\rangle = |\psi\rangle \phi(t). \quad (2.35)$$

By separation of variables, one obtains two differential equations,

$$\hat{H}_0 |\psi\rangle = E |\psi\rangle \quad (2.36)$$

$$i \frac{\partial}{\partial t} \phi(t) = E \phi(t). \quad (2.37)$$

The second equation has the trivial solution

$$\phi(t) = e^{-iEt}. \quad (2.38)$$

Eq. 2.36 is the time-independent Schrödinger equation (TISE) - an eigenvalue equation describing stationary states of the system. For bound states, the energy of the system,  $E$ , is quantized, allowing only discrete solutions, i.e.  $E \rightarrow E_n$  and  $|\psi\rangle \rightarrow |\psi_n\rangle$ . Since Eq. 2.36 is an eigenvalue equation for the Hermitian operator,  $\hat{H}_0$ , the time-independent state vectors,  $\{|\psi_n\rangle\}$ , build a complete basis of orthonormal vectors of the system. Therefore, we can write any bound state in the so-called spectral representation as a linear superposition of bound eigenstates with their respective time-dependent phase,

$$|\Psi(t)\rangle = \sum_n c_n |\psi_n\rangle e^{-iE_n t}. \quad (2.39)$$

This solution coincides with the time evolution of a state vector with a time-independent Hamiltonian, Eq. 2.23, with  $|\Psi(t_0)\rangle = \sum_n c_n |\psi_n\rangle$ .

## 2.2. Light-matter interaction

In this work, light-matter interactions are treated semi-classically, describing the light field classically, while the atom/molecule is described quantum mechanically. This section follows approaches from the literature<sup>[72-76]</sup>.

### 2.2.1. Light-matter interaction Hamiltonian

The basis of classic electrodynamics are the Maxwell equations<sup>[77]</sup>, where an electromagnetic field is characterized by the electric field,  $\mathcal{E}(\mathbf{r}, t)$ , and the magnetic field,  $\mathcal{B}(\mathbf{r}, t)$ . These are expressed as

$$\mathcal{E}(\mathbf{r}, t) = -\frac{\partial \mathcal{A}(\mathbf{r}, t)}{\partial t} - \nabla \phi(\mathbf{r}, t) \quad (2.40)$$

$$\mathcal{B}(\mathbf{r}, t) = \nabla \times \mathcal{A}(\mathbf{r}, t) \quad (2.41)$$

with the vector and scalar potentials,  $\mathcal{A}(\mathbf{r}, t)$  and  $\phi(\mathbf{r}, t)$ , respectively. These potentials are not uniquely defined since the electric and magnetic field are invariant under the so-called classical gauge transformation<sup>[74,78,79]</sup>,

$$\mathcal{A}(\mathbf{r}, t) \rightarrow \mathcal{A}'(\mathbf{r}, t) = \mathcal{A}(\mathbf{r}, t) + \nabla F(\mathbf{r}, t), \quad (2.42)$$

$$\phi(\mathbf{r}, t) \rightarrow \phi'(\mathbf{r}, t) = \phi(\mathbf{r}, t) - \frac{\partial F(\mathbf{r}, t)}{\partial t}. \quad (2.43)$$

Any arbitrary real, differentiable function  $F(\mathbf{r}, t)$  in the relations above leads to the same electromagnetic field. In order to obtain unique definitions for the potentials, an additional

condition, i.e. gauge fixing, is needed. A common gauge employed in semi-classical light-matter interaction is the Coulomb gauge (or minimal coupling),

$$\nabla \cdot \mathcal{A}(\mathbf{r}, t) = 0. \quad (2.44)$$

This is often used when additionally no scalar potential (no source) is present,  $\phi(\mathbf{r}, t) = 0$ , yielding the fields

$$\mathcal{E}(\mathbf{r}, t) = -\frac{\partial \mathcal{A}(\mathbf{r}, t)}{\partial t}, \quad (2.45)$$

$$\mathcal{B}(\mathbf{r}, t) = \nabla \times \mathcal{A}(\mathbf{r}, t). \quad (2.46)$$

Other gauges, such as the Lorentz gauge, lightcone gauge, temporal gauge, and axial gauge, can be found in the literature<sup>[75,78,79]</sup> but are not relevant to this work.

In order to arrive at a general expression describing light-matter interaction, we start with the non-relativistic Hamiltonian of one electron in an electromagnetic field. This is derived from the classic Lagrangian of a particle with mass  $m$  and charge  $q$  in an electromagnetic field<sup>[80]</sup>, yielding the Hamiltonian

$$H(t) = \frac{1}{2m} [\mathbf{p} - q\mathcal{A}(\mathbf{r}, t)]^2 + q\phi(\mathbf{r}, t) \quad (2.47)$$

$$= \frac{\mathbf{p}^2}{2m} + \frac{q}{2m} [\mathcal{A}(\mathbf{r}, t) \cdot \mathbf{p} + \mathbf{p} \cdot \mathcal{A}(\mathbf{r}, t)] + \frac{q^2}{2m} \mathcal{A}^2(\mathbf{r}, t) - q\phi(\mathbf{r}, t) \quad (2.48)$$

in the so-called external field approximation that assumes that the backreaction of the system on the electromagnetic field is negligible. Using the canonical quantization procedure (correspondence principle), momentum is substituted by the momentum operator,  $\hat{\mathbf{p}} = -i\hbar\nabla$ . Additionally, we assume no sources and the Coulomb gauge that allows the momentum operator and the vector potential in Eq. 2.48 to commute,

$$\hat{H}(t) = \frac{1}{2m} [\hat{\mathbf{p}} - q\mathcal{A}(\mathbf{r}, t)]^2 \quad (2.49)$$

$$= \frac{1}{2m} \hat{\mathbf{p}}^2 - \frac{q}{m} \hat{\mathbf{p}} \cdot \mathcal{A}(\mathbf{r}, t) + \frac{q^2}{2m} \mathcal{A}^2(\mathbf{r}, t) \quad (2.50)$$

$$= H_0 + H_{\text{int}}(t). \quad (2.51)$$

This results in an interaction Hamiltonian that is easily extended to  $N$ -particle systems,

$$\hat{H}_{\text{int}}(t) = -\sum_{i=1}^N \frac{q_i}{m_i} \hat{\mathbf{p}}_i \cdot \mathcal{A}(\mathbf{r}_i, t) + \sum_{i=1}^N \frac{q_i^2}{2m_i} \mathcal{A}^2(\mathbf{r}_i, t). \quad (2.52)$$

Thus, the TDSE describing the interaction of an  $N$ -particle system with an external

classical light field reads

$$i \frac{\partial}{\partial t} |\Psi(t)\rangle = [\hat{H}_0 + \hat{H}_{\text{int}}(t)] |\Psi(t)\rangle, \quad (2.53)$$

where  $\hat{H}_0$  is the system's time-independent Hamiltonian. Note that the interaction Hamiltonian,  $\hat{H}_{\text{int}}(t)$ , can be used in perturbation theory as a time-dependent interaction,  $\hat{W}(t)$ , as introduced in subsection 2.1.3. The perturbation order determines the number of interactions of the system with a single photon.

### 2.2.2. Dipole approximation and gauge transformation

In Eq. 2.42 and 2.43, we introduced the classical gauge transformations for electromagnetic fields. The same concept holds for semi-classical light-matter interaction where it is extended to the wave function, giving the quantum mechanical gauge transformation<sup>[72,74,75]</sup>,

$$\mathcal{A}(\mathbf{r}_i, t) \rightarrow \mathcal{A}'(\mathbf{r}_i, t) = \mathcal{A}(\mathbf{r}_i, t) + \nabla F(\mathbf{r}_i, t), \quad (2.54)$$

$$\phi(\mathbf{r}_i, t) \rightarrow \phi'(\mathbf{r}_i, t) = \phi(\mathbf{r}_i, t) - \frac{\partial F(\mathbf{r}_i, t)}{\partial t}, \quad (2.55)$$

$$|\Psi(t)\rangle \rightarrow |\Psi'(t)\rangle = e^{iq_i F(\mathbf{r}_i, t)} |\Psi(t)\rangle. \quad (2.56)$$

The TDSE for light-matter interaction of an  $N$ -particle system (Eq. 2.53) is invariant under these gauge transformations, where  $F(\mathbf{r}_i, t)$  is an arbitrary real, differentiable function depending on time and the spatial coordinates  $\mathbf{r}_i$  of each particle  $i$ .

For electromagnetic fields with a wavelength  $\lambda$  much larger than the spatial extent of the system  $d$ , i.e.  $\lambda \gg d$ , the dipole approximation is applied<sup>[59,81,82]</sup>. One assumes that the spatial variation of the electromagnetic field over the system is very small and, thus, the spatial dependence of the electromagnetic field is neglected. The vector potential becomes spatially homogeneous,  $\mathcal{A}(\mathbf{r}_i, t) = \mathcal{A}(t)$ , which automatically fulfils the Coulomb gauge (Eq. 2.44). Furthermore, the magnetic field vanishes, leaving the full description of the field as

$$\mathcal{E}(t) = -\frac{d}{dt} \mathcal{A}(t). \quad (2.57)$$

Within the dipole approximation, two quantum mechanical gauge transformations (recall Eq. 2.54 - 2.56) are readily applied. In the velocity gauge, the time-dependent function

$$F(t) = \sum_{i=1}^N \frac{q_i}{2m_i} \int_{-\infty}^t \mathcal{A}^2(t') dt' \quad (2.58)$$



is applied to give the velocity gauge expressions for the potentials and the state vector,

$$\mathcal{A}'(t) = \mathcal{A}(t), \quad (2.59)$$

$$\phi'(t) = -\sum_{i=1}^N \frac{q_i}{2m_i} \mathcal{A}^2(t), \quad (2.60)$$

$$|\Psi^v(t)\rangle = \exp \left[ i \sum_{i=1}^N \frac{q_i^2}{2m_i} \int_{-\infty}^t \mathcal{A}^2(t') dt' \right] |\Psi(t)\rangle. \quad (2.61)$$

The TDSE in the velocity gauge reads

$$i \frac{\partial}{\partial t} |\Psi^v(t)\rangle = \left[ H_0 - \sum_{i=1}^N \frac{q_i}{m_i} \hat{\mathbf{p}}_i \cdot \mathcal{A}(t) \right] |\Psi^v(t)\rangle. \quad (2.62)$$

Clearly, the  $\mathcal{A}^2(t)$  term is eliminated (compare Eq. 2.52), and the interaction Hamiltonian in the velocity gauge is

$$\hat{H}_{\text{int}}^v(t) = -\sum_{i=1}^N \frac{q_i}{m_i} \hat{\mathbf{p}}_i \cdot \mathcal{A}(t), \quad (2.63)$$

coupling the vector potential to the momentum operator. For the length gauge, a gauge transformation with

$$F(t) = -\sum_{i=1}^N \hat{\mathbf{r}}_i \cdot \mathcal{A}(t) \quad (2.64)$$

is performed, leading to

$$\mathcal{A}'(t) = 0, \quad (2.65)$$

$$\phi'(t) = -\sum_{i=1}^N \hat{\mathbf{r}}_i \cdot \mathcal{E}(t), \quad (2.66)$$

$$|\Psi^l(t)\rangle = \exp \left[ -i \sum_{i=1}^N q_i \hat{\mathbf{r}}_i \cdot \mathcal{A}(t) \right] |\Psi(t)\rangle. \quad (2.67)$$

The TDSE in the length gauge is of the form

$$i \frac{\partial}{\partial t} |\Psi^l(t)\rangle = \left[ H_0 - \sum_{i=1}^N q_i \hat{\mathbf{r}}_i \cdot \mathcal{E}(t) \right] |\Psi^l(t)\rangle \quad (2.68)$$

and gives the interaction Hamiltonian in the length gauge as

$$\hat{H}_{\text{int}}^l(t) = -\sum_{i=1}^N q_i \hat{\mathbf{r}}_i \cdot \mathcal{E}(t) = -\hat{\boldsymbol{\mu}} \cdot \mathcal{E}(t). \quad (2.69)$$

Thus, in the length gauge, the electric field couples to the position or, more precisely, the

dipole moment operator,  $\hat{\boldsymbol{\mu}} = \sum_{i=1}^N q_i \hat{\mathbf{r}}_i$ . Note that all formulas throughout this chapter have been for an arbitrarily charged particle. For electrons in specific, the length gauge couples the electric field to the electric dipole moment operator defined as  $\hat{\boldsymbol{\mu}}_{\text{el}} = -\sum_{i=j}^{N_{\text{el}}} \hat{\mathbf{r}}_j$ .

In Eq. 2.56, we have seen that a gauge transformation on the wave function is a unitary transformation, meaning that observables calculated in the different gauges give identical results. However, this is only true if no additional approximations are introduced. Moreover, from a numerical implementation point of view, one might prefer one gauge over the other. For example, propagating a free electron (i.e. no Coulomb interaction) under the influence of an external field can be done solely in momentum space if operating in the velocity gauge, whereas the length gauge needs both momentum and position representation, which is computationally more expensive. Additionally, by switching to a pure momentum space propagation once the Coulomb interaction is negligible, one does not need an infinitely large spatial grid and can use cut-off functions to collect outgoing electronic wave packets. This is used in section 4.1.

### 2.2.3. Light pulses and chirps

For the numerical TDSE implementations in this work, light-matter interaction is investigated using linearly polarised light pulses. Furthermore, the dipole approximation and the velocity gauge are applied. In this framework, we define a light pulse by its vector potential as  $\mathcal{A}(t) = \mathcal{A}(t)\mathbf{e}$ , where  $\mathbf{e}$  is the unit vector along the polarisation direction and

$$\mathcal{A}(t) = -\frac{f(t)}{\omega_0} \sin(\omega_0 t) \quad (2.70)$$

with  $f(t) = \mathcal{E}_0 g(t)$ , where  $f(t)$ ,  $g(t)$ ,  $\mathcal{E}_0$  and  $\omega_0$  are the field amplitude, the envelope function, the field strength and the carrier frequency, respectively. The electric field along the polarisation direction is obtained via Eq. 2.57,

$$\mathcal{E}(t) = -\frac{d}{dt} \mathcal{A}(t) \quad (2.71)$$

$$= \mathcal{E}_0 \left[ g(t) \cos(\omega_0 t) - \frac{dg(t)}{dt} \sin(\omega_0 t) \right]. \quad (2.72)$$

Notably, the second term depends on the time derivative of the envelope. In the slowly varying envelope approximation (SVEA), it is assumed that the envelope function varies little within one optical cycle<sup>[83]</sup> and, thus,

$$\mathcal{E}(t) = \mathcal{E}_0 g(t) \cos(\omega_0 t). \quad (2.73)$$

This approximation is valid for long pulses that consist of several optical cycles. For ultrashort, few-cycle pulses, the second term in Eq. 2.72 has to be incorporated. Its effects are part of the research work presented in section 4.2.

An alternative but equivalent description of the electric field is via its frequency domain

representation. This is obtained by Fourier decomposition into monochromatic waves,

$$\mathcal{E}(t) = \frac{1}{2\pi} \int_{-\infty}^{\infty} \tilde{\mathcal{E}}(\omega) e^{i\omega t} d\omega. \quad (2.74)$$

In turn, the complex-valued spectrum,  $\tilde{\mathcal{E}}(\omega)$ , is recovered by the Fourier inversion theorem,

$$\tilde{\mathcal{E}}(\omega) = \int_{-\infty}^{\infty} \mathcal{E}(t) e^{-i\omega t} dt. \quad (2.75)$$

Since the electric field in the time domain is real-valued,  $\tilde{\mathcal{E}}(\omega)$  is Hermitian and obeys

$$\tilde{\mathcal{E}}(\omega) = \tilde{\mathcal{E}}^*(-\omega). \quad (2.76)$$

This means that knowledge about positive frequencies is sufficient to fully characterize the spectrum, and we can define

$$\tilde{\mathcal{E}}^+(\omega) = \begin{cases} \tilde{\mathcal{E}}(\omega) & \text{for } \omega \geq 0 \\ 0 & \text{for } \omega < 0. \end{cases} \quad (2.77)$$

Analogous to Eq. 2.74, a complex-valued temporal function containing only the positive frequency part of the spectrum is obtained via

$$\mathcal{E}^+(t) = \frac{1}{2\pi} \int_{-\infty}^{\infty} \tilde{\mathcal{E}}^+(\omega) e^{i\omega t} d\omega. \quad (2.78)$$

In optics, this is known as the analytic signal. Because the actual electric field,  $\mathcal{E}(t)$ , is real, using the complex representation often simplifies Fourier analysis, as will be apparent soon. Similarly, the Fourier pair  $\tilde{\mathcal{E}}^-(\omega)/\mathcal{E}^-(t)$  with the negative frequency parts can be defined, and we get the relations

$$\begin{aligned} \mathcal{E}(t) &= \mathcal{E}^+(t) + \mathcal{E}^-(t) \\ &= 2\Re \{ \mathcal{E}^+(t) \} \\ &= 2\Re \{ \mathcal{E}^-(t) \} \quad \text{and} \end{aligned} \quad (2.79)$$

$$\tilde{\mathcal{E}}(\omega) = \tilde{\mathcal{E}}^+(\omega) + \tilde{\mathcal{E}}^-(\omega). \quad (2.80)$$

Since  $\mathcal{E}^+(t)$  and  $\tilde{\mathcal{E}}^+(\omega)$  are complex-valued, they can be expressed uniquely in terms of their amplitude and phase,

$$\mathcal{E}^+(t) = \frac{f(t)}{2} e^{i\Phi(t)}, \quad (2.81)$$

$$\tilde{\mathcal{E}}^+(\omega) = \tilde{f}(\omega) e^{-i\tilde{\Phi}(\omega)}. \quad (2.82)$$

Here,  $f(t)$  is the temporal amplitude (recall Eq. 2.70),  $\Phi(t)$  is the temporal phase,  $\tilde{f}(\omega)$  is

the spectral amplitude, and  $\tilde{\Phi}(\omega)$  is the spectral phase. The temporal phase,  $\Phi(t)$ , contains frequency vs time information yielding the definition for the instantaneous frequency,

$$\omega(t) = \frac{d\Phi(t)}{dt}, \quad (2.83)$$

while the spectral phase,  $\tilde{\Phi}(\omega)$ , contains time vs frequency information describing the relative temporal delay of a given spectral part as the group delay,

$$T_g(\omega) = \frac{d\tilde{\Phi}(\omega)}{d\omega}. \quad (2.84)$$

Moreover, one can define the spectral intensity as

$$\mathcal{I}(\omega) = \left| \tilde{\mathcal{E}}^+(\omega) \right|^2 = \tilde{f}^2(\omega), \quad (2.85)$$

proportional to the power spectrum density measured in experiments with a spectrometer.

In Eq. 2.73, the temporal phase was  $\Phi(t) = \omega_0 t$ , giving the constant instantaneous frequency  $\omega(t) = \omega_0$ . In a more general case, the temporal phase can be expanded into a Taylor series around  $t_0$ <sup>[73,84]</sup>,

$$\Phi(t) = \sum_{n=0}^{\infty} \frac{1}{n!} \left. \frac{\partial^n \Phi(t)}{\partial t^n} \right|_{t_0} (t - t_0)^n \quad (2.86)$$

$$= \phi(t_0) + \left. \frac{\partial \Phi(t)}{\partial t} \right|_{t_0} (t - t_0) + \frac{1}{2} \left. \frac{\partial^2 \Phi(t)}{\partial t^2} \right|_{t_0} (t - t_0)^2 + \dots \quad (2.87)$$

$$= \phi_{\text{CE}} + \omega_0(t - t_0) + \frac{\phi''}{2}(t - t_0)^2 + \dots \quad (2.88)$$

The first term  $\phi(t_0) = \phi_{\text{CE}}$  is the constant temporal phase, also known as the absolute phase or carrier-envelope phase (CEP). It describes the temporal relation of the pulse's envelope to the carrier oscillations and, therefore, becomes relevant for ultrashort pulses comprised of few optical cycles. The second term is the carrier frequency,  $\omega_0(t - t_0)$ , and the third term contains the quadratic temporal phase,  $\phi''$ . Including the first two terms leads to a light pulse with a constant instantaneous frequency (see above and Eq. 2.73). Such pulses are called Fourier-transform-limited or bandwidth-limited. The addition of the third term results in a so-called linear chirp with a non-constant instantaneous frequency, i.e. a non-zero temporal derivative of the instantaneous frequency,  $\phi'' = \frac{d\omega(t)}{dt} = \frac{d^2\Phi(t)}{dt^2}$ , that allows us to differentiate between

$$\frac{d\omega(t)}{dt} < 0 \quad (\text{down-chirped}), \quad (2.89)$$

$$\frac{d\omega(t)}{dt} = 0 \quad (\text{unchirped}), \quad (2.90)$$

$$\frac{d\omega(t)}{dt} > 0 \quad (\text{up-chirped}). \quad (2.91)$$

Thus, a positive linear chirp (up-chirped) leads to an increasing instantaneous frequency over time, while a negative linear chirp (down-chirped) gives a light pulse with a decreasing instantaneous frequency. Crucially, the temporal amplitude stays unchanged. The inclusion of higher-order terms in Eq. 2.88 is referred to as  $(n - 1)$ th order chirp. A temporal chirp leads to changes in the spectral intensity, which is contrary to the experimental means of light pulse chirping. Here, the spectral instead of the temporal phase is altered by propagating the light pulse through dispersive media. This corresponds to a Taylor series expansion of the spectral phase,  $\tilde{\Phi}(\omega)$ , around  $\omega_0$ ,

$$\tilde{\Phi}(\omega) = \sum_{n=0}^{\infty} \frac{1}{n!} \left. \frac{\partial^n \tilde{\Phi}(\omega)}{\partial \omega^n} \right|_{\omega_0} (\omega - \omega_0)^n \quad (2.92)$$

$$= \tilde{\phi}(\omega_0) + \left. \frac{\partial \tilde{\Phi}(\omega)}{\partial \omega} \right|_{\omega_0} (\omega - \omega_0) + \frac{1}{2} \left. \frac{\partial^2 \tilde{\Phi}(\omega)}{\partial \omega^2} \right|_{\omega_0} (\omega - \omega_0)^2 + \dots \quad (2.93)$$

$$= -\phi_{\text{CE}} + \tilde{\phi}'(\omega - \omega_0) + \frac{\tilde{\phi}''}{2} (\omega - \omega_0)^2 + \dots \quad (2.94)$$

The first term represents the absolute phase introduced above,  $\tilde{\phi}(\omega_0) = -\phi_{\text{CE}}$ , where the minus sign originates from the phase relations between  $\mathcal{E}^+(t)$  and  $\tilde{\mathcal{E}}^+(\omega)$  (see Eq. 2.81 and 2.82). The second term with the linear spectral phase of  $\tilde{\phi}'$  indicates a temporal translation of the pulse's envelope (via Fourier shift theorem). The second term contains the quadratic spectral phase,  $\tilde{\phi}''$ . It causes changes in the temporal structure of the pulse, influencing both instantaneous frequency and the temporal amplitude without altering the spectral amplitude. This stretches a pulse in time while maintaining its spectral intensity. We will revisit this in section 4.2. Depending on the sign of  $\tilde{\phi}''$ , the light pulse is linearly up- or down-chirped. Again, one can distinguish via  $\tilde{\phi}'' = \frac{dT_g(\omega)}{d\omega} = \frac{d^2\tilde{\Phi}(\omega)}{d\omega^2}$  between

$$\frac{dT_g(\omega)}{d\omega} < 0 \quad (\text{down-chirped}), \quad (2.95)$$

$$\frac{dT_g(\omega)}{d\omega} = 0 \quad (\text{unchirped}), \quad (2.96)$$

$$\frac{dT_g(\omega)}{d\omega} > 0 \quad (\text{up-chirped}). \quad (2.97)$$

A straightforward example to see some of these effects is using the commonly applied Gaussian envelope function,

$$g(t) = e^{-\beta t^2}, \quad (2.98)$$

$$f(t) = \mathcal{E}_0 g(t) = \mathcal{E}_0 e^{-\beta t^2} \quad (2.99)$$

with

$$\beta = \frac{4 \ln 2}{\tau_E^2} = \frac{2 \ln 2}{\tau_I^2} \quad (2.100)$$

and  $t_0 = 0$ . Here,  $\tau_E$  is the light pulse duration given as the full width at half maximum (FWHM) of the Gaussian, while  $\tau_I$  is the pulse duration based on the FWHM of the (experimentally accessible) temporal intensity function,

$$\mathcal{I}(t) = \frac{1}{2}\epsilon_0 c n f^2(t), \quad (2.101)$$

with the vacuum dielectric constant  $\epsilon_0$ , the speed of light  $c$ , and the refractive index  $n$ . We can write a Fourier-transform limited Gaussian light pulse in time and spectral regime as

$$\mathcal{E}^+(t) = \frac{\mathcal{E}_0}{2} e^{-\frac{2\ln 2}{\tau_I} t^2} e^{i[\omega_0 t + \phi_{CE}]} \quad (2.102)$$

$$= \frac{\mathcal{E}_0}{2} e^{-\beta t^2} e^{i[\omega_0 t + \phi_{CE}]} \quad \text{and} \quad (2.103)$$

$$\tilde{\mathcal{E}}^+(\omega) = \frac{\mathcal{E}_0 \tau_I}{2} \sqrt{\frac{\pi}{2 \ln 2}} e^{-\frac{\tau_I^2}{8 \ln 2} (\omega - \omega_0)^2} e^{i\phi_{CE}} \quad (2.104)$$

$$= \tilde{\mathcal{E}}_0 e^{-\tilde{\beta} (\omega - \omega_0)^2} e^{i\phi_{CE}} \quad (2.105)$$

with  $\tilde{\mathcal{E}}_0 = \frac{\mathcal{E}_0 \tau_I}{2} \sqrt{\frac{\pi}{2 \ln 2}}$ ,  $\tilde{\beta} = (4\beta)^{-1} = \frac{\tau_I^2}{8 \ln 2} = \frac{2 \ln 2}{\omega_I^2}$ , which gives us the relation of the temporal and spectral amplitude for Fourier-transform limited Gaussian light pulses as

$$\tau_I \bar{\omega}_I = 4 \ln 2, \quad (2.106)$$

$$\tau_E \bar{\omega}_E = 8 \ln 2. \quad (2.107)$$

Here,  $\bar{\omega}_E$  and  $\bar{\omega}_I$  are the FWHM of the spectral amplitude and spectral intensity, respectively. These relations show the inverse proportionality of time and spectral domain, i.e. an ultrashort light pulse has an extremely broad spectrum, while a long pulse has a narrow spectrum. Next, we add a quadratic spectral phase term (recall Eq. 2.94) to the spectrum in Eq. 2.105,

$$\tilde{\mathcal{E}}^+(\omega) = \tilde{\mathcal{E}}_0 e^{-\tilde{\beta} (\omega - \omega_0)^2} e^{-i\frac{1}{2}\tilde{\phi}'' (\omega - \omega_0)^2 + i\phi_{CE}}, \quad (2.108)$$

and the Fourier inversion (Eq. 2.78) gives us the electric field in time,

$$\mathcal{E}^+(t) = \frac{\mathcal{E}_0}{2 \left(1 + 4\beta^2 \tilde{\phi}''^2\right)^{1/4}} e^{-\frac{\beta}{1 + 4\beta^2 \tilde{\phi}''^2} t^2} e^{i[\omega_0 t + \phi_{CE}]} e^{i\frac{2\tilde{\phi}''^2 \beta^2}{1 + 4\beta^2 \tilde{\phi}''^2} t^2} \quad (2.109)$$

$$= \mathcal{E}_0^c e^{-\beta_c t^2} e^{i[\omega_0 t + \phi_{CE}]} e^{i(2\tilde{\phi}''^2 \beta_c \beta) t^2}, \quad (2.110)$$

with  $\beta_c = \beta / (1 + 4\beta^2 \tilde{\phi}''^2)$ . Thus, as discussed above, the quadratic spectral phase term,  $\frac{1}{2}\tilde{\phi}'' (\omega - \omega_0)^2$ , leads to linear chirp in time with a quadratic temporal phase of  $\phi'' = 2\tilde{\phi}''^2 \beta_c \beta$  and a broadening of the temporal amplitude ( $\beta \rightarrow \beta_c$ ). Since the quadratic spectral phase term only influences the spectral phase, the spectral amplitude and the spectral intensity

remain unchanged. The temporal broadening can be calculated as

$$\tau_E^c = \sqrt{\tau_E^2 + \left(8 \ln 2 \frac{\phi''}{\tau_E}\right)^2}, \quad (2.111)$$

$$\tau_I^c = \sqrt{\tau_I^2 + \left(4 \ln 2 \frac{\phi''}{\tau_I}\right)^2}. \quad (2.112)$$

How chirped pulses can be obtained for ultrashort, few-cycle pulses beyond the SVEA, is a part of the research presented in section 4.2.

## 2.3. Molecular systems

So far, we mainly presented the Hamiltonian as an abstract operator describing a system and its (external) interactions. In this section, we introduce the time-independent Hamiltonian for molecular systems and discuss common concepts applied in quantum chemistry and molecular excited-state dynamics. Throughout the section, we assume states and operators to be in coordinate space.

### 2.3.1. Molecular Hamiltonian

For a molecule consisting of  $N_e$  electrons with coordinate vectors  $\mathbf{r} = \{\mathbf{r}_1, \mathbf{r}_2, \dots, \mathbf{r}_{N_e}\}$  and  $N_N$  nuclei with coordinate vectors  $\mathbf{R} = \{\mathbf{R}_1, \mathbf{R}_2, \dots, \mathbf{R}_{N_N}\}$ , the time-independent Hamiltonian reads

$$\hat{H}(\mathbf{r}, \mathbf{R}) = \hat{T}_e(\mathbf{r}) + \hat{T}_N(\mathbf{R}) + \hat{V}_{e,e}(\mathbf{r}) + \hat{V}_{N,N}(\mathbf{R}) + \hat{V}_{e,N}(\mathbf{r}, \mathbf{R}) \quad (2.113)$$

with the kinetic energy operator for electrons and nuclei,

$$\hat{T}_e(\mathbf{r}) = - \sum_{i=1}^{N_e} \frac{1}{2} \nabla_i^2 \quad (2.114)$$

$$\hat{T}_N(\mathbf{R}) = - \sum_{\alpha=1}^{N_N} \frac{1}{2M_\alpha} \nabla_\alpha^2, \quad (2.115)$$

and the electron-electron, nucleus-nucleus, and electron-nucleus Coulomb interactions,

$$\hat{V}_{e,e}(\mathbf{r}) = \sum_{i=1}^{N_e} \sum_{j>i}^{N_e} \frac{1}{|\mathbf{r}_i - \mathbf{r}_j|} \quad (2.116)$$

$$\hat{V}_{N,N}(\mathbf{R}) = \sum_{\alpha=1}^{N_N} \sum_{\beta>\alpha}^{N_N} \frac{Z_\alpha Z_\beta}{|\mathbf{R}_\alpha - \mathbf{R}_\beta|} \quad (2.117)$$

$$\hat{V}_{e,N}(\mathbf{r}, \mathbf{R}) = - \sum_{i=1}^{N_e} \sum_{\alpha=1}^{N_N} \frac{Z_\alpha}{|\mathbf{r}_i - \mathbf{R}_\alpha|}. \quad (2.118)$$

Here,  $i$  and  $j$  refer to the electron coordinates,  $\alpha$  and  $\beta$  to the nuclear coordinates,  $\nabla_i = \frac{\partial}{\partial \mathbf{r}_i}$ ,  $\nabla_\alpha = \frac{\partial}{\partial \mathbf{R}_\alpha}$  are the gradients,  $M_\alpha$  is the mass of nucleus  $\alpha$ , and  $Z_\alpha$  the electromagnetic charge of nucleus  $\alpha$ . The coupling of electronic and nuclear degrees of freedom via the Coulomb interaction term  $\hat{V}_{e,n}(\mathbf{r}, \mathbf{R})$  presents a challenge for all but small model systems. For simple model systems, as presented in this work in sections 4.1 and 4.4, the eigenvalue problem corresponding to the molecular Hamiltonian can be solved numerically with the methods described in chapter 3. For most other molecular systems, quantum chemical methods need to be employed, which are briefly introduced in the next subsection.

### 2.3.2. Quantum chemistry

To describe molecular systems, it is common to separate the molecular eigenvalue problem into a nuclear and electronic Schrödinger equation by expanding the wave function,  $|\Psi\rangle$ , into a basis of electronic wave functions,  $\{|\varphi_n\rangle\}$ , which in coordinate space gives

$$\Psi(\mathbf{r}, \mathbf{R}) = \sum_n \varphi_n(\mathbf{r}; \mathbf{R}) \chi_n(\mathbf{R}) \quad (2.119)$$

with the nuclear wave function,  $\chi_n(\mathbf{R})$ , being the expansion coefficient. This allows the formulation of an electronic TISE,

$$\hat{H}_e(\mathbf{r}; \mathbf{R}) \varphi_n(\mathbf{r}; \mathbf{R}) = E_n(\mathbf{R}) \varphi_n(\mathbf{r}; \mathbf{R}), \quad (2.120)$$

with the electronic Hamiltonian,

$$\hat{H}_e(\mathbf{r}; \mathbf{R}) = \hat{T}_e(\mathbf{r}) + \hat{V}_{e,e}(\mathbf{r}) + \hat{V}_{N,N}(\mathbf{R}) + \hat{V}_{e,N}(\mathbf{r}; \mathbf{R}). \quad (2.121)$$

Crucially, the electronic Hamiltonian and the electronic wave function depend only parametrically on the nuclear coordinates. The eigenenergies of the electronic Schrödinger equation,  $E_n(\mathbf{R})$ , build the adiabatic potential energy landscape. Finding approximations to solve the electronic TISE and obtaining the potential energy landscape for molecules of various sizes is a cornerstone of quantum chemistry.

Using the expansion in Eq. 2.119 and the definition of the electronic Hamiltonian, the total TISE is

$$\sum_n \left[ \hat{T}_N(\mathbf{R}) + \hat{H}_e(\mathbf{r}; \mathbf{R}) \right] \varphi_n(\mathbf{r}; \mathbf{R}) \chi_n(\mathbf{R}) = E \sum_n \varphi_n(\mathbf{r}; \mathbf{R}) \chi_n(\mathbf{R}). \quad (2.122)$$

For a given electronic eigenstate  $|\varphi_m\rangle$ , this equation can be transformed to yield a coupled set of equations for the nuclear TISE in the basis of the electronic eigenstates,

$$\sum_n \left[ \hat{T}_N(\mathbf{R}) \delta_{mn} + T_{mn}^{(1)}(\mathbf{R}) + T_{mn}^{(2)}(\mathbf{R}) + E_n(\mathbf{R}) \delta_{mn} \right] \chi_n(\mathbf{R}) = E \chi_m(\mathbf{R}), \quad (2.123)$$



with the so-called non-adiabatic or kinetic coupling terms,

$$T_{mn}^{(1)}(\mathbf{R}) = - \sum_{\alpha=1}^{N_N} \frac{1}{M_\alpha} \langle \varphi_m | \nabla_\alpha | \varphi_n \rangle_r \nabla_\alpha, \quad (2.124)$$

$$T_{mn}^{(2)}(\mathbf{R}) = - \sum_{\alpha=1}^{N_N} \frac{1}{2M_\alpha} \langle \varphi_m | \nabla_\alpha^2 | \varphi_n \rangle_r. \quad (2.125)$$

In Eq. 2.123, the electronic eigenvalue, i.e. the potential energy landscape, becomes the diagonal potential energy operator, while the kinetic operator has off-diagonal elements. These describe the coupling of different electronic eigenstates via derivatives with respect to the nuclear degrees of freedom. Calculating these coupling elements poses a great challenge for systems with several nuclear degrees of freedom and many electronic states. Therefore, various approximations are commonly applied. Within the Born-Huang approximation<sup>[85]</sup>, the off-diagonal coupling terms are neglected, leading to the diagonal equation

$$\left[ T_N(\mathbf{R}) + E_m(\mathbf{R}) + T_{mm}^{(2)}(\mathbf{R}) \right] \chi_m(\mathbf{R}) = E \chi_m(\mathbf{R}). \quad (2.126)$$

Note that the first-order coupling term vanishes due to symmetry. The Born-Oppenheimer approximation<sup>[86]</sup> neglects the coupling terms altogether, yielding the nuclear TISE in a single electronic state  $|\varphi_m\rangle$  as

$$\left[ T_N(\mathbf{R}) + E_m(\mathbf{R}) \right] \chi_m(\mathbf{R}) = E \chi_m(\mathbf{R}). \quad (2.127)$$

Therefore, the nuclear wave functions in different electronic eigenstates are decoupled. This approximation becomes extremely crude near avoided crossings and conical intersections. For more detail, we refer the reader to standard quantum chemistry literature<sup>[87–90]</sup>.

### 2.3.3. Molecular excited-state dynamics

To unravel photophysical and photochemical processes, it is essential to understand the relaxation dynamics of nuclear wave packets along excited electronic states. Knowing the solutions to the electronic and nuclear TISE would allow a solution via the trivial time-dependence in the spectral representation as introduced in Eq. 2.39. However, calculating a sufficiently large amount of nuclear and electronic wave functions is cumbersome and restricted to a few degrees of freedom. Alternatively, the time-dependent nuclear wave packets can be directly introduced in the expansion above (Eq. 2.119), substituting the time-independent nuclear eigenstate to yield the time-dependent wave function,

$$\tilde{\Psi}(\mathbf{r}, \mathbf{R}, t) = \sum_{n=0}^{N_S} \varphi_n(\mathbf{r}; \mathbf{R}) \tilde{\chi}_n(\mathbf{R}, t). \quad (2.128)$$

The expansion is truncated to include  $N_S$  electronic states relevant to the dynamics. On each electronic state evolves one nuclear wave packet. One approach to solve this ansatz is to use numerical grid propagators (see, e.g. section 3.2). These require pre-calculation of the electronic TISE to obtain the potential energy landscape to, subsequently, propagate nuclear wave packets on these electronic states using a time-dependent version of Eq. 2.123. This is only possible in a few dimensions or model systems and necessitates the computation of the costly non-adiabatic couplings (Eq. 2.124 and 2.125) to describe transitions between electronic states.

A common alternative is the so-called direct dynamics method. Here, the nuclear wave packet,  $\tilde{\chi}_n(\mathbf{R}, t)$ , is approximated by  $N_{\text{traj}}$  classical or semi-classical trajectories that evolve on the electronic states and are defined by their position and momentum  $(\mathbf{R}_n(t), \mathbf{P}_n(t))$ . Importantly, the electronic TISE can be calculated on-the-fly for a given position  $\mathbf{R}_n$  of the trajectory, thus circumventing the need for a full dimensional pre-calculation of the potential energy landscape. The exact nature of the trajectories differentiates various methods in the field<sup>[91]</sup>. For example, surface hopping<sup>[92,93]</sup> uses  $\delta$ -functions for the nuclear wave packets that each evolve on a single electronic state at a time. Transitions between electronic states are realised via hopping probabilities. Other methods, like ab initio multiple spawning<sup>[94,95]</sup> and ab initio multiconfigurational Ehrenfest<sup>[96,97]</sup>, use Gaussian nuclear wave packets and allow simultaneous occupation of several electronic states or vary the number of trajectories during the dynamics.

## 3. Numerical methods

This chapter introduces the numerical methods employed to solve the TDSE on a grid. It is the basis for most of the research work described in chapter 4. We start with discretization for quantum mechanics on a grid, followed by common algorithms for time propagation and obtaining eigenstates. The chapter closely follows the theory introduced in section 2.1.

### 3.1. Quantum mechanics on a grid

Analytical solutions to the TDSE are only accessible for simple systems, such as the hydrogen atom. Numerical solutions are needed for any larger system and especially for a time-dependent Hamiltonian. To this end, the infinite-dimensional Hilbert space is projected on a finite, discrete basis, i.e. a grid. Thus, the wave function is not known at any arbitrary point in the Hilbert space but only at specific discrete points of the grid. Consequently, integration becomes summation over discrete points.

Commonly, position and momentum space are discretized,

$$\{|\mathbf{x}\rangle\} \rightarrow \{|\mathbf{x}_n\rangle\} \text{ and } \{|\mathbf{p}\rangle\} \rightarrow \{|\mathbf{p}_n\rangle\}, \quad (3.1)$$

which means that the wave function, defined in position and momentum space, as seen in Eq. 2.2 - 2.5, now reads

$$|\Psi(t)\rangle = \sum_n |\mathbf{x}_n\rangle \langle \mathbf{x}_n | \Psi(t) \rangle = \sum_n \Psi(\mathbf{x}_n, t) |\mathbf{x}_n\rangle \quad (3.2)$$

$$\text{with } \Psi(\mathbf{x}_n, t) = \langle \mathbf{x}_n | \Psi(t) \rangle \quad (3.3)$$

$$|\Psi(t)\rangle = \sum_n |\mathbf{p}_n\rangle \langle \mathbf{p}_n | \Psi(t) \rangle = \sum_n \Psi(\mathbf{p}_n, t) |\mathbf{p}_n\rangle \quad (3.4)$$

$$\text{with } \Psi(\mathbf{p}_n, t) = \langle \mathbf{p}_n | \Psi(t) \rangle. \quad (3.5)$$

Clearly, the wave function is only known at certain discrete points  $\mathbf{x}_n$  and  $\mathbf{p}_n$  in position and momentum space, respectively. This is trivially extended to higher dimensions in multi-particle cases (as done in section 4.1). As shown in Eq. 2.6 and 2.7, position and

momentum grid are related via Fourier transform,

$$\Psi(\mathbf{x}_n, t) = \frac{1}{\sqrt{2\pi}} \sum_m e^{+ip_m x_n} \Psi(\mathbf{p}_m, t) \quad (3.6)$$

$$\Psi(\mathbf{p}_n, t) = \frac{1}{\sqrt{2\pi}} \sum_m e^{-ip_n x_m} \Psi(\mathbf{x}_m, t). \quad (3.7)$$

This is known as discrete Fourier transform and can be implemented very efficiently, as shown by Frigo and Johnson<sup>[98]</sup>.

Regarding the implementation, a grid is defined by the number of grid points  $N_g$  and its spacing  $\Delta g$ . For a one-dimensional position grid, this means

$$\Delta x = \frac{x_{\text{end}} - x_{\text{start}}}{N_x - 1} \quad (3.8)$$

$$x_n = x_{\text{start}} + (n - 1)\Delta x \quad \text{with } n \in \{1, 2, \dots, N_x\} \quad (3.9)$$

with  $x_{\text{start}}$  and  $x_{\text{end}}$  defining the boundaries of the position grid. The corresponding momentum grid follows from Eq. 3.7 as

$$\Delta p = \frac{p_{\text{end}} - p_{\text{start}}}{N_x - 1} = \frac{2\pi}{N_x \Delta x} \quad (3.10)$$

$$p_n = \begin{cases} (n - 1)\Delta p & \text{for } n \in \{1, 2, \dots, N_x/2 + 1\} \\ -(N_x + 1 - n)\Delta p & \text{for } n \in \{N_x/2 + 2, \dots, N_x\} \end{cases} \quad (3.11)$$

where the upper (lower) case in Eq. 3.11 represents positive (negative) momenta.

In addition to position and momentum space, time can be discretized in numerical approaches. To this end, a time interval  $\Delta t$  and a number of time steps  $N_t$  are defined. Recalling subsection 2.1.2, the time evolution of a system is described by the time evolution operator (Eq. 2.14) with either a time-independent, commuting time-dependent, or general time-dependent Hamiltonian (Eq. 2.23 - 2.21). If the time interval is sufficiently small, the Hamiltonian (even if explicitly time-dependent) can be regarded as constant during  $\Delta t$ , giving rise to the short-time propagator,

$$\hat{U}(t + \Delta t, t) = e^{-i\hat{H}(t)\Delta t}. \quad (3.12)$$

In order to calculate a propagation of  $N_t$  steps from  $[t_0, t_{N_t}]$ , the short-time propagator is applied  $N_t$  times,

$$|\Psi(t_{N_t})\rangle = \prod_{n=1}^{N_t} \hat{U}(t_n, t_{n-1}) |\Psi(t_0)\rangle, \quad (3.13)$$

with  $t_n = t_{n-1} + \Delta t$ .

## 3.2. Split operator method

Next, we discuss the split operator technique that solves Eq. 3.13 by splitting the Hamiltonian into parts that each are diagonal in different representations of the wave function. Diagonal operators are applied by simple multiplication onto the wave function. If we recall Eq. 2.113, the time-independent molecular Hamiltonian consists of kinetic energy terms,  $\hat{T}$ , containing the second derivative in position space and potential energy terms,  $\hat{V}$ , diagonal in position space. The kinetic energy terms are diagonal in momentum space, which can be achieved by a single Fourier transform of the position space wave function,

$$e^{-i\hat{V}\Delta t}\Psi(\mathbf{x}_n, t) = e^{-iV(\mathbf{x}_n)\Delta t}\Psi(\mathbf{x}_n, t) \quad (3.14)$$

$$e^{-i\hat{T}\Delta t}\mathcal{FT}\{\Psi(\mathbf{x}_n, t)\} = e^{-iT(\mathbf{p}_n)\Delta t}\Psi(\mathbf{p}_n, t). \quad (3.15)$$

Therefore, the key idea behind the split operator method is to apply the kinetic energy terms in momentum space and the potential energy terms in position space, while the transformation between spaces is done by Fourier transform (Eq. 3.6 and 3.7). However, since  $\hat{T}$  and  $\hat{V}$  do not commute, a simple separation of the short-time propagator into

$$e^{-i(\hat{T}+\hat{V})\Delta t} = e^{-i\hat{T}\Delta t}e^{-i\hat{V}\Delta t} + \mathcal{O}\left((\Delta t)^2\right), \quad (3.16)$$

leads to an error in the order of  $(\Delta t)^2$  (for more general details, see Baker-Campbell-Hausdorff formula or Lie product formula<sup>[99–103]</sup>). This becomes evident by the Maclaurin series expansion of the short-time propagator,

$$e^{-i(\hat{T}+\hat{V})\Delta t} = \sum_{n=0}^{\infty} \frac{(-i(\hat{T} + \hat{V})\Delta t)^n}{n!} \quad (3.17)$$

$$= 1 - i(\hat{T} + \hat{V})\Delta t - \frac{1}{2}(\hat{T}^2 + \hat{T}\hat{V} + \hat{V}\hat{T} + \hat{V}^2)(\Delta t)^2 + \dots, \quad (3.18)$$

and comparison to the approximation in Eq. 3.16,

$$e^{-i\hat{T}\Delta t}e^{-i\hat{V}\Delta t} = \sum_{n=0}^{\infty} \frac{(-i\hat{T}\Delta t)^n}{n!} \sum_{m=0}^{\infty} \frac{(-i\hat{V}\Delta t)^m}{m!} \quad (3.19)$$

$$= 1 - i(\hat{T} + \hat{V})\Delta t - \frac{1}{2}(\hat{T}^2 + \hat{V}^2 + 2\hat{T}\hat{V})(\Delta t)^2 + \dots \quad (3.20)$$

Clearly, the expressions in Eq. 3.18 and 3.20 differ in second-order of  $\Delta t$ . An improved splitting of the short-time propagator was proposed by Feit, Fleck and Steiger as

$$e^{-i(\hat{T}+\hat{V})\Delta t} = e^{-i\frac{1}{2}\hat{V}\Delta t}e^{-i\hat{T}\Delta t}e^{-i\frac{1}{2}\hat{V}\Delta t} + \mathcal{O}\left((\Delta t)^3\right) \quad (3.21)$$

and is called the symmetric or second-order split operator method<sup>[104]</sup>. A Maclaurin expansion will result in the same expression as for the explicit short-time-propagator

(Eq. 3.18) up to second-order and, thus, has only an error of  $\mathcal{O}((\Delta t)^3)$ . For small time steps,  $\Delta t$ , the error can be neglected. The complete single-step time propagation of the wave function reads

$$\Psi(\mathbf{x}_n, t + \Delta t) = e^{-i\frac{1}{2}\hat{V}\Delta t} \mathcal{F}\mathcal{T}^{-1} \left\{ e^{-i\hat{T}\Delta t} \mathcal{F}\mathcal{T} \left\{ e^{-i\frac{1}{2}\hat{V}\Delta t} \Psi(\mathbf{x}_n, t) \right\} \right\}. \quad (3.22)$$

The same principle can be applied to a time dependent Hamiltonian,  $\hat{H}(t) = \hat{H}_0 + \hat{H}_{\text{int}}$  (recall subsection 2.2.1). If the time-dependent interaction part,  $\hat{H}_{\text{int}}$ , is in the length gauge (Eq. 2.69), it is diagonal in position space and applied together with the potential operators. If  $\hat{H}_{\text{int}}$  is defined in the velocity gauge (Eq. 2.63), it is diagonal in momentum space and applied with the kinetic terms. Lastly, we point out that the algorithm does not work if position and momentum operators are coupled in the Hamiltonian.

### 3.3. Imaginary time propagation

A common tool to obtain eigenvectors and eigenenergies of a system's Hamiltonian,  $\hat{H}_0$ , is the relaxation method by Kosloff and Tal-Ezer<sup>[105]</sup>, which utilises imaginary time propagation. Neatly, this method incorporates the short-time propagator and split operator method introduced above. We start by defining the imaginary time  $\tau = -it$  and the imaginary time step  $\Delta\tau$  in order to obtain the short-time propagator in imaginary time,

$$\hat{U}(\Delta\tau) = e^{-\Delta\tau\hat{H}_0}. \quad (3.23)$$

Since  $\hat{H}_0$  is time-independent, the short-time propagator is identical for any given time  $t$  or rather imaginary time  $\tau$ . Next, we apply it to the spectral representation introduced in Eq. 2.39,

$$|\bar{\Psi}(\Delta\tau)\rangle = \hat{U}(\Delta\tau) |\Psi(0)\rangle \quad (3.24)$$

$$= \sum_n c_n e^{-E_n\Delta\tau} |\psi_n\rangle, \quad (3.25)$$

where we expanded the wave function  $|\Psi(0)\rangle$  in the Hamiltonian's complete eigenbasis  $|\Psi(0)\rangle = \sum_n c_n |\psi_n\rangle$ . By applying the non-unitary short-time propagator in imaginary time, each eigenstate observes an exponential damping,  $e^{-E_n\Delta\tau}$ , depending on the eigenenergy. Thus, eigenstates of lower quantum number  $n$  are damped less. The overline in  $|\bar{\Psi}(\Delta\tau)\rangle$  (Eq. 3.24) indicates loss of norm due to the damping; hence, re-normalization in each time step is needed,

$$|\Psi(\tau)\rangle = |\bar{\Psi}(\tau)\rangle \langle\bar{\Psi}(\tau)|\bar{\Psi}(\tau)\rangle^{-\frac{1}{2}}. \quad (3.26)$$

The algorithm starts with a guess for the initial state,  $|\Psi(0)\rangle$ , and successively applies the short time propagator in imaginary time (Eq. 3.23), for example, by using the split

operator method. In the limit  $\tau \rightarrow \infty$ , the initial wave function converges to the ground state,  $|\psi_0\rangle$ , as its eigenenergy has the lowest damping factor,

$$\lim_{\tau \rightarrow \infty} |\bar{\Psi}(\tau + \Delta\tau)\rangle = \lim_{\tau \rightarrow \infty} \hat{U}(\Delta\tau) |\Psi(\tau)\rangle \quad (3.27)$$

$$= e^{-iE_0\Delta\tau} |\psi_0\rangle. \quad (3.28)$$

By projecting  $|\bar{\Psi}(\tau + \Delta\tau)\rangle$  onto Eq. 3.28 from the left, the eigenenergy is obtained from the change in norm within one time step,

$$E_0 = -\frac{1}{2\Delta\tau} \ln \left[ \lim_{\tau \rightarrow \infty} \langle \bar{\Psi}(\tau + \Delta\tau) | \bar{\Psi}(\tau + \Delta\tau) \rangle \right]. \quad (3.29)$$

Eigenstates of higher quantum number  $n > 0$ , i.e. excited states, are calculated by projecting out all states of lower quantum number  $m < n$  in each imaginary time step,

$$|\Psi_n(\tau)\rangle = |\Psi(\tau)\rangle - \sum_{m=0}^{n-1} \langle \psi_m | \Psi(\tau) \rangle |\psi_m\rangle. \quad (3.30)$$





## 4. Results

We now present the theoretical results and discuss three kinds of high-frequency light-matter interaction in atoms and molecule: XUV ionisation (sections 4.1 and 4.2), x-ray absorption (section 4.3), and x-ray scattering (section 4.4).

Ionisation with XUV pulses is often regarded as a simple one-photon process in the single active electron picture. Section 4.1 will show that this simple picture disregards prominent (dynamic) particle correlation in molecules, such as electron-electron and nuclear-electron correlation. Incorporating particle correlation leads to interesting effects like shake and knock processes, time-delayed ionisation, and imprints in the photoelectron spectrum. Moreover, the dynamics induced by modulated, few-cycle XUV pulses in atomic photoionisation are discussed, and novel insight into the properties of such pulses is provided (section 4.2).

Going to the x-ray regime of high-frequency light-matter interaction gives rise to various phenomena, e.g. excitation or ionisation of core electrons, Auger-Meitner effect, or x-ray scattering. In section 4.3, we discuss how attosecond soft x-ray pulses from a table-top source can probe furan's complex non-adiabatic relaxation dynamics through core-level x-ray absorption near-edge spectroscopy (XANES). The experiment resolves - for the first time - the interplay of electron and vibrational coherences upon photoexcitation in a neutral molecule. We report the theoretical results that aided and explained the experiment.

X-ray scattering is the topic of section 4.4. Here, the contribution of ionisation to static and ultrafast x-ray scattering is discussed. Additionally, we contrast two theories to calculate scattering signals beyond the independent atom model and provide guidance for future developments in scattering simulations and experiments.

## 4.1. Correlation dynamics in molecular XUV ionisation

This section is based on:

- 1) F.G. Fröbel\*, K.M. Ziem\*, U. Peschel, S. Gräfe, A. Schubert, The impact of electron-electron correlation in ultrafast attosecond single ionization dynamics, *J. Phys. B.: At. Mol. Opt. Phys.*, **2020**, *53*, 144005 (section D.1)
- 2) K.M. Ziem\*, J. Bruhnke, V. Engel, S. Gräfe, Nuclear-electron correlation effects and their photoelectron imprint in molecular XUV ionisation, *Front. Chem.*, **2022**, *10*, 942633 (section D.2)

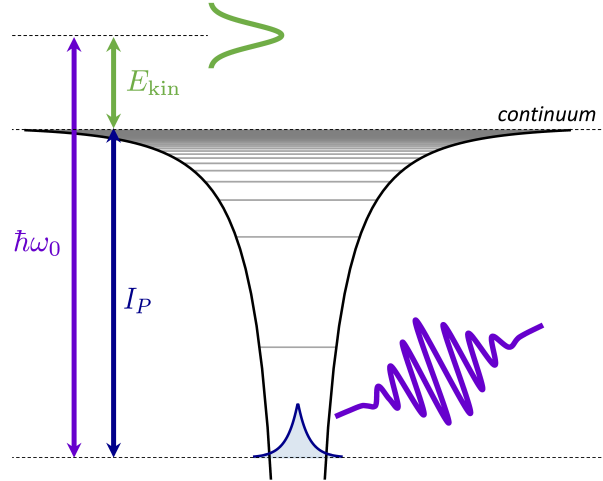


Figure 4.1.: Depiction of XUV ionisation as a single photon process: If a light pulse with energy  $\hbar\omega_0 > I_P$  interacts with a bound state, a continuum electron wave packet is created with  $E_{\text{kin}} = \hbar\omega_0 - I_P$ .

XUV ionisation is often described as a one-photon process that removes one electron from a bound state with energy  $E_0$  and places it in the continuum. The mean energy of the continuum electron wave packet is given by energy conservation as

$$E_{\text{kin}} = \hbar\omega_0 - I_P, \quad (4.1)$$

where  $\hbar\omega_0$  is the energy of the light pulse, and  $I_P = -E_0$  is the ionisation potential. This process is visualised in Fig. 4.1. However, this simple picture employs the single active electron approximation assuming that all other particles of the system do not interact with the light pulse or any other particle. In reality, particle correlation is crucial to describe ionisation properly and affects the system's state and dynamics during and after the ionisation process.

Describing correlation dynamics theoretically is a complex multi-particle problem. Especially dynamic correlation, i.e. the concerted time-dependent movement of all particles, is crucial yet challenging to model. Thus, most work focuses on atoms and especially Helium as the simplest two-electron system<sup>[57,106–109]</sup>. A prominent example is the joint experimental-theoretical study by Ossiander et al.<sup>[57]</sup>, where they used attosecond streaking spectroscopy to observe correlation dynamics. Upon photoemission of one electron,

the Helium cation can either reside in its ground state or an excited state. The population of the excited parent ion state during light pulse interaction originates from electron-electron correlation and is called shake-up. Moreover, this ionisation channel observes a small correlation-induced attosecond time delay. Theoretical work on Helium<sup>[108,109]</sup> revealed an additional electron-electron correlation-driven ionisation channel: knock processes. These are post-ionisation interactions of the outgoing electron with the parent ion electron that lead to the transient population of excited states and proceed on a much larger timescale (100's of attoseconds) than the shake process.

The goal of this project is to extend correlation dynamics to molecular systems. Going from atoms to molecules sees the inclusion of additional effects, most prominently, nuclear-electron correlation. Furthermore, the nuclear structure can lead to multi-centred electrons at various positions in space that are differently influenced by the Coulomb potential. Therefore, the questions arise: *Do the findings of correlation dynamics in atoms hold for molecules?*; *What is the influence of coupled nuclear-electron dynamics during and after ionisation?*; *How does the multi-centred nature of electrons manifests itself?*; *Are there observables suitable for tracking the correlation dynamics?*

#### 4.1.1. The extended Shin-Metiu model system

Extending simulations from atoms to molecules necessitates including and coupling many electrons and many nuclear degrees of freedom whilst maintaining a complete quantum description of the light-induced ionisation. This is computationally out of reach at present and, thus, motivates the use of molecular quantum model systems that mimic a molecule by reducing its dimensionality but keeping its essential effects and properties. Therefore, instead of describing quantitative effects in a specific molecule, qualitative effects, generally occurring in molecules, can be extracted with a high level of theory.

Shin and Metiu proposed such model to study nuclear-electron correlation effects<sup>[110,111]</sup>. It consists of one electron and one nucleus, both moving in one dimension. Additionally, two fixed outer nuclei (positive point charges) represent the molecular boundary such that the central moving nucleus represents a non-dissociative mode. While this model was originally derived to describe charge-transfer processes, it has been applied to a plethora of problems, for example, coupled nuclear-electron quantum dynamics<sup>[32,112–114]</sup>, classical dynamics<sup>[115]</sup>, photoionisation<sup>[116–118]</sup>, or two-dimensional coherent femtosecond spectroscopy<sup>[119]</sup>. In 2004, Erdmann et al. extended the model by a second electron allowing the description of electron-electron correlation<sup>[120]</sup>. Their study used the model to introduce time-dependent electron localisation functions and their nuclear dependency. Later the model was used to study the wave-packet dynamics in spin-coupled electronic states<sup>[121]</sup>. This so-called extended Shin-Metiu model is shown in Fig. 4.2 and fulfils all the above mentioned parameters needed to qualitatively describe correlation dynamics in molecular XUV ionisation on a quantum dynamical level: electron-electron correlation, nuclear-electron correlation, asymmetric structure, and multi-centred electrons.

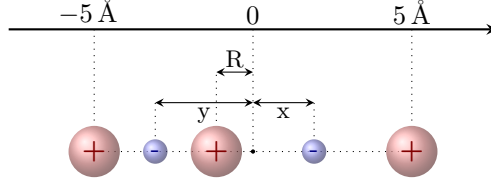


Figure 4.2.: The extended Shin-Metiu model system as described in the text with electronic coordinates,  $x$  and  $y$ , and nuclear coordinate  $R$ . The outer point charges are at  $\pm 5 \text{ \AA}$ . Adapted from Ziemis et al.<sup>[122]</sup>.

We now shortly introduce the model but refer the reader to the underlying publications for more details (see sections D.1 and D.2). The relevant quantum dynamics and numerics background has been presented in chapter 3. The molecular Hamiltonian for our model is

$$\hat{H}_0 = \frac{\hat{P}^2}{2M} + \frac{\hat{p}_x^2}{2} + \frac{\hat{p}_y^2}{2} + \hat{V}^{2e}(x, y, R), \quad (4.2)$$

with the nuclear mass  $M$ , the nuclear momentum operator  $\hat{P}$ , and the electron momentum operators  $\hat{p}_x, \hat{p}_y$ . The potential operator in coordinate space is defined as

$$\begin{aligned} \hat{V}^{2e}(x, y, R) = & \frac{Z_1 Z}{|L/2 - R|} + \frac{Z_2 Z}{|L/2 + R|} - \frac{Z \operatorname{erf}(|R - y|/R_c)}{|R - y|} \\ & - \frac{Z_1 \operatorname{erf}(|L/2 - y|/R_f)}{|L/2 - y|} - \frac{Z_2 \operatorname{erf}(|L/2 + y|/R_f)}{|L/2 + y|} \\ & - \frac{Z \operatorname{erf}(|R - x|/R_c)}{|R - x|} - \frac{Z_1 \operatorname{erf}(|L/2 - x|/R_f)}{|L/2 - x|} \\ & - \frac{Z_2 \operatorname{erf}(|L/2 + x|/R_f)}{|L/2 + x|} + \frac{\operatorname{erf}(|x - y|/R_e)}{|x - y|}, \end{aligned} \quad (4.3)$$

using soft Coulomb interactions parametrised by error functions,  $\operatorname{erf}(\dots)$ . The charges are  $Z_1 = Z_2 = Z = 1$ , the screening parameters  $R_c = R_f = R_e = 1.5 \text{ \AA}$ , and  $L = 10 \text{ \AA}$  for the outer point charges. The use of soft Coulomb interactions allows the moving particles to pass each other in this one-dimensional setup. This is crucial to describe photoionisation, where one electron leaves the molecular structure. Note that in the nuclear equilibrium (as displayed in Fig. 4.2), the asymmetric structure leads to one electron being stronger bound (left electron) and the other being weaker bound (right electron).

The interaction with an XUV light pulse is described using semi-classical light-matter interaction (recall section 2.2) with the interaction Hamiltonian in the velocity gauge (Eq. 2.63). This results in the overall time-dependent Hamiltonian,

$$\hat{H}(t) = \frac{\hat{P}^2}{2M} + \frac{\hat{p}_x^2}{2} + \frac{\hat{p}_y^2}{2} + \hat{V}^{2e}(x, y, R) + e \mathcal{A}(t) \left( -\frac{\hat{P}}{M} + \hat{p}_x + \hat{p}_y \right). \quad (4.4)$$

The light pulse itself is defined by a Gaussian envelope function in the vector potential (see subsection 2.2.3). The TDSE is solved numerically on a grid using the split operator method (see section 3.2).

Throughout the research, we refer to the extended Shin-Metiu model as ‘two-electron model’ while the standard Shin-Metiu model is called ‘one-electron model’. The one-electron model is the parent ion to the two-electron model. In our simulations, the pulse interaction with the two-electron model leads to the emission of one electron. The dynamics of the remaining electron in the parent ion can be described by the eigenstates of the one-electron model. The Hamiltonian of the one-electron model is readily adapted by removing one electronic degree of freedom from the equations above.

#### 4.1.2. Electron-electron correlation and time delays

The questions we set out to answer in the first publication (section D.1) are: *Do the findings of correlation dynamics in atoms hold for molecules?* and *How does the multi-centred nature of electrons manifests itself?* For this, we set up our model system in the nuclear equilibrium structure and simulate the interaction with a short XUV pulse.

We start by analysing the time-resolved population of the parent ion states during photoionisation of the two-electron model (see Fig. 4.3). It reveals that excited parent ion states get populated in the same two timescales as previously reported for atoms. Firstly, we have the quasi-instantaneous population of excited states during the light pulse interaction, i.e. shake-up processes. Secondly, after the light pulse has vanished, we see population exchange as post-ionisation interaction. This proceeds on the timescale of hundreds of attoseconds after the initial light pulse interaction, thus, being mediated by electron-electron correlation between the outgoing photoelectron and the parent ion

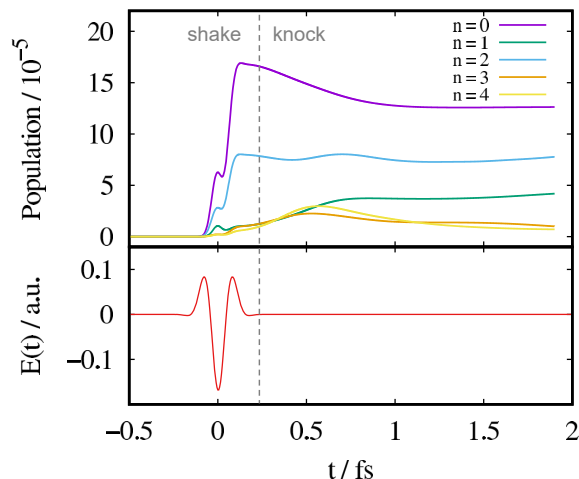


Figure 4.3.: Population dynamics of the first five electronic states in the parent ion (one-electron system) during and after light interaction of the XUV pulse ( $\tau_E = 140$  as,  $\omega_0 = 80$  nm,  $I = 10^{15}$  W/cm<sup>2</sup>) with the two-electron system. Adapted from Fröbel et al.<sup>[123]</sup>.

electron. These are the knock processes analogous to the Helium atom<sup>[108,109]</sup>.

Knowing that the basic concepts of shake and knock hold also in the molecular frame, we next want to understand the electron-electron correlation in more detail, i.e. how exactly the photoelectron travels through space in the potential of the parent ion electron. This constitutes translating the quantum dynamical processes into semi-classical pictures of the two electrons propagating and interacting in space. To this end, we propose replacing the fermionic wave function with that of two ‘distinguishable’ electrons and restricting the light pulse interaction to a specific electron (for more details see section D.1). This approach allows us to identify different single ionisation pathways that lead to the population of excited states in the parent ion. In general, three different paths can be distinguished for each electron: *(i)* direct photoemission of one electron without passing the other electron and only influencing it via the changed electrostatic environment (shake process), *(ii)* ‘scattered’ photoemission of one electron via passing the other electron, leading to immediate electron-electron interaction (knock process), and *(iii)* indirect photoemission, where one electron is accelerated by the light pulse but (partly) exchanges momentum with the other electron that subsequently gets emitted instead (knock process). Each of these processes occurs for each of the differently-centred electrons. The magnitude of the three processes is different for the left and right electron due to the asymmetric structure. This leads to a difference in the state of the parent ion after ionisation and different timescales for each ionisation process. Direct photoemission *(i)* does not include post light pulse interaction between the two electrons. In the molecular case of asymmetric structure and multi-centred electrons, this means the right electron leaves to the right, and the left electron leaves to the left (see Fig. 4.4). Since the left electron is stronger bound, this process is approximately 20as delayed to the direct emission of the right electron. On the other hand, processes *(ii)* and *(iii)* are both electron-electron correlation-driven and classified as knock processes (see green arrows in Fig. 4.4). The difference is, in *(ii)*,

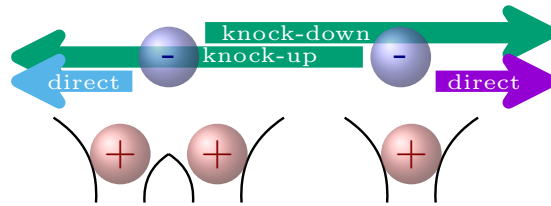


Figure 4.4.: Selected ionisation pathways. Direct ionisation means the left (right) electron leaves the molecule to the left (right) without directly interacting with the other electron. Knock processes are driven by electron-electron correlation and the two electrons passing each other. The colours of the arrows reflect the parent ion state the molecule will be predominantly in following this specific ionisation pathway with  $n = 0$  (violet),  $n = 1$  (green), and  $n = 2$  (blue). Knock-up and -down refers to a change in the electronic state compared to the direct ionisation process. The knock processes can occur via process *(ii)* or *(iii)*, as described in the text. Taken from Ziems et al.<sup>[122]</sup>.

the electron initially accelerated by the light pulse is the electron emitted, while in (iii), momentum exchange between the two electrons leads to the emission of the electron that is not initially accelerated by the light pulse. The direct interaction of the two electrons during these processes leads to the transient population of excited parent ion states. In terms of delay time with respect to the fastest process (direct emission of the weakly bound electron), process (ii) is a few hundred attoseconds delayed and process (iii) up to 1 fs.

In summary, we showed that the concept of shake and knock hold in molecules and can be further dissected into various pathways on different timescales, describing the movement of the multi-centred electrons in molecules.

### 4.1.3. Nuclear-electron correlation and photoelectron imprints

After having analysed electron-electron correlation, we set out to study the additional impact of nuclear-electron correlation in the second publication (section D.2). Specifically, we address the questions: *What is the influence of coupled nuclear-electron dynamics during and after ionisation?* and *Are there observables suitable for tracking the correlation dynamics?* To this end, we study XUV ionisation of the two-electron model in non-equilibrium configurations, investigate the dynamics beyond the first few femtoseconds to observe non-adiabatic effects in the parent ion after ionisation, and calculate photoelectron spectra as observables. In order to obtain spectra that can be clearly analysed by means of energy conservation and in order to avoid few-cycle effects, a  $\tau_E = 5$  fs long XUV pulse comprised of several optical cycles was used. Few-cycle XUV pulses and their effect on the photoelectron spectrum are discussed in section 4.2.

The dynamics are started from two different non-equilibrium positions that lead to the following general behaviour, which is depicted in Fig. 4.5 (a) in terms of potential energy curves of the two-electron (bottom) and one-electron (top) system: (1) The nuclear wave packet is placed in the electronic ground state of the two-electron model system in a nuclear non-equilibrium state, either left (green wave packet) or right (red wave packet) to the equilibrium. For comparison, simulations with the nuclear wave packet at the equilibrium geometry (blue wave packet) are performed. Starting the propagation, the nuclear wave packet at the left (right) non-equilibrium position will relax towards the equilibrium and gain positive (negative) momentum. (2) At the time of passing the equilibrium, the XUV pulse with an energy of  $\hbar\omega_0 = 15.5$  eV interacts, i.e. the light pulse is centred around the time the nuclear wave packet passes the equilibrium. (3) This will lead to the creation of a photoelectron moving away from the molecule (not depicted in Fig. 4.5 (a)), and an electronic wave packet in the parent ion comprised of several parent ion electronic states. On each electronic state evolves a coupled nuclear wave packet (purple, dark green, and light blue wave packet). The dynamics of these nuclear wave packets is given by the gradient of the potential energy curve of the corresponding electronic state (indicated with small purple, dark green, and light blue arrows). (4) The coupled evolution of electronic and nuclear wave packets defines the post-ionisation dynamics. Strong nuclear-electron

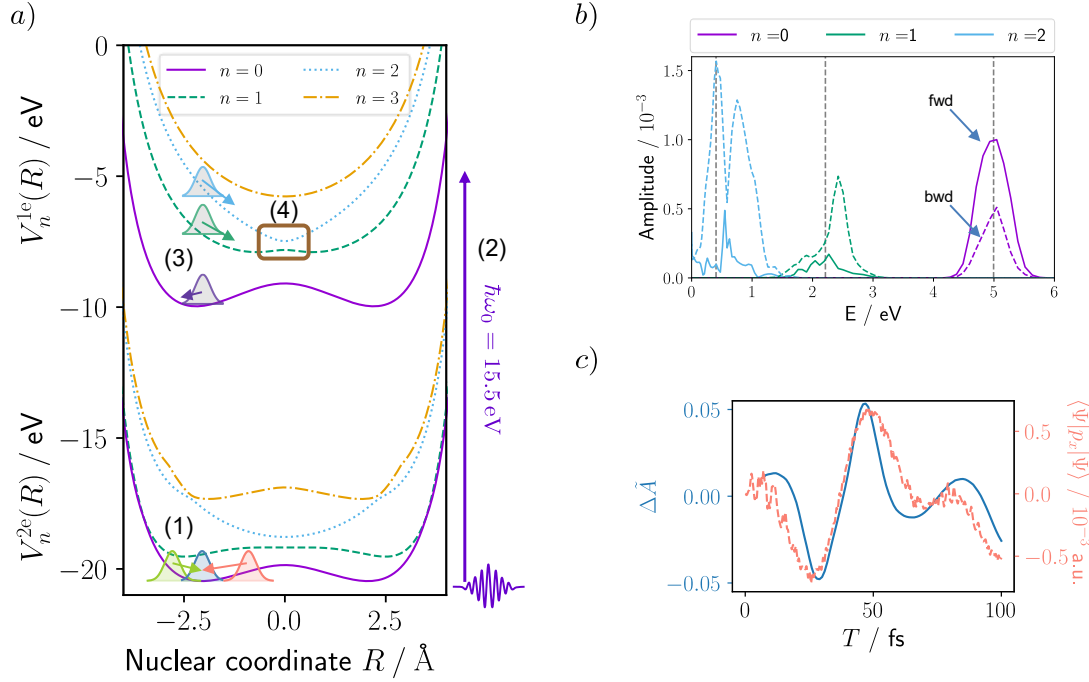


Figure 4.5.: (a) First four potential energy curves of the two-electron system (bottom) and one-electron system (top). The numbers (1) - (4) highlight the processes discussed in the text. (1) Non-equilibrium nuclear wave packets (green and red) relax to the equilibrium (blue). (2) XUV light pulse interaction with  $\hbar\omega_0 = 15.5$  eV. (3) Creation of electronic and nuclear wave packets in the parent ion due to ionisation by the XUV pulse. Little arrows show the gradient exerted by the potential energy curve on the nuclear wave packets. (4) Non-adiabatic transition important for the post-ionisation dynamics. (b) Photoelectron spectrum for ionisation from the nuclear equilibrium position. Each of the three peaks has a forward (fwd, solid line) / backward (bwd, dashed line) asymmetry discussed in the text. (c) Nuclear-electron correlation imprint of the electron momentum expectation value,  $\langle\Psi|p_x|\Psi\rangle$ , via the integrated photoelectron spectrum,  $\Delta\tilde{A}$ . Values are given at various times,  $T$ , defined as the delay between the start of the non-equilibrium dynamics and the XUV pulse interaction. Adapted from Ziems et al.<sup>[122]</sup>.



correlation arises when the electronic states come close in energy, e.g. at avoided crossings.

Using this procedure, we discuss (i) the influence of the nuclear degree of freedom and the nuclear momentum at the time of ionisation on the creation of the electronic wave packet in the parent ion (process (3)), (ii) electron-nuclear correlation in the post-ionisation dynamics (process (4)), and (iii) the imprints of coupled nuclear-electron dynamics on the photoelectron.

(i) By comparing the early attosecond electronic populations in the parent ion (similar to Fig. 4.3) of the non-equilibrium and equilibrium cases, we show that the influence of the moving nucleus during XUV ionisation is only marginally affecting the initial electronic wave packet. The only slight deviation ( $< 10\%$ ) in electronic population occurs when the nuclear wave packet's shape gets distorted prior to the light pulse interaction due to propagation on anharmonic surfaces. This is an important result for creating new approximated methods for molecular XUV ionisation.

(ii) The post-ionisation dynamics occur on the electronic surfaces of the one-electron system, i.e. the parent ion. At  $R = 0$ , we observe a non-adiabatic transition between the states  $n = 1$  and  $n = 2$  (see (4) in Fig. 4.5). Here, nuclear-electron correlation changes the electronic population due to the nuclear wave packet relaxing into this crossing. Interestingly, the timing of the non-adiabatic transition changes depending on the initial setup prior to ionisation. This originates from nuclear momentum conservation between the two-electron system before and the one-electron system after ionisation. Thus, starting in the left (right) non-equilibrium configuration leads to a positive (negative) nuclear momentum before ionisation that is conserved in the parent ion and results in a faster (slower) nuclear wave packet relaxation into the crossing.

(iii) In this section's introduction, the energy conservation relation for a single active electron promoted into the continuum (Eq. 4.1) was mentioned. With electron-electron correlation, we observe the population of several parent ion states that each have a correlated photoelectron state (recall subsection 4.1.2). Each parent ion state  $n$  has a defined energy and, thus, specific ionisation potential,  $E_n = -I_{P_n}$ , which extends the energy conservation relation to

$$E_{\text{kin},n} = \hbar\omega_0 - I_{P_n}. \quad (4.5)$$

For our case of an XUV pulse with  $\hbar\omega_0 = 15.5\text{eV}$  that interacts with a nuclear wave packet in the equilibrium, three parent ion states are energetically accessible, which leads to three distinct photoelectron peaks (see Fig. 4.5 (b)). Moreover, in subsection 4.1.2, we reported that electron-electron correlation leads to various ionisation pathways that differ in magnitude for the left (strongly bound) and right (weakly bound) electron. Interestingly, these differences also manifest in the photoelectron spectrum's forward/backward asymmetry (see Fig. 4.5 (b)). For example, the photoelectron peak at 5 eV is correlated to a parent ion state of  $n = 0$ . This state is predominantly populated by direct ionisation of

the right electron leaving to the right (forward), thus, resulting in a forward asymmetry of the photoelectron peak at 5 eV. The same logic can be applied to all photoelectron peaks and shows the correlation between the photoelectron and the parent ion electron (see publication in section D.2). The integrated photoelectron spectrum reveals an additional asymmetry based on nuclear-electron correlation (see Fig. 4.5 (c)). The coupled nuclear-electron dynamics in the bound two-electron system prior to ionisation can be visualised in terms of the electronic momentum expectation value (Fig. 4.5 (c), orange line). This is a direct electronic response to the nuclear motion. An XUV pulse that ionises the system at different times of the coupled nuclear-electron motion imprints the electronic momentum expectation value (orange line) on the photoelectron spectrum's integrated asymmetry (blue line). A proposed experiment would initiate coupled nuclear-electron dynamics in a target system and probe it by time-delayed XUV ionisation. Calculating this averaged asymmetry would reveal the coupled nuclear-electron dynamics at each time of ionisation. The details of how to differentiate the electron-electron correlation-based and nuclear-electron correlation-based asymmetry are presented in section D.2.

In summary, we revealed strong correlation effects between electrons and nuclei in molecular XUV ionisation showing *(i)* robustness of the electronic wave packet build-up with regard to the nuclear movement, *(ii)* nuclear momentum conservation between target and parent ion, and *(iii)* the imprint of electron-electron and nuclear-electron correlation in the photoelectron spectrum.

## 4.2. Attosecond ionisation dynamics of modulated, few-cycle XUV pulses

This section is based on:

3) K.M. Ziems, M. Wollenhaupt, S. Gräfe, A. Schubert, Attosecond ionization dynamics of modulated, few-cycle XUV pulses, *J. Phys. B.: At. Mol. Opt. Phys.*, **2023**, *56*, 105602 (section D.3)

In section 4.1, XUV ionisation was described as creating a continuum electron wave packet with its central energy given by energy conservation (Eq. 4.1). Subsequently, in subsection 4.1.3 we saw that the incorporation of particle correlation leads to asymmetries in the photoelectron spectrum. However, the peak positions still adhere to energy conservation (Eq. 4.5). With few-cycle XUV pulses, we enter a regime of light-matter interaction sensitive to the envelope and phases of the field. The few-cycle regime skews the intuitive energy conservation picture for ionisation dynamics, and creates additional asymmetries in the photoelectron spectrum. To separate few-cycle pulse effects from the above-discussed effects of particle correlation, we investigate single active electron photoionisation in a 1D atomic model system (validated against the 3D hydrogen atom in section D.3). The dynamics are studied on a grid by numerical integration of the TDSE (see chapter 3), as well as first-order perturbation theory (introduced in subsection 2.1.3), and semi-analytical approaches.

Few-cycle pulses are characterised by a steep rise and fall of the envelope within a few optical cycles. This means that the slowly varying envelope approximation (SVEA) cannot be assumed. In subsection 2.2.3, we thoroughly introduced the theory of light pulses within the SVEA and showed how temporal and spectral modulations (i.e. chirping) can be performed. Crucially, the envelope-depending term in Eq. 2.72 is neglected in the early stage of the derivations. Here, we start from Eq. 2.72 and derive analytical expressions for the electric field and vector field beyond the SVEA for unchirped and spectrally modulated XUV pulses. A strong focus is on understanding the additional effects created by the few-cycle nature of the light pulse. For the case of an unchirped few-cycle pulse, we obtain

$$\mathcal{E}(t) = \mathfrak{E}(t) \cos(\omega_0 t + \phi_{\text{CE}} + \phi(t)), \quad (4.6)$$

$$\tilde{\mathcal{E}}(\omega) = -\tilde{\mathcal{E}}_0 \frac{\omega}{\omega_0} \left\{ e^{-\beta_\omega(\omega-\omega_0)^2 + i\phi_{\text{CE}}} - e^{-\beta_\omega(\omega+\omega_0)^2 - i\phi_{\text{CE}}} \right\}, \quad (4.7)$$

with the envelope and time-dependent phase,

$$\mathfrak{E}(t) = -\mathcal{E}_0 e^{-\beta t^2} \left( \frac{4\beta^2 t^2}{\omega_0^2} + 1 \right)^{\frac{1}{2}} \quad \text{and} \quad (4.8)$$

$$\phi(t) = \arctan\left(\frac{2\beta}{\omega_0} t\right), \quad (4.9)$$

respectively. Note that  $\tilde{\mathcal{E}}_0 = \mathcal{E}_0 \sqrt{\beta_\omega/2}$ ,  $\beta = 4 \ln(2) \tau^{-2}$ , and  $\beta_\omega = (4\beta)^{-1}$ . Here, the Gaussian FWHM definition (recall Eq. 2.100) is applied. An example of such a pulse

is visualised in Fig. 4.6. It shows how the electric field in time possesses a temporal modulation due to the time-dependent envelope-induced frequency  $\omega_\phi(t) = \frac{d}{dt}\phi(t)$ . As a result, the instantaneous frequency of the pulse is shifted to  $\tilde{\omega}_0(t) = \omega_0 + \omega_\phi(t)$ , with a maximum blue shift at  $t = 0$  of  $\tilde{\omega}_0(t = 0) = \omega_0 + 2\beta\omega_0^{-1}$ . The spectral representation (see Eq. 4.7 and Fig. 4.6 (b)) shows the same blue shift in terms of the multiplicative  $\omega$  term, scaling the analytical spectrum:  $\tilde{\mathcal{E}}_{\text{carrier}}^\pm(\omega) = \frac{-\tilde{\mathcal{E}}_0}{\omega_0} e^{-\beta_\omega(\omega \mp \omega_0)^2 \pm i\phi_{\text{CE}}}$ . Crucially, the linear factor in  $\omega$  ensures a vanishing DC component,  $\tilde{\mathcal{E}}(0) = 0$ , necessary for obtaining a propagating pulse<sup>[124,125]</sup>. Similar to pulse modulation within the SVEA (presented in subsection 2.2.3), a quadratic spectral phase,  $\phi_2$ , can be introduced to few-cycle pulses beyond the SVEA, which leads to a linear temporal chirp in the electric field,

$$\mathcal{E}_c(t) = -\frac{\tilde{\mathcal{E}}_0}{\sqrt{8}\omega_0} \left( \frac{2 \left[ \beta_\omega + i\frac{\phi_2}{2} \right] \omega_0 + it}{\left[ \beta_\omega + i\frac{\phi_2}{2} \right]^{3/2}} e^{-\beta_c t^2 + i(\omega_0 + 2\phi_2\beta_c\beta t)t + i\phi_{\text{CE}}} + \text{c.c.} \right), \quad (4.10)$$

$$\tilde{\mathcal{E}}_c(\omega) = -\tilde{\mathcal{E}}_0 \frac{\omega}{\omega_0} \left\{ e^{-\beta_\omega(\omega - \omega_0)^2 + i\phi_{\text{CE}} - i\frac{\phi_2}{2}(\omega - \omega_0)^2} - e^{-\beta_\omega(\omega + \omega_0)^2 - i\phi_{\text{CE}} + i\frac{\phi_2}{2}(\omega + \omega_0)^2} \right\}. \quad (4.11)$$

As for pulses within the SVEA (see Eq. 2.110), we have  $\beta_c = \beta/(1 + 4\phi_2^2\beta^2)$  that constitutes a temporal broadening.

After understanding few-cycle pulses beyond the SVEA and modulations therein, we turn towards the atomic photoionisation dynamics induced by such pulses. Different intensity regimes – from  $10^{13}$  to  $10^{17}$  W/cm<sup>2</sup> – are studied, and first- and higher-order effects are differentiated. We contrast ionisation by unchirped and modulated few-cycle XUV pulses to understand effects arising from the spectral and temporal properties.

First-order effects, applicable to weak and moderate intensities, lead to a dipole re-shaping of the spectrum towards lower kinetic energies. In first-order, the photoelectron spectrum can be derived as the product of the transition dipole moment into the continuum,  $\mu(p)$ , and the spectral intensity profile,  $\tilde{\mathcal{I}}(\omega)$  (absolute square of the spectral field representation, power spectral density), shifted by the ground state energy,  $E_0$ . Assuming a continuum of plane waves, this gives

$$\sigma(p) \approx |\mu(p)|^2 \tilde{\mathcal{I}}(\tilde{E}_p - E_0), \quad (4.12)$$

with

$$\begin{aligned} \tilde{\mathcal{I}}(\omega) &= \left| \tilde{\mathcal{E}}_c(\omega) \right|^2 \\ &= \tilde{\mathcal{E}}_0^2 \frac{\omega^2}{\omega_0^2} \left\{ e^{-2\beta_\omega(\omega - \omega_0)^2} + e^{-2\beta_\omega(\omega + \omega_0)^2} - 2e^{-2\beta_\omega(\omega^2 + \omega_0^2)} \cos[\phi_2(\omega^2 + \omega_0^2) - 2\phi_{\text{CE}}] \right\}. \end{aligned} \quad (4.13)$$

(4.14)

Few-cycle pulses are ultrashort in time and, thus, broad in spectral representation. Fig. 4.7 contrasts a few-cycle and a long 5 fs pulse. For the few-cycle pulse, the broad spectral in-

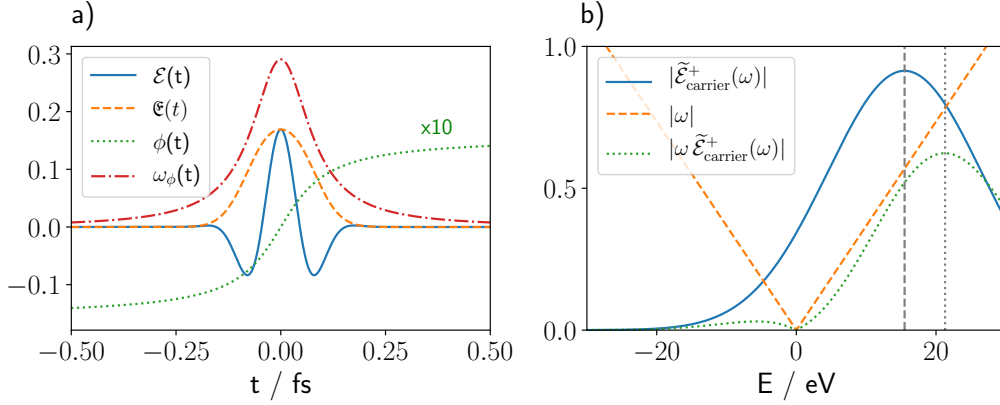


Figure 4.6.: Unchirped, few-cycle XUV pulse with  $\tau = 140$  as,  $\mathcal{E}_0 = -0.169$  a.u., and  $\omega_0 = 0.570$  a.u. (15.5 eV). a) Temporal representation based on Eq. 4.6 and b) spectral representation based on Eq. 4.7. The vertical dashed line indicates the carrier frequency,  $\omega_0$ , while the dotted line is the central frequency,  $\tilde{\omega}_0$ , showing the blue shift discussed in the text. Adapted from Ziems et al. [126].

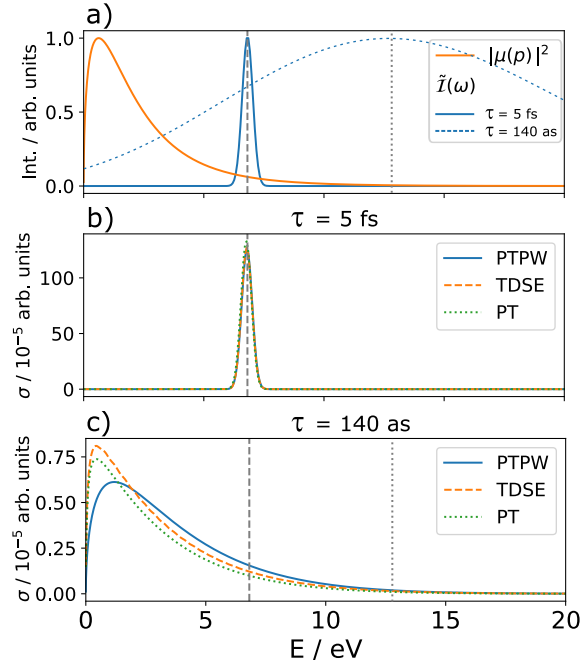


Figure 4.7.: (a) Transition dipole moment into a plane wave continuum (orange line), and spectral intensity profile of a few-cycle ( $\tau = 140$  as) and long ( $\tau = 5$  fs) XUV pulse. (b) and (c): Spectrum for a long and a few-cycle pulse, respectively, obtained via numerical solution of the TDSE, first-order perturbation theory (PT), and PT with plane wave continuum (PTPW, see Eq. 4.12). The latter is a product of the two terms in a) and shows the effect of the broad spectral intensity of ultrashort pulses. Adapted from Ziems et al. [126].

tensity leads to the transition dipole moment becoming the limiting contribution and imprinting the photoelectron spectrum. Since  $\mu(p)$  is largest at small energies, the photoelectron spectrum is red-shifted even though the spectral intensity profile is blue-shifted, as explained above, due to the few-cycle effects beyond the SVEA. As this is a linear effect in the spectral representation, an XUV pulse with a quadratic spectral phase (Eq. 4.10 and 4.11), which influences the pulse profile only in time, shows the same red shift.

Additionally, we find a first-order CEP-depended asymmetry in the photoelectron spectrum due to the cosine cross term in the spectral intensity profile of attosecond XUV pulses (see Eq. 4.14). This cross term is unique to attosecond pulses beyond the SVEA and varies the total pulse intensity. For half-integer CEPs, a maximum yield in the PES is observed, whereas for whole-integer CEPs, a minimum yield follows (Fig. 4.8 (a)).

In the non-perturbative regime, a CEP- and intensity-depended forward/backward asymmetry is reported based on polarisation and interference effects in the continuum (see publication in section D.3). This asymmetry becomes evident in Fig. 4.8 (b) and (c). Again, a comparison with spectrally modulated pulses (linear chirp in time) is performed. The higher-order effects only show for attosecond pulses and not for spectrally modulated ones, marking it as an effect of the temporal behaviour of the few-cycle pulse.

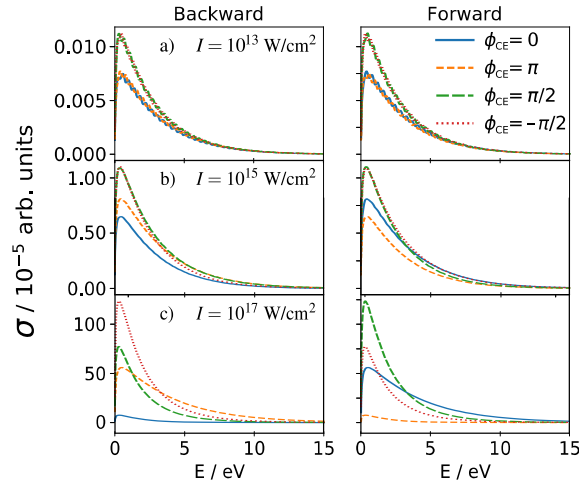


Figure 4.8.: Photoelectron spectra in forward/backward direction (right/left column), obtained by numerical TDSE solution for a few-cycle pulse with  $\tau = 140$  as and  $I = 10^{13}$  W/cm<sup>2</sup> (a),  $I = 10^{15}$  W/cm<sup>2</sup> (b), and  $I = 10^{17}$  W/cm<sup>2</sup> (c). a) shows the linear effect based on the cosine cross term of the spectral intensity, while (b) and (c) show the CEP- and intensity-dependent non-linear effect based on polarisation and continuum interference. Adapted from Ziems et al. <sup>[126]</sup>.

In summary, we thoroughly discussed the properties of few-cycle XUV pulses that cannot be treated within the slowly varying envelope approximation (SVEA), and emphasised temporal and spectral modulations unique to the attosecond nature of the pulses. Applying these fields to atomic photoionisation revealed a red shift of the photoelectron spectrum and asymmetries in first- and higher-order.

### 4.3. Non-adiabatic relaxation dynamics of furan - theoretically addressed for attosecond x-ray absorption

This section is based on:

4) S. Severino\*, [K.M. Ziems\\*](#), M. Reduzzi, A. Summers, H.-W. Sun, Y.-H. Chien, S. Gräfe, J. Biegert, Non-adiabatic electronic and vibrational ring-opening dynamics resolved with attosecond core-level spectroscopy, *Nature*, **2023** (submitted)(section D.4)

X-ray photons can be used to probe molecules via core-level spectroscopy, which encompasses a variety of techniques that differ in the detection scheme applied to the light-matter interaction. The absorption of an x-ray photon leads to a core electron being either excited into an unoccupied (valence) orbital or promoted to the continuum, i.e. ionised. Detecting the transmission of the x-ray photon through a sample is used in x-ray absorption spectroscopy (XAS), while measuring the liberated photoelectron is used in x-ray photoelectron spectroscopy (XPS). Moreover, an electron from a higher energetic level can fill the core hole created by the x-ray interaction. The energy released from this process can either trigger the emission of a photon or an electron. The latter process is known as Auger-Meitner decay<sup>[127,128]</sup>. Detecting the photon of the recombination process is done in x-ray emission spectroscopy (XES), while Auger electron spectroscopy (AES) measures the Auger-Meitner electron. All these techniques reveal element-specific information about the local geometry and electronic structure around an atomic site<sup>[129–131]</sup>.

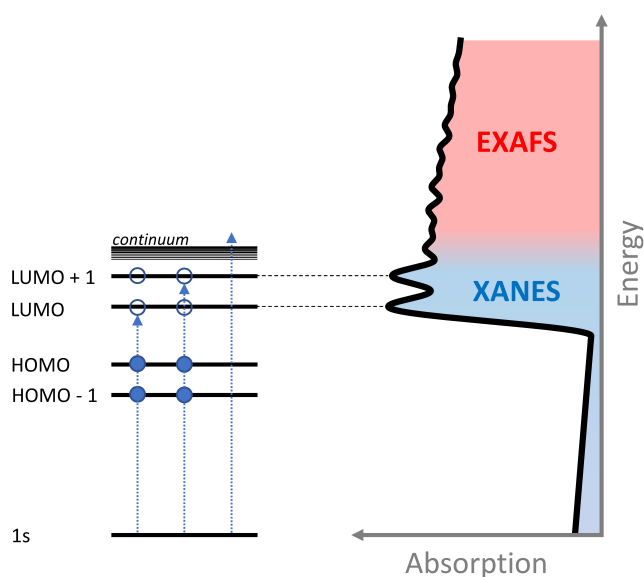


Figure 4.9.: Visualisation of XAS from a K-edge (1s orbital) and its characteristic two regions. XANES: Transition into unoccupied orbitals, e.g. LUMO and LUMO+1, lead to specific signals in the absorption signal around the edge. EXAFS: For energies larger than the binding potential, electrons scatter off their neighbouring electrons, leading to modulations.

In XAS, the photon energy needed to excite a core electron is associated with the so-called K-, L-, and M-edges for, respectively, excitation of an orbital with quantum number  $n = 1, 2,$  and  $3$ . The wording ‘edge’ refers to the sudden rise in x-ray absorption when the x-ray photon energy is in proximity to the core electron’s binding energy. For the case of carbon, the K-edge refers to the excitation of a  $1s$  core electron at around  $284$  eV. An XAS spectrum comprises two main regions (see Fig. 4.9). X-ray absorption near-edge structure (XANES) occurs nearest the absorption edge and exhibits sharp resonance peaks, corresponding to specific core transitions into bound states. This signal is used to extract element- and orbital-specific information. On the other hand, extended x-ray absorption fine structure (EXAFS) appears at higher energies and has oscillations in the measured signal caused by the ejected core electron scattering off surrounding atoms. This signal contains information about the neighbouring atoms, such as bond lengths and chemical coordination. Historically, the sum of the XANES and EXAFS spectra is also referred to as x-ray absorption fine structure (XAFS). A big appeal of XAS is its sensitivity to the electronic environment and molecular structure<sup>[132,133]</sup>. Moreover, the site-specific core-to-valence transitions have limited spectral congestion compared to valence-to-valence transitions<sup>[132,134,135]</sup>.

Until recently, most core-level spectroscopy experiments were only feasible in synchrotron facilities. With the advances of attosecond technology and the emergence of HHG, table-top x-ray spectroscopy became available and offered a prominent tool to understand details about the dynamics of quantum systems<sup>[136]</sup>. Using attosecond soft x-ray pulses from HHG complements the site-specificity and electronic and structural sensitivity of XAS with attosecond temporal resolution. This technique is termed AttoXAFS. A pioneering step was the extension of soft x-rays from HHG sources to the water window ( $280$  eV– $532$  eV)<sup>[137–140]</sup>. In this spectral region, water is transparent, while core resonances of elements common to organic compounds are found, such as carbon ( $284$  eV) and Nitrogen ( $402$  eV). Thus, spectroscopy in the water window is perfectly suitable for investigating organic substances and biological processes. Additionally, since AttoXAFS offers attosecond temporal resolution and sensitivity to the electronic environment and nuclear geometry, the method can be used to investigate dynamics involving CIs in organic compounds. A few first attosecond absorption experiments in the water window have been performed on small systems such as NO<sup>[141]</sup> and the ethylene cation<sup>[61]</sup>. Moreover, it was reported that AttoXAFS can observe electronic coherences<sup>[142]</sup>.

In this work, we showcase AttoXAFS’ capabilities to unravel the complex dynamics of larger and biologically relevant systems by revealing the non-adiabatic electronic and vibrational dynamics of neutral furan across its conical intersections and dark states in real time. Furan is a prototypical system for heterocyclic organic rings, which are essential building blocks of polymers, fuels, pharmaceuticals, atmospheric constituents, organic electronics, light-harvesting systems, agrochemicals, and more<sup>[143–146]</sup>. The specific pump-probe setup is shown in Fig. 4.10: A non-ionising,  $1.85$   $\mu\text{m}$ , CEP-stable,  $17$  fs strong-field



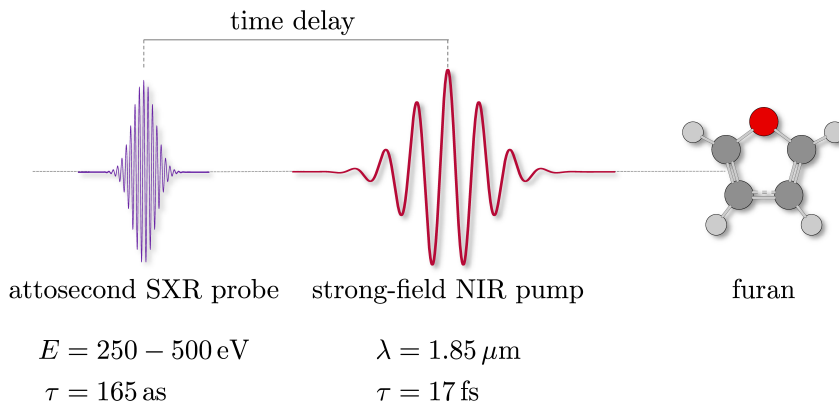


Figure 4.10.: Pump-probe setup used in the experiment.

pump with  $6.4 \times 10^{13} \text{ W/cm}^2$  peak intensity multi-photon excites the furan molecule. Then, a time-delayed, isolated attosecond SXR pulse probes the excited-state dynamics via XANES at the carbon K-edge.

From the theory side, we employ a multi-physics approach comprised of three complementing simulations: *(i)* One-dimensional potential energy surfaces are calculated along specific relaxation pathway coordinates to obtain an intuitive picture of the dynamics. *(ii)* The non-adiabatic excited-state dynamics are simulated via ab initio on-the-fly surface hopping, including non-adiabatic and laser coupling. This enables us to sample all possible excited states relaxation pathways without presuming reaction modes while incorporating all relevant quantum and strong-field effects. *(iii)* X-ray absorption spectra are calculated parametrically at various nuclear geometries and in different electronic states to compare to the experimental signal.

All approaches use standard quantum chemistry packages to solve the electronic TISE (recall subsection 2.3.2). For *(i)* and *(ii)*, the ground and excited states are obtained using the Gaussian 16 programme<sup>[147]</sup> with (time-dependent) density functional theory ((TD-)DFT), the hybrid functional PBE0<sup>[148,149]</sup> and a valence triple-zeta basis set with diffuse and polarisation functions, 6-311++G(d,p)<sup>[150,151]</sup>. The molecular excited-state dynamics in *(ii)* are performed using the direct dynamics programme Sharc 2.1<sup>[152,153]</sup> (recall subsection 2.3.3). In *(iii)*, we use QChem 5.3<sup>[154]</sup> to calculate core excitations from the electronic ground state on the equation of motion coupled cluster level, including singles and doubles (EOM-CCSD)<sup>[155,156]</sup>. Excitations from a valence excited state employ the core-valence-separation scheme<sup>[157]</sup> in the frozen-core equation of motion model for electronically excited states on the coupled cluster singles and doubles level of theory (fc-CVS-EOM-EE-CCSD)<sup>[158,159]</sup>. Both methods use the aug-cc-pVDZ basis set<sup>[160,161]</sup>.

In the following, we focus on the theoretical investigation of our publication (full work in section D.4). Upon multi-photon, strong-field excitation into the bright  $\pi\pi^*$  ( $S_2$ ) state, furan undergoes ultrafast dynamics through two main non-adiabatic relaxation pathways,

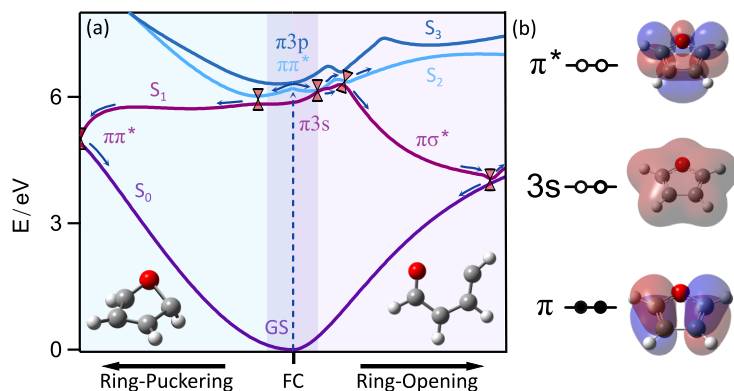


Figure 4.11.: (a) Potential energy curves along linear interpolated coordinates showing furan’s non-adiabatic relaxation dynamics following a  $\pi\pi^*$  excitation along RP (left, light blue background) or RO (right, light red background) through different crossings and CIs. The dark blue shaded area in the centre represents the Franck-Condon (FC) region. The excited states  $S_0$ ,  $S_1$ , and  $S_2$  refer to the respective adiabatic states and change their electronic configurations through several crossings along the pathways. (b) Highest occupied molecular orbital ( $\pi$ ) and the two lowest unoccupied molecular orbitals ( $3s$  and  $\pi^*$ ) at the FC region for the electronic GS. Adapted from Severino et al. [162].

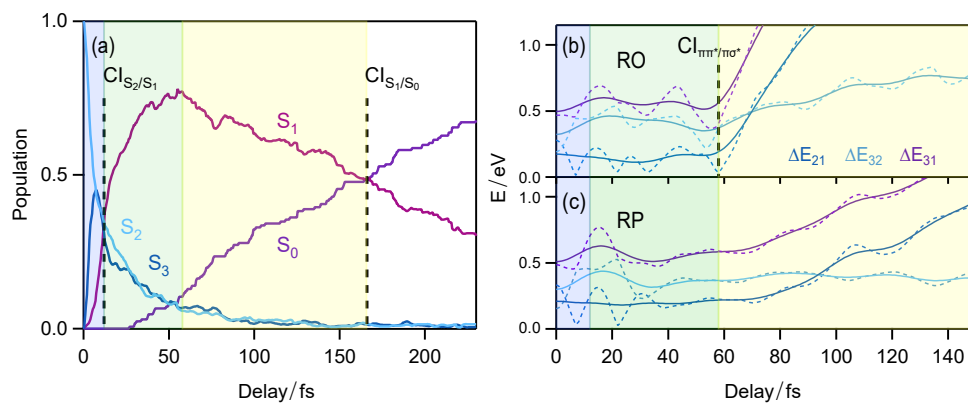


Figure 4.12.: Analysis of the semi-classical dynamics. (a) Time evolution of the electronic population starting from  $S_2$  ( $\pi\pi^*$  at FC) involving the first three excited states ( $S_1$ ,  $S_2$ ,  $S_3$ ) and the ground state ( $S_0$ ). (b) and (c): Time evolution of the electronic states’ energy gap,  $\Delta E$ , between the first three excited states along, respectively, the RO and the RP trajectories (dashed lines) and their Gaussian smoothed versions based on the pump pulse width (continuous lines). In (a), (b), and (c), the passage through  $CI_{S_2/S_1}$  (12fs),  $CI_{\pi\pi^*/\pi\sigma^*}$  (58fs), and  $CI_{S_1/S_0}$  (158fs) are labelled. The different characteristic regions of the dynamics that are discussed in the text are highlighted by the shaded areas. Adapted from Severino et al. [162].

namely ring-opening (RO) and ring-puckering (RP). Both pathways evolve on several excited states through avoided crossings and CIs back to the electronic ground state<sup>[163–165]</sup>. This is visualised in Fig. 4.11 in terms of one-dimensional potential energy curves along a coordinate obtained by linear interpolation between the Franck-Condon (FC) region and, respectively, the ring-opening conical intersection (ROCI) and ring-puckering conical intersection (RPCI). Fig. 4.12 (a) shows the results of the semi-classical dynamics, where 200 trajectories were started in the excited  $\pi\pi^*$  state. Within 15 fs, the  $S_3$  ( $\pi 3p$ ) state gets partially populated (blue area). This is followed by passing  $CI_{S_2/S_1}$ , which leads to a partial population transfer to the  $S_1$  state (green area). Crucially, this creates a so-called CI-mediated coherent electronic wave packet<sup>[166]</sup> as the evolution of the nuclear wave packet proceeds on two almost parallel excited electronic states ( $S_1$  and  $S_2$ ; see  $\Delta E_{21}$  in Fig. 4.12 (b)), ensuring a constant phase relation. This electronic wave packet migrates between the two distinct carbon atoms of furan (see C1 and C2 top right sketch in Fig. 4.13) and is resolved in the experimental data as out-of-phase quantum beatings. The passage of  $CI_{S_2/S_1}$  leads to a diabatic transition, meaning the adiabatic  $S_1$  and  $S_2$  state switch electronic character. Thus, when the population is dominant in  $S_1$  at around 60 fs, the electronic character is still of  $\pi\pi^*$ . After 60 fs (yellow area), the RO pathway decays through a second conical intersection,  $CI_{\pi\pi^*/\pi\sigma^*}$ , that transiently populates a dissociative dark  $\pi\sigma^*$  state and, subsequently, results in the C-O bond breaking. The RP pathway maintains  $\pi\pi^*$  character. This pathways difference is also evident from the static potential energy surface picture (see Fig. 4.11). A normal mode analysis of the dynamics along the RO shows the emergence of a RO vibrational mode after 60 fs. Relaxation along this dissociative pathway leads to an energetic separation of the electronic states (see Fig. 4.11 and  $\Delta E_{21}$  in Fig. 4.12 (b)), subsequently leading to the dephasing of the aforementioned electronic wave packet. The disappearance of electronic quantum beating around 60 fs, followed by the emergence of the vibrational RO frequency, is confirmed in the experiment and is a real-time measurement of nuclear-electron correlation. At  $t > 160$  fs (white area), the ROCI and RPCI ( $CI_{S_1/S_0}$ ) lead to the relaxation to the electronic ground state. The theory identifies that 74% of the trajectories follow the RO pathway, which concurs with the experimental findings of a dominant RO (see section D.4).

Selected calculated spectra at the FC region and ROCI are shown in Fig. 4.13. The top panel shows the effect of the initial  $\pi\pi^*$  photoexcitation on the x-ray absorption spectrum. Here, the key feature is the SOMO peak at 282 eV. The photoexcitation pump creates a hole in the  $\pi$  orbital, allowing a probe  $1s \rightarrow \pi$  transition by the x-ray pulse. Going back to Fig. 4.9, this resembles a hole in the HOMO due to the pump pulse excitation, which subsequently causes a pre-edge peak in the x-ray spectrum due to the newly opened  $1s \rightarrow$  HOMO transition. At the ROCI, the molecular symmetry is broken from  $C_{2v}$  to  $C_s$  making each carbon's chemical environment unique. Consequently, the SOMO peak is not made out of two but rather four unique transitions, as indicated in Fig. 4.13 (b). The SOMO peak's appearance and the splitting can be found in the experimental data.

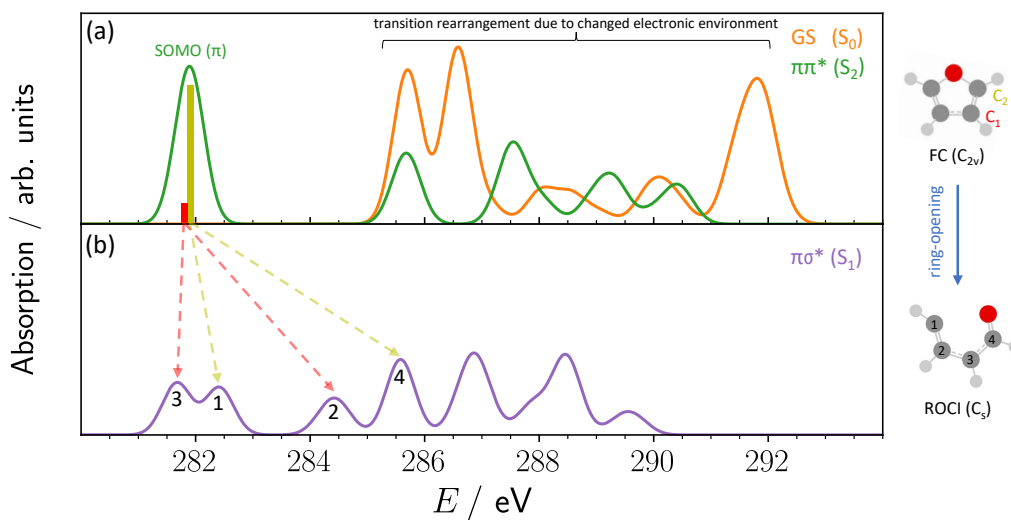


Figure 4.13.: XAS for different electronic configurations at (a) FC region and (b) ROCI geometry. In (a), the creation of the SOMO peak and transition rearrangement due to the change from the GS (orange) to the  $\pi\pi^*$  state (green) is shown. Arrows in (b) indicate the splitting of the SOMO peak due to symmetry breaking in the molecular structure, as depicted on the right. Adapted from Severino et al.<sup>[162]</sup>.

In summary, we presented the theoretical part of a joint experimental and theoretical study that used attosecond core-level absorption spectroscopy to investigate the non-adiabatic dynamics of furan. We revealed the passage through CIs, creation of electronic coherence, dephasing due to nuclear-electron correlation, and identified ring-opening as the major relaxation pathway.

## 4.4. The contribution of ionisation to static and ultrafast x-ray scattering

This section is based on:

5) K.M. Ziems, M. Simmermacher, S. Gräfe, A. Kirrander, The contribution of Compton ionization to ultrafast x-ray scattering, *J. Chem. Phys.*, **2023**, *159*, 044108 (section D.5)

In section 4.3, XANES was introduced as resonant x-ray matter interaction, where a soft x-ray pulse promotes an electron from a core level to an unoccupied orbital creating an absorption edge in the spectrum (see Fig. 4.9). Non-resonant x-ray scattering occurs at higher photon energies, beyond any absorption edges, and describes the scattering of hard x-rays by a material. The signal is recorded as differential x-ray scattering cross section,  $d\sigma/d\Omega$ , referring to the number of scattered photons per solid angle  $\Omega$ .

Historically, x-ray scattering has been used to analyse crystal structures, but over the last decades found its way into femtochemistry thanks to the construction of XFELs<sup>[10–12]</sup>. These facilities generate very short pulses of x-rays with unprecedented brightness, enabling experiments that resolve the nuclear dynamics of photochemical reactions on the femtosecond time scale<sup>[13,62,167,168]</sup>. Moreover, due to the high photon flux and repetition rate, more subtle features like changes in the electronic state are captured<sup>[169,170]</sup>. In the future, XFELs are poised to provide attosecond pulses in the hard x-ray regime<sup>[26–30]</sup>, which will open the possibility to observe real-time electron dynamics<sup>[63,171–175]</sup>.

Common analysis of scattering experiments still relies on the independent atom model (IAM) that describes the scattering cross section as an incoherent sum of tabulated atomic form factors<sup>[176,177]</sup>. This method gives fairly good agreement for nuclear structure retrievals but cannot be applied to electronic features or electron dynamics. Hence, several groups are working on a more rigorous framework to describe static and ultrafast x-ray scattering, such as derivation within non-relativistic quantum electrodynamics and first-order perturbation theory<sup>[171,178]</sup>. We apply this theory to a purely electronic version of our one-dimensional molecular model system (recall subsection 4.1.1) at its nuclear equilibrium structure, i.e. a two-electron system with fixed nuclei. In the spectral representation (recall Eq. 2.39), the system is described via its electronic eigenstates,  $\{|\varphi_i\rangle\}$ , as

$$|\Psi(t)\rangle = \sum_i^{N_s} c_i e^{iE_i t/\hbar} |\varphi_i\rangle, \quad (4.15)$$

with eigenenergies,  $E_i$ , amplitudes,  $c_i$ , and number of electronic states in the superposition,  $N_s$ . For  $N_s = 1$ , we have a single, stationary electronic state, while for  $N_s > 1$ , we have an electronic wave packet. For this, the differential x-ray scattering cross section in terms of the one-dimensional momentum transfer coordinate,  $q$ , is obtained as

$$\frac{d\sigma}{d\Omega} = \left(\frac{d\sigma}{d\Omega}\right)_{\text{Th}} \sum_{i,j}^{N_s} c_j^* c_i \Lambda_{ji}(q) \int_{-\infty}^{+\infty} I(t-\tau) e^{i\omega_{ji}t} dt, \quad (4.16)$$

with the Thomson scattering cross section of a free electron,  $(d\sigma/d\Omega)_{\text{Th}}$ , the photon-number intensity of the x-ray pulse,  $I(t - \tau)$ , centred around time  $\tau$ , and the angular frequency,  $\omega_{ji} = (E_i - E_j)/\hbar$ . The molecular property enters via the two-electron scattering matrix element,  $\Lambda_{ji}(q)$ , of two electronic states,  $|\varphi_i\rangle$  and  $|\varphi_j\rangle$ . The sum over  $i$  and  $j$  includes all  $N_s$  states in the electronic superposition of Eq. 4.15. Thus, for  $N_s = 1$ , we observe static x-ray scattering, while for  $N_s > 1$ , we have a time-dependent scattering signal from a wave packet. The two-electron scattering matrix elements from Eq. 4.16 are

$$\Lambda_{ji}(q) = \langle \varphi_j | \hat{L}^\dagger(q) \hat{L}(q) | \varphi_i \rangle \quad (4.17)$$

$$= \delta_{ij} N_e + 2 \iint e^{iq(x-y)} \Gamma_{ji}(x, y) dx dy, \quad (4.18)$$

with the scattering operator,

$$\hat{L}(q) = e^{iqx} + e^{iqy}, \quad (4.19)$$

and the two-electron (transition) density,

$$\Gamma_{ji}(x, y) = \varphi_j^*(x, y) \varphi_i(x, y). \quad (4.20)$$

Assuming an ultrashort x-ray pulse and normalising the photon-number intensity,  $I(t - \tau)$ , allows us to express scattering signals in units of the Thomson scattering cross section. This recasts Eq. 4.16 into

$$S(q, \tau) = \sum_{i,j}^{N_s} c_j^* c_i e^{i\omega_{ji}\tau} \Lambda_{ji}(q). \quad (4.21)$$

This can be classified into two contributions. For  $i = j$ , we obtain the so-called total scattering signal,

$$S_t(q) = \sum_i^{N_s} |c_i|^2 \Lambda_{ii}(q). \quad (4.22)$$

For ultrafast electron dynamics of an electronic wave packet, i.e.  $N_s > 1$ , and  $i \neq j$ , we obtain the additional time-dependent, coherent mixed (cm) scattering signal,

$$S_{\text{cm}}(q, \tau) = 2 \sum_i^{N_s-1} \sum_{j>i}^{N_s} \text{Re} \left[ c_j^* c_i e^{i\omega_{ji}\tau} \Lambda_{ji}(q) \right]. \quad (4.23)$$

These two expressions,  $S_t(q)$  and  $S_{\text{cm}}(q, \tau)$ , can be further dissected and cast in terms of the one-electron density matrix elements (also termed scattering amplitudes),

$$L_{fi}(q) = \langle \varphi_f | L(q) | \varphi_i \rangle = \int e^{iqx} \rho_{fi}(x) dx, \quad (4.24)$$

which are based on the one-electron (transition) density,

$$\rho_{fi}(x) = 2 \int \varphi_f^*(x, y) \varphi_i(x, y) dy. \quad (4.25)$$

Equations based on this formalism are obtained by introducing the identity,

$$1 = \sum_f \infty |\varphi_f\rangle \langle \varphi_f|, \quad (4.26)$$

into Eq. 4.22 and 4.23. This dissects the total scattering signal,  $S_t(q)$ , into elastic and inelastic signal,

$$S_{\text{el}}(q) = \sum_i^{N_s} |c_i|^2 |L_{ii}(q)|^2, \quad (4.27)$$

$$S_{\text{in}}(q) = \sum_i^{N_s} |c_i|^2 \sum_{f \neq i}^{\infty} |L_{fi}(q)|^2, \quad (4.28)$$

and reformulates the coherent mixed signal,

$$S_{\text{cm}}(q, \tau) = 2 \sum_i^{N_s-1} \sum_{j>i}^{N_s} \text{Re} \left[ c_j^* c_i e^{i\omega_{ji}\tau} \sum_f^{\infty} L_{fj}^*(q) L_{fi}(q) \right]. \quad (4.29)$$

Fig. 4.14 visualises the three distinct contributions in this theoretical framework. Elastic scattering,  $S_{\text{el}}(q)$ , has no energy exchange and probes the populated electronic state(s). Inelastic scattering,  $S_{\text{in}}(q)$ , implies energy transfer to or from the x-ray photon. Coherent

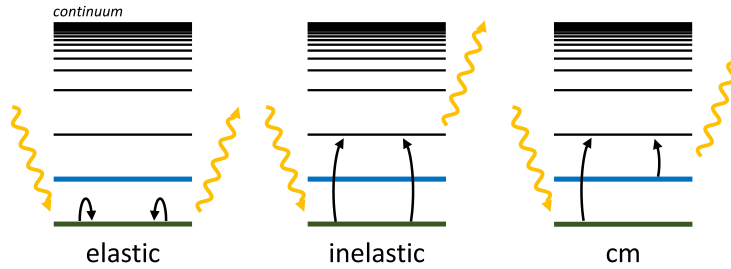


Figure 4.14.: Illustration of the three contributions to x-ray scattering in the framework of one-electron density matrix elements (scattering amplitudes), namely elastic (Eq. 4.27), inelastic (Eq. 4.28), and coherent mixed (Eq. 4.29) scattering. Populated electronic states are shown as bold horizontal lines (green and blue), vacant states as solid black lines, and scattering amplitudes as curved black arrows. Incident and scattered x-rays are shown as curly yellow arrows. Accurately calculating the inelastic and cm signal necessitates a sum over all possible one-electron transitions into bound and continuum states. Adapted from Simmermacher et al. [179,180].

mixed scattering,  $S_{\text{cm}}(q, \tau)$ , arises from interferences between the scattering amplitudes of coherently populated electronic states in an electronic wave packet. As evident from Eq. 4.28 and 4.29, simulating the inelastic and coherent mixed signal involves an infinite sum over states. First proof-of-principle simulations of ultrafast scattering have used an arbitrary truncation of this sum over electronic states and, thus, excluded most of the implied electronic transitions<sup>[63,171,173,174]</sup>.

We shed light on the open question of how these disregarded transitions, especially into continuum states, affect the static and ultrafast scattering signal. By employing our molecular model system (recall subsection 4.1.1), we have access to numerically exact solutions of the electronic Schrödinger equation and obtain a complete continuum basis using an orthonormalised plane wave ansatz. Crucially, scattering signals obtained from an infinite sum over one-electron scattering matrix elements are compared to calculations via the two-electron scattering matrix elements. Moreover, we provide an orbital-based interpretation of our results (details in section D.5).

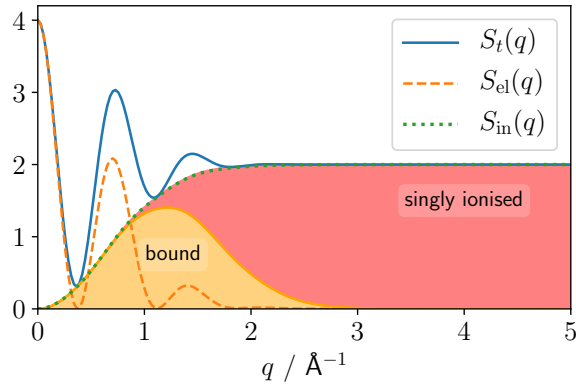


Figure 4.15.: Total x-ray scattering signal,  $S_t(q)$ , and its elastic and inelastic components,  $S_{\text{el}}(q)$  and  $S_{\text{in}}(q)$ . The coloured areas indicate the decomposition of the inelastic signal into bound-to-bound (yellow) and single ionisation (red) contributions. Adapted from Ziems et al.<sup>[181]</sup>.

Static x-ray scattering from the electronic ground state is shown in Fig. 4.15. The total signal,  $S_t(q)$  (Eq. 4.22), is comprised of the elastic,  $S_{\text{el}}(q)$  (Eq. 4.27), and inelastic,  $S_{\text{in}}(q)$  (Eq. 4.28), component. Computing the complete manifold of bound and continuum states dissects the infinite sum of the inelastic signal into contributions from bound-to-bound (orange) and bound-to-continuum transitions, i.e. single ionisation (red). The inelastic signal is dominated by bound-to-bound transitions at low momentum transfer, while single ionisation dominates at intermediate to high momentum transfer. Interestingly, we find that for transitions into high-energy continuum states, the momentum transfer value correlates with the continuum state’s kinetic energy.

Scattering off an electronic wave packet leads to the additional, time-dependent coherent mixed signal,  $S_{\text{cm}}(q, \tau)$ . Measuring this component is a direct probe of electron dynamics.



For a superposition of the system's first and second excited state, we have an energy spacing of  $\Delta E_{21} = 1.785$  eV. This results in an electronic wave packet whose dynamics, i.e. quantum beating, is characterised by an angular frequency of  $\omega_{21} = 2.712$  fs $^{-1}$  and a period of  $T_{21} = 2.317$  fs. In Fig. 4.16 (a), the coherent mixed signal for  $\tau_a = 0$  and  $\tau_b = 1/2 T_{21}$  is shown on top of the static, total scattering signal,  $S_t(q)$ . This constitutes the extrema between which the coherent mixed component modulates the total signal with a frequency of  $\omega_{21}$ . The separation of the coherent mixed signal into minimal, bound-to-bound, and singly ionised contributions is shown in Fig. 4.16 (b). The minimal contribution signal includes only transitions between the populated states in the coherent superposition, in our case,  $|\varphi_f^{2e}\rangle \leftarrow |\varphi_1^{2e}\rangle$  and  $|\varphi_f^{2e}\rangle \leftarrow |\varphi_2^{2e}\rangle$  with  $f \in [1, 2]$ . Ultrafast x-ray scattering studies have so far either used the minimal contribution or a small subset of bound-to-bound transitions<sup>[63,171,173,174,182–185]</sup>. Our results show that the minimal contribution roughly matches the full coherent mixed signal at low momentum transfer but fails at intermediate to high  $q$ . Moreover, it is clear from Fig. 4.16 (b) that the inclusion of more transitions does not result in a clear and simple trend as seen for the inelastic signal. Contrary to the inelastic signal, the scattering amplitudes in the coherent mixed signal interfere constructively or destructively. Thus, including more electronic transitions does not increase the signal by specific,  $q$ -dependent magnitudes; rather, a complex signal build-up is observed. Only the inclusion of all bound and continuum states guarantees a correct signal via one-electron scattering matrix elements that matches the two-electron scattering matrix simulation. Unquestionably, considering all electronic transitions is not

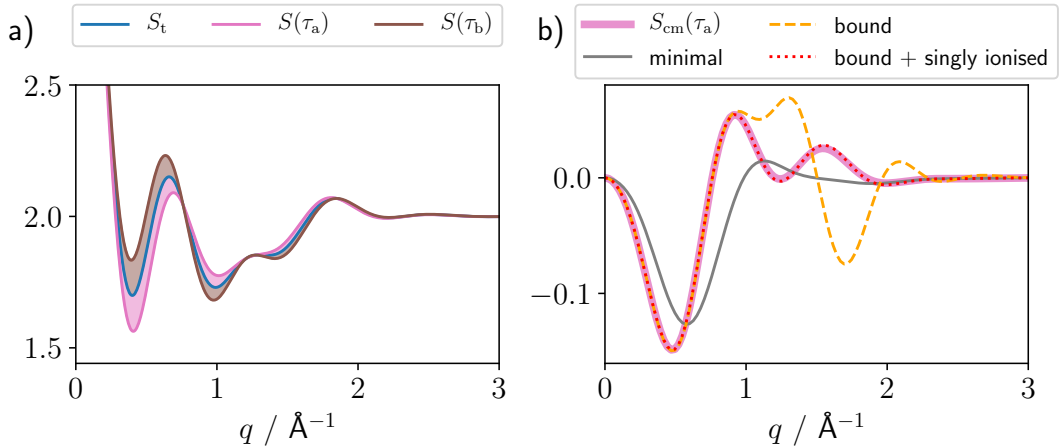


Figure 4.16.: (a) Complete scattering signal,  $S(q, \tau)$ , for a coherent superposition of the first and second excited electronic states. The complete signal is comprised of the static total and coherent mixed components,  $S_t(q)$  and  $S_{cm}(q, \tau)$ , respectively. Times  $\tau_a = 0$  and  $\tau_b = 1/2 T_{21}$  are displayed. The filled areas show how the coherent mixed component modulates the scattering signal over the course of one period. (b) Decomposition of the coherent mixed signal at  $\tau_a$  into its contributions from different electronic transitions. Adapted from Ziems et al.<sup>[181]</sup>.

feasible for real molecules. Therefore, future calculations of coherent mixed scattering should be based on two-electron scattering matrix elements. This is especially important for systems with inversion symmetry. It has been shown that the coherent mixed signal vanishes for an electronic wave packet whose electronic states transform differently under inversion<sup>[63,186,187]</sup>. By setting up our model system with an inversion symmetry ( $R = 0$ ), we show that the coherent mixed signal only vanishes in the limit  $f \rightarrow \infty$ . Any finite truncation of the sum over states leads to a spurious signal (see section D.5).

In summary, using a molecular model system allowed us to include the complete manifold of bound and single continuum states in the calculation of static and ultrafast x-ray scattering. We found significant contributions of scattering-induced ionisation in the inelastic and coherent mixed signal at intermediate to high momentum transfer. This means that in the standard approach of simulating scattering via one-electron matrix elements, the truncation of states can lead to incorrect or spurious signals. In order to achieve qualitative and quantitative accuracy, we advise the computation via two-electron scattering matrix elements.

## 5. Summary and Outlook

The field of attosecond science is a novel and fast-evolving research area that aims at unravelling the motion of particles in atoms, molecules, and solids. Therein, attochemistry thrives to understand, monitor, and one-day control the movement of electrons in molecules, which will open a new path to steer nuclear dynamics and photochemical reactions. In order to observe the motion of electrons, attosecond resolution and, thus, attosecond light pulses are needed. These attosecond pulses are inherently rooted in the high-frequency regime, ranging from XUV to soft and hard x-ray radiation. Depending on the energy, intensity, and aimed-at observable, different light-matter interactions can be studied.

In this work, we tackled three different kinds of high-frequency light-matter interaction that originate in three different energy regimes and allow us to gain novel insight into the dynamics of molecules. In the XUV regime, the ionisation dynamics of correlated, multi-particle systems was studied together with few-cycle effects. In the soft x-ray regime, attosecond x-ray absorption was introduced as a novel tool to observe coupled electron and nuclear dynamics in a neutral molecule. In the hard x-ray regime, we focussed on ultrafast, non-resonant x-ray scattering, which can be transformed into a future technology capable of observing electron dynamics.

So far, correlation dynamics induced by XUV ionisation has mainly been addressed for atoms. In section 4.1, we investigated how correlation dynamics translates from atoms to molecules. To this end, we employed a grid-based, reduced-dimensionality molecular quantum model system, which allows us to qualitatively understand particle correlation in molecules during and after XUV light pulse interaction. The particle correlation within this model is treated numerically exactly, and the dynamics are described beyond the single active electron approximation and frozen nuclei approximation. The light pulse interaction is included explicitly within the dipole approximation, and the grid incorporates the electron continuum. The results showed that electron-electron correlation leads to shake and knock process as previously reported for atomic systems. In molecules, electrons are multi-centred around the nuclei, which leads to shake and knock processes being further dissected into various ionisation pathways. Importantly, these pathways lead to unique forward/backward asymmetries in the one-photon peaks of the photoelectron spectrum. Thus, observing these asymmetries directly measures dynamic electron-electron correlation in molecules during and after the light pulse interaction. Moreover, these pathways exhibit different ionisation time delays ranging from a few tenths of attoseconds to one fem-

tosecond. On top of the electron-electron correlation-based asymmetry, nuclear-electron correlation leads to an asymmetry in the integrated photoelectron spectrum, imprinting the coupled nuclear-electron dynamics of a bound system in a nuclear non-equilibrium state. These results show the fundamental impact of correlation on the molecular XUV ionisation process and open the possibility of measuring correlation dynamics in molecules via asymmetries in the photoelectron spectrum or via time delays. While the complete description of the correlated XUV ionisation process is only feasible for model systems, approximated methods could be used to calculate only the effects imprinted in the observables, with our work providing the underlying physical reasoning. For example, approximate theories can calculate continuum resonances and hole states, which would allow inferring the ionisation pathways discovered in this work. Moreover, one can simulate the non-equilibrium nuclear dynamics in the bound state that are imprinted on the spectrum. From a theoretical method development point of view, we also showed how approximations could be incorporated into future theories to allow the treatment of larger systems. For example, the attosecond electronic population dynamics in the parent ion is only marginally influenced by the propagating nuclear wave packet during ionisation. Thus, instead of a fully quantum dynamical approach to the nuclear degree of freedom, a classical sampling approach of the nuclear wave packet, or even a purely electronic treatment, is possible. Moreover, the nuclear momentum conservation between the target and parent ion could be incorporated into classical approximations. These are points of interest for future research.

An asymmetry in the photoelectron spectrum cannot just originate from particle correlation but also from a high-intensity, few-cycle XUV pulse, which is important to keep in mind when designing future experiments. This was revealed in section 4.2 for atoms, where we provided a detailed analysis of few-cycle XUV pulses beyond the slowly varying envelope approximation and discussed the atomic photoionisation dynamics initiated by such pulses. In first-order, we reported a red shift in the photoelectron spectrum via dipole reshaping and a CEP-dependent asymmetry in the photoelectron spectrum due to the few-cycle nature of the pulse. In higher-orders, polarisation and continuum interference lead to intricate CEP- and intensity-dependent photoelectron spectrum asymmetries. Investigating the interplay of correlation-driven asymmetries and few-cycle pulse-driven asymmetries is a future research question. Moreover, for long, high-frequency pulses, dynamic interference processes have been reported<sup>[188–190]</sup>, and it will be of future interest to see their influence on the processes reported in this work with (un)chirped few-cycle XUV pulses.

The project in section 4.3 encompassed a joint experimental and theoretical study of the photo-induced relaxation dynamics of neutral furan, revealed by attosecond x-ray absorption spectroscopy. The experiment used a strong-field pump and an attosecond soft x-ray probe pulse. The latter was from an HHG source and allowed us to combine the site selectivity and electronic and nuclear sensitivity of x-ray absorption with sub-fs temporal resolution. The theory utilized a multi-physics approach combining several methods to

---

model each pulse interaction and the induced relaxation dynamics along all possible nuclear pathways. Upon excitation, we identify electronic coherence between excited states mediated by a conical intersection. This manifests as carbon-site sensitive electronic quantum beating in the absorption signal. Furthermore, we detect nuclear-electron correlation as a dephasing of electronic coherence and build-up of nuclear coherence along the ring-opening pathway. Moreover, we spectrally assign changes in the system’s electronic character (electronic state switching) during the ultrafast dynamics and reveal vibrational cooling to the ring-opening ground state. The combined energy and time resolution revealed hitherto inaccessible insight into the real-time electronic and nuclear dynamics of furan and, thus, demonstrates the efficacy of attosecond core-level spectroscopy for investigating real-time dynamics in neutral and complex molecular systems. We strongly believe this method can be applied to many molecules and pioneer new experiments in ultrafast dynamics and attochemistry. Consequently, the intricate knowledge revealed about relaxation dynamics, different couplings, and phase evolution may provide a decisive new basis for an engineered approach to quantum control. An interesting first application would be to investigate the influence of the pump’s CEP on the relaxation dynamics. In the future, the experimental approach can be further developed. With technological advances, improvements in the photon flux and, thus, the signal-to-noise ratio are possible, and new IR sources might make the oxygen K-edge energetically accessible for SXR pulses from HHG. Furthermore, substituting the strong-field pump with an optical UV pulse will allow the selective excitation of organic systems.

Lastly, in section 4.4, static and ultrafast x-ray scattering was studied using our previously introduced molecular model system. We thoroughly introduced the theory based on one-electron and two-electron scattering matrix elements and adapted it to our model. By using an orthonormalised plane wave ansatz, we revealed that single ionisation plays a crucial role in the inelastic and coherent mixed scattering signal at intermediate to high momentum transfer. This has decisive implications for the common approach of simulation via one-electron matrix elements, as it shows that an incomplete account of bound and continuum transitions can lead to incorrect or spurious scattering signals. Consequently, it is advisable to compute scattering signals from two-electron scattering matrix elements that inherently account for all accessible electronic transitions in the bound and single ionisation manifold. We expect these findings to be crucial for future simulations and method development in x-ray scattering. Furthermore, an extension of this work to electron scattering, where the coupling to the nuclear degree of freedom becomes relevant, could be elucidated in future works. Another natural extension would be to use x-ray scattering to probe correlation dynamics or charge migration in our molecular model system and hereby reveal how features like various ionisation pathways, coherent parent ion wave packets, and non-adiabatic transitions imprint on the x-ray scattering signal.

In the introduction, some of the current interests in the field were outlined, such as correlation dynamics in molecules, photoionisation time delays, new methods for investi-

gating the light-induced dynamics in neutral systems, and the potential of x-ray scattering and x-ray absorption as novel approaches to attosecond experiments. In this work, we tackled these pressing questions. On a fundamental level, we enhanced our understanding of molecular correlation dynamics, modulated few-cycle light-matter interaction, and non-resonant x-ray scattering. Furthermore, we proposed correlation-driven observables in photoelectron spectroscopy and showed the potential of ultrafast x-ray scattering for future attosecond experiments. Additionally, in a pioneering, joint experimental and theoretical study, the correlated electron and nuclear dynamics in neutral furan were revealed in real time using attosecond x-ray absorption spectroscopy. We are confident that this work will benefit the general understanding of high-frequency light-matter interaction in atoms and molecules, as well as aid and initiate new experiments in the field of attochemistry using XUV ionisation, x-ray absorption, and x-ray scattering.

---

Das Gebiet der Attosekundenforschung ist ein neuartiges und sich schnell entwickelndes Forschungsgebiet, das darauf abzielt, die Bewegung von Teilchen in Atomen, Molekülen und Festkörpern zu entschlüsseln. Der Teilbereich der Attochemie strebt danach, die Bewegung von Elektronen in Molekülen zu verstehen, zu messen und eines Tages zu kontrollieren. Dies könnte einen neuen Weg zur Kontrolle von Kerndynamik und photochemischer Reaktionen eröffnen. Um die Bewegung der Elektronen zu beobachten, ist eine Auflösung im Attosekundenbereich und damit Attosekundenpulse erforderlich. Diese Lichtpulse sind von Natur aus im Hochfrequenzbereich angesiedelt, der von XUV bis zu weicher und harter Röntgenstrahlung reicht. Je nach Energie, Intensität und angestrebter Observable können verschiedene Licht-Materie-Wechselwirkungen untersucht werden. In dieser Arbeit wurden drei verschiedene Arten von hochfrequenter Licht-Materie-Wechselwirkungen untersucht, die in drei verschiedenen Energieregimen verwurzelt sind und uns neue Einblicke in die Dynamik von Molekülen gewähren. Im XUV-Regime wurde die Ionisationsdynamik von korrelierten Mehrteilchensystemen und Effekte von Pulsen weniger optischer Zyklen untersucht. Im weichen X-ray Bereich wurde die attosekunden X-ray Absorption als neues Instrument zur Beobachtung der gekoppelten Elektronen- und Kerndynamik in einem neutralen Molekül vorgestellt. Im Bereich der harten Röntgenstrahlung konzentrierten wir uns auf ultraschnelle, nicht-resonante Röntgenstreuung, die zu einer zukünftigen Technologie für die Beobachtung von Elektronendynamik werden könnte.

Bisher wurde Korrelationsdynamik, die durch XUV-Ionisierung hervorgerufen wird, hauptsächlich für Atome untersucht. In Abschnitt 4.1 haben wir uns mit der Übertragung der Korrelationsdynamik von Atomen auf Moleküle beschäftigt. Zu diesem Zweck nutzten wir ein gitterbasiertes, dimensionsreduziertes molekulares Quantenmodellsystem, das uns ein qualitatives Verständnis der Teilchenkorrelation in Molekülen während und nach der XUV-Wechselwirkung ermöglicht. Die Teilchenkorrelation in diesem Modell wird numerisch exakt behandelt, und die Dynamik wird jenseits der Näherung eines einzelnen aktiven Elektrons und eingefrorener Atomkerne beschrieben. Die Lichtpuls-Wechselwirkung wird explizit mittels Dipolnäherung einbezogen, und das Gitter enthält das Elektronenkontinuum. Die Ergebnisse zeigen, dass die Elektron-Elektron-Korrelation zu einem shake und knock Prozess führt, wie er bereits für atomare Systeme berichtet wurde. In Molekülen sind die Elektronen in mehreren Zentren um die Kerne herum angeordnet, und die shake und knock Prozesse können in verschiedene Ionisierungswege unterteilt werden. Wichtig ist, dass diese Wege zu einzigartigen Vorwärts/Rückwärts-Asymmetrien in den Ein-Photonen-Signalen des Photoelektronenspektrums führen. Durch die Beobachtung dieser Asymmetrien lässt sich die dynamische Elektron-Elektron-Korrelation in den Molekülen während und nach der Lichtpulswechselwirkung direkt messen. Darüber hinaus weisen diese Pfade unterschiedliche Ionisierungszeitverzögerungen auf, die von einigen Zehntel Attosekunden bis zu einer Femtosekunde reichen. Zusätzlich zu der auf der Elektron-Elektron-Korrelation basierenden Asymmetrie führt die Kern-Elektron-Korrelation zu einer Asymmetrie im integrierten Photoelektronenspektrum, die durch die gekoppelte Kern-Elektron-Dynamik

eines gebundenen Systems in einem nuklearen Nicht-Gleichgewichtszustand geprägt ist. Diese Ergebnisse zeigen den fundamentalen Einfluss der Korrelation auf den molekularen XUV-Ionisierungsprozess und eröffnen die Möglichkeit, die Korrelationsdynamik in Molekülen über Asymmetrien im Photoelektronenspektrum oder über Zeitverzögerungen zu messen. Während die vollständige Beschreibung des korrelierten XUV-Ionisationsprozesses nur für Modellsysteme möglich ist, könnten approximative Methoden verwendet werden, um nur die in den Observablen eingepprägten Effekte zu berechnen, wobei unsere Arbeit die zugrundeliegenden physikalischen Überlegungen liefert. Mit Hilfe von Näherungstheorien können beispielsweise Kontinuumsresonanzen und Lochzustände berechnet werden, die Rückschlüsse auf die in dieser Arbeit entdeckten Ionisierungswege zulassen würden. Außerdem kann man die Nichtgleichgewichts-Kerndynamik im gebundenen Zustand simulieren, die dem Spektrum über die Kern-Elektronen-Korrelation aufgeprägt wird. Im Hinblick auf die Entwicklung theoretischer Methoden haben wir auch gezeigt, wie Näherungen in künftige Theorien aufgenommen werden könnten, um die Behandlung größerer Systeme zu ermöglichen. Beispielsweise wird die Dynamik der elektronischen Population im Kation nur geringfügig durch das sich bewegende Kernwellenpaket während der Ionisierung beeinflusst. Anstelle eines vollständig quantendynamischen Ansatzes für den Kern-Freiheitsgrad ist daher ein klassischer Ansatz des Kernwellenpakets oder sogar eine rein elektronische Behandlung möglich. Darüber hinaus könnte die Impulserhaltung in den Kernen zwischen dem Molekül und dem Kation in klassische Näherungen einbezogen werden. Dies sind Punkte, die für künftige Forschungen von Interesse sind.

Eine Asymmetrie im Photoelektronenspektrum kann nicht nur von der Teilchenkorrelation herrühren, sondern auch von einem hochintensiven XUV-Puls mit wenigen Zyklen, was bei der Planung künftiger Experimente berücksichtigt werden muss. Dies wurde in Abschnitt 4.2 für Atome gezeigt, wo wir eine detaillierte Analyse von XUV-Pulsen mit wenigen Zyklen jenseits der Näherung der langsam variierenden Einhüllenden lieferten. Außerdem zeigten wir die durch solche Pulse ausgelöste Dynamik der atomaren Photoionisation auf. In erster Ordnung berichten wir von einer Rotverschiebung des Photoelektronenspektrums durch Dipolformung und eine CEP-abhängige Asymmetrie des Photoelektronenspektrums, die auf den Wenige-Zyklen-Charakter des Pulses zurückzuführen ist. Bei höheren Ordnungen führen Polarisation und Kontinuumsinterferenz zu komplizierten CEP- und intensitätsabhängigen Asymmetrien im Photoelektronenspektrum. Die Untersuchung des Zusammenspiels von korrelationsgetriebenen Asymmetrien und pulsgetriebenen Asymmetrien mit wenigen Zyklen ist eine zukünftige Forschungsfrage. Darüber hinaus wurde für lange, hochfrequente Pulse über dynamische Interferenzprozesse berichtet<sup>[188–190]</sup>. Es wird von Interesse sein, dies auf unsere Arbeit mit (un)gechirpten XUV-Pulsen mit wenigen Zyklen zu übertragen. Das Projekt in Abschnitt 4.3 umfasste eine gemeinsame experimentelle und theoretische Studie der photoinduzierten Relaxationsdynamik von neutralem Furan mittels attosekunden Röntgenabsorptionsspektroskopie. Das Experiment verwendete einen intensiven NIR pump Lichtpuls und einen attosekunden



---

probe Puls aus einer HHG-Quelle, der es uns ermöglichte, die Ortsselektivität und die elektronische und nukleare Empfindlichkeit der Röntgenabsorption mit einer zeitlichen Auflösung im sub-fs Bereich zu kombinieren. Die Theorie verwendet einen multiphysikalischen Ansatz, der mehrere Methoden kombiniert, um die Wechselwirkungen der einzelnen Pulse und die induzierte Relaxationsdynamik entlang aller möglichen Pfade zu modellieren. Nach der Anregung stellen wir eine elektronische Kohärenz zwischen angeregten Zuständen fest, die durch eine konische Durchschneidung ausgelöst wird. Diese manifestiert sich als kohlenstoffsensitives elektronisches quantum beating im Absorptionssignal. Kern-Elektronen-Korrelation führt zu einer Dephasierung der elektronischen Kohärenz und Aufbau einer Kernkohärenz entlang des Ringöffnungsweges. Darüber hinaus ordnen wir Änderungen im elektronischen Charakter des Systems (elektronischer Zustandswechsel) während der ultraschnellen Dynamik spektral zu und zeigen eine Schwingungskühlung entlang der Ringöffnung. Die kombinierte Energie- und Zeitauflösung ermöglichte bisher unzugängliche Einblicke in die elektronische und nukleare Echtzeitdynamik von Furan und demonstriert damit die Wirksamkeit der attosekunden Röntgenabsorptionsspektroskopie zur Untersuchung der Echtzeitdynamik in neutralen und komplexen molekularen Systemen. Wir sind der festen Überzeugung, dass diese Methode auf viele Moleküle angewendet werden kann und neue Experimente im Bereich der ultraschnellen Dynamik und Attochemie ermöglicht. Das komplexe Wissen über die Relaxationsdynamik, die verschiedenen Kopplungen und die Phasenentwicklung könnte eine entscheidende neue Grundlage für einen technischen Ansatz zur Quantenkontrolle bilden. Eine interessante erste Anwendung wäre es, den Einfluss des CEP des pump Pulses auf die Relaxationsdynamik zu untersuchen. In Zukunft kann der experimentelle Ansatz weiterentwickelt werden. Mit technologischen Fortschritten sind Verbesserungen des Photonenflusses und damit des Signal-Rausch-Verhältnisses möglich, und neue IR-Quellen könnten die Sauerstoff-K-Kante für SXR-Pulse aus HHG energetisch zugänglich machen. Darüber hinaus wird die Ersetzung des Starkfeld pump Pulses durch einen optischen UV-Puls die selektive Anregung organischer Systeme ermöglichen.

Schließlich wurde in Abschnitt 4.4 die statische und ultraschnelle Röntgenstreuung unter Verwendung unseres zuvor eingeführten molekularen Modellsystems untersucht. Wir haben die Theorie, die auf Ein-Elektronen- und Zwei-Elektronen-Streuungsmatrixelementen basiert, gründlich dargelegt und an unser Modell angepasst. Durch die Verwendung eines orthonormierten Ansatzes für ebene Wellen konnten wir zeigen, dass die Einzelionisation eine entscheidende Rolle für das Signal der inelastischen und kohärent gemischten Streuung bei mittleren bis hohen Impulsübertrag spielt. Dies hat entscheidende Auswirkungen auf den üblichen Simulationsansatz über Ein-Elektronen-Matrixelemente, da es zeigt, dass eine unvollständige Berücksichtigung von gebundenen und Kontinuumsübergängen zu falschen Streusignalen führen kann. Folglich ist es ratsam, Streusignale mit Hilfe von Zwei-Elektronen-Matrixelementen zu berechnen. Wir gehen davon aus, dass diese Erkenntnisse für zukünftige Simulationen und Methodenentwicklungen in der Röntgenstreuung von ent-

scheidender Bedeutung sein werden. Darüber hinaus könnte die Elektronenstreuung, bei der die Kopplung an den Kren-Freiheitsgrad relevant wird, in zukünftigen Arbeiten untersucht werden. Eine weiterer Anknüpfungspunkt wäre die Verwendung der Röntgenstreuung zur Untersuchung der Korrelationsdynamik oder der Ladungsmigration in unserem molekularen Modellsystem, um zu zeigen, wie Merkmale wie verschiedene Ionisierungspfade, kohärente Wellenpakete und nicht-adiabatische Übergänge das Streusignal beeinflussen.

In der Einleitung wurden einige der aktuellen Interessen auf diesem Gebiet umrissen, wie z.B. Korrelationsdynamik in Molekülen, Zeitverzögerungen bei der Photoionisation, neue Methoden zur Untersuchung der lichtinduzierten Dynamik in neutralen Systemen und das Potential von Röntgenstreuung und Röntgenabsorption als neue Ansätze für Attosekunden-Experimente. In dieser Arbeit haben wir uns mit diesen drängenden Fragen beschäftigt. Auf fundamentaler Ebene haben wir unser Verständnis der molekularen Korrelationsdynamik, der modulierten Licht-Materie-Wechselwirkung von Pulsen mit wenigen Zyklen und der nicht-resonanten Röntgenstreuung bereichert. Darüber hinaus haben wir korrelationsgetriebene Observablen in der Photoelektronenspektroskopie vorgeschlagen und das Potential der ultraschnellen Röntgenstreuung für zukünftige Attosekunden-Experimente aufgezeigt. In einer bahnbrechenden, experimentellen und theoretischen Studie wurde die korrelierte Elektronen- und Kerndynamik in neutralem Furan in Echtzeit mit Hilfe der attosekunden Röntgenabsorptionsspektroskopie aufgezeigt. Wir sind zuversichtlich, dass diese Arbeit zum allgemeinen Verständnis der hochfrequenten-Licht-Materie-Wechselwirkung in Atomen und Molekülen beiträgt und neue Experimente auf dem Gebiet der Attochemie unter Verwendung von XUV-Ionisation, Röntgenabsorption und Röntgenstreuung unterstützen und initiieren wird.

## Bibliography

- [1] Lépine, F.; Ivanov, M. Y.; Vrakking, M. J. J. *Nature Photonics* **2014**, *8*, 195–204.
- [2] Nisoli, M.; Decleva, P.; Calegari, F.; Palacios, A.; Martín, F. *Chemical Reviews* **2017**, *117*, 10760–10825.
- [3] Domcke, W.; Yarkony, D. R. *Annual review of physical chemistry* **2012**, *63*, 325–352.
- [4] Ashfold, M. N. R.; Cronin, B.; Devine, A. L.; Dixon, R. N.; Nix, M. G. D. *Science* **2006**, *312*, 1637–1640.
- [5] Gray, H. B.; Winkler, J. R. *Quarterly reviews of biophysics* **2003**, *36*, 341–372.
- [6] Barbara, P. F.; Meyer, T. J.; Ratner, M. A. *The Journal of Physical Chemistry* **1996**, *100*, 13148–13168.
- [7] Zewail, A. H. *Science* **1988**, *242*, 1645–1653.
- [8] Zewail, A. H. *The Journal of Physical Chemistry A* **2000**, *104*, 5660–5694.
- [9] Emma, P. et al. *Nature Photonics* **2010**, *4*, 641–647.
- [10] Bostedt, C.; Bozek, J. D.; Bucksbaum, P. H.; Coffee, R. N.; Hastings, J. B.; Huang, Z.; Lee, R. W.; Schorb, S.; Corlett, J. N.; Denes, P. *Journal of Physics B: Atomic, Molecular and Optical Physics* **2013**, *46*, 164003.
- [11] Yabashi, M.; Tanaka, H.; Tanaka, T.; Tomizawa, H.; Togashi, T.; Nagasono, M.; Ishikawa, T.; Harries, J. R.; Hikosaka, Y.; Hishikawa, A.; Nagaya, K.; Saito, N.; Shigemasa, E.; Yamanouchi, K.; Ueda, K. *Journal of Physics B: Atomic, Molecular and Optical Physics* **2013**, *46*, 164001.
- [12] Feldhaus, J.; Krikunova, M.; Meyer, M.; Möller, T.; Moshhammer, R.; Rudenko, A.; Tschentscher, T.; Ullrich, J. *Journal of Physics B: Atomic, Molecular and Optical Physics* **2013**, *46*, 164002.
- [13] Odate, A.; Kirrander, A.; Weber, P. M.; Minitti, M. P. *Advances in Physics: X* **2023**, *8*, 2126796.
- [14] Strickland, D.; Mourou, G. *Optics Communications* **1985**, *56*, 219–221.
- [15] Nisoli, M.; De Silvestri, S.; Svelto, O. *Applied Physics Letters* **1996**, *68*, 2793–2795.

- [16] Stolen, R. H.; Lin, C. *Physical Review A* **1978**, *17*, 1448–1453.
- [17] Baltuška, A.; Udem, T.; Uiberacker, M.; Hentschel, M.; Goulielmakis, E.; Gohle, C.; Holzwarth, R.; Yakovlev, V. S.; Scrinzi, A.; Hänsch, T. W.; Krausz, F. *Nature* **2003**, *421*, 611–615.
- [18] Szipöcs, R.; Ferencz, K.; Spielmann, C.; Krausz, F. *Optics Letters* **1994**, *19*, 201–203.
- [19] McPherson, A.; Gibson, G.; Jara, H.; Johann, U.; Luk, T. S.; McIntyre, I. A.; Boyer, K.; Rhodes, C. K. *JOSA B* **1987**, *4*, 595–601.
- [20] Krause, J. L.; Schafer, K. J.; Kulander, K. C. *Physical Review Letters* **1992**, *68*, 3535.
- [21] Kienberger, R.; Goulielmakis, E.; Uiberacker, M.; Baltuska, A.; Yakovlev, V.; Bammer, F.; Scrinzi, A.; Westerwalbesloh, T.; Kleineberg, U.; Heinzmann, U.; Drescher, M.; Krausz, F. *Nature* **2004**, *427*, 817–821.
- [22] Sansone, G.; Benedetti, E.; Calegari, F.; Vozzi, C.; Avaldi, L.; Flammini, R.; Polletto, L.; Villoresi, P.; Altucci, C.; Velotta, R.; Stagira, S.; De Silvestri, S.; Nisoli, M. *Science* **2006**, *314*, 443–446.
- [23] Hentschel, M.; Kienberger, R.; Spielmann, C.; Reider, G. A.; Milosevic, N.; Brabec, T.; Corkum, P.; Heinzmann, U.; Drescher, M.; Krausz, F. *Nature* **2001**, *414*, 509–513.
- [24] Krausz, F.; Ivanov, M. *Reviews of Modern Physics* **2009**, *81*, 163–234.
- [25] Corkum, P. B.; Krausz, F. *Nature Physics* **2007**, *3*, 381–387.
- [26] Duris, J. et al. *Nature Photonics* **2020**, *14*, 30–36.
- [27] Malyzhenkov, A.; Arbelo, Y. P.; Craievich, P.; Dijkstal, P.; Ferrari, E.; Reiche, S.; Schietinger, T.; Juranić, P.; Prat, E. *Physical Review Research* **2020**, *2*, 042018.
- [28] Huang, S.; Ding, Y.; Feng, Y.; Hemsing, E.; Huang, Z.; Krzywinski, J.; Lutman, A.; Marinelli, A.; Maxwell, T.; Zhu, D. *Physical Review Letters* **2017**, *119*, 154801.
- [29] Marinelli, A.; MacArthur, J.; Emma, P.; Guetg, M.; Field, C.; Kharakh, D.; Lutman, A. A.; Ding, Y.; Huang, Z. *Applied Physics Letters* **2017**, *111*, 151101.
- [30] Hartmann, N. et al. *Nature Photonics* **2018**, *12*, 215–220.
- [31] Nisoli, M. *Optics and Photonics News* **2019**, *30*, 32–39.
- [32] Hader, K.; Albert, J.; Gross, E. K. U.; Engel, V. *The Journal of Chemical Physics* **2017**, *146*, 074304.

- 
- [33] Polli, D.; Altoè, P.; Weingart, O.; Spillane, K. M.; Manzoni, C.; Brida, D.; Tomasello, G.; Orlandi, G.; Kukura, P.; Mathies, R. A.; Garavelli, M.; Cerullo, G. *Nature* **2010**, *467*, 440–443.
- [34] Crespo-Hernández, C. E.; Cohen, B.; Hare, P. M.; Kohler, B. *Chemical Reviews* **2004**, *104*, 1977–2020.
- [35] Wolter, B.; Pullen, M. G.; Baudisch, M.; Sclafani, M.; Hemmer, M.; Senftleben, A.; Schröter, C. D.; Ullrich, J.; Moshhammer, R.; Biegert, J. *Physical Review X* **2015**, *5*, 021034.
- [36] Zuo, T.; Bandrauk, A. D.; Corkum, P. B. *Chemical Physics Letters* **1996**, *259*, 313–320.
- [37] Blaga, C. I.; Xu, J.; DiChiara, A. D.; Sistrunk, E.; Zhang, K.; Agostini, P.; Miller, T. A.; DiMauro, L. F.; Lin, C. D. *Nature* **2012**, *483*, 194–197.
- [38] Meckel, M.; Comtois, D.; Zeidler, D.; Staudte, A.; Pavičić, D.; Bandulet, H. C.; Pépin, H.; Kieffer, J. C.; Dörner, R.; Villeneuve, D. M.; Corkum, P. B. *Science* **2008**, *320*, 1478–1482.
- [39] Huismans, Y. et al. *Science* **2011**, *331*, 61–64.
- [40] Bian, X.-B.; Huismans, Y.; Smirnova, O.; Yuan, K.-J.; Vrakking, M. J. J.; Bandrauk, A. D. *Physical Review A* **2011**, *84*, 043420.
- [41] Eckle, P.; Pfeiffer, A. N.; Cirelli, C.; Staudte, A.; Dörner, R.; Müller, H. G.; Büttiker, M.; Keller, U. *Science* **2008**, *322*, 1525–1529.
- [42] Pfeiffer, A. N.; Cirelli, C.; Smolarski, M.; Dimitrovski, D.; Abu-samha, M.; Madsen, L. B.; Keller, U. *Nature Physics* **2012**, *8*, 76–80.
- [43] Smirnova, O.; Mairesse, Y.; Patchkovskii, S.; Dudovich, N.; Villeneuve, D.; Corkum, P.; Ivanov, M. Y. *Nature* **2009**, *460*, 972–977.
- [44] McFarland, B. K.; Farrell, J. P.; Bucksbaum, P. H.; Gühr, M. *Science* **2008**, *322*, 1232–1235.
- [45] Shafir, D.; Mairesse, Y.; Villeneuve, D. M.; Corkum, P. B.; Dudovich, N. *Nature Physics* **2009**, *5*, 412–416.
- [46] Pazourek, R.; Nagele, S.; Burgdörfer, J. *Reviews of Modern Physics* **2015**, *87*, 765–802.
- [47] Sansone, G. et al. *Nature* **2010**, *465*, 763–766.

- [48] Siu, W.; Kelkensberg, F.; Gademann, G.; Rouzée, A.; Johnsson, P.; Dowek, D.; Lucchini, M.; Calegari, F.; De Giovannini, U.; Rubio, A.; Lucchese, R. R.; Kono, H.; Lépine, F.; Vrakking, M. J. J. *Physical Review A* **2011**, *84*, 063412.
- [49] Cörlin, P.; Fischer, A.; Schönwald, M.; Sperl, A.; Mizuno, T.; Thumm, U.; Pfeifer, T.; Moshhammer, R. *Physical Review A* **2015**, *91*, 043415.
- [50] Sandhu, A. S.; Gagnon, E.; Santra, R.; Sharma, V.; Li, W.; Ho, P.; Ranitovic, P.; Cocke, C. L.; Murnane, M. M.; Kapteyn, H. C. *Science* **2008**, *322*, 1081–1085.
- [51] Znakovskaya, I.; von den Hoff, P.; Zherebtsov, S.; Wirth, A.; Herrwerth, O.; Vrakking, M. J. J.; de Vivie-Riedle, R.; Kling, M. F. *Physical Review Letters* **2009**, *103*, 103002.
- [52] Lucchini, M.; Kim, K.; Calegari, F.; Kelkensberg, F.; Siu, W.; Sansone, G.; Vrakking, M. J. J.; Hochlaf, M.; Nisoli, M. *Physical Review A* **2012**, *86*, 043404.
- [53] Eckstein, M.; Yang, C.-H.; Kubin, M.; Frassetto, F.; Poletto, L.; Ritze, H.-H.; Vrakking, M. J. J.; Kornilov, O. *The Journal of Physical Chemistry Letters* **2015**, *6*, 419–425.
- [54] Neidel, C. et al. *Physical Review Letters* **2013**, *111*, 033001.
- [55] Calegari, F.; Ayuso, D.; Trabatttoni, A.; Belshaw, L.; De Camillis, S.; Anumula, S.; Frassetto, F.; Poletto, L.; Palacios, A.; Decleva, P.; Greenwood, J. B.; Martín, F.; Nisoli, M. *Science* **2014**, *346*, 336–339.
- [56] Cederbaum, L. S.; Zobeley, J. *Chemical Physics Letters* **1999**, *307*, 205–210.
- [57] Ossiander, M.; Siegrist, F.; Shirvanyan, V.; Pazourek, R.; Sommer, A.; Latka, T.; Guggenmos, A.; Nagele, S.; Feist, J.; Burgdörfer, J.; Kienberger, R.; Schultze, M. *Nature Physics* **2017**, *13*, 280–285.
- [58] Beaulieu, S. et al. *Nature Physics* **2018**, *14*, 484–489.
- [59] Ludwig, A.; Maurer, J.; Mayer, B.; Phillips, C.; Gallmann, L.; Keller, U. *Physical Review Letters* **2014**, *113*, 243001.
- [60] Kaldun, A.; Blättermann, A.; Stooß, V.; Donsa, S.; Wei, H.; Pazourek, R.; Nagele, S.; Ott, C.; Lin, C. D.; Burgdörfer, J.; Pfeifer, T. *Science* **2016**, *354*, 738–741.
- [61] Zinchenko, K. S.; Ardana-Lamas, F.; Seidu, I.; Neville, S. P.; van der Veen, J.; Lanfaloni, V. U.; Schuurman, M. S.; Wörner, H. J. *Science* **2021**, *371*, 489–494.
- [62] Young, L. et al. *Journal of Physics B: Atomic, Molecular and Optical Physics* **2018**, *51*, 032003.

- 
- [63] Simmermacher, M.; Henriksen, N. E.; Møller, K. B.; Moreno Carrascosa, A.; Kirrander, A. *Physical Review Letters* **2019**, *122*, 073003.
- [64] Cohen-Tannoudji, C.; Diu, B.; Laloe, F. *Quantum Mechanics, Volume 1*; 1986; Vol. 1.
- [65] Cohen-Tannoudji, C.; Diu, B.; Laloe, F. *Quantum Mechanics, Volume 2*; 1986; Vol. 2.
- [66] Sakurai, J. J. *Modern quantum mechanics* Addison. 1994.
- [67] Tannor, D. J. *Introduction to Quantum Mechanics: A Time-Dependent Perspective*; 2007.
- [68] Born, M. *Zeitschrift für Physik* **1926**, *38*, 803–827.
- [69] Bence, S. J.; Riley, K. F.; Hobson, M. P. *Mathematical Methods for Physics and Engineering: a Comprehensive Guide*. 2006.
- [70] Schrödinger, E. *Annalen der Physik* **1926**, *385*, 437–490.
- [71] Dirac, P. A. M. *The principles of quantum mechanics* The Clarendon Press. 1930.
- [72] Joachain, C. J.; Kylstra, N. J.; Potvliege, R. M. *Atoms in intense laser fields*; Cambridge University Press: Cambridge ; New York, 2011.
- [73] Wollenhaupt, M.; Assion, A.; Baumert, T. In *Springer Handbook of Lasers and Optics*; Träger, F., Ed.; Springer Handbooks; Springer: Berlin, Heidelberg, 2012; pp 1047–1094.
- [74] Bandrauk, A. D.; Fillion-Gourdeau, F.; Lorin, E. *Journal of Physics B: Atomic, Molecular and Optical Physics* **2013**, *46*, 153001.
- [75] Dupont-Roc, J.; Grynberg, G. *Photons and atoms: introduction to quantum electrodynamics*; Wiley, 1997.
- [76] Scully, M. O.; Zubairy, M. S. *Quantum Optics*; Cambridge University Press: Cambridge, 1997.
- [77] Maxwell, J. C. *Philosophical Transactions of the Royal Society of London* **1997**, *155*, 459–512.
- [78] Jackson, J. D. *American Journal of Physics* **2002**, *70*, 917–928.
- [79] Jackson, J. D.; Okun, L. B. *Reviews of Modern Physics* **2001**, *73*, 663.
- [80] Jackson, J. D. *Classical Electrodynamics*; John Wiley & Sons, 2021.

- [81] Walser, M. W.; Keitel, C. H.; Scrinzi, A.; Brabec, T. *Physical Review Letters* **2000**, *85*, 5082.
- [82] Reiss, H. R. *Physical Review Letters* **2008**, *101*, 043002.
- [83] Diels, J.-C.; Rudolph, W. *Ultrashort Laser Pulse Phenomena*; Elsevier, 2006.
- [84] McMullen, J. D. *JOSA* **1977**, *67*, 1575–1578.
- [85] Born, M. K. Huang *Dynamical theory of crystal lattices*. 1954.
- [86] Born, M.; Oppenheimer, R. *Annalen der Physik* **1927**, *389*, 457–484.
- [87] Szabo, A.; Ostlund, N. S. *Modern quantum chemistry: introduction to advanced electronic structure theory*; Courier Corporation, 2012.
- [88] Levine, I. N.; Busch, D. H.; Shull, H. *Quantum chemistry*; Pearson Prentice Hall Upper Saddle River, NJ, 2009; Vol. 6.
- [89] McQuarrie, D. A. *Quantum chemistry*; University Science Books, 2008.
- [90] Jensen, F. *Introduction to computational chemistry*; John Wiley & Sons, 2017.
- [91] Lindh, R.; González, L. *Quantum Chemistry and Dynamics of Excited States: Methods and Applications*; John Wiley & Sons, 2020.
- [92] Tully, J. C.; Preston, R. K. *The Journal of Chemical Physics* **1971**, *55*, 562–572.
- [93] Tully, J. C. *The Journal of Chemical Physics* **1990**, *93*, 1061–1071.
- [94] Ben-Nun, M.; Martínez, T. J. *The Journal of Chemical Physics* **1998**, *108*, 7244–7257.
- [95] Ben-Nun, M.; Quenneville, J.; Martínez, T. J. *The Journal of Physical Chemistry A* **2000**, *104*, 5161–5175.
- [96] Shalashilin, D. V. *The Journal of Chemical Physics* **2009**, *130*, 244101.
- [97] Shalashilin, D. V. *The Journal of Chemical Physics* **2010**, *132*, 244111.
- [98] Frigo, M.; Johnson, S. FFTW: an adaptive software architecture for the FFT. Proceedings of the 1998 IEEE International Conference on Acoustics, Speech and Signal Processing, ICASSP '98 (Cat. No.98CH36181). Seattle, WA, USA, 1998; pp 1381–1384.
- [99] Cohen, J. E.; Friedland, S.; Kato, T.; Kelly, F. P. *Linear Algebra and its Applications* **1982**, *45*, 55–95.
- [100] Suzuki, M. *Communications in Mathematical Physics* **1976**, *51*, 183–190.



- 
- [101] Hall, B. C.; Hall, B. C. *Lie groups, Lie algebras, and representations*; Springer, 2013.
- [102] Rossmann, W. *Lie groups: an introduction through linear groups*; Oxford University Press on Demand, 2006; Vol. 5.
- [103] Achilles, R.; Bonfiglioli, A. *Archive for History of Exact Sciences* **2012**, *66*, 295–358.
- [104] Feit, M. D.; Fleck, J. A.; Steiger, A. *Journal of Computational Physics* **1982**, *47*, 412–433.
- [105] Kosloff, R.; Tal-Ezer, H. *Chemical Physics Letters* **1986**, *127*, 223–230.
- [106] Hino, K.-i.; Ishihara, T.; Shimizu, F.; Toshima, N.; McGuire, J. H. *Physical Review A* **1993**, *48*, 1271–1276.
- [107] Pazourek, R.; Feist, J.; Nagele, S.; Burgdörfer, J. *Physical Review Letters* **2012**, *108*, 163001.
- [108] Kheifets, A. S.; Ivanov, I. A.; Bray, I. *Journal of Physics B: Atomic, Molecular and Optical Physics* **2011**, *44*, 101003.
- [109] Sukiasyan, S.; Ishikawa, K. L.; Ivanov, M. *Physical Review A* **2012**, *86*, 033423.
- [110] Shin, S.; Metiu, H. *The Journal of Chemical Physics* **1995**, *102*, 9285–9295.
- [111] Shin, S.; Metiu, H. *The Journal of Physical Chemistry* **1996**, *100*, 7867–7872.
- [112] Albert, J.; Hader, K.; Engel, V. *The Journal of Chemical Physics* **2017**, *147*, 064302.
- [113] Schaupp, T.; Engel, V. *The Journal of Chemical Physics* **2019**, *151*, 084309.
- [114] Schaupp, T.; Engel, V. *The Journal of Chemical Physics* **2022**, *156*, 074302.
- [115] Schaupp, T.; Engel, V. *The Journal of Chemical Physics* **2019**, *150*, 034301.
- [116] Falge, M.; Engel, V.; Gräfe, S. *The Journal of Chemical Physics* **2011**, *134*, 184307.
- [117] Falge, M.; Engel, V.; Gräfe, S. *The Journal of Physical Chemistry Letters* **2012**, *3*, 2617–2620.
- [118] Falge, M.; Fröbel, F. G.; Engel, V.; Gräfe, S. *Physical Chemistry Chemical Physics* **2017**, *19*, 19683–19690.
- [119] Albert, J.; Falge, M.; Gomez, S.; Sola, I. R.; Hildenbrand, H.; Engel, V. *The Journal of Chemical Physics* **2015**, *143*, 041102.
- [120] Erdmann, M.; Gross, E. K. U.; Engel, V. *The Journal of Chemical Physics* **2004**, *121*, 9666–9670.

- [121] Falge, M.; Engel, V.; Lein, M.; Vindel-Zandbergen, P.; Chang, B. Y.; Sola, I. R. *The Journal of Physical Chemistry A* **2012**, *116*, 11427–11433.
- [122] Ziems, K. M.; Bruhnke, J.; Engel, V.; Gräfe, S. *Frontiers in Chemistry* **2022**, *10*.
- [123] Fröbel, F. G.; Ziems, K. M.; Peschel, U.; Gräfe, S.; Schubert, A. *Journal of Physics B: Atomic, Molecular and Optical Physics* **2020**, *53*, 144005.
- [124] Rauch, J.; Mourou, G. *Proceedings of the American Mathematical Society* **2006**, *134*, 851–858.
- [125] Chelkowski, S.; Bandrauk, A. D. *Physical Review A* **2005**, *71*, 053815.
- [126] Ziems, K. M.; Wollenhaupt, M.; Gräfe, S.; Schubert, A. *Journal of Physics B: Atomic, Molecular and Optical Physics* **2023**, *56*, 105602.
- [127] Meitner, L. *Zeitschrift für Physik* **1922**, *9*, 131–144.
- [128] Auger, P. *CR Acad. Sci.(F)* **1923**, *177*, 169.
- [129] Bunker, G. *Introduction to XAFS: a practical guide to X-ray absorption fine structure spectroscopy*; Cambridge University Press, 2010.
- [130] Als-Nielsen, J.; McMorrow, D. *Elements of modern X-ray physics*; John Wiley & Sons, 2011.
- [131] Newville, M. *Reviews in Mineralogy and Geochemistry* **2014**, *78*, 33–74.
- [132] Milne, C. J.; Penfold, T. J.; Chergui, M. *Coordination Chemistry Reviews* **2014**, *277-278*, 44–68.
- [133] Chergui, M.; Collet, E. *Chemical reviews* **2017**, *117*, 11025–11065.
- [134] De Groot, F. *Coordination Chemistry Reviews* **2005**, *249*, 31–63.
- [135] De Groot, F.; Kotani, A. *Core level spectroscopy of solids*; CRC press, 2008.
- [136] Buades, B. et al. *Applied Physics Reviews* **2021**, *8*, 011408.
- [137] Silva, F.; Teichmann, S. M.; Cousin, S. L.; Hemmer, M.; Biegert, J. *Nature communications* **2015**, *6*, 6611.
- [138] Cousin, S. L.; Silva, F.; Teichmann, S.; Hemmer, M.; Buades, B.; Biegert, J. *Optics letters* **2014**, *39*, 5383–5386.
- [139] Cousin, S. L.; Di Palo, N.; Buades, B.; Teichmann, S. M.; Reduzzi, M.; Devetta, M.; Kheifets, A.; Sansone, G.; Biegert, J. *Physical Review X* **2017**, *7*, 041030.

- [140] Buades, B.; Moonshiram, D.; Sidiropoulos, T. P.; León, I.; Schmidt, P.; Pi, I.; Di Palo, N.; Cousin, S. L.; Picón, A.; Koppens, F. *Optica* **2018**, *5*, 502–506.
- [141] Saito, N.; Sannohe, H.; Ishii, N.; Kanai, T.; Kosugi, N.; Wu, Y.; Chew, A.; Han, S.; Chang, Z.; Itatani, J. *Optica* **2019**, *6*, 1542–1546.
- [142] Matselyukh, D. T.; Despré, V.; Golubev, N. V.; Kuleff, A. I.; Wörner, H. J. *Nature Physics* **2022**, *18*, 1206–1213.
- [143] Clarke, T. M.; Durrant, J. R. *Chemical reviews* **2010**, *110*, 6736–6767.
- [144] Dalvie, D. K.; Kalgutkar, A. S.; Khojasteh-Bakht, S. C.; Obach, R. S.; O'Donnell, J. P. *Chemical research in toxicology* **2002**, *15*, 269–299.
- [145] Meotti, F. C.; Silva, D. O.; Dos Santos, A. R.; Zeni, G.; Rocha, J. B. T.; Nogueira, C. W. *Environmental toxicology and pharmacology* **2003**, *15*, 37–44.
- [146] Xu, N.; Gong, J.; Huang, Z. *Renewable and Sustainable Energy Reviews* **2016**, *54*, 1189–1211.
- [147] Frisch, M. J. et al. Gaussian 16 Rev. C.01. 2016.
- [148] Adamo, C.; Barone, V. *The Journal of Chemical Physics* **1999**, *110*, 6158–6170.
- [149] Ernzerhof, M.; Scuseria, G. E. *The Journal of Chemical Physics* **1999**, *110*, 5029–5036.
- [150] Clark, T.; Chandrasekhar, J.; Spitznagel, G. W.; Schleyer, P. V. R. *Journal of Computational Chemistry* **1983**, *4*, 294–301.
- [151] Krishnan, R.; Binkley, J. S.; Seeger, R.; Pople, J. A. *The Journal of Chemical Physics* **1980**, *72*, 650–654.
- [152] Richter, M.; Marquetand, P.; González-Vázquez, J.; Sola, I.; González, L. *Journal of Chemical Theory and Computation* **2011**, *7*, 1253–1258.
- [153] Mai, S.; Marquetand, P.; González, L. *WIREs Computational Molecular Science* **2018**, *8*, e1370.
- [154] Shao, Y. et al. *Molecular Physics* **2015**, *113*, 184–215.
- [155] Purvis, G. D.; Bartlett, R. J. *The Journal of Chemical Physics* **1982**, *76*, 1910–1918.
- [156] Stanton, J. F.; Bartlett, R. J. *The Journal of Chemical Physics* **1993**, *98*, 7029–7039.
- [157] Cederbaum, L. S.; Domcke, W.; Schirmer, J. *Physical Review A* **1980**, *22*, 206–222.
- [158] Vidal, M. L.; Feng, X.; Epifanovsky, E.; Krylov, A. I.; Coriani, S. *Journal of Chemical Theory and Computation* **2019**, *15*, 3117–3133.

- [159] Coriani, S.; Koch, H. *The Journal of Chemical Physics* **2015**, *143*, 181103.
- [160] Dunning, T. H. *The Journal of Chemical Physics* **1989**, *90*, 1007–1023.
- [161] Kendall, R. A.; Dunning, T. H.; Harrison, R. J. *The Journal of Chemical Physics* **1992**, *96*, 6796–6806.
- [162] Severino, S.; Ziemis, K. M.; Reduzzi, M.; Summers, A.; Sun, H.-W.; Chien, Y.-H.; Gräfe, S.; Biegert, J. **2022**, arXiv:2209.04330 [physics].
- [163] Stenrup, M.; Larson, . *Chemical Physics* **2011**, *379*, 6–12.
- [164] Gromov, E. V.; Trofimov, A. B.; Vitkovskaya, N. M.; Schirmer, J.; Köppel, H. *The Journal of Chemical Physics* **2003**, *119*, 737–753.
- [165] Gromov, E. V.; Trofimov, A. B.; Vitkovskaya, N. M.; Köppel, H.; Schirmer, J.; Meyer, H.-D.; Cederbaum, L. S. *The Journal of Chemical Physics* **2004**, *121*, 4585–4598.
- [166] Neville, S. P.; Stolow, A.; Schuurman, M. S. *Journal of Physics B: Atomic, Molecular and Optical Physics* **2022**, *55*, 044004.
- [167] Minitti, M. et al. *Physical Review Letters* **2015**, *114*, 255501.
- [168] Stankus, B.; Yong, H.; Ruddock, J.; Ma, L.; Carrascosa, A. M.; Goff, N.; Boutet, S.; Xu, X.; Zotev, N.; Kirrander, A. *Journal of Physics B: Atomic, Molecular and Optical Physics* **2020**, *53*, 234004.
- [169] Yong, H. et al. *The Journal of Physical Chemistry Letters* **2018**, *9*, 6556–6562.
- [170] Yong, H. et al. *Nature Communications* **2020**, *11*, 2157.
- [171] Dixit, G.; Vendrell, O.; Santra, R. *Proceedings of the National Academy of Sciences* **2012**, *109*, 11636–11640.
- [172] Dixit, G.; Slowik, J. M.; Santra, R. *Physical Review A* **2014**, *89*, 043409.
- [173] Simmermacher, M.; E. Henriksen, N.; B. Møller, K. *Physical Chemistry Chemical Physics* **2017**, *19*, 19740–19749.
- [174] Kowalewski, M.; Bennett, K.; Mukamel, S. *Structural Dynamics* **2017**, *4*, 054101.
- [175] Simmermacher, M.; Moreno Carrascosa, A.; E. Henriksen, N.; B. Møller, K.; Kirrander, A. *The Journal of Chemical Physics* **2019**, *151*, 174302.
- [176] Debye, P. *Physikalische Zeitschrift* **1930**, *31*, 348.
- [177] Bewilogua, L. *Phys. Z* **1932**, *33*, 688–692.

- 
- [178] Henriksen, N. E.; Møller, K. B. *The Journal of Physical Chemistry B* **2008**, *112*, 558–567.
- [179] Simmermacher, M.; Moreno, A.; Henriksen, N.; Møller, K.; Kirrander, A. **2022**, 10.13140/RG.2.2.31342.08005.
- [180] Simmermacher, M.; Weber, P. M.; Kirrander, A. *Scattering Techniques for Molecular Dynamics*; Royal Society of Chemistry, to be published.
- [181] Ziems, K. M.; Simmermacher, M.; Gräfe, S.; Kirrander, A. *The Journal of Chemical Physics* **2023**, *159*, 044108.
- [182] Yong, H.; Cavaletto, S. M.; Mukamel, S. *The Journal of Physical Chemistry Letters* **2021**, *12*, 9800–9806.
- [183] Giri, S.; Tremblay, J. C.; Dixit, G. *Physical Review A* **2021**, *104*, 053115.
- [184] Yong, H.; Rouxel, J. R.; Keefer, D.; Mukamel, S. *Physical Review Letters* **2022**, *129*, 103001.
- [185] Giri, S.; Tremblay, J. C.; Dixit, G. *Physical Review A* **2022**, *106*, 033120.
- [186] Lorenz, U.; Møller, K. B.; Henriksen, N. E. *Physical Review A* **2010**, *81*, 023422.
- [187] Allum, F. et al. *Faraday Discussions* **2021**, *228*, 161–190.
- [188] Toyota, K.; Tolstikhin, O. I.; Morishita, T.; Watanabe, S. *Physical Review Letters* **2009**, *103*, 153003.
- [189] Shao, H.-C.; Robicheaux, F. *Physical Review A* **2016**, *93*, 053414.
- [190] Ning, Q.-C.; Saalman, U.; Rost, J. M. *Physical Review Letters* **2018**, *120*, 033203.



## A. Acknowledgement

Mein größter Dank gilt meiner wundervollen Familie, allen voran Marie Therese Ziems, Wolfgang Ziems, und Annemarie Ziems. Unser Zusammenhalt und eure Unterstützung hat mir mein Studium im In- und Ausland ermöglicht und war maßgeblich für den Erfolg meiner Promotion. And to my dear partner, Tara Sallis, thank you for your unwavering support. I am so lucky to have you by my side along this journey and the ones to come. You are always supporting and motivating my work. I could not have done this without you.

During my PhD, I was fortunate to spend time with and get support from great friends. My thanks go to Kyle Acheson, Jan-Hendrik Kruse, Rešad Kahvedžić, Andrej Kržič, Adrian Saal, Winfried Schmidt, Patrik Steidl, Markus Wohlfahrt, and Ze Pelikans. A special thanks goes to Robin Kampes. I loved our time living together, exploring the culinary depths of the world, discussing and complaining about our days, and always having an open ear. The morning coffee wake-up was pivotal for the success and speed of this work. And of course thank you, Kevin Fiederling. From (lockdown) hikes, to our trip to Slovenia, and our joint obsession with coffee, I am really thankful for your friendship.

I would like to thank Prof. Stefanie Gräfe for the opportunity to work on these interesting topics and for giving me the freedom to explore and learn about various areas. Thank you for the scientific discussions, supervision, and constant support during my research. I am grateful for the advice and relentless support in my academic adventure.

Moreover, I want to thank my second supervisor Prof. Matthias Kling for the many fruitful discussions and the great scientific and career advice.

I extend my gratitude to the whole Gräfe group, especially my K010 office friends, Kevin Fiederling and Rešad Kahvedžić. You guys made the time truly fun and exciting. Between coffee breaks, lunchtime, table tennis, hikes, pizza and feuerzangenbowle evenings, and after-work beers, we surely managed some great scientific discussions and supported each other's research significantly.

Prof. Adam Kirrander and Dr. Mats Simmermacher introduced me to x-ray scattering and took me in with great hospitality, only surpassed by the inspiring scientific environment created. I am grateful for the time I spend with you in Edinburgh and the ongoing support since then.

Crucially, this work would not have been possible without the great co-workers and collaboration partners involved. Thank you, Prof. Jens Biegert, Prof. Volker Engel, Prof.

Adam Kirrander, Prof. Matthias Wollenhaupt, Dr. Georg Fröbel, Dr. Alexander Schubert, Dr. Stefano Severino, Dr. Mats Simmermacher, and Jakob Bruhnke for the great scientific exchange and the chance to learn from you.

I acknowledge the funding agencies involved, foremost the Max Planck School of Photonics for taking me into their graduate school and for providing an interesting and fun programme over the years. Moreover, I acknowledge the funding bodies that facilitated my research stay at the University of Edinburgh: ScotCHEM and funding received from the Scottish Government as well as HPC-EUROPA3 with the support of the EC Research Innovation Action under the H2020 Programme.

I want to thank Prof. Stefanie Gräfe, Kevin Fiederling, Rešad Kahvedžić, Tara Sallis, and Martin Thümmeler for proofreading this thesis.



## B. Documentation of authorship

Here, we provide a list of the contributions of all authors to the publications discussed in this thesis. Bold names indicate PhD students, asterisks indicate equally contributing authors.

### Publication 1:

F.G. Fröbel\*, K.M. Ziems\*, U. Peschel, S. Gräfe, A. Schubert, The impact of electron-electron correlation in ultrafast attosecond single ionization dynamics, *J. Phys. B.: At. Mol. Opt. Phys.*, **2020**, *53*, 144005

Author	Fröbel	<b>Ziems</b>	Peschel	Gräfe	Schubert
<b>Conceptual contribution</b>			x	x	x
<b>Code writing</b>	x	x			
<b>Executing the simulations</b>	x	x			
<b>Data analysis and visualisation</b>	x	x			x
<b>Research discussion</b>	x	x	x	x	x
<b>Preparation of the manuscript</b>	x	x			x
<b>Corrections to the manuscript</b>	x	x	x	x	x
<b>Proposal for publication equivalents</b>	1.0				

### Publication 2:

K.M. Ziems, J. Bruhnke, V. Engel, S. Gräfe, Nuclear-electron correlation effects and their photoelectron imprint in molecular XUV ionisation, *Front. Chem.*, **2022**, *10*, 942633

Author	<b>Ziems</b>	Bruhnke	Engel	Gräfe
<b>Conceptual contribution</b>	x			x
<b>Code writing</b>	x			
<b>Executing the simulations</b>	x	x		
<b>Data analysis and visualisation</b>	x	x		
<b>Research discussion</b>	x	x	x	x
<b>Preparation of the manuscript</b>	x		x	
<b>Corrections to the manuscript</b>	x	x	x	x
<b>Proposal for publication equivalents</b>	1.0			

**Publication 3:**

K.M. Ziems, M. Wollenhaupt, S. Gräfe, A. Schubert, Attosecond ionization dynamics of modulated, few-cycle XUV pulses, *J. Phys. B.: At. Mol. Opt. Phys.*, **2023**, 56, 105602

Author	Ziems	Wollenhaupt	Gräfe	Schubert
Conceptual contribution	x	x	x	x
Code writing	x			
Executing the simulations	x			
Data analysis and visualisation	x			
Research discussion	x	x	x	x
Preparation of the manuscript	x			
Corrections to the manuscript	x	x	x	x
Proposal for publication equivalents	1.0			

**Publication 4:**

S. Severino\*, K.M. Ziems\*, M. Reduzzi, A. Summers, H.-W. Sun, Y.-H. Chien, S. Gräfe, J. Biegert, Non-adiabatic electronic and vibrational ring-opening dynamics resolved with attosecond core-level spectroscopy, *Nature*, **2023** (submitted)

Author	Severino	Ziems	Reduzzi	Gräfe	Biegert
Conceptual contribution				x	x
Code writing		x			
Executing the simulations		x			
Data analysis and visualisation	x	x			
Research discussion	x	x	x	x	x
Preparation of the manuscript	x	x			x
Corrections to the manuscript	x	x	x	x	x
Proposal for publication equivalents	1.0				

This is a joint experimental and theoretical study but only the contributors and their contributions to the theory work are indicated.

**Publication 5:**

K.M. Ziems, M. Simmermacher, S. Gräfe, A. Kirrander, The contribution of Compton ionization to ultrafast x-ray scattering, *J. Chem. Phys.*, **2023**, 159, 044108

Author	Ziems	Simmermacher	Gräfe	Kirrander
Conceptual contribution	x	x	x	x
Code writing	x			
Executing the simulations	x			
Data analysis and visualisation	x	x		
Research discussion	x	x	x	x
Preparation of the manuscript	x	x		
Corrections to the manuscript	x	x	x	x
Proposal for publication equivalents	1.0			

## C. Declaration of authorship

### **Selbstständigkeitserklärung:**

Ich erkläre, dass ich die vorliegende Arbeit selbständig und unter Verwendung der angegebenen Hilfsmittel, persönlichen Mitteilungen und Quellen angefertigt habe.

Jena, den 04.05.2023

.....  
Karl Michael Ziems

**Erklärung zu den Eigenanteilen der Promovendin/des Promovenden sowie der weiteren Doktorandinnen/Doktoranden als Co-Autorinnen/-Autoren an den Publikationen und Zweitpublikationsrechten bei einer kumulativen Dissertation.**

Für alle in dieser kumulativen Dissertation verwendeten Manuskripte liegen die notwendigen Genehmigungen der Verlage („Reprint permissions“) für die Zweitpublikation vor.

Die Co-Autorinnen/-Autoren der in dieser kumulativen Dissertation verwendeten Manuskripte sind sowohl über die Nutzung, als auch über die oben angegebenen Eigenanteile der weiteren Doktorandinnen/Doktoranden als Co-Autorinnen/-Autoren an den Publikationen und Zweitpublikationsrechten bei einer kumulativen Dissertation informiert und stimmen dem zu (es wird empfohlen, diese grundsätzliche Zustimmung bereits bei Einreichung der Veröffentlichung einzuholen bzw. die Gewichtung der Anteile parallel zur Einreichung zu klären).

Die Anteile der Promovendin/des Promovenden sowie der weiteren DoktorandInnen/Doktoranden als Co-Autorinnen/Co-Autoren an den Publikationen und Zweitpublikationsrechten bei einer kumulativen Dissertation sind in der Anlage aufgeführt.

Karl Michael Ziems, 04.05.2023, Jena, .....

Ich bin mit der Abfassung der Dissertation als publikationsbasierte Dissertation, d.h. kumulativ, einverstanden und bestätige die vorstehenden Angaben.

Prof. Dr. Stefanie Gräfe, 04.05.2023, Jena, .....



## D. Publications

The following publications are part of this thesis:

- 1) F.G. Fröbel\*, K.M. Ziems\*, U. Peschel, S. Gräfe, A. Schubert, The impact of electron-electron correlation in ultrafast attosecond single ionization dynamics, *J. Phys. B.: At. Mol. Opt. Phys.*, **2020**, *53*, 144005
- 2) K.M. Ziems, J. Bruhnke, V. Engel, S. Gräfe, Nuclear-electron correlation effects and their photoelectron imprint in molecular XUV ionisation, *Front. Chem.*, **2022**, *10*, 942633
- 3) K.M. Ziems, M. Wollenhaupt, S. Gräfe, A. Schubert, Attosecond ionization dynamics of modulated, few-cycle XUV pulses, *J. Phys. B.: At. Mol. Opt. Phys.*, **2023**, *56*, 105602
- 4) S. Severino\*, K.M. Ziems\*, M. Reduzzi, A. Summers, H.-W. Sun, Y.-H. Chien, S. Gräfe, J. Biegert, Non-adiabatic electronic and vibrational ring-opening dynamics resolved with attosecond core-level spectroscopy, *Nature*, **2023** (submitted)
- 5) K.M. Ziems, M. Simmermacher, S. Gräfe, A. Kirrander, The contribution of Compton ionization to ultrafast x-ray scattering, *J. Chem. Phys.*, **2023**, *159*, 044108

Asterisks indicate equally contributing authors.

# The impact of electron–electron correlation in ultrafast attosecond single ionization dynamics

F G Fröbel<sup>1,2,5</sup>, K M Ziems<sup>1,3,5</sup> , U Peschel<sup>2,4</sup>, S Gräfe<sup>1,2,3</sup>   
and A Schubert<sup>1,6</sup> 

<sup>1</sup> Institute of Physical Chemistry, Friedrich Schiller University Jena, Germany

<sup>2</sup> Abbe Center of Photonics, Friedrich Schiller University Jena, Germany

<sup>3</sup> Max Planck School of Photonics, Jena, Germany

<sup>4</sup> Institute for Condensed Matter Theory and Solid State Optics, Friedrich Schiller University Jena, Germany

E-mail: [Alexander.Schubert@uni-jena.de](mailto:Alexander.Schubert@uni-jena.de)

Received 11 February 2020, revised 23 March 2020

Accepted for publication 22 April 2020

Published 17 June 2020



CrossMark

## Abstract

The attosecond ultrafast ionization dynamics of correlated two- or many-electron systems have, so far, been mainly addressed investigating atomic systems. In the case of single ionization, it is well known that electron–electron correlation modifies the ionization dynamics and observables beyond the single active electron picture, resulting in effects such as the Auger effect or shake-up/down and knock-up/down processes. Here, we extend these works by investigating the attosecond ionization of a molecular system involving correlated two-electron dynamics, as well as non-adiabatic nuclear dynamics. Employing a charge-transfer molecular model system with two differently bound electrons, a strongly and a weakly bound electron, we distinguish different pathways leading to ionization, be it direct ionization or ionization involving elastic and inelastic electron scattering processes. We find that different pathways result in a difference in the electronic population of the parent molecular ion, which, in turn, involves different subsequent (non-adiabatic) postionization dynamics on different time scales.

Keywords: photoemission, single-photon ionization & excitation, ultrafast phenomena

(Some figures may appear in colour only in the online journal)

## 1. Introduction


For many elementary processes in multi-electron systems, such as in photoionization, electron-impact ionization, the Auger effect, and other radiative processes, the impact of correlated electron–electron dynamics plays a crucial role [1]. In the case of ionization, these electron correlations affect the state and the dynamics of the residual cation on

an atto- and femtosecond timescale. As a consequence, the remaining bound electron(s) can be excited (shake-up/knock-up processes [2]), relaxed (shake-down/knock-down), or even ejected subsequently (Auger process) [3]. Such time-resolved ionization dynamics of multi-electron systems have been investigated in various theoretical and experimental studies, for a review see for example reference [4].

On the experimental side, the advent of ultrashort femto- or even attosecond pulses in the extreme ultraviolet (XUV) regime being available either via table-top high-order harmonic generation or the newest generation of (X)FEL sources, for example, paved the way for the observation of these processes in real time, e.g. employing the attosecond

<sup>5</sup> These authors contributed equally to this work.

<sup>6</sup> Author to whom any correspondence should be addressed.

 Original content from this work may be used under the terms of the [Creative Commons Attribution 4.0 licence](https://creativecommons.org/licenses/by/4.0/). Any further distribution of this work must maintain attribution to the author(s) and the title of the work, journal citation and DOI.

streaking technology [5–9]. However, resolving the details of these complex correlated many-body phenomena involving nuclear and electronic degrees of freedom still poses a challenge for computational simulations.

Most of the theoretical work has been focused on the helium atom as the simplest two-electron system [2, 9–11]. Effects which have been examined are the Wigner–Smith time delay and electron–electron correlation under the influence of an (infrared) laser field in the context of streaking spectroscopy [2, 4, 11–13]. For molecules, the physics becomes even more complex, also due to the multi-scatterer nature compared to the centrosymmetric atoms. Ning *et al* have investigated the simplest, prototypical molecule,  $\text{H}_2^+$ , and found pronounced interference effects (Cohen–Fano interferences, [14]) caused by the two scattering centers [15]. However, this prototype case inherently does not involve any multi-electron effects. Other molecular systems investigated theoretically include endohedral complexes of type  $\text{A}@C_{60}$  [16, 17] or, employing multi-configurational approaches, ionization and subsequent charge migration of small amino acids [18–23]. A few works have considered both, the correlated electron dynamics and the nuclear motion [24–27].

In order to reduce computational costs, numerical simulations commonly employ approximations such as the sudden approximation, frozen nuclear degrees of freedom, or the single-active electron approximation [28]. Within the framework of the latter, one assumes that the dynamics of the active electrons is sufficiently fast so that the ‘inactive’ electrons do not adapt within its time scale, i.e. no electron correlated dynamics occurs. However, it has been shown by Awasthi *et al* that electron correlation even upon XUV- or x-ray-induced ionization of multi-electron systems plays an important role and cannot be neglected [29, 30].

In this work, we investigate the effects of such electron–electron correlation as well as non-adiabatic effects on the postionization dynamics of a molecular charge transfer model system in a time-resolved picture. Moreover, we aim to thoroughly distinguish the processes contributing to the electron–nuclear post-ionization dynamics. The model system, which has been originally suggested by Shin and Metiu [31, 32], has been extended by the group of Engel to include two electrons [33, 34]. This system, which will be introduced in more detail in section 2, possesses, due to asymmetric initial conditions, one stronger and one weaker bound electron with anti-parallel spin. Interaction with an attosecond XUV pulse leads to the emission of one electron. We show that several processes occur on different timescales which have an impact on the electronic configuration of the residual molecular ion: (a) direct photoemission of either the weaker or the stronger bound electron, without passing the respective other electron, yet, affecting its quantum state due to an altered electrostatic environment (shake-up/shake-down processes); (b) emission processes, where upon photoabsorption, the accelerated electron needs to ‘pass’ the other electron. The latter process involves an immediate electron–electron interaction, which leads to both, inelastic and elastic scattering. As a result, the second electron is either excited into higher

bound states (knock-up), relaxed into lower states (knock-down) [2], or adopts the momentum of the electron originally accelerated by the electric field and is emitted in its stead (‘indirect’ photoemission); and (c) non-adiabatic transition processes during the postionization dynamics.

The paper is organized as follows: after a short description of the model and the numerical methods utilized in section 2, we will present the different pathways, analyzed additionally with the help of desymmetrized wave functions and restricted interactions of the electrons with the external electric field. The resulting dynamics is discussed by means of the final state-dependence in the residual ion in section 3. The paper ends with a summary and conclusion in section 4.

## 2. Theory

### 2.1. The full model system

The model we apply in this work represents an extension to the one originally suggested by Shin and Metiu [31, 32]. In their work, a linear, one-dimensional charge-transfer model system was employed consisting of two fixed nuclei with charges  $Z_1$  and  $Z_2$  at the positions  $\pm L/2$ , one moving nucleus ( $Z$ ) in between with coordinate  $R$ , and one electron, here with coordinate  $y$ , giving rise to the potential:

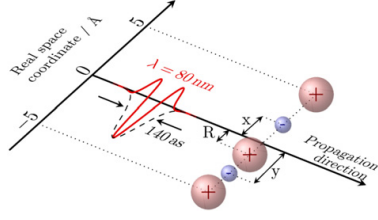
$$V^{1e}(y, R) = \frac{e^2}{4\pi\epsilon_0} \left[ \frac{Z_1 Z}{|L/2 - R|} + \frac{Z_2 Z}{|L/2 + R|} - \frac{Z \operatorname{erf}(|R - y|/R_c)}{|R - y|} - \frac{Z_1 \operatorname{erf}(|L/2 - y|/R_f)}{|L/2 - y|} - \frac{Z_2 \operatorname{erf}(|L/2 + y|/R_f)}{|L/2 + y|} \right], \quad (1)$$

where the error functions (erf) describe a truncated Coulomb interaction between individual particles. The truncation parameters  $R_f$  and  $R_c$  specify the interaction strength between the electron and the fixed nuclei and the mobile nucleus, respectively [31, 32].

Here, we use an extension to this model introduced by Engel and coworkers, where a second electron,  $x$ , is added to the system [33, 34]. The whole particle configuration is shown in figure 1. The system’s potential takes on the form

$$V^{2e}(x, y, R) = V^{1e}(y, R) + \frac{e^2}{4\pi\epsilon_0} \left[ -\frac{Z \operatorname{erf}(|R - x|/R_c)}{|R - x|} - \frac{Z_1 \operatorname{erf}(|L/2 - x|/R_f)}{|L/2 - x|} - \frac{Z_2 \operatorname{erf}(|L/2 + x|/R_f)}{|L/2 + x|} + \frac{\operatorname{erf}(|x - y|/R_c)}{|x - y|} \right], \quad (2)$$

where  $R_c$  scales the electron–electron interaction [34–40]. The fixed nuclei have a distance of  $L = 10 \text{ \AA}$ . Nuclear charges are  $Z = Z_1 = Z_2 = 1$ . All truncation parameters have been set to  $R_f = R_c = R_e = 1.5 \text{ \AA}$ , corresponding to the weak non-adiabatic coupling regime [38], where the electrons adiabatically follow the nuclear dynamics [36]. We want to emphasize that, thus, the model system qualitatively represents a generic molecular environment for the electrons rather than a



**Figure 1.** Configuration of the extended Shin–Metiu system: an ultrashort XUV pulse is used to ionize a linear molecule aligned with the pulse’s polarization axis. The molecule consists of two fixed nuclei at  $\pm 5$  Å, two mobile electrons with coordinates  $x$  and  $y$ , and a movable central nucleus at  $R$ . The mobile nucleus is initially localized at negative  $R$  values, whereas the two electrons reside on both sides. Thus, in the electronic ground state, the electron at negative coordinates is stronger bound than the electron located at positive values.

specific class of molecules, such as linear molecules. Also note that the unscreened interaction of the fixed nuclei with the central nucleus prevents the system from dissociation. Such effects are crucial in the interaction of strong fields with seemingly similar small molecules, such as  $\text{H}_3^+$ , but are not in the focus of our investigation of excitation and ionization dynamics of molecular systems.

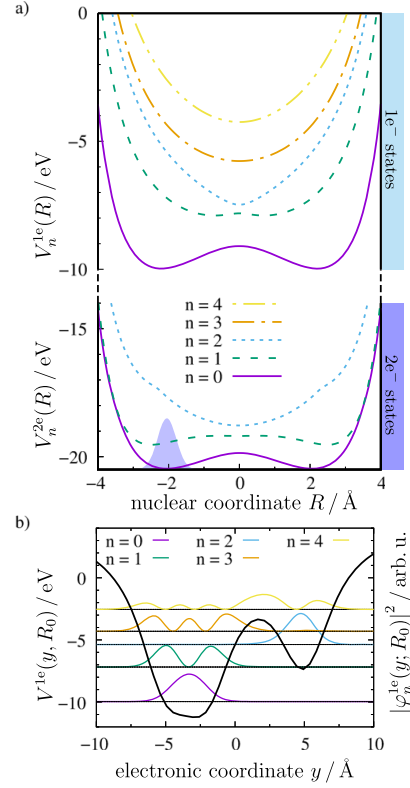
The three particle configuration of the model and its dynamics can be fully solved numerically. However, for interpretation, we calculate for the one-electron (1e) and the two-electron (2e) systems the (adiabatic) electronic eigenfunctions,  $\varphi_n^{1e}(y; R)$  and  $\varphi_n^{2e}(x, y; R)$ , with eigenvalues  $V_n^{1e}(R)$  and  $V_n^{2e}(R)$ , respectively, by solving the following eigenvalue equations:

$$\left[ \frac{p_y^2}{2m_e} + V^{1e}(y, R) \right] \varphi_n^{1e}(y; R) = V_n^{1e}(R) \varphi_n^{1e}(y; R) \quad (3)$$

$$\left[ \frac{p_x^2}{2m_e} + \frac{p_y^2}{2m_e} + V^{2e}(x, y, R) \right] \varphi_n^{2e}(x, y; R) = V_n^{2e}(R) \varphi_n^{2e}(x, y; R), \quad (4)$$

where  $m_e$  is the electron mass and  $p_x$  and  $p_y$  refer to the electronic momenta. For the two-electron case, the wavefunctions are symmetrized according to Pauli’s principle and correspond to an anti-parallel spin configuration. The obtained potential energy curves,  $V_n^{1e/2e}(R)$ , are shown in figure 2(a) for one (upper panel) and two bound electrons (bottom panel). The one-electron model will be used to analyze the postionization dynamics of one ( $y$ ) electron remaining in the parent ion after removal of the other ( $x$ ) electron upon ionization. The first five electronic eigenfunctions of the single electron model,  $\varphi_n^{1e}(y; R_0)$ , are shown in figure 2(b) for an asymmetric nuclear configuration,  $R_0 = -2.05$  Å, corresponding to the system initialization (see below). Note, that among these states, for  $n = 0, 1$ , and  $3$ , the electron is mostly localized on the left-hand side ( $y < 0$ ), i.e. at the two close nuclei (in a strongly bound location), whereas for  $n = 2$  and  $4$  it is predominantly located at the right-hand side ( $y > 0$ ), i.e. at the single nucleus (weakly bound).

The system interacts with an ultrashort attosecond XUV pulse which, using the dipole approximation and velocity



**Figure 2.** (a) Potential energy curves  $V_n^{1e, 2e}(R)$  for the lowest electronic eigenstates  $\varphi_n^{1e, 2e}$  of the one-electron (1e) and two-electron (2e) systems. The blue-shaded area depicts the initial nuclear wave packet  $\chi(R)$  centered around the minimum at  $R_0 = -2.05$  Å. (b) Potential energy  $V^{1e}(y, R_0)$  (solid black line) and first five electronic eigenfunctions of the single-electron system,  $|\varphi_n^{1e}(y; R_0)|^2$ , at the initial, near-equilibrium nuclear geometry  $R_0$ .

gauge, results in the Hamiltonian:

$$\mathcal{H}(t) = \frac{P^2}{2M} + \frac{p_x^2}{2m_e} + \frac{p_y^2}{2m_e} + V^{2e}(x, y, R) + e \mathcal{A}(t) \left( -\frac{Z}{M} P + \frac{p_x}{m_e} + \frac{p_y}{m_e} \right), \quad (5)$$

where  $M$  is the proton mass and  $P$  the nuclear momentum. The electric field of the ultrashort ionizing XUV pulse is described via its vector potential  $\mathcal{A}(t)$  with a polarization along the molecular axis:

$$\mathcal{A}(t) = -\frac{E_0}{\omega} g(t - T) \sin(\omega(t - T) + \phi) \quad (6)$$

here,  $E_0 = -8.7 \text{ V \AA}^{-1}$  (or  $-0.169 \text{ au}$ ) is the electric field strength (corresponding to an intensity of  $1.0 \times 10^{15} \text{ W cm}^{-2}$ ),  $\omega$  the field’s angular frequency, and  $g(t - T)$  a Gaussian pulse envelope function centered around  $T = 0$  fs with a full-width half-maximum (FWHM) of 140 as (2.894 au). The angular frequency corresponds to a wavelength of  $\lambda = 80 \text{ nm}$  ( $\hat{=} 15.5 \text{ eV}$



or 0.570 au), which is sufficient to singly ionize the molecule through single photon absorption, see figure 2(a). The spectral width of the attosecond pulse intensity is 18.4 eV (0.676 au). The carrier-envelope phase (CEP)  $\phi$  is set to zero, corresponding to a sine-shaped vector potential or an approximately cosine-shaped electric field.

## 2.2. Propagation and initialization

The full system's wave function  $\Psi(x, y, R, t)$  is represented on a three-dimensional grid with a range of  $[-240, 240]$  Å with 1024 grid points in  $x$ - and  $y$ -direction, respectively, and of  $[-4.99, 4.99]$  Å with 128 points along the  $R$ -direction. The time-dependent Schrödinger equation for the Hamiltonian defined in equation (5) is solved numerically with a timestep of 5 as using the split-operator technique [41] and the FFTW 3 library [42] for Fourier transforms. For the details on the numerics please see our previous publications, e.g. reference [38]. The simulation starts at  $t_0 = -4$  fs, well before the XUV pulse enters the system. Reflection at the grid boundaries is suppressed by multiplying  $\Psi(x, y, R, t)$  at each timestep with a splitting function [43]

$$f(x, y) = \left[1 + e^{\zeta_1(|x| - \zeta_2)}\right]^{-1} \left[1 + e^{\zeta_1(|y| - \zeta_2)}\right]^{-1} \quad (7)$$

with the parameters  $\zeta_1 = 5.67$  Å<sup>-1</sup> and  $\zeta_2 = 235$  Å.

**2.2.1. Full fermionic wave function.** The initial state is assumed to be a product state of the two-electron adiabatic electronic ground state,  $\varphi_0^{2e}(x, y; R)$ , and a nuclear wave function

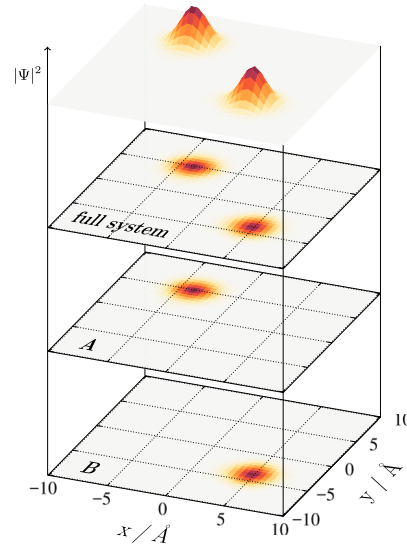
$$\Psi(x, y, R, t_0) = \varphi_0^{2e}(x, y; R) \chi(R). \quad (8)$$

The adiabatic electronic eigenstates are obtained by solving the field-free electronic Schrödinger equations, equations (3) and (4), via the relaxation method [44].

The nuclear part of the initial wave function,  $\chi(R)$ , is assumed to be a Gaussian-shaped vibrational wave packet centered around the left local minimum of the double-well potential at  $R_0 = -2.05$  Å (see shaded area in figure 2(a)):

$$\chi(R) = N_0 e^{-\beta_R(R-R_0)^2} \quad (9)$$

here,  $N_0$  serves as normalization constant and the width  $\beta_R = 7.14$  Å<sup>-2</sup>. This way, the Gaussian closely resembles the left-hand side of the vibrational ground state eigenfunction, which is symmetric around  $R = 0$ . We note that the factorized, asymmetric initial state does not correspond to the total ground state of the system. It rather corresponds to one of two energetically equal realizations. This is a common situation, where the system resides in one potential well as encountered, for example, in NH<sub>3</sub> inversion or isomerization processes. Restricting the nuclear density asymmetrically to a single potential well gives rise to a specific molecular structure (e.g. one isomer), which allows to distinguish two different binding sites for the electrons, i.e. a strongly bound site (negative electron coordinate) for electrons in the vicinity of the two nuclei at the left-hand side and a weakly bound site (positive electron coordinates) at the single nucleus on the right.



**Figure 3.** Initial two-electron densities,  $\int |\Psi(x, y, R, t_0)|^2 dR$ , entering the propagation. Top plane: fully symmetric spatial wave function calculated via the relaxation method. Descending from top to bottom: projection onto the 2D plane of the full system and the artificial subsystems, (A) and (B), respectively.

The initial two-electron density, i.e.  $\int |\Psi(x, y, R, t_0)|^2 dR$ , is displayed in the top layer of figure 3. Note that cuts through the spatial distribution of the electronic part—given by the two-electron groundstate wavefunction  $\varphi_0^{2e}(x, y; R)$ —approximately correspond to the one-electron functions  $\varphi_0^{1e}(y; R)$  and  $\varphi_0^{1e}(x; R)$ . The simulation results obtained for these initial conditions (and their relation to the one-electron electronic eigenfunctions) are discussed in section 3.1. Please note that as we neglect any spin-dependent interaction, spin and spatial coordinates factorize. We therefore only consider the (symmetric) spatial part of the full wave function.

**2.2.2. Artificial subsystems with distinguishable electrons.** For analysis purposes, the full wave function, equation (8), is partitioned into two desymmetrized subsystems with

$$(A) \psi_A(x, y, R, t_0) \equiv \sqrt{2} \Psi(x, y, R, t_0) \Theta(y - x), \quad (10a)$$

$$(B) \psi_B(x, y, R, t_0) \equiv \sqrt{2} \Psi(x, y, R, t_0) \Theta(x - y), \quad (10b)$$

respectively (figure 3, lower panels). In above equation,  $\Theta(x)$  is the Heaviside step function. These partial wave functions each describing one half of the full system, split along the  $x = y$ -diagonal. By doing so, the wave functions  $\psi_A(x, y, R, t_0)$  and  $\psi_B(x, y, R, t_0)$  vaguely resemble a wave function in Hartree-product form, because now  $x$  and  $y$  effectively describe identical, yet *distinguishable* electrons. In the initial configuration of subsystem A (B), the  $x$  ( $y$ ) electron is strongly bound (with an approximate binding energy of  $E_B^{\text{strong}} = V_2^{1e}(R_0) - V_0^{2e}(R_0) = 15.1$  eV), whereas the  $y$  ( $x$ ) electron ( $E_B^{\text{weak}} = V_0^{1e}(R_0) - V_0^{2e}(R_0) = 10.5$  eV) is weakly

bound. Technically, the abrupt cut-off of the wavefunction leads to a weak field-free ionization signal. This background signal is removed from the propagated wave function until  $t = -250$  as, i.e. before the ionizing XUV pulse interacts with the system, by truncating  $\Psi(x, y, R, t \leq -250 \text{ as})$  through multiplication with  $\Theta(25 \text{ \AA} - |x|)\Theta(25 \text{ \AA} - |y|)$ . The different ionization pathways revealed by these subsystems' dynamics are discussed in section 3.2.

**2.2.3. Restricted field interaction.** For analysis, further disentanglement of individual ionization pathways and their underlying intramolecular dynamics is achieved by artificially restricting the field interaction. To this end, simulations on subsystems A and B are performed with the modified Hamiltonian

$$\mathcal{H}'(t) = \frac{p^2}{2M} + \frac{p_x^2}{2m_e} + \frac{p_y^2}{2m_e} + V^{2e}(x, y, R) + e \mathcal{A}(t) \left( -\frac{Z}{M}P + \frac{p_\xi}{m_e} \right), \quad (11)$$

where  $\xi \in \{x, y\}$  refers to either the  $x$  or the  $y$  electron. Thus, field interaction is limited to a specific electron. This restriction allows us to distinguish direct and electron correlation driven photoionization pathways. Obtained results are presented and discussed in section 3.3.

### 2.3. Identification of single ionization

To isolate fractions of the wave functions that belong to the singly ionized system, the photoelectron dynamics are evaluated via the ionization signal in regions far from the molecule using the mask function

$$c(x, y) = c_x(x) \cdot [1 - c_y(y)] \quad (12)$$

with

$$c_\xi(\xi) = \begin{cases} 0 & \text{if } 0 < |\xi| \leq \xi_c \\ \sin^2 \left( \frac{|\xi| - \xi_c}{\Delta\xi} \frac{\pi}{2} \right) & \text{if } \xi_c < |\xi| \leq \xi_c + \Delta\xi \\ 1 & \text{if } \xi_c + \Delta\xi < |\xi| \leq \xi_{\text{end}}, \end{cases} \quad (13)$$

where  $\xi \in \{x, y\}$  with corresponding  $x_c = y_c = 25 \text{ \AA}$ ,  $\Delta x = \Delta y = 10 \text{ \AA}$ , and  $x_{\text{end}} = y_{\text{end}} = 240 \text{ \AA}$  marking the end points of the simulation grid. As a result, the mask  $c(x, y)$  selects parts of the electronic wave functions

$$\psi_{\text{out}}(x, y, R, t) \equiv c(x, y) \psi(x, y, R, t) \quad (14)$$

at large  $x$  and low  $y$  coordinates, corresponding to the emission of the  $x$  electron, whereas the other ( $y$ ) electron remains bound at the parent molecular ion. Due to symmetry in the electronic coordinates, it is sufficient to only evaluate signals along the  $x$  direction. Note, that this mask is independent of  $R$ , as the nuclear part of the wave function remains well confined between the two outer nuclei. Further

segmentation of  $\psi_{\text{out}}(x, y, R, t)$  into subregions  $S$  will be introduced in section 3.1.

## 3. Results and discussion

### 3.1. Fully correlated fermionic wave function

Interaction of the initial state with the ultrashort XUV pulse induces electron dynamics within the (non-ionized) two-electron system and leads to single ionization. While for atomic systems, an ionization signal can be extracted via projection of the wave function onto a set of Coulomb waves [11], such an approach is not feasible for the multi-centered potential of the molecular model employed here. Instead, we remove the two-electron components for the first 35 two-electron states, for which both electrons are bound, from the total wavefunction. Then we project the remainder (containing only a single bound electron) onto the basis spanned by the electronic eigenfunctions  $\{\varphi_n^{1e}(y; R)\}$  of the one-electron system [2]:

$$P_n(t) = \iint \left| \int \varphi_n^{1e}(y; R) \Psi^{1e}(x, y, R, t) dy \right|^2 dx dR, \quad (15)$$

using the following definitions:

$$\Psi^{1e}(x, y, R, t) \equiv \Psi(x, y, R, t) - \sum_{m=0}^{34} a_m^{2e}(R, t) \varphi_m^{2e}(x, y; R), \quad (16)$$

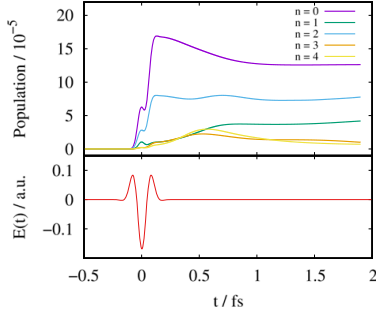
$$a_m^{2e}(R, t) \equiv \iint \varphi_m^{2e}(x, y; R) \Psi(x, y, R, t) dx dy. \quad (17)$$

The populations  $P_n(t)$  are shown in figure 4 upper panel. Note, that in the basis considered here, only contributions are obtained, where the  $y$  electron remains bound, while the  $x$  electron is ejected. Projection onto  $\{\varphi_n^{1e}(x; R)\}$  yields the same results for reversed roles. One finds that the first five one-electron states are considerably populated through the ultrashort XUV pulse (figure 4 lower panel) around  $t = 0$ .

For comparison, within the single active electron approximation, the *sudden* removal of one of the electrons would yield time-independent one-electron state occupations obtained by projection of  $\varphi_0^{2e}(x, y; R)$  onto  $\{\varphi_n^{1e}(y; R)\}$ :

$$b_n^{1e} \equiv \iint \left| \int \varphi_n^{1e}(y; R) \varphi_0^{2e}(x, y; R) dy \right|^2 dx dR. \quad (18)$$

For the initial conditions considered here, only the states  $n = 0$  (ejecting the weakly bound electron) and  $n = 2$  (ejecting the strongly bound electron) would be populated significantly, leaving the remaining electron more tightly bound in the molecular system (*shake-down* process [9]). The occupation of higher one-electron states, i.e.  $n = 1, 3$ , and 4, corresponding to a *shake-up* process [9], would be approximately two orders of magnitudes lower ( $b_1^{1e}/b_0^{1e} = 0.013$ ,  $b_3^{1e}/b_0^{1e} = 0.008$ ,  $b_4^{1e}/b_2^{1e} = 0.006$ ).

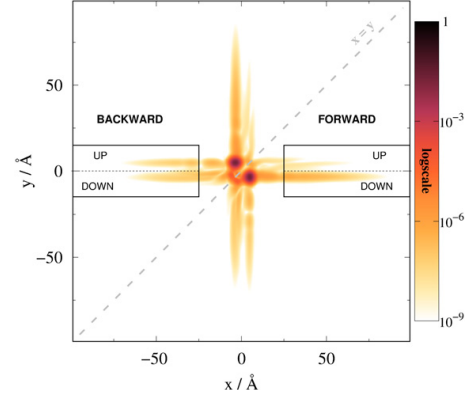


**Figure 4.** Population of the single-electron states upon projection onto the basis spanned by  $\{\varphi_n^{(s)}(y; R)\}$  after removal of all two-electron states (upper panel) and temporal profile of the XUV pulse's electric field (lower panel).

In contrast, in our simulation with fully correlated electrons, depicted in figure 4, these three states show significant occupations. It is also noteworthy, that their population continues to rise after the XUV pulse has passed the system, while in particular the population of the one-electron groundstate ( $n = 0$ ) declines. Since non-adiabatic transitions occur on a much longer timescale (see below), we trace these phenomena back to the continued interaction between the bound ( $y$ ) and the ejected ( $x$ ) electron on early timescales, where a transition to higher bound states is associated with a *knock-up* process and one to lower states corresponds to a *knock-down* process [2].

In the following, we aim to disentangle and quantify the various correlation-induced processes that occur during different ionization pathways. To this end, we will evaluate the postionization dynamics. Figure 5 depicts a snapshot of the two-electron density,  $\int |\Psi(x, y, R, t)|^2 dR$ , of the full antisymmetric system at  $t = 3$  fs after XUV-pulse interaction. As can be gathered, the dominant part of the wave function remains around the origin (corresponding to the non-ionized part of the system), with minor parts being delocalized into the  $x$  or  $y$  direction. These four double-stripe structures, where either  $x$  or  $y$  coordinate stays localized within  $\pm 10 \text{ \AA}$ , represent different single ionization processes. Electron densities in regions of high values of both coordinates,  $|x|$  and  $|y|$ , simultaneously, corresponding to double ionization, are approximately four orders of magnitudes lower due to the much larger energy threshold for double ionization. Consequently, such contributions are not visible in figure 5. In the following, we will concentrate on the single ionization dynamics occurring during the interval of 1 to 20 fs after pulse arrival.

Naturally, the electron densities are symmetric with respect to the  $x = y$ -diagonal. It is therefore sufficient to restrict the analysis to electron densities emitted along one axis. Here we chose the  $x$  axis and ascribe the labels *forward/backward* for positive/negative values in  $x$ . An apparent feature of the single ionization channels is the occurrence of two ionization pathways in every direction. This indicates that the remaining electron eventually stays at different potential minima (around the origin), for which we introduce the labels *up/down* for positive/negative values in  $y$ , respectively, as indicated



**Figure 5.** Two-electron density,  $\int |\Psi(x, y, R, t = 3\text{fs})|^2 dR$ , of the fully antisymmetric system (mirror symmetry w.r.t. the  $x = y$  diagonal) 3 fs after ionization with an 140 as XUV pulse centered at  $T = 0$  fs. Four different ionization channels can be distinguished, here illustrated for the emission of the  $x$ -electron ( $x$  direction): emission occurs either in *forward* ( $x > +25 \text{ \AA}$ ) or *backward* ( $x < -25 \text{ \AA}$ ) direction for positive (*up*) or negative (*down*) positions of the remaining  $y$  electron. The corresponding channels along the  $y$ -axis are equivalent.

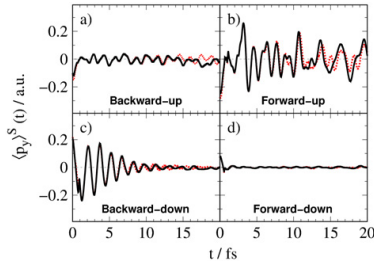
in figure 5. The electron densities in these four distinct ionization channels differ from each other in shape and amplitude. To distinguish the underlying processes, an evaluation region is defined according to equations (12) and (13) and further separated into subregions  $S$  according to the ascribed labels, allowing us to collect and analyze the emitted wave function  $\psi_{\text{out}}^S(x, y, R, t)$  of each channel separately. As the region of ionization is defined for  $|x| \geq 25 \text{ \AA}$ , no emission signal is detected until  $t \approx 1$  fs, when the fastest components of the ionized wave function enter the evaluation region. Ionization signal, i.e.  $I_S(t) = \iint |\psi_{\text{out}}^S(x, y, R, t)|^2 dx dy dR$ , builds up within a subregion  $S$  mainly over the period of  $\sim 5$  fs. The build up is traced back to a kinetic energy distribution whose central 80% lie between 0.3 and 4.5 eV with a maximum at 1.4 eV. After 5 fs the overall probability to find both electrons in each subregion continues to increase only slightly due to parts of the wave packet with lower kinetic energy entering the subregion. The respective probabilities at 5 fs are  $3.9 \times 10^{-6}$ ,  $1.1 \times 10^{-4}$ ,  $1.8 \times 10^{-5}$ , and  $2.8 \times 10^{-5}$  for the *forward-up*, *forward-down*, *backward-up*, and *backward-down* subregion, respectively.

Figure 6 shows the time evolution of the average momentum,  $\langle p_y \rangle^S(t)$ , of electron  $y$ , which remains bound in the molecular ion after electron  $x$  has been emitted. The quantity  $\langle p_y \rangle^S(t)$  is calculated via the density distribution for the remaining  $y$  electron,  $\rho_S(p_y, t)$  by integrating over  $\psi_{\text{out}}^S$  in each individual channels  $S$ :

$$\langle p_y \rangle^S(t) = \frac{\int p_y \rho_S(p_y, t) dp_y}{\int \rho_S(p_y, t) dp_y}, \quad (19)$$

where

$$\rho_S(p_y, t) = \iint |\tilde{\psi}_{\text{out}}^S(p_x, p_y, P, t)|^2 dp_x dP, \quad (20)$$



**Figure 6.** Time-resolved momentum expectation values  $\langle p_y \rangle^S(t)$  of the remaining  $y$  electron (black solid lines) after ionization of the full system for the different ionization channels, see figure 5, as indicated. For comparison, results from a simulation with a frozen nuclear configuration are added (red dotted lines). The expectation value  $\langle p_y \rangle^S(t)$  of the remaining bound electron  $y$  serves as an indicator for electron scattering during the emission process.

here,  $\tilde{\psi}_{\text{out}}^S$  is the Fourier-transformed wave function  $\psi_{\text{out}}^S$ . The average momentum  $\langle p_y \rangle^S(t)$  illustrates that all four regions differ in the dynamics induced in the parent ion.

In the following, we will interpret the different dynamics seen in figure 6(a)–(d) based on the leading contributions to photoemission into each evaluation region. However, there are further contributions to each channel, which will be isolated and investigated in sections 3.2 and 3.3.

We interpret the observations as follows: in the *forward-down* channel, figure 6(d), the signal stems primarily from the *direct emission* of the weakly bound electron on the right-hand side of the molecule towards positive  $x$  values, i.e. without passing the parent ion (and in particular the other electron) first. The strongly bound electron therefore remains on the left-hand side and is hardly affected by the ionization dynamics which is reflected in the nearly constant momentum expectation value of the remaining electron. In contrast, the oscillating signal in the *forward-up* channel, figure 6(b), can be primarily traced back to the strongly bound electron at negative  $x$  values being released towards positive  $x$  values, such that it first passes the parent ion and the other electron. Its inelastic scattering with the remaining, weakly bound electron induces oscillations of the latter being reflected by the strong time dependence of the remaining electron's average momentum. We note that the temporal behavior significantly changes for times  $t > 10$  fs, if the nuclear configuration is frozen during the simulation (red dotted lines) suppressing non-adiabatic transitions.

A similar situation but with reversed roles can be seen for emission into the *backward* direction: here, the *down* channel, figure 6(c), corresponds to emission of the weakly bound electron after passing the strongly bound one. Thereby, inelastic scattering leads to a regular oscillation in the residual electron's average momentum  $\langle p_y \rangle(t)$ . Fourier analysis of this oscillation occurring between  $t = 0$  and 10 fs indicates that the corresponding energy of 2.89 eV can be assigned to the energy gap between the electronic ground and first excited state of the one-electron system (2.78 eV at  $R_0$ ), see figure 2(a). Thus, upon ionization, an electronic wave packet

in the residual molecular ion is excited oscillating around the left well's minimum.

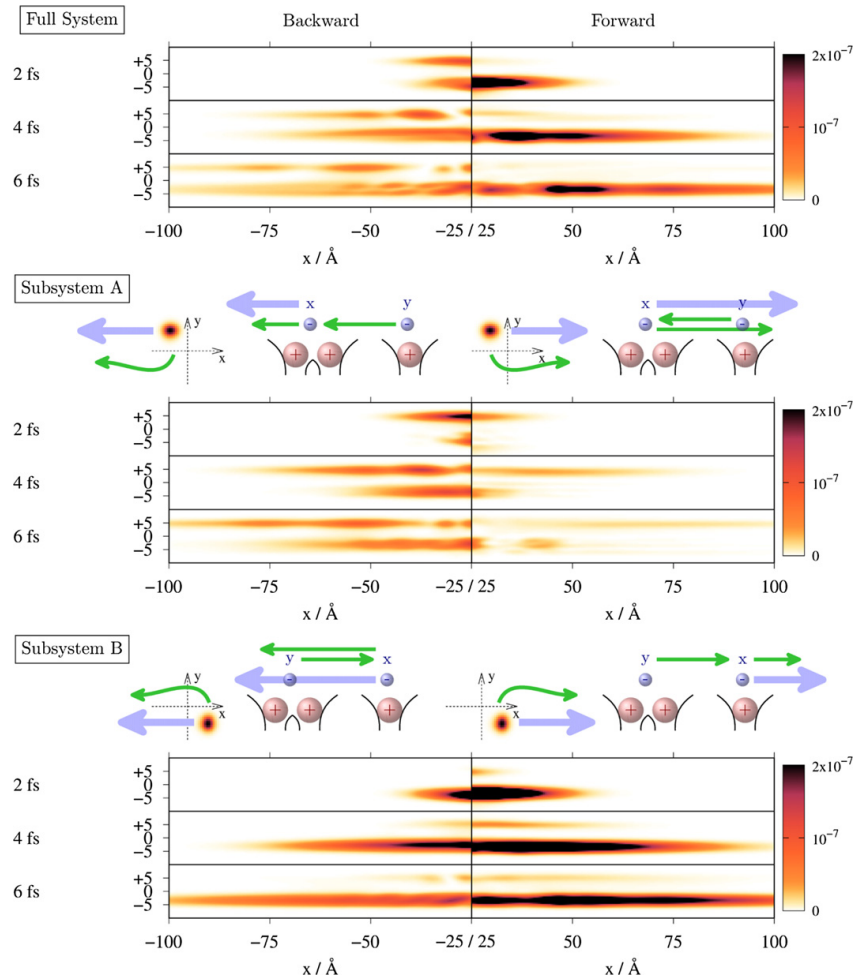
The *backward-up* channel, figure 6(a), on the other hand, corresponds to the direct emission of the strongly bound electron without passing the parent ion. A weak response towards a negative average momentum of the remaining electron, can be seen, in particular between 17 and 20 fs, despite the absence of an immediate interaction between the escaping and the remaining electron. This feature is not present if the simulation is performed with a frozen nuclear configuration (dotted red lines). It originates in the induced nuclear dynamics leading to non-adiabatic transitions (intramolecular charge transfer), which will be discussed in more detail in section 3.3.

### 3.2. Reduced wave function: distinguishable electrons

The previous analysis provided a first intuitive picture of intramolecular scattering effects in the course of ionization. However, as electrons are indistinguishable, the roles of emitted and remaining electrons during the scattering process cannot clearly be identified. To this end, the artificially truncated wave functions  $\psi_A$  and  $\psi_B$ , see equations (10a) and (10b), are employed as initial conditions, thus rendering the two electrons distinguishable, see section 2.2.2. This way, electron–electron correlation originating from the anti-symmetry of the wave function and interference effects between the two distinct initial density distributions (localized near  $x = \pm 5 \text{ \AA}$  &  $y = \mp 5 \text{ \AA}$ ) are neglected. However, a comparison of the probabilities to find the particles in the evaluation regions,  $I_S(t)$ , between the full system and the sum of the subsystems A and B shows very good agreement, indicating that for the present system these types of correlation effects are of minor importance.

In figure 7 the time-dependent two-electron densities of the full system with two indistinguishable electrons (upper part) and the subsystems, A (middle part) and B (lower part) with distinguishable electrons, are shown for an area corresponding to the emission of electron  $x$  in *backward* (left panels) and *forward* direction (right panels), while electron  $y$  remains bound to the parent ion. Above the two lower panels, a schematic picture indicates different underlying processes (blue/green arrows) in the  $x, y$ -configuration space (left) and the one-dimensional coordinate space (right). The thick blue arrows correspond to the four main contributions, i.e. photoemission with and without intramolecular electron–electron scattering, discussed in section 3.1, where either the strongly (A) or the weakly bound electron (B) interacts with the electromagnetic field and is released to either side of the molecule.

The first electron wave packet components enter the evaluation region at  $x = \pm 25 \text{ \AA}$  between 1 and 2 fs after the interaction with the ionizing pulse. At this instant, electron density is mostly found in the *backward-up* channel for subsystem A and in the *forward-down* channel for subsystem B (blue arrows) corresponding to direct photoemission from the side of the molecule closest to the respective subregion. Additionally, a strong slightly delayed signal can be



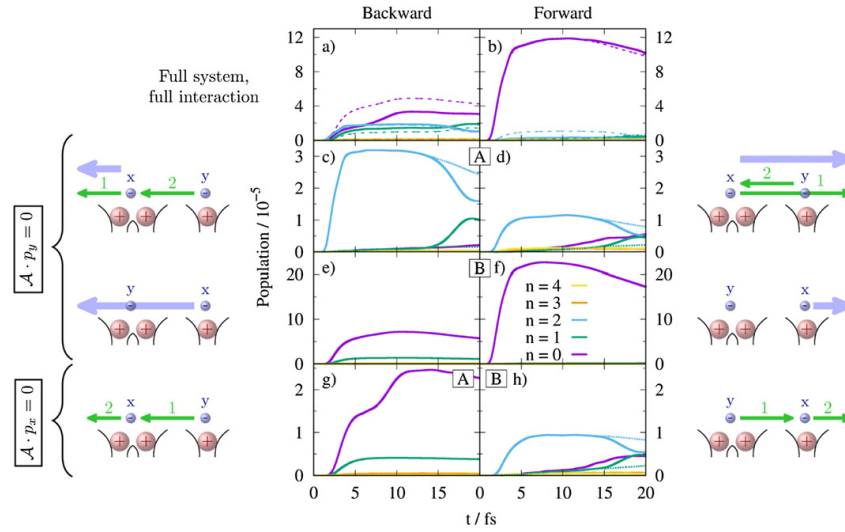
**Figure 7.** Snapshots of the integrated 2D electronic density  $\int |\Psi(x, y, R, t)|^2 dR$  at  $t = 2, 4,$  and  $6$  fs after ionization of the full system (top panel) and the two subsystems,  $\psi_A$  (middle panel) and  $\psi_B$  (bottom panel), with headers illustrating the ionization process (2D view of initial density distribution in the configuration space and 1D view in the real coordinate space). Top: ionization dynamics of the full system. Middle: subsystem A with its initial wave packet centered at negative  $x$  and positive  $y$  values. The *up* pathways primarily contribute to the total ionization signals (blue arrows) as opposed to the *down* pathways (green arrows). The initially strongly bound  $x$ -electron (negative  $x$ -values) is emitted and the initially weakly bound  $y$ -electron (positive  $y$ -values) stays. Bottom: subsystem B with its initial wave packet centered at positive  $x$  and negative  $y$  values: here, the *down* pathways primarily contribute to the total ionization signals. The initially weakly bound  $x$ -electron (positive  $x$ -values) is emitted while the initially strongly bound  $y$ -electron (negative  $y$ -values) stays. Oversaturation in the colorbars' range is used to highlight substructures in the probability density as well as small contributions in the non-dominating pathways. The largest occurring values of the electronic density in *forward* direction are: (A)  $8.3 \times 10^{-8}$ , (B)  $1.3 \times 10^{-6}$ ; and in *backward* direction: (A)  $2.4 \times 10^{-7}$ , (B)  $4.0 \times 10^{-7}$ .

noted stemming from an emission into the opposite direction (blue arrows, A: *forward-up*, B: *backward-down*), corresponding to photoemission channels involving intramolecular electron–electron scattering, i.e. the  $x$  electron first passing the  $y$  electron before being finally emitted.

The A/B distinction reveals additional signals with a smaller but still significant probability appearing in the *down* (A) channels and—to an even smaller extent—in the *up* (B) channels, which are not visible in figure 5 due to the

larger amplitude of the more dominant signals (blue arrows). Their appearance reveals a correlated motion between the two electrons (indicated by green arrows), where the remaining  $y$  electron is relocated (intramolecular charge-transfer) either prior to the photoelectron emission of the  $x$  electron or afterwards. This question is addressed in the following section 3.3, by further dissecting the ionization pathways through restricting the electrons' interaction with the electric field.





**Figure 8.** Evolution of the population of the electronic states by the remaining bound  $y$ -electron calculated via equation (21), after the XUV pulse ionizes the two-electron system at  $t = 0$  fs. The upper panels, (a) and (b), contain the dynamics of the full antisymmetric system, whereas lower panels, (c)–(h), show the dynamics of distinguishable electrons selectively interacting with the electric field as indicated. Dashed lines in panels (a) and (b) correspond to the sum of all individual pathways with restricted field interaction displayed throughout panels (c)–(h). The dotted lines in panels (c), (d), and (h) represent evolution for a molecule with fixed core position. A comprehensive list of all processes can be found in table 1.

### 3.3. Restricted electron–field interactions

To further investigate the intramolecular dynamics during and after the electron emission process, we perform simulations of the subsystems A and B, i.e. using distinguishable electrons, and restrict the interaction of the electromagnetic field to either the  $x$  (ejected) or  $y$  (remaining) electron by employing the modified Hamiltonian  $\mathcal{H}'(t)$  defined in equation (11). This way, the absorption process of a system with distinguishable electrons is strictly limited to one specific single electron.

The ionization wave function,  $\psi_{\text{out}}^S(x, y, R, t)$ , i.e. the part of the wave function entering the analysis region defined via the mask function, equation (13), is projected onto the set of adiabatic eigenfunctions  $\{\varphi_n^{1e}(y; R)\}$ ,  $n \in \{0, \dots, 4\}$  of the one-electron system, obtained from equation (3) and shown in figure 2(b) exemplarily for  $R = R_0$ . Note that these states differ in the electron's spatial distributions: while for states with the quantum numbers  $n \in \{0, 1, 3\}$ , the  $y$  electron is located on the (strongly bound) left-hand side, for  $n \in \{2, 4\}$  electron distribution is predominantly found on the (weakly bound) right-hand side. Thus, a transition between states from different sides corresponds to an intramolecular charge transfer. The population  $P_n^S(t)$  of the  $n$ th one-electron state by the  $y$  electron is calculated as

$$P_n^S(t) = \iint \left| \int \varphi_n^{1e}(y; R) \psi_{\text{out}}^S(x, y, R, t) dy \right|^2 dx dR, \quad (21)$$

where the domain  $S'$  limits the  $x$  integration to either positive or negative values corresponding to the *forward* ( $S' = \text{fwd}$ ) or *backward* ( $S' = \text{bwd}$ ) channel, respectively, but does not distinguish between *up*- and *down*-channels anymore. Thus,

$P_n^S(t)$  are the populations of the single-electron states in the evaluation region, i.e. in the molecular parent ion after photoionization. Sketches next to the panels illustrate the dominant ionization pathways with labels '1' and '2' indicating the temporal order.

The populations are shown in figure 8 in *backward* (left panels,  $x < 0$ ) and *forward* direction (right panels,  $x > 0$ ) for the fully antisymmetric wave function (top panels, a and b) and the subsystems A and B as indicated (lower panels, c–h). The rise in the period of 1 to 5 fs in all panels corresponds to the main part of the wave packet entering the evaluation region. In the subsequent time evolution, the overall probability within the evaluation region remains mostly constant leading to distinct plateau regions in  $P_n^S(t)$ . However, small contributions with low kinetic energy (of the emitted  $x$  electron) continue to enter the evaluation region at later times, while components with high kinetic energy are removed at the grid boundaries. Note that a transient population of metastable states, for example through electronic excitation of  $2e$  states or direct excitation of high-lying vibrational states [45], which further decay into the  $1e$  states, would manifest itself by a delayed ionization signal. Such delayed signals are not observed within the investigated time window. We therefore expect the impact of such states to be negligible in the present case.

Several processes (indicated by boldface roman numerals) can be identified and separated from each other. They are summarized with their associated ionization channel  $S$  in table 1. We first consider the cases, in which the electron (here, the  $x$  electron) interacting with the electric field is the one

**Table 1.** Various in parts interdependent processes occur during photoionization and contribute to the signal in different evaluation regions for the two subsystems A (with a strongly bound  $x$  electron and weakly bound  $y$  electron) and B (vice versa). The build up time (BU) describes the time frame of the initial wave packet entering the analyzing region (defined by signal above the noise level) until a stable population is reached.  $P_n^S(t)$  in the last column represents the maximum population of this process.

Channel $S$	$x$	$y$	Process	Figure 8	BU/fs	$P_n^S/10^{-5}$		
A	<i>backward-up</i>	$< -25 \text{ \AA}$	$> 0$	<b>III</b> <b>Direct emission</b> of the strongly bound electron	c, blue	0.7–5.5	3.1	
	<i>backward-down</i>	$< -25 \text{ \AA}$	$< 0$	<b>VI</b> <b>Indirect emission</b> via elastic collision with charge transfer and subsequent <b>knock up</b> (inelastic scattering)	g, green	1.2–14.0	2.5	
				<b>IX</b> Charge transfer via <b>non-adiabatic transition</b> (following <b>III</b> )	c, green	11.2–19.0	1.0	
	<i>forward-up</i>	$> +25 \text{ \AA}$	$> 0$	<b>IV</b> <b>Scattered emission</b> of the strongly bound electron and subsequent <b>knock up</b> (inelastic scattering)	d, blue	1.0–5.9	1.1	
				<b>X</b> Charge transfer via <b>non-adiabatic transition</b> (following <b>IV</b> )	d, green	11.2–19.0	0.5	
	<i>forward-down</i>	$> +25 \text{ \AA}$	$< 0$	<b>V</b> <b>Knock down</b> induced charge transfer (following <b>IV</b> )	d, green	6.2–16.2	0.5	
				<b>X</b> Charge transfer via <b>non-adiabatic transition</b> (following <b>IV</b> )	d, green	11.2–19.0	0.5	
	<i>backward-up</i>	$< -25 \text{ \AA}$	$> 0$	—	Process not visible	—	—	0.0
	<i>backward-down</i>	$< -25 \text{ \AA}$	$< 0$	<b>II</b> <b>Scattered emission</b> of the weakly bound electron and subsequent <b>knock up</b> (inelastic scattering)	e, blue	0.8–7.2	6.6	
						1.6–7.0	1.3	
B	<i>forward-up</i>	$> +25 \text{ \AA}$	$> 0$	<b>VII</b> <b>Indirect emission</b> via elastic collision with charge transfer and subsequent <b>knock up</b> (inelastic scattering)	h, green	1.5–7.1	0.9	
						2.5–4.6	0.04	
	<i>forward-down</i>	$> +25 \text{ \AA}$	$< 0$	<b>I</b> <b>Direct emission</b> of the weakly bound electron	f, blue	0.7–5.3	22.0	
				<b>VIII</b> <b>Knock-down</b> induced charge transfer (following <b>VII</b> )	h, —	4.2–18.5	0.5	
			<b>XI</b> Charge transfer via <b>non-adiabatic transition</b> (following <b>VII</b> )	h, green	9.9–19.3	0.5		

being eventually emitted (figures 8(c)–(f)). The strongest signal (panel f) corresponds to the emission of the weakly bound electron, initially located near  $x = +5 \text{ \AA}$  (subsystem B), in *forward* direction corresponding to a direct photoemission (**I**) without scattering with the remaining electron. In this case, the strongly bound  $y$  electron remains almost unaffected in its position located at the left-hand side (*down*), corresponding to the electronic ground state of the one-electron system,  $n = 0$  (see figure 2(b)).

However, the removal of the  $x$  electron results in an increase of the  $y$  electron’s binding energy corresponding to a shake-down process. The energy change corresponding to a sudden electron removal can be estimated from the potential energy curves at  $R_0$ ,  $\Delta E_B \approx V^{0e}(R_0) + V_0^{2e}(R_0) - V_0^{1e}(R_0) - V_2^{1e}(R_0)$  (where  $V^{0e}$  corresponds to the repulsion energy between the movable and the two fixed nuclei only) and accounts for 1.8 eV. Comparing the relative populations at  $t = 5$  fs, only a very weak shake-up into the one-electron states  $n = 1$  and 3 is noticed with populations of  $P_1^{\text{fwd}}/P_0^{\text{fwd}} = 0.0045$  and  $P_3^{\text{fwd}}/P_0^{\text{fwd}} = 0.0004$  relative to the groundstate. This is in line with the almost constant average momentum seen in figure 6(d) for the full (fermionic) system, indicating no coherent dynamics induced.

In contrast, emitting the weaker bound  $x$  electron in the opposite (*backward*) direction, figure 8(e), such that inelastic scattering with the remaining strongly-bound  $y$  electron occurs, entails a significant relative population of the first and third excited one-electron states of  $P_1^{\text{bwd}}/P_0^{\text{bwd}} = 0.21$  and  $P_3^{\text{bwd}}/P_0^{\text{bwd}} = 0.02$ , respectively. Note, that these excited states are still localized on the left-hand side of the molecule

(*down* channel). Since such an excitation does not occur in the *forward* direction, it must be a result of dynamical correlation between the accelerated  $x$  electron and the ‘inactive’  $y$  electron. This interaction corresponds therefore to a pure knock-up process (**II**) [2]. As a consequence, within 2 and 5 fs, a  $y$  electron wave packet can be seen, oscillating within the left potential well, which is reflected in the damped oscillation pattern of the average momentum shown in figure 6(c).

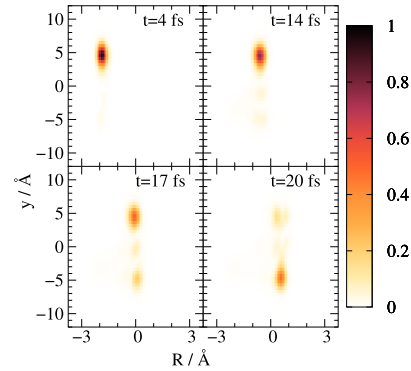
A similar situation is encountered, when the stronger bound electron (figures 8(c) and (d)) interacts with the electric field and is ultimately emitted. If the  $x$  electron emission occurs in the *backward* direction, figure 8(c), again, no intramolecular scattering occurs (**III**), and the weaker bound  $y$  electron remains (initially) in its place, corresponding predominantly to the second excited state,  $n = 2$ , which is localized on the molecule’s right-hand side (*up* channel). Again, a shake-down stabilization of the binding energy of approximately 1.8 eV is expected and only a very weak shake-up to state  $n = 4$  is noted ( $P_4^{\text{bwd}}/P_2^{\text{bwd}} = 0.0048$ ).

In the *forward* direction, i.e. with immediate electron–electron interaction (**IV**), figure 8(d), the second excited state is dominant, too but also shows a considerable knock-up process ( $P_4^{\text{fwd}}/P_2^{\text{fwd}} = 0.10$ ). Additionally, an increase in the population of the one-electron ground state,  $n = 0$ , can be noted. Therefore, inelastic intramolecular scattering with the weaker bound  $y$  electron must have taken place resulting in a knock-down process (**V**) of the  $y$  electron during the  $x$  electron emission from the (stronger bound) lower energy levels. Comparing their respective peaks, the relative population achieved through the knock-down process is  $P_0^{\text{fwd}}/P_2^{\text{fwd}} = 0.45$ . Since

in the energetically lower  $n = 0$  state, the  $y$  electron is located on the left-hand side, this correlation-driven process coincides with an intramolecular charge transfer (green arrows).

Finally, the lowest panels, figures 8(g) and (h), correspond purely to correlation-driven processes, in which the energy provided by the electric field is absorbed by electron  $y$ , but results eventually in the emission of electron  $x$ . Therefore, a nearly elastic collision between the two electrons must have occurred, in which the absorbing electron ( $y$ ) transfers most of its acquired kinetic energy to the electron originally unaffected by the field ( $x$ ). This ‘indirect photoemission’ process (VI, VII), is very similar to the two-step-one (TS1) process in double ionization, where the electron emitted first pushes another electron out of an atom in a second step after photoabsorption [10]. But in our case, the initially accelerated electron is not released in the end but rather takes the place of the subsequently emitted electron—similar to the elastic collision between billiard balls. Consequently, the resulting populations of the single-electron states of the remaining electron shown in figure 8(g) for subsystem A resemble the one of subsystem B, seen in panel e, where the remaining electron is located at the strongly bound side. The same applies for subsystem B’s elastic collision process, figure 8(h), which rather resembles the populations found in A’s inelastic scattering, panel d including knock-up (within VII) and knock-down (VIII) features. Again, this is traced back to the accelerated  $y$  electron taking  $x$ ’s place *prior* to the emission of the  $x$  electron. Note that the indirect photoemission leads to a charge transfer (through elastic collision) immediately after photoabsorption. We therefore conclude that the significant early signals, seen in figure 7 in subsystem A’s *backward-down* channel (and with a lower amplitude also in subsystem B’s *forward-up* channel) correspond to the elastic collision process preceding the  $x$  electron’s emission.

In panels c, d, and h of figure 8, where the  $n = 2$  state is predominantly occupied, a decrease occurs in  $P_2^S(t)$  after approximately  $t \approx 15$  fs with a simultaneous increase of the  $n = 1$  state,  $P_1^S(t)$ . This time-dependent feature can be traced back to the non-adiabatic nuclear reorganization dynamics (IX, X, XI) induced by the ionization process. Note that these transitions do not occur, if the simulation is performed with a frozen nuclear configuration (dotted lines). Figure 9 shows the correlated electron–nuclear dynamics for subsystem A with emission in backward direction (corresponding to figure 8(c)) through the density function  $\int |\psi_{\text{out}}^{\text{bwd}}(x, y, R, t)|^2 dx$ . It can be seen that during the first 14 fs, the shape of the electronic part only marginally changes, while the center of the nuclear distribution moves from  $R_0 = -2.05$  Å towards larger values. This dynamics is induced by the Coulomb attraction between the remaining electron and the mobile nucleus, but is also consistent with the potential energy surface of the second state,  $V_2^{1e}(R)$ , see figure 2(a) upper panel. The latter one exhibits a large gradient towards the molecular center ( $R = 0$ ), where a coupling region with the first excited state,  $V_1^{1e}(R)$ , is found. Indeed, at 17 fs, the center of the nuclear distribution passes the origin and the electronic distribution begins to shift towards the left-hand side (to negative  $y$  values), which is reflected in a slightly negative instantaneous average electronic momen-



**Figure 9.** Electron–nuclear density of subsystem A in the *backward* channel,  $\int |\psi_{\text{out}}^{\text{bwd}}(x, y, R)|^2 dx$ . Here, the strongly bound  $x$  electron is emitted and the  $y$  electron remains initially on weakly bound side ( $y > 0$ ), before non-adiabatic transitions around  $R = 0$  lead to a charge transfer with significant electron density at the molecule’s left-hand side ( $y < 0$ ).

tum  $\langle p_y \rangle^{\text{backward-up}}(t)$  in the case of direct photoionization in the *backward-up* channel, cf figure 6(a), which is not present in the case of frozen nuclei (red dotted line). Therefore, upon ionization, nuclear dynamics is initiated, driving the system via non-adiabatic transition from the second to the first electronically excited state,  $\varphi_2^{1e}(y; R) \rightarrow \varphi_1^{1e}(y; R)$  corresponding to an intramolecular charge transfer. Note, however, that this process is significantly slower than the charge transfer process driven by electronic correlation.

It is noteworthy that, here, despite these non-adiabatic transitions, the nuclear dynamics does not seem to affect the various ionization processes discussed above. We attribute this to the chosen near-equilibrium initial conditions for  $\chi(R)$ . Previous studies have shown, that nuclear dynamics following initial non-equilibrium configurations is reflected in the photoelectron momentum distribution [37, 38]. Investigations of such effects on the correlation-driven knock-up and knock-down processes are currently under way in our workgroup.

To summarize, all observed processes, i.e. direct photoemission with and without inelastic scattering leading to knock-up and knock-down transitions, as well as indirect photoemission through elastic collision, and non-adiabatic transitions, are summarized in table 1 together with their individual amplitudes at their respective maximum and build up times, i.e. the time span the corresponding wave packet requires to achieve approximately stable populations within the observed time window. These times differ for the individual processes mostly due to the different traveling distances (direct emission vs. scattered and indirect emissions) for the ejected electron to reach the evaluation zone and because of differences in their kinetic energies. However, the slightly longer timescales of knock-down processes in particular indicate a more complex electron–electron dynamics within the molecular system prior to the electron release.

Regarding the relative amplitudes, we note, that the correlation-driven pathways through elastic and inelastic scattering appear to be nearly of the same order of magnitude



as the direct photoemission. This can be seen in figures 8(a) and (b), where the dynamics of the fully antisymmetric initial wave function without any restrictions on the electric–field interaction (solid lines) is qualitatively reproduced by the artificially restricted subsystems (dashed lines, corresponding to the direct sum of all individual pathways with restricted field interaction). Remaining discrepancies stem most likely from the missing simultaneous interaction of the XUV pulse with both electrons and also from the omission of interference effects between emitted density from the two initial localized electronic density distributions, which we have dropped by regarding electrons as distinguishable particles.

We conclude that the final state of the molecular parent ion after ionization depends strongly on dynamical correlation between electrons through elastic and inelastic intramolecular scattering events preceding the electron emission beyond static shake-up effects. Furthermore, we showed that such effects also significantly contribute to the total ionization probability. In particular, quantifying the effect of correlation-driven knock-up/knock-down processes and the indirect photoemission processes on the same magnitude as direct photoionization processes, underlines the deficiencies of the commonly applied single active electron approximation as well as the sudden approximation—even in the context of single-photon ionization of molecules.

#### 4. Summary

We investigated the correlated electron–electron and electron–nuclear dynamics in a one-dimensional molecular charge-transfer model by solving the time-dependent Schrödinger equation numerically for two electronic and one nuclear degree of freedom. To this end, we considered ionization of a single electron by an ultrashort XUV pulse and investigated the exact scattering mechanism by carefully backtracking the electron’s interaction with the residual cation and in particular with the remaining bound electron.

We introduced different theoretical approaches to investigate the correlated electron dynamics and nuclear motion during and after the pulse interaction. First, by removing all unionized components from the total wave function and projection on the one-electron system to quantify shake and knock processes. Second, we dissected these processes and identified different contributions of ionization pathways by replacing the fermionic wave functions by that of two ‘distinguishable’ electrons and by restricting the interaction of the XUV pulse to a specific electron within the molecule. Using this approach, time-dependent signatures in the evolution of the molecular parent ion were identified and traced back to various intramolecular scattering events on different time scales.

Thereby, we went beyond commonly employed approximations such as the sudden approximation, frozen nuclear degrees of freedom, or the single active electron approximation. Thus, significant contributions from electron–electron interactions within the single-photon ionization process were revealed on the atto- and femtosecond timescale, subsequently leading to non-adiabatic dynamics in the parent molecular ion. In particular, relevant pathways to the overall signal were iso-

lated, in which inelastic scattering resulted in knock-up and knock-down phenomena beyond the typically regarded (sudden) shake effects. Additional pathways of significant contribution involving elastic scattering were found, where the electron originally accelerated by the electric field transfers its momentum to a different electron within the molecule and takes its place instead (indirect photoemission). Our analysis revealed differences in the temporal signatures of all identified processes and allowed to estimate their relevance within the overall photoemission process. It was shown that electron-correlation driven processes occur on the same order of magnitude as the direct photoemission. While for a two-electron system the amplitude of the elastic collision process may be overestimated due to the reduced dimensionality of the model system, we expect this process to become even more relevant in larger, multi-electron systems. Furthermore, it was shown that different ionization pathways leave the parent molecular ion in different electronic states. As a consequence, correlated electron–nuclear reorganization dynamics is induced.

We believe that the observations made here for a model system are representative for molecular systems and consequently that both, elastic and inelastic scattering among electrons, contribute significantly to the ionization processes and the postionization dynamics through various pathways beyond the single active electron picture.

#### Acknowledgments

FGF, SG, and UP highly acknowledge support from the German Science Foundation DFG, IRTG 2101. AS and SG also acknowledge the ERC Consolidator Grant QUEM-CHEM (grant number 772676). KMZ and SG are part of the Max Planck School of Photonics supported by BMBF, Max Planck Society, and Fraunhofer Society.

#### ORCID iDs

K M Ziems  <https://orcid.org/0000-0001-5369-7778>  
S Gräfe  <https://orcid.org/0000-0002-1747-5809>  
A Schubert  <https://orcid.org/0000-0002-8560-6436>

#### References

- [1] Matveev V I and Parilis É S 1982 Shake-up processes accompanying electron transitions in atoms *Sov. Phys. - Usp.* **25** 881
- [2] Sukiasyan S, Ishikawa K L and Ivanov M 2012 Attosecond cascades and time delays in one-electron photoionization *Phys. Rev. A* **86** 033423
- [3] Auger P 1925 Sur l’effet photoélectrique composé *J. Phys. Radium* **6** 205
- [4] Pazourek R, Nagele S and Burgdörfer J 2015 Attosecond chronoscopy of photoemission *Rev. Mod. Phys.* **87** 765
- [5] Uiberacker M *et al* 2007 Attosecond real-time observation of electron tunnelling in atoms *Nature* **446** 627
- [6] Corkum P B and Krausz F 2007 Attosecond science *Nat. Phys.* **3** 381
- [7] Calegari F, Trabattoni A, Palacios A, Ayuso D, Castrovillani M C, Greenwood J B, Decleva P, Martin F and Nisoli M 2016

- Charge migration induced by attosecond pulses in bio-relevant molecules *J. Phys. B: At. Mol. Opt. Phys.* **49** 142001
- [8] Zherebtsov S et al 2011 Attosecond imaging of XUV-induced atomic photoemission and auger decay in strong laser fields *J. Phys. B: At. Mol. Opt. Phys.* **44** 105601
- [9] Ossiander M et al 2017 Attosecond correlation dynamics *Nat. Phys.* **13** 280
- [10] Hino K, Ishihara T, Shimizu F, Toshima N and McGuire J H 1993 Double photoionization of helium using many-body perturbation theory *Phys. Rev. A* **48** 1271
- [11] Pazourek R, Feist J, Nagele S and Burgdörfer J 2012 Attosecond streaking of correlated two-electron transitions in helium *Phys. Rev. Lett.* **108** 163001
- [12] Klünder K, Johnsson P, Swoboda M, L'Huillier A, Sansone G, Nisoli M, Vrakking M J J, Schafer K J and Mauritsson J 2013 Reconstruction of attosecond electron wave packets using quantum state holography *Phys. Rev. A* **88** 033404
- [13] Kazansky A K and Kabachnik N M 2007 An attosecond time-resolved study of strong-field atomic photoionization *J. Phys. B: At. Mol. Opt. Phys.* **40** F299
- [14] Cohen H D and Fano U 1966 Interference in the photo-ionization of molecules *Phys. Rev.* **150** 30
- [15] Ning Q-C, Peng L-Y, Song S-N, Jiang W-C, Nagele S, Pazourek R, Burgdörfer J and Gong Q 2014 Attosecond streaking of cohen–fano interferences in the photoionization of  $H_2^+$  *Phys. Rev. A* **90** 013423
- [16] Deshmukh P C, Mandal A, Saha S, Kheifets A S, Dolmatov V K and Manson S T 2014 Attosecond time delay in the photoionization of endohedral atoms  $A@C_{60}$ : a probe of confinement resonances *Phys. Rev. A* **89** 053424
- [17] Pazourek R, Nagele S and Burgdörfer J 2013 Time-resolved photoemission on the attosecond scale: opportunities and challenges *Faraday Discuss.* **163** 353
- [18] Remacle F and Levine R D 2011 Attosecond pumping of nonstationary electronic states of LiH: charge shake-up and electron density distortion *Phys. Rev. A* **83** 013411
- [19] Hennig H, Breidbach J and Cederbaum L S 2005 Electron correlation as the driving force for charge transfer: charge migration following ionization in n-methyl acetamide *J. Phys. Chem. A* **109** 409
- [20] Kuleff A I and Cederbaum L S 2007 Charge migration in different conformers of glycine: the role of nuclear geometry *Chem. Phys.* **338** 320
- [21] Remacle F and Levine R D 2006 An electronic time scale in chemistry *Proc. Natl Acad. Sci.* **103** 6793
- [22] Ayuso D, Palacios A, Decleva P and Martín F 2017 Ultrafast charge dynamics in glycine induced by attosecond pulses *Phys. Chem. Chem. Phys.* **19** 19767
- [23] Lepine F, Ivanov M Y and Vrakking M J J 2014 Attosecond molecular dynamics: fact or fiction? *Nat. Photon.* **8** 195
- [24] Despré V, Marciniak A, Lorient V, Galbraith M C E, Rouzée A, Vrakking M J J, Lépine F and Kuleff A I 2015 Attosecond hole migration in benzene molecules surviving nuclear motion *J. Phys. Chem. Lett.* **6** 426
- [25] Vacher M, Bearpark M J, Robb M A and Malhado J P 2017 Electron dynamics upon ionization of polyatomic molecules: coupling to quantum nuclear motion and decoherence *Phys. Rev. Lett.* **118** 083001
- [26] Vacher M, Steinberg L, Jenkins A J, Bearpark M J and Robb M A 2015 Electron dynamics following photoionization: decoherence due to the nuclear-wave-packet width *Phys. Rev. A* **92** 040502(R)
- [27] Sun S, Mignolet B, Fan L, Li W, Levine R D and Remacle F 2017 Nuclear motion driven ultrafast photodissociative charge transfer of the penna cation: an experimental and computational study *J. Phys. Chem. A* **121** 1442
- [28] Kulander K C 1988 Time-dependent theory of multiphoton ionization of xenon *Phys. Rev. A* **38** 778
- [29] Awasthi M, Vanne Y V, Saenz A, Castro A and Decleva P 2008 Single-active-electron approximation for describing molecules in ultrashort laser pulses and its application to molecular hydrogen *Phys. Rev. A* **77** 063403
- [30] Awasthi M and Saenz A 2010 Breakdown of the single-active-electron approximation for one-photon ionization of the  $B^1\Sigma_u^+$  state of  $H_2$  exposed to intense laser fields *Phys. Rev. A* **81** 063406
- [31] Shin S and Metiu H 1995 Nonadiabatic effects on the charge transfer rate constant: a numerical study of a simple model system *J. Chem. Phys.* **102** 9285
- [32] Shin S and Metiu H 1996 Multiple time scale quantum wavepacket propagation: electron–nuclear dynamics *J. Phys. Chem.* **100** 7867
- [33] Erdmann M, Gross E K U and Engel V 2004 Time-dependent electron localization functions for coupled nuclear-electronic motion *J. Chem. Phys.* **121** 9666
- [34] Falge M, Engel V, Lein M, Vindel-Zandbergen P, Chang B Y and Sola I R 2012 Quantum wave-packet dynamics in spin-coupled vibronic states *J. Phys. Chem. A* **116** 11427
- [35] Erdmann M and Engel V 2004 Combined electronic and nuclear dynamics in a simple model system. II. Spectroscopic transitions *J. Chem. Phys.* **120** 158
- [36] Falge M, Engel V and Gräfe S 2012 Fingerprints of adiabatic versus diabatic vibronic dynamics in the asymmetry of photoelectron momentum distributions *J. Phys. Chem. Lett.* **3** 2617
- [37] Falge M, Engel V and Gräfe S 2011 Time-resolved photoelectron spectroscopy of coupled electron–nuclear motion *J. Chem. Phys.* **134** 184307
- [38] Falge M, Fröbel F G, Engel V and Gräfe S 2017 Time-resolved photoelectron spectroscopy of IR-driven electron dynamics in a charge transfer model system *Phys. Chem. Chem. Phys.* **19** 19683
- [39] Erdmann M, Marquetand P and Engel V 2003 Combined electronic and nuclear dynamics in a simple model system *J. Chem. Phys.* **119** 672
- [40] Erdmann M, Baumann S, Gräfe S and Engel V 2004 Electronic predissociation: a model study *Eur. Phys. J. D* **30** 327
- [41] Feit M D, Fleck J A Jr and Steiger A 1982 Solution of the Schrödinger equation by a spectral method *J. Comput. Phys.* **47** 412
- [42] Johnson S G and Frigo M 1998 FFTW: an adaptive software architecture for the FFT *ICASSP '98 (Cat. No.98CH36181)* vol 3 p 1381
- [43] Heather R and Metiu H 1987 An efficient procedure for calculating the evolution of the wave function by fast Fourier transform methods for systems with spatially extended wave function and localized potential *J. Chem. Phys.* **86** 5009
- [44] Kosloff R and Tal-Ezer H 1986 A direct relaxation method for calculating eigenfunctions and eigenvalues of the schrödinger equation on a grid *Chem. Phys. Lett.* **127** 223
- [45] Wustelt P, Oppermann F, Yue L, Möller M, Stöhlker T, Lein M, Gräfe S, Paulus G G and Sayler A M 2018 Heteronuclear limit of strong-field ionization: fragmentation of  $HeH^+$  by intense ultrashort laser pulses *Phys. Rev. Lett.* **121** 073203



# Nuclear–Electron Correlation Effects and Their Photoelectron Imprint in Molecular XUV Ionisation

Karl Michael Ziems<sup>1,2</sup>, Jakob Bruhnke<sup>1</sup>, Volker Engel<sup>3</sup> and Stefanie Gräfe<sup>1,2,4,5\*</sup>

<sup>1</sup>Institute of Physical Chemistry, Friedrich Schiller University Jena, Jena, Germany, <sup>2</sup>Max Planck School of Photonics, Jena, Germany, <sup>3</sup>Institut für Physikalische und Theoretische Chemie, Universität Würzburg, Würzburg, Germany, <sup>4</sup>Abbe Center of Photonics, Friedrich Schiller University, Jena, Germany, <sup>5</sup>Fraunhofer Institute for Applied Optics and Precision Engineering, Jena, Germany

The ionisation of molecules by attosecond XUV pulses is accompanied by complex correlated dynamics, such as the creation of coherent electron wave packets in the parent ion, their interplay with nuclear wave packets, and a correlated photoelectron moving in a multi-centred potential. Additionally, these processes are influenced by the dynamics prior to and during the ionisation. To fully understand and subsequently control the ionisation process on different time scales, a profound understanding of electron and nuclear correlation is needed. Here, we investigate the effect of nuclear–electron correlation in a correlated two-electron and one-nucleus quantum model system. Solving the time-dependent Schrödinger equation allows to monitor the correlation impact pre, during, and post-XUV ionisation. We show how an initial nuclear wave packet displaced from equilibrium influences the post-ionisation dynamics by means of momentum conservation between the target and parent ion, whilst the attosecond electron population remains largely unaffected. We calculate time-resolved photoelectron spectra and their asymmetries and demonstrate how the coupled electron–nuclear dynamics are imprinted on top of electron–electron correlation on the photoelectron properties. Finally, our findings give guidelines towards when correlation resulting effects have to be incorporated and in which instances the exact correlation treatment can be neglected.

**Keywords:** ultrafast phenomena, XUV, attosecond dynamics, photoionisation, TDSE, correlation effects, entanglement, photoelectron spectrum

## OPEN ACCESS

### Edited by:

Yuichi Fujimura,  
Tohoku University, Japan

### Reviewed by:

Nadia Rega,  
University of Naples Federico II, Italy  
Sabyashachi Mishra,  
Indian Institute of Technology  
Kharagpur, India

### \*Correspondence:

Stefanie Gräfe  
s.graefe@uni-jena.de

### Specialty section:

This article was submitted to  
Physical Chemistry and Chemical  
Physics,  
a section of the journal  
Frontiers in Chemistry

**Received:** 12 May 2022

**Accepted:** 20 June 2022

**Published:** 05 August 2022

### Citation:

Ziems KM, Bruhnke J, Engel V and  
Gräfe S (2022) Nuclear–Electron  
Correlation Effects and Their  
Photoelectron Imprint in Molecular  
XUV Ionisation.  
Front. Chem. 10:942633.  
doi: 10.3389/fchem.2022.942633

## 1 INTRODUCTION

The fact that, if formerly non-interacting particles have interacted at some time, their wave function can no longer be expressed in a simple product form (Blum, 2012), has far-reaching consequences in many particle systems. For example, this situation appears in electronic structure calculations and there is termed electron–electron correlation (Kutzelnigg, 1994). The latter determines—to a great deal—the structure and behaviour of matter. In the field of quantum information, this correlation effect is associated with the entanglement of particles (Nielson and Chuang, 2000; Horodecki et al., 2009). As for molecules, not only electron–electron but also electron–nuclear and nuclear–nuclear interactions are of importance. Here, nuclear geometry deformations, in general, lead to the modification of the electronic density, which is responsible for chemical bonding.

The interaction of molecules with strong and ultrashort laser pulses leads, besides many other strong-field phenomena (Wolter et al., 2015; Pukhov, 2002; Krausz and Ivanov, 2009; Corkum and Krausz, 2007; Joachain et al., 2012), to single or multiple ionisation. A single XUV pulse is able to directly produce photoelectrons with different kinetic energies. With respect to the particle correlations mentioned previously, several questions arise where some of these are: What does a coupled electronic–nuclear motion look like during and after the ionisation process? Can features appearing in photoelectron spectra be related to electron–electron and electron–nuclear correlation? What characteristics appear in the post-ionisation dynamics of the charged particles?

Such fundamental issues will be taken up in the present work. Naturally, regarding the complexity of a molecule possessing many electronic and nuclear degrees of freedom, a complete quantum description of a field-triggered ionisation is simply out of reach today. One may then search for physically reasonable models to address the questions posed. It should be clear that they have to go beyond single active electron approximations and include the motion of the nuclei, most desirably on the same level as the electrons. In an early study, Lein et al. (2002) studied the single and double ionisation of the hydrogen molecule involving the motion of all particles in a single dimension and Sukiasyan et al. (2012) described the one-electron photoionisation for a 1D-Helium atom with two active electrons. To understand the impact of ionisation on the parent ion dynamics in real molecules, approximated quantum chemical methods neglecting the explicit ionisation pump can be applied and are powerful tools to unravel electron dynamics post ionisation (Ayuso et al., 2017; Nisoli et al., 2017) and study the nuclear decoherence effect on electronic wave packets (Vacher et al., 2015, 2017).

A useful model to study electron–nuclear correlation effects is the so-called Shin–Metiu model (Shin and Metiu, 1995, 1996). It consists of an electron and a nucleus that move in one dimension in an additional field of two positive charges. Originally devised to describe charge-transfer processes, it was later used to illustrate features of, e.g., coupled electronic–nuclear quantum (Hader et al., 2017; Albert et al., 2017; Schaupp and Engel, 2019b, 2022) and classical dynamics (Schaupp and Engel, 2019a) or two-dimensional coherent femtosecond spectroscopy (Albert et al., 2015). The model was also used to study photoionisation (Falge et al., 2011, 2012a, 2017).

The simple Shin–Metiu model was later extended to include the motion of a second electron, which made it possible to introduce time-dependent electron localisation functions (ELF) and characterise the influence of nuclear motion on these (Erdmann et al., 2004). Also, the wave-packet dynamics in spin-coupled electronic states could be described (Falge et al., 2012b).

Here, we extend our work on XUV ionisation in a molecular model system comprised of fully correlated two electrons and one nucleus (Fröbel et al., 2020). We study the impact of electron–nuclear correlation upon electron–electron correlation on the complete XUV ionisation process monitoring the influence pre, during, and post ionisation. Consequently, we dissect the effects on the parent ion, as well as on the photoelectron. Finally, we report on an imprint of the two-electron correlated bound dynamics on the photoelectron spectrum’s asymmetry, thus yielding an observable to measure the

electrons’ density behaviour caused by nuclear correlation. This is a natural extension of our former work limited to a single active electron system (Falge et al., 2012a, 2017) and shows that the concept also holds for more complex systems. Moreover, by thoroughly dissecting the different effects present in a full quantum dynamical study with correlated particles, we provide guidance for future investigations resting on more approximated methods.

This study is organised as follows: In **Section 2**, we briefly introduce the model system, its potential energy surface, the numerical details for solving the time-dependent Schrödinger equation (TDSE), and different analysis tools. In presenting our results, we start by introducing the laser-free non-equilibrium dynamics and, subsequently, report on the impact of correlation effects on 1) the attosecond electron dynamics during ionisation, 2) the post-ionisation dynamics in the parent ions, and 3) the photoelectron. In the last section, we discuss how the asymmetry of the integrated photoelectron spectra shows imprints of resonance dependencies into the continuum and the coupled electron–nuclear dynamics.

## 2 THEORETICAL BACKGROUND

In the following, we briefly describe the model system and numerical procedure. For more details, we refer to our recent work (Fröbel et al., 2020), where we introduce the model in the context of ionisation. Atomic units are used throughout the study.

### 2.1 Molecular Model System

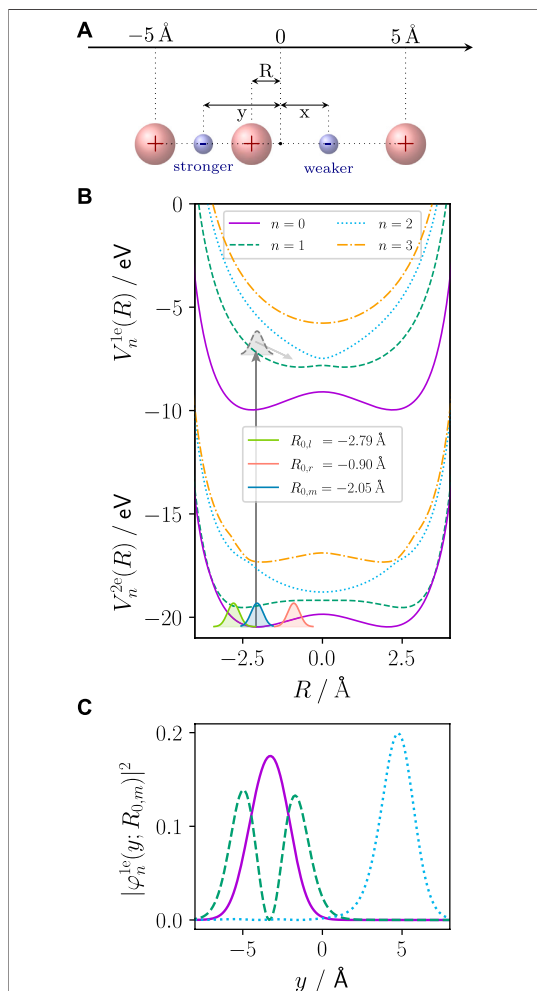
#### 2.1.1 Full Three-Dimensional Model

To capture electron–nuclear and electron–electron correlation in molecular XUV ionisation, we use the one-dimensional extended Shin–Metiu model system, which includes two electrons ( $x, y$ ) and a central nucleus with coordinate  $R$  (Shin and Metiu, 1995, 1996; Erdmann et al., 2004). Furthermore, two fixed nuclear point charges ( $Z_1, Z_2$ ) at  $\pm L/2$  define the outer potential barriers. The particle configuration is sketched in **Figure 1A**. The molecular Hamiltonian reads:

$$\mathcal{H}_0 = \frac{\hat{P}^2}{2M} + \frac{\hat{P}_x^2}{2} + \frac{\hat{P}_y^2}{2} + \hat{V}^{2e}(x, y, R), \quad (1)$$

where  $M$  is the nuclear mass,  $\hat{P}$  the nuclear momentum operator, and  $\hat{P}_x, \hat{P}_y$  the electron momentum operators. The potential is defined as:

$$\hat{V}^{2e}(x, y, R) = \frac{Z_1 Z}{|L/2 - R|} + \frac{Z_2 Z}{|L/2 + R|} - \frac{Z \operatorname{erf}(|R - y|/R_c)}{|R - y|} - \frac{Z_1 \operatorname{erf}(|L/2 - y|/R_f)}{|L/2 - y|} - \frac{Z_2 \operatorname{erf}(|L/2 + y|/R_f)}{|L/2 + y|} - \frac{Z \operatorname{erf}(|R - x|/R_c)}{|R - x|} - \frac{Z_1 \operatorname{erf}(|L/2 - x|/R_f)}{|L/2 - x|} - \frac{Z_2 \operatorname{erf}(|L/2 + x|/R_f)}{|L/2 + x|} + \frac{\operatorname{erf}(|x - y|/R_e)}{|x - y|}. \quad (2)$$



**FIGURE 1** | (A) Extended Shin-Metiu model system: two electrons ( $x, y$ ) and one nucleus  $l$  move in one dimension in the field of the two outer fixed (point charge) nuclei ( $R$ ). For  $R < 0$  as in the focus of investigation here, the left electron (here:  $y$ ) is stronger bound, while the right electron (here:  $x$ ) is weaker bound. The electrons are indistinguishable and are just given defined labels here for visualisation purposes. (B) PECs of the 2e system,  $V_n^{2e}(R)$ , and the 1e parent ion,  $V_n^{1e}(R)$ . The vertical line indicates one-photon ionisation and the population of the parent ion states. As an example, the nuclear wave packet in the  $n = 1$  ion state is shown together with the gradient exerted by the PEC on it (grey shaded Gaussian). In the 2e system ground state ( $n = 0$ ), the three different initial nuclear wave packets investigated in this work are shown. The nuclear wave packet near the equilibrium position of  $R_{0,m} = -2.05 \text{ \AA}$  (blue shaded Gaussian), and the two non-equilibrium starting wave packets starting at the isopotential turning points left,  $R_{0,l} = -2.79 \text{ \AA}$  (green shaded Gaussian), and right,  $R_{0,r} = -0.90 \text{ \AA}$  (red shaded Gaussian), of the equilibrium. (C) The absolute square of the first three 1e parent ion wave functions shows that  $n = 2$  (blue dotted) is located at  $y > 0$  (weaker bound).

Here, we set the charges  $Z_1 = Z_2 = Z = 1$ ,  $M$  to the proton mass, the screening parameters  $R_c = R_f = R_e = 1.5 \text{ \AA}$  and  $L = 10 \text{ \AA}$  for the outer point charges. The potential contains soft Coulomb interactions between the moving particles, parameterised by error functions (erf). The model mimics a generic molecular system leading to a qualitative description of processes. It does not represent a specific class of molecules, such as linear molecules, especially since the central moving nucleus has unscreened interactions with the outer fixed nuclei preventing dissociation. Such effect would be essential for strong-field interactions with seemingly similar linear triatomic systems, but they are not in the scope of this work. Moreover, we are restricted to one nuclear degree of freedom, thus, not investigating nuclear-nuclear correlation. Since the model is one-dimensional, effects of the orbital angular momentum of the electrons are not regarded. We note that the system is already of ionic type. Nevertheless, in what follows, we will refer to the removal of an electron by the external field as an ionisation process.

While the reduced dimensionality of the model allows for solving the dynamics of all three particles, for interpretation, it is useful to obtain the electronic eigenstates and the potential energy curves (PECs) of the two-electron (2e) system. Therefore, we solve the time-independent electronic Schrödinger equation:

$$\left[ \frac{\hat{p}_x^2}{2} + \frac{\hat{p}_y^2}{2} + \hat{V}^{2e}(x, y, R) \right] \varphi_n^{2e}(x, y, R) = V_n^{2e}(R) \varphi_n^{2e}(x, y, R). \quad (3)$$

where  $\hat{p}_x$  and  $\hat{p}_y$  are the electronic momentum operators. This yields the adiabatic electronic eigenstates  $\varphi_n^{2e}(x, y, R)$  and the potentials  $V_n^{2e}(R)$ . All our calculations are restricted to the singlet case, i.e., the appearing wave functions are symmetric upon exchanging  $x$  and  $y$ . Upon removal of an electron through the XUV interaction, the remaining one-electron (1e) parent ion system has the potential:

$$\hat{V}^{1e}(y, R) = \frac{Z_1 Z}{|L/2 - R|} + \frac{Z_2 Z}{|L/2 + R|} - \frac{Z \operatorname{erf}(|R - y|/R_c)}{|R - y|} - \frac{Z_1 \operatorname{erf}(|L/2 - y|/R_f)}{|L/2 - y|} - \frac{Z_2 \operatorname{erf}(|L/2 + y|/R_f)}{|L/2 + y|}. \quad (4)$$

The respective electronic eigenstates ( $\varphi_n^{1e}(y, R)$ ) and the PECs ( $V_n^{1e}(R)$ ) are determined by the time-independent electronic Schrödinger equation

$$\left[ \frac{\hat{p}_y^2}{2} + \hat{V}^{1e}(y, R) \right] \varphi_n^{1e}(y, R) = V_n^{1e}(R) \varphi_n^{1e}(y, R). \quad (5)$$

The PECs of both the 2e and 1e systems are shown in **Figure 1B** for the lowest four electronic eigenstates. It is important to point out that for the 1e system (parent ion), and  $R < 0$  (which is the case throughout this work), the electron resides either left, at negative  $y$  values (stronger



bound), or right, at positive  $y$  values (weaker bound), of the central nucleus depending on its electronic state. For the  $n = 2$  1e state, the electronic eigenfunction's probability density,  $|\varphi_{2e}^{1e}(y; R)|^2$ , is located at the weaker bound site. The other 1e states shown in **Figure 1C** are located left of the central nucleus (stronger bound site).

We define the initial wave function as the product of the 2e adiabatic ground state ( $n = 0$ ) and a Gaussian-shaped vibrational wave packet,  $\chi(R)$ :

$$\chi(R) = N_0 e^{-\beta_R (R - R_{0,l}/m)^2}, \quad (6)$$

$$\Psi(x, y, R, t_0) = \varphi_0^{2e}(x, y; R) \chi(R), \quad (7)$$

with the normalisation constant  $N_0$  and  $\beta_R = 7.14 \text{ \AA}^{-2}$ . As shown in **Figure 1B**, we regard three different initial vibrational wave packets, which differ with respect to the centre of the Gaussian in **Eq. 6**. In particular, we use the equilibrium configuration  $R_{0,m} = -2.05 \text{ \AA}$  (blue shaded Gaussian), and two non-equilibrium configurations, where one is placed to the left  $R_{0,l} = -2.79 \text{ \AA}$  (green shaded Gaussian) and the other to the right  $R_{0,r} = -0.90 \text{ \AA}$  (red shaded Gaussian) of  $R_{0,m}$ . The two non-equilibrium positions were chosen isopotentially.

The system interacts with a linearly polarised XUV pulse defined via its vector potential,  $\mathcal{A}(t)$ , with polarisation aligned along with the molecular axis of the model:

$$\mathcal{A}(t) = \frac{E_0}{\omega} g(t + t_0) \sin(\omega(t + t_0)). \quad (8)$$

We use an electric field strength of  $E_0 = 0.169$  a.u. (corresponding to an intensity of  $I = 10^{15} \text{ W/cm}^2$ ), an angular frequency of  $\omega = 0.570$  a.u. ( $\lambda = 80 \text{ nm} = 15.5 \text{ eV}$ ), and a full-width at half-maximum (FWHM) of  $\tau = 5$  fs for the Gaussian pulse envelope function  $g(t)$ . The comparatively long FWHM was chosen to avoid possible few-cycle effects leading to pulse-dependent intrinsic asymmetries in the photoelectron spectrum (PES). For the parameters chosen here, the light pulse does not influence the asymmetry of the PES, and despite the high field strength, the simple one-photon picture of energy conservation between light pulse, parent ion, and photoelectron holds. The different pulse interaction times  $t_0$ , for different simulation setups are discussed and introduced as follows: the propagation starts at  $t = t_0 - 2\tau$ . The full time-dependent Hamiltonian in velocity gauge and dipole approximation reads:

$$\mathcal{H}(t) = \frac{\hat{p}^2}{2M} + \frac{\hat{p}_x^2}{2} + \frac{\hat{p}_y^2}{2} + \hat{V}^{2e}(x, y, R) + e \mathcal{A}(t) \left( -\frac{\hat{p}}{M} + \hat{p}_x + \hat{p}_y \right), \quad (9)$$

### 2.1.2 Approximations: Frozen and Single Point Charge Nucleus

In order to understand the role of the nuclear degree-of-freedom in the quantum dynamical simulations, we compare the complete electron–nuclear dynamics to the case of 1) a frozen nuclear wave packet and 2) a single point charge calculation. In the frozen nuclear wave packet approximation, 1), the nuclear dimension

becomes parametric and is only used to sample the nuclear wave packet on the grid by several 2D simulations of the electronic degrees of freedom. Hence, the Hamiltonian, **Eq. 9**, is missing the nuclear kinetic energy and XUV interaction term. The  $R$ -dimension in the potential and the wave function becomes parametric. The single point calculation, 2), completely neglects the wave packet nature of the central nucleus and treats the central nucleus as a point charge at a fixed position leading to a single 2D simulation of the electronic degrees of freedom. This leaves the Hamiltonian of **Eq. 9** without any explicit or parametric  $R$  dependence, yielding a two-dimensional wave function depending on  $x, y$ .

## 2.2 Numerical Details

The time-dependent Schrödinger equation is as follows:

$$i \frac{\partial}{\partial t} \Psi(x, y, R, t) = \mathcal{H}(t) \Psi(x, y, R, t), \quad (10)$$

with the Hamiltonian defined in **Eq. 9** is solved numerically on a grid of dimensions  $[-240, 240] \text{ \AA}$  with 1,024 grid points for  $x$  and  $y$  (electronic dimensions) and  $[-4.99, 4.99] \text{ \AA}$  with 128 grid points for  $R$  (nuclear dimension). The integration is performed with a time step of 5as using the split-operator technique (Feit et al., 1982) and the FFTW three libraries (Frigo and Johnson, 1998) for Fourier transforms. This setup is used for all calculations unless stated otherwise. The time-independent 2e and 1e Schrödinger equations defined in **Eqs. (3)** and **(5)**, respectively, are numerically solved with the relaxation method, solving the TDSE in imaginary time (Kosloff and Tal-Ezer, 1986).

To avoid grid reflection, cut-off functions are applied each time step to the full wave function in the asymptotic region of the molecular potential

$$f(x, y) = \left[ 1 + e^{\zeta_1 (|x| - \zeta_1)} \right]^{-1} \left[ 1 + e^{\zeta_2 (|y| - \zeta_2)} \right]^{-1} \quad (11)$$

with the parameters  $\zeta_1 = 0.085$  a.u. and  $\zeta_2 = 492$  a.u. (Heather and Metiu, 1987).

In the following, we introduce three analysis tools of the full-wave function,  $\Psi(x, y, R, t)$ , in order to arrive at a deeper understanding of the ionisation dynamics. The exact ionised wave function comprised of having one electron in the continuum, whilst the other electron is still bound in the parent ion is unknown for such molecular, many-particle, and multi-centred systems. The following approaches circumvent this problem by using grid-based functions and projection operators.

### 2.2.1 Outer Wave Functions, $\Psi_{\text{out}}^{\text{fwd/bwd}}(p_x, y, R, t)$ , Long-Time Limit

To obtain the part of the wave function representing the ionised system at long times, the outgoing parts of the wave function in  $x$  direction are collected. Since the wave function is fully mirror symmetric in  $x$  and  $y$ , we arbitrarily choose  $x$  as a dimension of ionisation, while  $y$  characterises the bound electron in the parent ion. To this end, we define a mask function in forward (fwd),  $x > 0$ , and backward (bwd),  $x < 0$ , direction using the same values of  $\zeta_1, \zeta_2$  as mentioned previously.

$$\tilde{f}^{\text{fwd}}(x, y) = \left(1 - \left[1 + e^{\zeta_1(x-\zeta_2)}\right]^{-1}\right) \Theta(25 \text{ \AA} - |y|), \quad (12)$$

$$\tilde{f}^{\text{bwd}}(x, y) = \left(1 - \left[1 + e^{\zeta_1(-x-\zeta_2)}\right]^{-1}\right) \Theta(25 \text{ \AA} - |y|), \quad (13)$$

where the Heaviside function restricts the outer wave function to grid values of  $-25 \text{ \AA} < y < 25 \text{ \AA}$ , thus, neglecting double ionisation. At each time step,  $\tilde{f}^{\text{fwd/bwd}}(x, y)$  is applied to the total wave function, Fourier-transformed (FT) with respect to the electronic coordinate  $x$  and added coherently to the parts already localised in the outer regions in order to yield the outer wave functions:

$$\Psi_{\text{out}}^{\text{fwd/bwd}}(p_x, y, R, t) = \Psi_{\text{out}}^{\text{fwd/bwd}}(p_x, y, R, t - \Delta t) + \mathcal{FT}_x \left[ \tilde{f}^{\text{fwd/bwd}}(x, y) \Psi(x, y, R, t) \right]. \quad (14)$$

Consequently,  $\Psi_{\text{out}}^{\text{fwd/bwd}}(p_x, y, R, t)$  is only propagated in momentum space in  $x$  dimension. The outer wave functions are used to calculate the PESs, state resolved to particular 1e states in the parent ion,  $\sigma_n^{\text{fwd/bwd}}(p_x)$ , and to obtain the total integrated asymmetry  $A$ . The former is obtained by projection on the adiabatic 1e states at the end of the time propagation, in the limit  $t \rightarrow \infty$

$$\sigma_n^{\text{fwd/bwd}}(p_x) = \int \left| \int \varphi_n^{1e}(y; R) \Psi_{\text{out}}^{\text{fwd/bwd}}(p_x, y, R, t \rightarrow \infty) dy \right|^2 dR. \quad (15)$$

The total integrated asymmetry of the PES is calculated as

$$A = \sum_n \int \frac{\sigma_n^{\text{fwd}}(p_x) - \sigma_n^{\text{bwd}}(p_x)}{\sigma_n^{\text{fwd}}(p_x) + \sigma_n^{\text{bwd}}(p_x)} dp_x. \quad (16)$$

### 2.2.2 Channel Wave Functions, $\Psi_{\text{ch}}^{\text{fwd/bwd}}(x, y, R, t)$ , Intermediate Times

In order to investigate the ionised system at intermediate times in fwd and bwd directions, we define the channel wave functions.

$$\Psi_{\text{ch}}^{\text{fwd}}(x, y, R, t) = \Theta(-25 \text{ \AA} + x) \Theta(25 \text{ \AA} - |y|) \Psi(x, y, R, t), \quad (17)$$

$$\Psi_{\text{ch}}^{\text{bwd}}(x, y, R, t) = \Theta(-25 \text{ \AA} - x) \Theta(25 \text{ \AA} - |y|) \Psi(x, y, R, t). \quad (18)$$

Again, these wave functions represent the ionised system and monitor the parent ion electron ( $y$ ) located in the grid range  $-25 \text{ \AA} < y < 25 \text{ \AA}$ , while the photoelectron ( $x$ ) is at larger position values on the grid,  $|x| > 25 \text{ \AA}$ .

### 2.2.3 Bound/Continuum Wave Function, $\Psi_{1b/1c}(x, y, R, t)$ , Early Times

Additionally, to understand the attosecond electron dynamics at early times during XUV pulse interaction, the exact 1e-bound/1e-continuum (1b/1c) wave function is needed. For this, we define a bound/continuum wave function, i.e., 1e-

bound/1e-continuum, by projecting out the 2e bound states at each time step

$$\Psi_{1b/1c}(x, y, R, t) = \Psi(x, y, R, t) - \sum_{n=0}^{19} \left( \iint \varphi_n^{2e}(x', y'; R) \Psi(x', y', R, t) dx' dy' \right) \varphi_n^{2e}(x, y; R). \quad (19)$$

This procedure is computationally very demanding and, therefore, limited to the early few femtoseconds. A maximum of 20 2e bound states has shown to be sufficient to obtain convergence. The as such calculated wave function can be used to identify trends in the integrated asymmetry of the PES without having to propagate the full wave function for long times. This is achieved by integrating the bound/continuum wave function once over positive (fwd) and once over negative (bwd)  $x$  direction, yielding the asymmetry as:

$$n^{\text{fwd}}(t) = \int_0^{120 \text{ \AA}} dx \iint \Theta(25 \text{ \AA} - |y|) |\Psi_{1b/1c}(x, y, R, t)|^2 dy dR, \quad (20)$$

$$n^{\text{bwd}}(t) = \int_{-120 \text{ \AA}}^0 dx \iint \Theta(25 \text{ \AA} - |y|) |\Psi_{1b/1c}(x, y, R, t)|^2 dy dR, \quad (21)$$

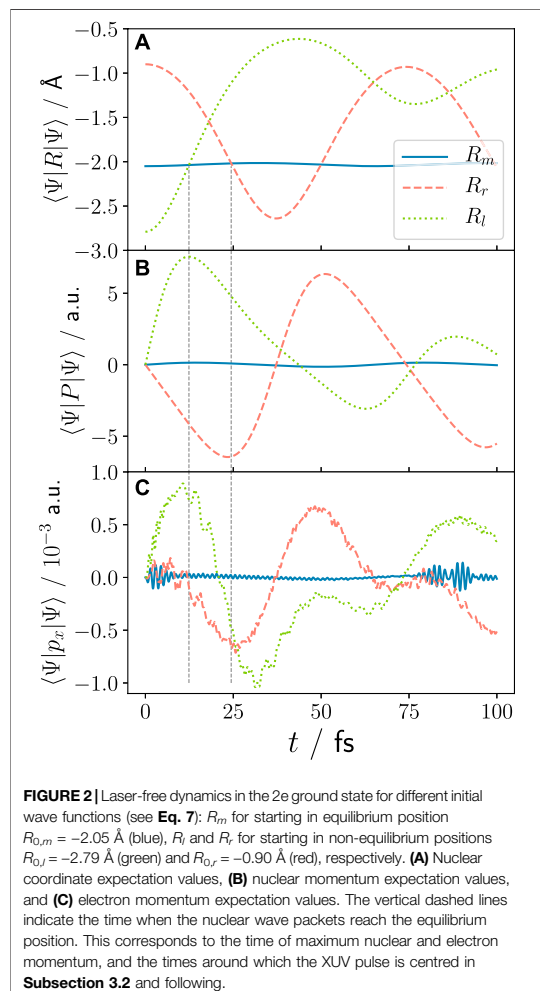
$$\tilde{A}(t) = \frac{n^{\text{fwd}}(t) - n^{\text{bwd}}(t)}{n^{\text{fwd}}(t) + n^{\text{bwd}}(t)}. \quad (22)$$

Hereby, the grid boundaries and grid points of the electronic grid were halved to reduce the computational costs. Because this procedure is only performed to investigate the very early attosecond dynamics, the shorter grid is sufficient to get an insight into the early ionisation dynamics. As will be seen, the asymmetry defined by Eq. 22 produces quantitatively similar results to the asymmetry given by Eq. 16.

## 3 RESULTS

### 3.1 Laser-Free Dynamics

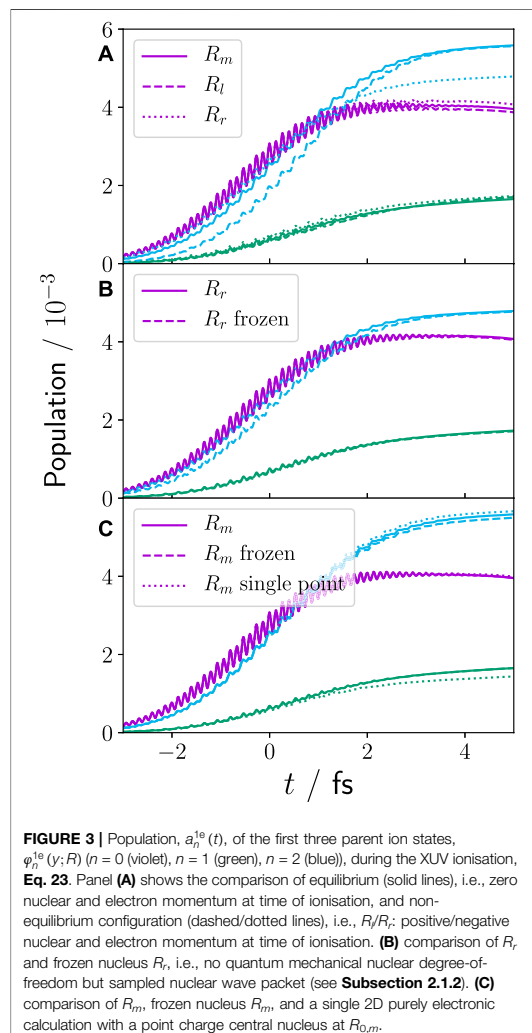
In Figures 2A,B, we show the nuclear coordinate and momentum expectation values obtained for the three different initial nuclear wave packet starting positions  $R_{0,l/m/r}$ . In 3), the corresponding mean electron momentum is displayed. Starting with the nuclear case, we see that for  $R_r$  an oscillating dynamics within the left potential well takes place (recall Figure 1B) with the nuclear momentum behaving accordingly. For  $R_b$  there is partial nuclear density transfer to the right potential well after approximately  $t > 25$  fs, destroying the simple oscillatory motion of the nucleus. This is due to higher momenta being present in the nuclear wave packet that originate from the steep gradient left of the centre of  $R_{0,l}$ . The electron response, i.e., the electron density's momentum  $\langle \Psi(t) | p_x | \Psi(t) \rangle$ , follows qualitatively the nuclear momentum,  $\langle \Psi(t) | P | \Psi(t) \rangle$ , however, with small discrepancies. For both non-equilibrium starting positions, the maximum nuclear and electron momentum expectation value is reached



when the nucleus passes the minimum of the potential well, as indicated with the vertical, dashed lines in Figure 2.

### 3.2 Attosecond Dynamics

We aim at investigating the impact of nuclear motion and nuclear–electron correlation on the ultrafast ionisation dynamics. For this, we compare the ionisation process of the nuclear equilibrium configuration ( $R_{0,m}$ ) with ionisation of the initial non-equilibrium nuclear configuration ( $R_{0,l/r}$ ) with the pulse centred around the time of equilibrium passage, i.e., when  $\langle R_{l/r}(t_0) \rangle = R_{0,m}$ . These times are indicated previously in Figure 2 with the dashed vertical lines and correspond to a maximum positive (negative) nuclear and electron momentum for  $R_l$  ( $R_r$ ). The times are  $t_0 = 12.30$  fs for



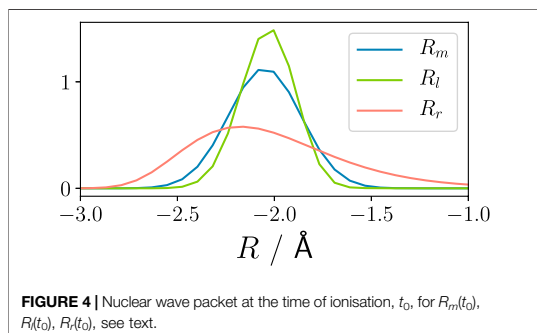
$R_l(t_0) = R_{0,m}$  and  $t_0 = 24.405$  fs for  $R_r(t_0) = R_{0,m}$ . From now on, referring to  $R_l$  and  $R_r$  implicates this procedure, while  $R_{0,l/r/m}$  refers to the initial nuclear positions.

First, we analyse the attosecond dynamics during the XUV pulse interaction leading to the population of the parent ion states,  $\varphi_n^{1e}(y; R)$ . Thus, we project the 1e states on the bound/continuum wave function

$$a_n^{1e}(t) = \iiint \left| \int \varphi_n^{1e}(y; R) \Psi_{1b/1c}(x, y, R, t) dy \right|^2 dx dR. \quad (23)$$

Figure 3A shows the population of the first three electronic parent ion states for the equilibrium and non-equilibrium cases ( $R_l$ ,  $R_r$ ). It can be seen that the previously discussed





**FIGURE 4** | Nuclear wave packet at the time of ionisation,  $t_0$ , for  $R_m(t_0)$ ,  $R_l(t_0)$ ,  $R_r(t_0)$ , see text.

dynamics prior to ionisation, which leads to non-zero electron momentum at the time of ionisation, have almost no impact on the attosecond electronic population dynamics. The only small difference is visible for the  $n = 2$  state in the case of  $R_r$  (blue dotted line). However, this difference does not originate from the nuclear–electron correlation but is rather due to the deformation of the nuclear wave packet prior to ionisation, see **Figure 4**, depicting the nuclear wave packet at the time of ionisation for  $R_m(t_0)$ ,  $R_l(t_0)$ , and  $R_r(t_0)$ . The deformation of the  $R_r$  nuclear wave packet, caused by the anharmonic PEC, leads to a small change in resonance conditions into the 1e-bound/1e-continuum and, consequently, to a slight change in the 1e state population. This becomes also evident by comparing the attosecond dynamics of  $R_r$  with a frozen nucleus calculation using the nuclear wave packet obtained at the time of ionisation from the 3D  $R_r$  simulation (recall **Subsection 2.1.2**, see **Figure 3B**). Although in the frozen nuclear wave packet simulation no nuclear or electron momentum is present, it shows identical attosecond dynamics. The frozen nuclear wave packet calculation without intrinsic quantum mechanical nuclear dimension reproduces the attosecond dynamics also for the other two investigated cases ( $R_m$ ,  $R_r$ ). More so, **Figure 3C** shows that for  $R_m$ , a single 2D calculation with the classical point charge nucleus centred at  $-2.05$  Å (the centre of the  $R_m$  wave packet) is sufficient to reproduce the attosecond dynamics and population of ionic states.

In other words, to describe the correct attosecond dynamics of the parent ion population upon ionisation, the quantum mechanical description of the nuclear degree of freedom can be neglected—a frozen nucleus approach of sampling the nuclear wave packet is sufficient. Moreover, if the nuclear dynamics prior to ionisation only proceeded on a harmonic PEC, leading to a compact Gaussian-like nuclear wave packet, a purely electronic TDSE simulation is able to reproduce the correct behaviour. This is an important finding for future approximations in the field of attosecond ionisation dynamics.

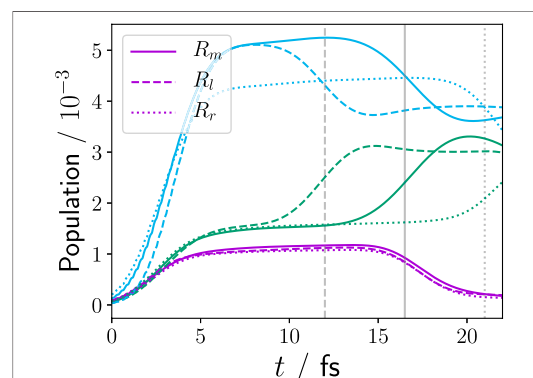
### 3.3 Momentum Conservation in Parent Ion Dynamics

As seen in the previous section, within the first 4 fs upon XUV pulse interaction, the population in the parent ion is created and

reaches stable values. Subsequently, in the parent ion, the nuclear wave packet moves on the corresponding PECs contained in the electronic wave packet acquiring momenta determined by the PEC's gradients. In particular, the nuclear wave packet propagating on  $n = 2$  and moving towards  $R = 0$  undergoes a pronounced non-adiabatic transition with  $n = 1$ . Passing through  $R = 0$  will lead to a change in the population of the parent ion states in the electronic wave packet. If ionisation into  $n = 2$  and the subsequent nuclear relaxation would be independent of the initial nuclear momentum at  $t_0$ ,  $P^{2e}(t_0)$ , gained during propagation in the 2e electronic ground state (cf. **Figure 2**), the crossing at  $R = 0$  would always be reached approximately 17fs after ionisation. However, if this initial nuclear momentum is retained upon ionisation, this will become visible through the timing of the non-adiabatic transition. Thus, the time at which the non-adiabatic crossing occurs is a direct measurement for pre-ionisation momentum dynamics. **Figure 5** shows the parent ion state-resolved population obtained in bwd direction using the channel wave function

$$b_n^{1e}(t) = \iiint \left| \int \varphi_n^{1e}(y; R) \Psi_{\text{ch}}^{\text{bwd}}(x, y, R, t) dy \right|^2 dx dR \quad (24)$$

for  $R_m$ ,  $R_l$  and  $R_r$ . The non-adiabatic transition leading to depopulation of  $n = 2$  and population of  $n = 1$  is clearly visible for all three cases. Moreover, the time of the transition is shifted to earlier (later) times for  $R_l$  ( $R_r$ ), demonstrating that the pre-ionisation momentum acquired by the nuclear wave packet propagating in the electronic ground state is retained upon ionisation. This is even more evident in **Table 1** where the nuclear momentum expectation value of the individual nuclear



**FIGURE 5** | Population of parent ion 1e states using the bwd channel wave function (**Eq. 24**) to visualise the timing of the non-adiabatic transition between the  $n = 2$  (blue) and  $n = 1$  (green) state for  $R_m$  (solid lines),  $R_l$  (dashed lines), and  $R_r$  (dotted lines). The  $n = 0$  population (violet) decreases as the channel wave function for this ion ground state with corresponding highest photoelectron momenta reaches the absorber after 15 fs. The difference in population of the  $n = 2$  state for  $R_r$ , compared to  $R_m$ , is based on the nuclear wave packet deformation as discussed in the text for the bound/continuum wave function.

**TABLE 1** | Nuclear momentum expectation value of the different nuclear wave packets on different parent ion states, see Eq. 26, for the three different initial nuclear positions (first to third row). The fourth and fifth rows show the difference of non-equilibrium to equilibrium momentum, emphasising momentum conservation upon ionisation.

Starting position	$P_0^{1e}(t_0 + 2.5 \text{ fs})$	$P_1^{1e}(t_0 + 2.5 \text{ fs})$	$P_2^{1e}(t_0 + 2.5 \text{ fs})$
$R_m$	-0.24	2.92	5.42
$R_l$	6.95	10.23	12.87
$R_r$	-6.38	-3.57	-1.28
$R_l - R_m$	7.18	7.30	7.45
$R_r - R_m$	-6.15	-6.49	-6.70

wave packet propagating on one of the first three parent ion states is shown at  $t = t_0 + 2.5 \text{ fs}$  for the three initial starting positions. This is calculated by projecting bwd channel wave function on the corresponding ionic state and calculating the momentum expectation value:

$$\Psi_{\text{ch},n}^{\text{bwd},1e}(x, R, t) = \int \varphi_n^{1e}(y; R) \Psi_{\text{ch}}^{\text{bwd}}(x, y, R, t) dy, \quad (25)$$

$$P_n^{1e}(t) = \iint \Psi_{\text{ch},n}^{\text{bwd},1e*}(x, R, t) P \Psi_{\text{ch},n}^{\text{bwd},1e}(x, R, t) dR dx. \quad (26)$$

It can be gathered from Table 1 that the nuclear momentum is different depending on the PEC the nuclear wave packet evolves on, e.g., for  $R_m$  (first row) the momentum is negative for  $n = 0$ , while it is positive for  $n = 1$  and further increased for  $n = 2$  as expected from the PEC gradients (Figure 1). Second, the momenta for the non-equilibrium cases  $R_l$  ( $R_r$ ) (second and third row) are uniformly shifted to higher (lower) momentum values. The lower rows,  $R_l - R_m$  and  $R_r - R_m$ , quantify the difference to the equilibrium case (no initial momentum). These concur with the momentum in the bound  $2e$  system at time of ionisation, which is for  $R_l$ :  $P^{2e}(t_0) = 7.6 \text{ a.u.}$  and for  $R_r$ :  $P^{2e}(t_0) = -6.4 \text{ a.u.}$  (seen vertical dashed lines in Figure 2B). Therefore, we have unambiguously shown that the nuclear momentum in the bound  $2e$  system is conserved upon ionisation manifesting itself in a change in timing for the non-adiabatic transition.

### 3.4 Photoelectron Spectra and Asymmetry

We now investigate to which extent these nuclear-electron correlation dynamics impact the PES. It has been reported that for simple one active electron systems, the coupled nuclear-electron dynamics are imprinted in the integrated photoelectron asymmetry (Falge et al., 2012a, 2017). So far, it is an open question, whether this also holds for multi-electron systems.

#### 3.4.1 Resonance Condition

The major difference to our previous work using single active electron systems is that upon ionisation, there is no ionisation into a single continuum state but rather complex transitions into several  $1e$ -bound/ $1e$ -continuum states depending on the XUV pulse's central frequency. Moreover, ionisation into these different states features varying resonance conditions for the

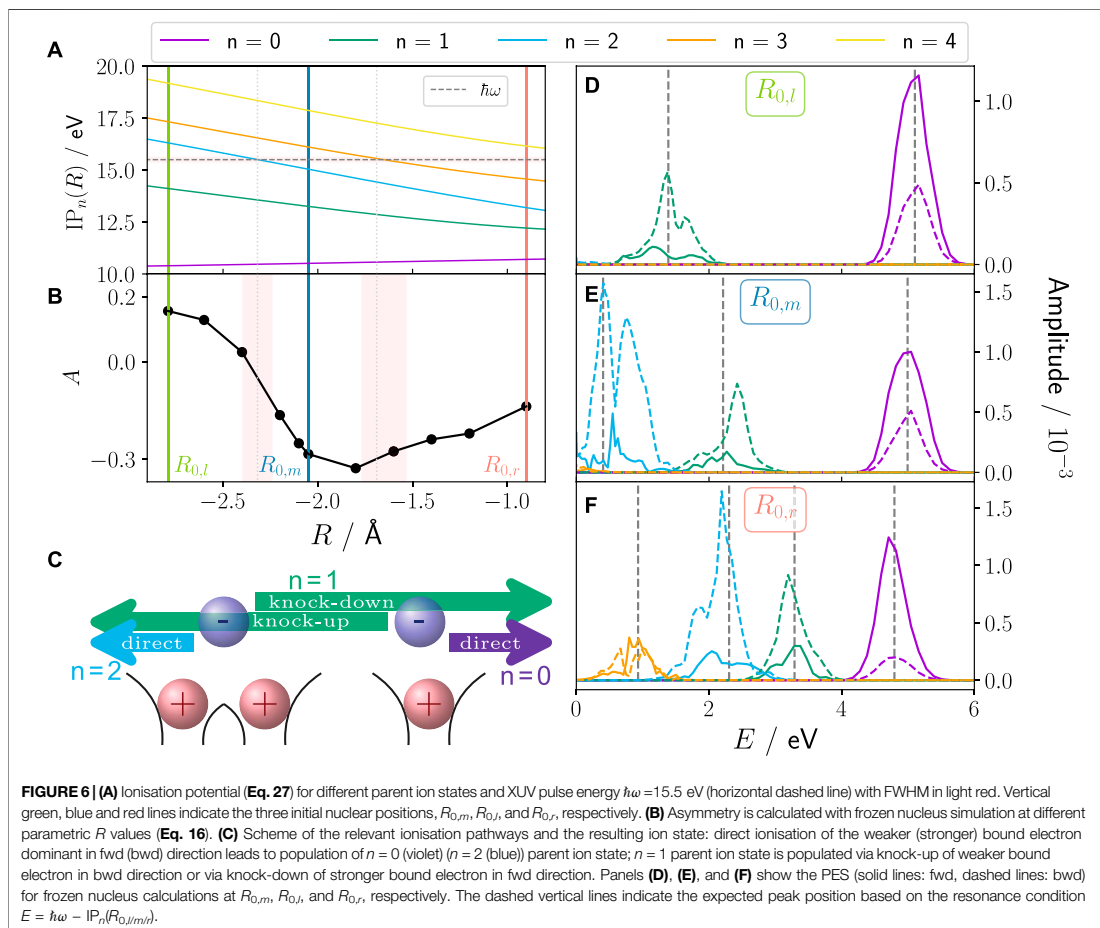
various ion states. The resonance conditions are visualised in Figure 6A as a function of the parametric nuclear position

$$IP_n(R) = V_0^{2e}(R) - V_n^{1e}(R). \quad (27)$$

For the three initial nuclear positions ( $R_{0,m}$ ,  $R_{0,b}$ ,  $R_{0,r}$ ), respectively, 3, 2, or 4 parent ion states are energetically accessible for the XUV pulse used in this work ( $\hbar\omega = 15.5 \text{ eV}$ ). Figures 6D–F show the respective PES with exactly those 3, 2, or 4 peaks. Additionally, ionisation in these ionic states comes together with static and dynamic electron–electron correlation effects on top of any electron–nuclear correlation due to coupled dynamics. Therefore, depending on the position of the nuclear wave packet at the time of ionisation, there is a state-intrinsic inherent fwd/bwd asymmetry independent of any nuclear–electron coupling, originating from electron–electron interaction. Thus, each peak in the PES has a unique fwd/bwd asymmetry (see Figures 6D–F) leading to the overall photoelectron integrated asymmetry. The origin of the asymmetry for each peak is rooted in the different ionisation processes that lead to its population and are purely based on electron–electron interaction as reported in Fröbel et al. (2020) (see scheme in Figure 6C):  $n = 0$  is predominantly populated via direct ionisation of the weaker bound electron (right of the central nucleus), which is favourable in fwd direction since it does not have to pass the other electron.  $n = 2$  is the respective direct ionisation of the stronger bound electron (left of nucleus), which proceeds predominantly into bwd direction.  $n = 1$  is in a bwd direction dominated knock-up ionisation process with smaller parts as knock-down process in fwd direction. As for different (parametric)  $R$  values, a different number of ionic states is accessible, with each of them featuring this intrinsic preference in the emission direction of the photoelectron, this leads to the overall parametric  $R$ -dependent asymmetry behaviour shown in Figure 6B. These results have been obtained by frozen nucleus calculations using Eq. 16 to calculate the asymmetry, thus, showing that it is a purely electron–electron correlation driven inherent asymmetry. Its  $R$ -dependency can be easily understood: starting from  $R_{0,m}$ , the asymmetry rises for more negative  $R$  positions since the bwd-dominated  $n = 2$  state becomes energetically inaccessible (Eq. 27). Equally, the overall asymmetry rises for larger  $R$  as the fwd/bwd neutral  $n = 3$  state becomes energetically accessible. For a nuclear wave packet rather than a point-like  $R$ -value (see Figure 1) these two effects are smeared.

#### 3.4.2 Nuclear–Electron Correlation Imprint

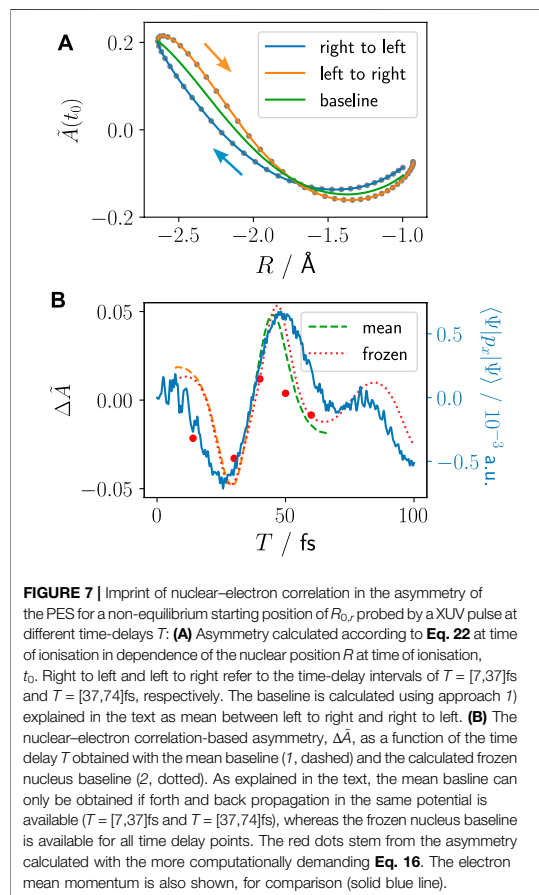
The procedure to visualise the imprint of pre-ionisation nuclear–electron correlation dynamics on the photoelectron is the following: we start at  $R_{0,r}$  and probe the integrated asymmetry by scanning the time delay of the XUV pulse interaction from  $T = [7, 100] \text{ fs}$  in 1 fs interval steps. We start the integrated asymmetry calculation earliest at 7 fs to ensure sufficient time for the 5 fs broad XUV pulse.  $R_{0,r}$  was chosen as a starting point since the nuclear dynamics are constricted to the left potential well exhibiting a more distinct dynamics with larger imprinted momenta (see Figure 2). During the propagation, the nuclear



wave packet propagates on the  $2e$  electronic ground state PEC from the inner turning point  $R_{0,r}$  (right) to the outer turning point  $R_{0,l}$  (left) and back to  $R_{0,r}$ , corresponding to the time-delay intervals of  $T = [7, 37]$ fs and  $T = [37, 74]$ fs, respectively (see Figures 1, 2). To save computational cost, we calculate the asymmetry from the bound/continuum wave function using Eq. 22, since it allows us to obtain converged asymmetries with fewer time steps and compare with some selected calculations using Eq. 16 that require propagation for long times. As is seen in Figure 6B, due to the changing resonance conditions, the inherent electron–electron correlation-based asymmetry varies for different parametric nuclear positions. The nuclear–electron correlation-based asymmetry is, thus, imprinted on top of the inherent electron–electron correlation-based asymmetry. Consequently, to extract the nuclear–electron correlation-based asymmetry, a “baseline” of the electron–electron correlation-based asymmetry during the nuclear propagation is required. This is carried out here in two approaches whose merits and shortcomings will

discuss shortly: 1) a mean baseline is obtained from relating the asymmetry from forth and back movement of the nucleus (right to left vs left to right, Figure 7A). 2) A baseline is calculated for each interval step using frozen nuclear wave packet calculations with the nucleus set to its position at the time of ionisation. Approach 1) resembles more an experimental setup where a nuclear wave packet could be propagated forth and back in a potential, whereas a baseline from frozen nucleus calculations (approach 2) cannot be obtained in the experimental setup, however, is not restricted to a forth and back movement of the nucleus in the same potential.

Figure 7A shows how the nuclear–electron correlation-based asymmetry is imprinted on top of the purely electron–electron correlation-based inherent asymmetry baseline that shows the same behaviour as shown in Figure 6B. The right to left (blue) and left to right (orange) curves are obtained by relating the corresponding time intervals  $T = [7, 37]$ fs and  $T = [37, 74]$ fs to the  $R$  value at the time of ionisation. In Figure 7B, the difference of the asymmetry to the two baselines 1) mean (dashed) and 2) frozen (dotted) is shown with



respect to the time-delay  $T$ . Comparison with the electron density's momentum in the 2e bound system (solid blue line) shows very good agreement.

This means that starting the nucleus in a non-equilibrium position, which experimentally could be realised, e.g., by a first pump pulse, leads to coupled nuclear–electron bound dynamics that are imprinted on the electron density's momentum. That, in turn, is imprinted on the photoelectron spectrum. Thus, we have demonstrated here that imprints of both, nuclear–electron and electron–electron correlated dynamics, are visible in the photoelectron spectra and the asymmetry of the photoelectron emission direction. We have generalised previous work and analysis on single-electron systems for the here investigated correlated system involving two electrons.

#### 4 SUMMARY

We set out to answer questions of particle correlation in molecular XUV ionisation and shed light on how these effects manifest in observables. To this end, we have

employed a fully correlated molecular quantum model system comprised of two active electrons and one active nucleus that mimics a generic molecular system and allows us to report qualitative effects.

First, we examine what a coupled electronic–nuclear motion looks like in the bound system and showed the adiabatic imprint of the nuclear motion on the electronic momentum. Next, we focused on the implication of these coupled dynamics on the molecular XUV ionisation process, in particular to answer the question regarding characteristics in the attosecond population dynamics and post-ionisation dynamics. We report that the nuclear momentum is conserved during the XUV ionisation from the target to the parent ion and impacts the post-ionisation dynamics. On the other hand, the attosecond electron population dynamics are largely unaffected by the coupled nuclear–electron dynamics in the bound system. Finally, we turned towards features appearing in the photoelectron spectra and their relation to electron–electron and electron–nuclear correlation. The results drastically show how all particles are strongly correlated and imprint each other's properties. Each photoelectron peak has an inherent asymmetry rooted in its electron–electron correlation-based ionisation pathways with its bound counterpart. The underlying complex bound/continuum resonances change when the nucleus is displaced leading to a change in electron–electron correlation-based photoelectron properties. On top of this, the initial coupled nuclear–electron momentum in the bound system is imprinted on the entangled photoelectron via its spectrum's asymmetry and could be used as an experimental observable. While we have seen that correlation impacts pre, during, and post ionisation in various ways, well-designed approximations can be introduced at different stages depending on the intended outcome of the simulation. For example, the attosecond population dynamics are only influenced by a deformation of the nuclear wave packet pre-ionisation, which is not based on nuclear–electron correlation and can be reproduced by a sampling approach to the nuclear wave packet. In the case of harmonic PECs yielding a compact Gaussian-like nuclear wave packet, the nuclear degree of freedom can be safely ignored and a purely electronic description of the system with single-point nuclei reproduces the correct electronic parent ion wave packet population. Moreover, the momentum conservation in the nuclei between target and parent ion can be incorporated into classical approximations. Combining these ideas will be the subject of future research. The photoelectron asymmetries are purely based on the correlation effects of all particles and, thus, can only be observed when treating all particles quantum dynamically and with the corresponding exact correlation. However, approximated methods could be used to calculate the effect that is imprinted in the photoelectron asymmetry rather than the full correlated XUV ionisation process. For example, approximate theories can calculate the change in continuum resonances that lead to a change in the electron–electron correlation-based asymmetry, or the nuclear dynamics in the bound state that are imprinted on the spectrum via nuclear–electron correlation.

We are confident that our findings not only widen our understanding of fundamental correlation-driven processes in XUV ionisation but will also guide future experiments and approximated theory towards which effects have to be taken into account to properly describe correlation in molecular ionisation.

## DATA AVAILABILITY STATEMENT

The raw data supporting the conclusion of this article will be made available by the authors, without undue reservation.

## AUTHOR CONTRIBUTIONS

KMZ and JB performed simulations and data analysis. KMZ and SG conceived and designed the study. VE and SG supervised the

research. All authors discussed the research and contributed to manuscript revision, read, and approved the submitted version.

## FUNDING

KMZ and SG are part of the Max Planck School of Photonics supported by BMBF, Max Planck Society, and Fraunhofer Society. JB would like to acknowledge generous funding by the “Honours Programme for Future Researchers” of the Friedrich-Schiller-Universität Jena. SG acknowledges the ERC Consolidator Grant QUEM-CHEM (grant number 772676).

## ACKNOWLEDGMENTS

All calculations have been performed at the Universitätsrechenzentrum of the Friedrich Schiller University Jena.

## REFERENCES

- Albert, J., Falge, M., Gomez, S., Sola, I. R., Hildenbrand, H., and Engel, V. (2015). Communication: Vibrational and Vibronic Coherences in the Two Dimensional Spectroscopy of Coupled Electron-Nuclear Motion. *J. Chem. Phys.* 143, 041102. doi:10.1063/1.4927396
- Albert, J., Hader, K., and Engel, V. (2017). Coupled Electron-Nuclear Quantum Dynamics through and Around a Conical Intersection. *J. Chem. Phys.* 147, 064302. doi:10.1063/1.4989780
- Ayuso, D., Palacios, A., Decleva, P., and Martin, F. (2017). Ultrafast Charge Dynamics in glycine Induced by Attosecond Pulses. *Phys. Chem. Chem. Phys.* 19, 19767–19776. doi:10.1039/C7CP01856H
- Blum, K. (2012). *Density Matrix Theory and Applications*. third edn. Heidelberg: Springer.
- Corkum, P. B., and Krausz, F. (2007). Attosecond Science. *Nat. Phys.* 3, 381–387. doi:10.1038/nphys620
- Erdmann, M., Gross, E. K. U., and Engel, V. (2004). Time-dependent Electron Localization Functions for Coupled Nuclear-Electronic Motion. *J. Chem. Phys.* 121, 9666–9670. doi:10.1063/1.1806812
- Falge, M., Engel, V., and Gräfe, S. (2012a). Fingerprints of Adiabatic versus Diabatic Vibronic Dynamics in the Asymmetry of Photoelectron Momentum Distributions. *J. Phys. Chem. Lett.* 3, 2617–2620. doi:10.1021/jz3009826
- Falge, M., Engel, V., and Gräfe, S. (2011). Time-resolved Photoelectron Spectroscopy of Coupled Electron-Nuclear Motion. *J. Chem. Phys.* 134, 184307. doi:10.1063/1.3585692
- Falge, M., Engel, V., Lein, M., Vindel-Zandbergen, P., Chang, B. Y., and Sola, I. R. (2012b). Quantum Wave-Packet Dynamics in Spin-Coupled Vibronic States. *J. Phys. Chem. A* 116, 11427–11433. doi:10.1021/jp306566x
- Falge, M., Fröbel, F. G., Engel, V., and Gräfe, S. (2017). Time-resolved Photoelectron Spectroscopy of IR-Driven Electron Dynamics in a Charge Transfer Model System. *Phys. Chem. Chem. Phys.* 19, 19683–19690. doi:10.1039/C7CP01832K
- Feit, M. D., Fleck, J. A., and Steiger, A. (1982). Solution of the Schrödinger Equation by a Spectral Method. *J. Comput. Phys.* 47, 412–433. doi:10.1016/0021-9991(82)90091-2
- Frigo, M., and Johnson, S. (1998). “FFTW: An Adaptive Software Architecture for the FFT,” in *Proceedings of the 1998 IEEE International Conference on Acoustics, Speech and Signal Processing, ICASSP '98 (Cat. No.98CH36181)* (Seattle, WA, USA: IEEE), Vol. 3, 1381–1384. doi:10.1109/ICASSP.1998.681704
- Fröbel, F. G., Ziems, K. M., Peschel, U., Gräfe, S., and Schubert, A. (2020). The Impact of Electron-Electron Correlation in Ultrafast Attosecond Single Ionization Dynamics. *J. Phys. B At. Mol. Opt. Phys.* 53, 144005. doi:10.1088/1361-6455/ab8c21
- Hader, K., Albert, J., Gross, E. K. U., and Engel, V. (2017). Electron-nuclear Wave-Packet Dynamics through a Conical Intersection. *J. Chem. Phys.* 146, 074304. doi:10.1063/1.4975811
- Heather, R., and Metiu, H. (1987). An Efficient Procedure for Calculating the Evolution of the Wave Function by Fast Fourier Transform Methods for Systems with Spatially Extended Wave Function and Localized Potential. *J. Chem. Phys.* 86, 5009–5017. doi:10.1063/1.452672
- Horodecki, R., Horodecki, P., Horodecki, M., and Horodecki, K. (2009). Quantum Entanglement. *Rev. Mod. Phys.* 81, 865–942. doi:10.1103/RevModPhys.81.865
- Joachain, C. J., Kylstra, N. J., and Potvliege, R. M. (2012). *Atoms in Intense Laser Fields*. Cambridge: Cambridge University Press.
- Kosloff, R., and Tal-Ezer, H. (1986). A Direct Relaxation Method for Calculating Eigenfunctions and Eigenvalues of the Schrödinger Equation on a Grid. *Chem. Phys. Lett.* 127, 223–230. doi:10.1016/0009-2614(86)80262-7
- Krausz, F., and Ivanov, M. (2009). Attosecond Physics. *Rev. Mod. Phys.* 81, 163–234. doi:10.1103/revmodphys.81.163
- Kutzelnigg, W. (1994). *Einführung in die Theoretische Chemie, Band 2*. Weinheim: VCH.
- Lein, M., Gross, E., Kreibich, T., and Engel, V. (2002). Strong-Field Ionization Dynamics of a Model H<sub>2</sub> Molecule. *Phys. Rev. A* 65, 033403. doi:10.1103/physreva.65.033403
- [Dataset] Nielson, M. A., and Chuang, I. L. (2000). *Quantum Computation and Quantum Information*.
- Nisoli, M., Decleva, P., Calegari, F., Palacios, A., and Martin, F. (2017). Attosecond Electron Dynamics in Molecules. *Chem. Rev.* 117, 10760–10825. doi:10.1021/acs.chemrev.6b00453
- Pukhov, A. (2002). Strong Field Interaction of Laser Radiation. *Rep. Prog. Phys.* 66, 47–101. doi:10.1088/0034-4885/66/1/202
- Schaupp, T., and Engel, V. (2019a). A Classical Ride through a Conical Intersection. *J. Chem. Phys.* 150, 034301. doi:10.1063/1.5080399
- Schaupp, T., and Engel, V. (2022). Correlated Three-Dimensional Electron-Nuclear Motion: Adiabatic Dynamics vs Passage of Conical Intersections. *J. Chem. Phys.* 156, 074302. doi:10.1063/5.0082597
- Schaupp, T., and Engel, V. (2019b). Electronic and Nuclear Flux Dynamics at a Conical Intersection. *J. Chem. Phys.* 151, 084309. doi:10.1063/1.5111922
- Shin, S., and Metiu, H. (1996). Multiple Time Scale Quantum Wavepacket Propagation: Electron–Nuclear Dynamics. *J. Phys. Chem.* 100, 7867–7872. doi:10.1021/jp952498a
- Shin, S., and Metiu, H. (1995). Nonadiabatic Effects on the Charge Transfer Rate Constant: A Numerical Study of a Simple Model System. *J. Chem. Phys.* 102, 9285–9295. doi:10.1063/1.468795
- Sukiasyan, S., Ishikawa, K. L., and Ivanov, M. (2012). Attosecond Cascades and Time Delays in One-Electron Photoionization. *Phys. Rev. A* 86, 033423. doi:10.1103/physreva.86.033423
- Vacher, M., Bearpark, M. J., Robb, M. A., and Malhado, J. P. (2017). Electron Dynamics upon Ionization of Polyatomic Molecules: Coupling to Quantum

- Nuclear Motion and Decoherence. *Phys. Rev. Lett.* 118, 083001. doi:10.1103/PhysRevLett.118.083001
- Vacher, M., Steinberg, L., Jenkins, A. J., Bearpark, M. J., and Robb, M. A. (2015). Electron Dynamics Following Photoionization: Decoherence Due to the Nuclear-Wave-Packet Width. *Phys. Rev. A* 92, 040502. doi:10.1103/physreva.92.040502
- Wolter, B., Pullen, M. G., Baudisch, M., Sclafani, M., Hemmer, M., Senfleben, A., et al. (2015). Strong-Field Physics with Mid-ir Fields. *Phys. Rev. X* 5, 021034. doi:10.1103/physrevx.5.021034

**Conflict of Interest:** The authors declare that the research was conducted in the absence of any commercial or financial relationships that could be construed as a potential conflict of interest.

**Publisher's Note:** All claims expressed in this article are solely those of the authors and do not necessarily represent those of their affiliated organizations, or those of the publisher, the editors, and the reviewers. Any product that may be evaluated in this article, or claim that may be made by its manufacturer, is not guaranteed or endorsed by the publisher.

Copyright © 2022 Ziems, Bruhnke, Engel and Gräfe. This is an open-access article distributed under the terms of the Creative Commons Attribution License (CC BY). The use, distribution or reproduction in other forums is permitted, provided the original author(s) and the copyright owner(s) are credited and that the original publication in this journal is cited, in accordance with accepted academic practice. No use, distribution or reproduction is permitted which does not comply with these terms.

## OPEN ACCESS

IOP Publishing

Journal of Physics B: Atomic, Molecular and Optical Physics

J. Phys. B: At. Mol. Opt. Phys. **56** (2023) 105602 (15pp)<https://doi.org/10.1088/1361-6455/acc4fa>

# Attosecond ionization dynamics of modulated, few-cycle XUV pulses

Karl Michael Ziems<sup>1,2,\*</sup> , Matthias Wollenhaupt<sup>3</sup> , Stefanie Gräfe<sup>1,2,4,5</sup>   
and Alexander Schubert<sup>1,6</sup> 

<sup>1</sup> Institute of Physical Chemistry, Friedrich Schiller University, Jena 07743, Germany

<sup>2</sup> Max Planck School of Photonics, Jena 07743, Germany

<sup>3</sup> Institute for Physics, Carl von Ossietzky University Oldenburg, Oldenburg 26129, Germany

<sup>4</sup> Abbe Center of Photonics, Friedrich Schiller University, Jena 07743, Germany

<sup>5</sup> Fraunhofer Institute for Applied Optics and Precision Engineering, Jena 07745, Germany

E-mail: [karl-michael.ziems@uni-jena.de](mailto:karl-michael.ziems@uni-jena.de)

Received 18 December 2022, revised 10 March 2023

Accepted for publication 16 March 2023

Published 14 April 2023



CrossMark

## Abstract

Few-cycle, attosecond extreme ultraviolet (XUV) pulses in the strong field regime are becoming experimentally feasible, prompting theoretical investigating of the ionization dynamics induced by such pulses. Here, we provide a systematic study of the atomic ionization dynamics beyond the regime of the slowly varying envelope approximation. We discuss the properties of such XUV pulses and report on temporal and spectral modulations unique to the attosecond nature of the pulse. By employing different levels of theory, namely the numerical solution to the time-dependent Schrödinger equation, perturbation theory and a semi-analytical approach, we investigate the ionization of atoms by modulated, few-cycle XUV pulses and distinguish first and higher order effects. In particular, we study attosecond ionization in different intensity regimes aided by a general wave function splitting algorithm. Our results show that polarization and interference effects in the continuum prominently drive ionization in the few-cycle regime and report on carrier-envelope phase (CEP)- and intensity-dependent asymmetries in the photoelectron spectra. The use of spectrally modulated attosecond pulses allows us to distinguish between temporal effects causing asymmetries and dynamic interference, and spectral effects inducing a redshift of the photoelectron spectrum.

Keywords: ultrafast phenomena, ultrashort pulses, modulated pulses, single- and few-photon ionization & excitation

(Some figures may appear in colour only in the online journal)

<sup>6</sup> Present address: Merck Electronics KGaA, Frankfurter Straße 250, 64293 Darmstadt, Germany.

\* Author to whom any correspondence should be addressed.



Original Content from this work may be used under the terms of the [Creative Commons Attribution 4.0 licence](https://creativecommons.org/licenses/by/4.0/). Any further distribution of this work must maintain attribution to the author(s) and the title of the work, journal citation and DOI.



## 1. Introduction

The attosecond timescale (1 as =  $10^{-18}$  s) is the natural time scale of electronic motion, and its study motivates the large current interest in attosecond science [1, 2]. While in the beginning, the research focus of femtosecond dynamics was on the infrared regime, in recent years, research has been extended to the high frequency regime [1–3]. Due to the advances in light-source technology, such as free-electron lasers [4] and high-harmonic generation [5], short light pulses in the extreme ultraviolet (XUV) down to the soft x-ray are nowadays accessible not only in large facilities but also in table-top research labs [5–8]. XUV pulses of a few 100 as down to 50 as have been demonstrated [9]. Moreover, few-cycle XUV attosecond pulses with stable carrier–envelope phase (CEP) have been realized [10–12] and great effort is put into increasing the intensity of attosecond pulses [13, 14].

These extremely short XUV pulses have been used to investigate light–matter interaction down to the attosecond time scale to probe, e.g. ultrafast electron dynamics and charge migration [3, 15–19]. Commonly, single ionization by XUV wave length is well described within linear response by single-photon interaction. Therefore, for moderate and weak intensities, the impact of pulse shape and/or spectral phase variations on the ionization dynamics is negligible. This does not apply to higher intensities, when CEP- and other phase-modulations of the spectrally extremely broadband pulses are involved, as has been shown by several theoretical works. Firstly, in the area of double photoionization of the helium atom, an asymmetric photoelectron angular distribution has been reported that can be controlled by the CEP of the pulse [20–24]. Secondly, approaches to extend holographic mapping into the XUV regime using two-cycle pulses have been theoretically proposed [25–27]. Thirdly, molecular attosecond photoionization with few-cycle XUV pulses has been studied and, with the help of perturbative models, the redshift in the photoelectron spectra was rationalized [28].

In this work, we theoretically investigate the interaction of moderately to intense broadband XUV pulses with an atom. We emphasize that the common description of spectral phase modulation including chirping for femtosecond pulses with wavelengths in the visible spectral range, need to be adapted to account for the very broad spectral range of the attosecond XUV pulses as we will show below. We present atomic calculations on different levels of theory, specifically numerically exact solutions to the time-dependent Schrödinger equation (TDSE), perturbation theory (PT), and analytical approaches. We examine spectral shifts in the photoelectron spectra, analyze the interaction with spectrally modulated attosecond XUV pulses, distinguish temporal and spectral effects, and reveal a CEP-dependent asymmetry for intense few-cycle XUV pulses. The latter is related to constructive and destructive interference during the ionization process and strongly dependent on the light intensity. The results are analyzed by using a wave function splitting algorithm that allows a unique view on the ionization processes. We demonstrate its capabilities on the example of few-cycle effects in XUV ionization.

The paper is organized as follows: In the theory section, the properties of ultrashort XUV pulses and the employed model system are introduced. Special emphasis is put on temporal and spectral modulations in the few-cycle XUV regime. Furthermore, the different levels of theory are presented. Lastly, in section 3 the numerical results of the model system are discussed, with an emphasis on intense spectrally and CEP-modulated pulses. Finally, we summarize and conclude our findings. In the appendix, we present simulations on the 3D hydrogen atom and explain our wave function splitting algorithm in detail.

## 2. Theory

### 2.1. Properties of Ultrashort XUV Pulses

The electric field of a XUV pulse is described via its time-dependent vector potential:

$$\mathcal{A}(t) = \frac{\mathcal{E}_0}{\omega_0} e^{-\beta t^2} \sin(\omega_0 t + \phi_{\text{CEP}}) \quad (1a)$$

$$= \frac{\mathcal{E}_0}{2i\omega_0} e^{-\beta t^2} \left\{ e^{i(\omega_0 t + \phi_{\text{CEP}})} - e^{-i(\omega_0 t + \phi_{\text{CEP}})} \right\}, \quad (1b)$$

where  $\mathcal{E}_0$  is the electric field strength,  $\omega_0$  is the field's carrier angular frequency,  $\phi_{\text{CEP}}$  is the CEP, and  $\beta = 4 \ln(2) \tau^{-2}$  is the coefficient of the Gaussian envelope function, with  $\tau$  being the full width at half maximum (FWHM) pulse duration. This corresponds to the electric field

$$\mathcal{E}(t) = -\frac{d\mathcal{A}(t)}{dt} \quad (2a)$$

$$= -\mathcal{E}_0 e^{-\beta t^2} \left[ -\frac{2\beta}{\omega_0} t \sin(\omega_0 t + \phi_{\text{CEP}}) + \cos(\omega_0 t + \phi_{\text{CEP}}) \right]. \quad (2b)$$

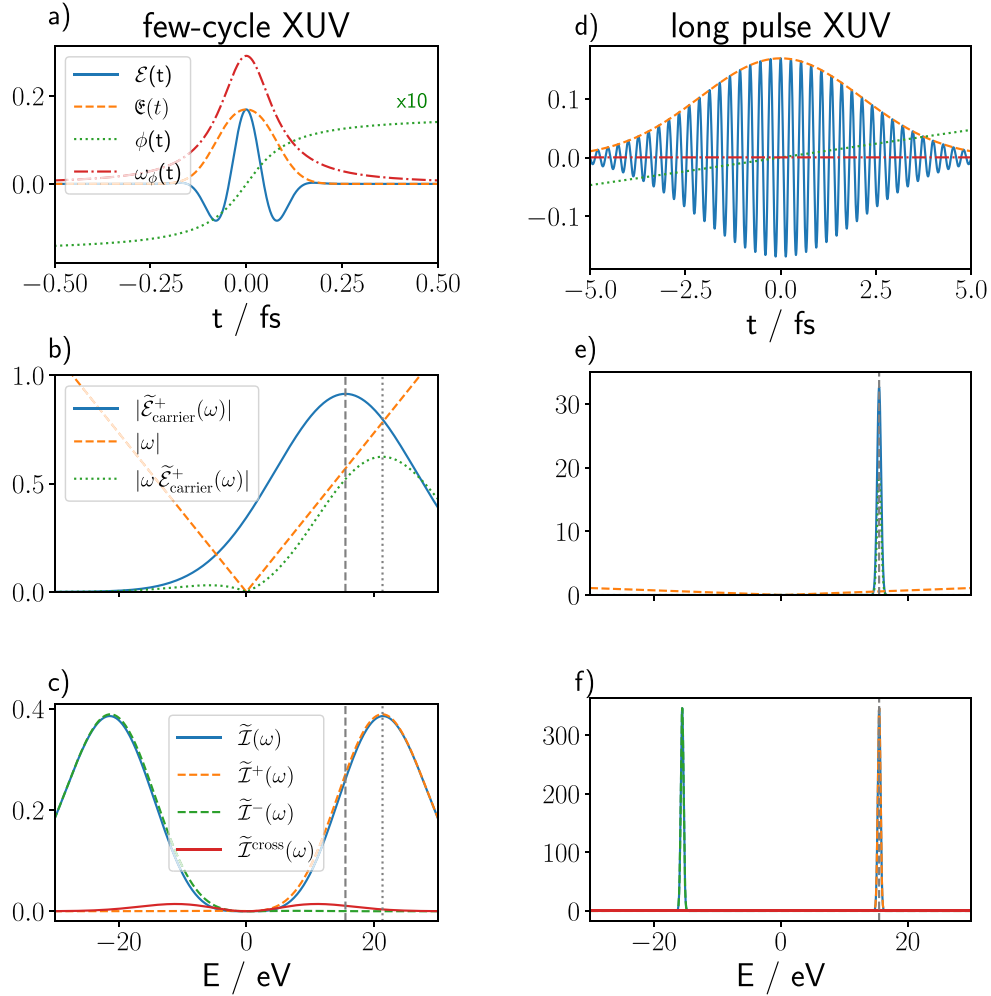
For comparatively long pulses with many optical cycles, the slowly varying envelope approximation (SVEA) is commonly assumed [29] and the first term in equation (2b) is negligible. However, for ultrashort, few-cycle pulses, the SVEA is generally not valid. The influence of the first term on the spectral properties of the pulse becomes clear by considering the following form:

$$\mathcal{E}(t) = -\mathcal{E}_0 e^{-\beta t^2} \left( \frac{4\beta^2 t^2}{\omega_0^2} + 1 \right)^{\frac{1}{2}} \times \cos \left( \omega_0 t + \phi_{\text{CEP}} + \arctan \left( \frac{2\beta}{\omega_0} t \right) \right) \quad (3)$$

$$= \mathcal{E}(t) \cos(\omega_0 t + \phi_{\text{CEP}} + \phi(t)) \quad (4)$$

and is shown in figure 1 for a ultrashort, attosecond few-cycle XUV pulse (a), compared to a femtosecond XUV pulse (d). For ultrashort, few-cycle pulses (a), the rapidly varying envelope defines the pulses's spectral properties. The





**Figure 1.** Ultrashort, few-cycle XUV pulse with  $\tau = 140$  as (left: a,b,c) and long XUV pulse with  $\tau = 5$  fs (right: d,e,f) in temporal (first row: a,d) and spectral representation (second/third row: b,c,e,f). The different terms are explained in the text. The grey dashed line in panel b,c,e,f is the carrier frequency,  $\omega_0$ . The grey dotted line in b and c is the central frequency of the electric field,  $\tilde{\omega}_0$ , showing the blue shift for ultrashort pulses outside the SVEA. The laser parameters are:  $\mathcal{E}_0 = -0.169$  a.u.,  $\omega_0 = 0.570$  a.u. (15.5 eV),  $\phi_2 = 0$  (unchirped).

contribution in front of the cosine term defines the envelope of the electric field as  $\mathcal{E}(t) = -\mathcal{E}_0 e^{-\beta t^2} \left( \frac{A\beta^2 t^2}{\omega_0^2} + 1 \right)^{\frac{1}{2}}$  (dashed line). More importantly, the time-dependent phase  $\phi(t) = \arctan\left(\frac{2\beta t}{\omega_0}\right)$  (dotted line) introduces an additional time-dependent envelope-induced frequency,  $\omega_\phi(t) = \frac{d}{dt}\phi(t)$  (dashed-dotted line) and shifts the instantaneous frequency of the pulse as  $\tilde{\omega}_0(t) = \omega_0 + \omega_\phi(t)$ . At the maximum envelope intensity at  $t=0$ , this results in a frequency of  $\tilde{\omega}_0(t=0) = \omega_0 + 2\beta\omega_0^{-1}$ , giving rise to a blueshift with respect to the carrier frequency,  $\omega_0$  [30, 31]. This blueshift is inversely proportional to the pulse length squared. Thus, it becomes particularly pronounced for attosecond pulses as used in the high

frequency regime. In figure 1, for  $\omega_0 = 15.5$  eV and a pulse length  $\tau = 140$  as, the shift accounts for 5.8 eV. For long pulses (d), where the SVEA is applicable, the time-dependent phase  $\phi(t)$  (dotted line) and its gradient are negligible compared to ultrashort, few-cycle pulses. Therefore, there is no envelope-induced frequency (dashed-dotted line).

The spectral representation of the electric field is obtained via the (forward) Fourier transform (FT),  $\tilde{\mathcal{E}}(\omega) = FT\{\mathcal{E}(t)\}$ . Alternatively, starting from the Euler decomposition of the vector field in equation (1b), we can write

$$\tilde{\mathcal{A}}(\omega) = \frac{\tilde{\mathcal{E}}_0}{i\omega_0} \left\{ e^{-\beta\omega(\omega-\omega_0)^2 + i\phi_{CE}} - e^{-\beta\omega(\omega+\omega_0)^2 - i\phi_{CE}} \right\}. \quad (5)$$

Making use of the  $FT$  properties, the (negative) derivative in time corresponds to a multiplication by  $-i\omega$  in spectral representation to obtain equation (6) using the identities  $\beta_\omega = (4\beta)^{-1}$  and  $\tilde{\mathcal{E}}_0 = \mathcal{E}_0\sqrt{\beta_\omega/2}$ ,

$$\tilde{\mathcal{E}}(\omega) = -\tilde{\mathcal{E}}_0 \frac{\omega}{\omega_0} \left\{ e^{-\beta_\omega(\omega-\omega_0)^2 + i\phi_{\text{CE}}} - e^{-\beta_\omega(\omega+\omega_0)^2 - i\phi_{\text{CE}}} \right\}. \quad (6)$$

The linear factor in  $\omega$ , which arises from the temporal derivative of the vector potential envelope function in equation (1a), guarantees a vanishing DC component,  $\tilde{\mathcal{E}}(0) = 0$ , which is necessary to obtain a propagating pulse [32–34]. The linear frequency factor,  $\omega$ , in the spectral representation (equation (6)) is another way to account for the effects of the envelope in ultrashort pulses, resulting in a blueshift of the central frequency,  $\tilde{\omega}_0$ , by scaling the analytical spectrum  $\tilde{\mathcal{E}}_{\text{carrier}}^\pm(\omega) = \frac{-\tilde{\mathcal{E}}_0}{\omega_0} e^{-\beta_\omega(\omega \mp \omega_0)^2 \pm i\phi_{\text{CE}}}$  associated with the carrier frequency,  $\omega_0$ . Due to the ultrashort pulse duration, the positive and negative frequency components overlap at low energies. In figures 1(b) and (e), the two spectra, plotted for positive frequencies, are contrasted. The vertical dotted line indicates the blueshift of the central frequency,  $\tilde{\omega}_0$ , from the carrier frequency,  $\omega_0$ , (dashed line). Note that although the spectral phase is flat, there is a non-vanishing temporal phase,  $\phi(t)$ , due to the asymmetry of the spectrum.

In the following, we disentangle properties of the photoelectron spectra caused by the spectral width from temporal effects, i.e. effects that are explained by the attosecond nature and not the broad spectral width. To this end, we investigate ionization from spectrally modulated pulses with quadratic spectral modulation [35]. We introduce a quadratic spectral phase,  $\phi_2$ , in the frequency domain:

$$\tilde{\mathcal{E}}_c(\omega) = -\tilde{\mathcal{E}}_0 \frac{\omega}{\omega_0} \left\{ e^{-\beta_\omega(\omega-\omega_0)^2 + i\phi_{\text{CE}} - i\frac{\phi_2}{2}(\omega-\omega_0)^2} - e^{-\beta_\omega(\omega+\omega_0)^2 - i\phi_{\text{CE}} + i\frac{\phi_2}{2}(\omega+\omega_0)^2} \right\}. \quad (7)$$

The quadratic phase  $\phi_2$  causes a linear chirp in time domain and significantly elongates the pulse duration:

$$\begin{aligned} \mathcal{E}_c(t) &= FT^{-1} \{ \tilde{\mathcal{E}}_c(\omega) \} \\ &= -\frac{\tilde{\mathcal{E}}_0}{\sqrt{8}\omega_0} \left( \frac{2 \left[ \beta_\omega + i\frac{\phi_2}{2} \right] \omega_0 + it}{\left[ \beta_\omega + i\frac{\phi_2}{2} \right]^{3/2}} e^{-\beta_c t^2 + i(\omega_0 + 2\phi_2\beta_c\beta t)t + i\phi_{\text{CE}}} \right. \\ &\quad \left. + \text{c.c.} \right), \end{aligned} \quad (8)$$

where c.c. denotes the complex conjugate of the previous term, and  $\beta_c = \beta/(1 + 4\phi_2^2\beta^2)$  defines the temporal profile with a FWHM of  $\tau_c = \sqrt{4\ln 2/\beta_c}$ . Figures 2(a) and (c) display an example of a spectrally modulated few-cycle and long XUV pulse. The spectral intensity profile (power spectral density) of the unchirped ( $\phi_2 = 0$ ) and spectrally modulated pulses reads:

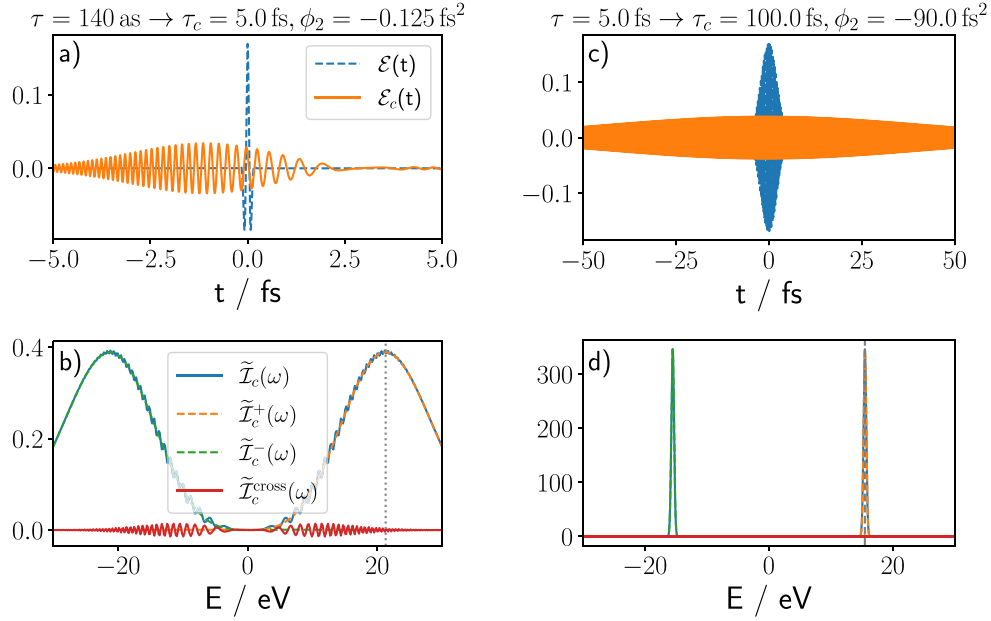
$$\begin{aligned} \tilde{\mathcal{I}}(\omega) &\propto \left| \tilde{\mathcal{E}}_c(\omega) \right|^2 \\ &= \tilde{\mathcal{E}}_0^2 \frac{\omega^2}{\omega_0^2} \left\{ e^{-2\beta_\omega(\omega-\omega_0)^2} + e^{-2\beta_\omega(\omega+\omega_0)^2} - 2e^{-2\beta_\omega(\omega^2+\omega_0^2)} \right. \\ &\quad \left. \times \cos[\phi_2(\omega^2 + \omega_0^2) - 2\phi_{\text{CE}}] \right\} \end{aligned} \quad (9)$$

and consists of three terms: the term with positive and the term with negative frequency contributions,  $\tilde{\mathcal{I}}^+(\omega) = \tilde{\mathcal{E}}_0^2 \frac{\omega^2}{\omega_0^2} e^{-2\beta_\omega(\omega-\omega_0)^2}$  and  $\tilde{\mathcal{I}}^-(\omega) = \tilde{\mathcal{E}}_0^2 \frac{\omega^2}{\omega_0^2} e^{-2\beta_\omega(\omega+\omega_0)^2}$  (dashed orange and green lines), respectively, as well as the cosine cross term  $\tilde{\mathcal{I}}^{\text{cross}}(\omega) = -\tilde{\mathcal{E}}_0^2 \frac{\omega^2}{\omega_0^2} 2e^{-2\beta_\omega(\omega^2+\omega_0^2)} \cos[\phi_2(\omega^2 + \omega_0^2) - 2\phi_{\text{CE}}]$  (solid red line). All three terms include a scaling by the frequency,  $\omega^2$ , that ensures  $\tilde{\mathcal{I}}(0) = 0$ , as seen in equation (6). Spectrally modulated and unchirped pulses are shown in figures 2(b), (d) and 1(c), (f), respectively.

The spectral intensity profile of unchirped and spectrally modulated pulse are identical in width but differ in the cross term,  $\tilde{\mathcal{I}}^{\text{cross}}(\omega)$ . The latter depends (on the CEP and) on the quadratic phase  $\phi_2$  that introduces amplitude modulations in the cross term, which are imprinted on the overall profile,  $\tilde{\mathcal{I}}(\omega)$ . The amplitude modulated cross term is only relevant for attosecond pulses with a rapidly varying envelope, i.e. a broad spectral width (meaning a small value of  $\beta_\omega$ ). Another way of looking at this observation is this: The quadratic spectral phase,  $\phi_2$ , as introduced in equation (7), leads to different modulation of the positive and negative frequency components. For long XUV pulses, this solely results in a broadened temporal pulse with no effect on the spectral behaviour. However, for ultrashort XUV pulses, the positive and negative frequency components overlap (recall figure 1(b) dotted line). As a result, the spectra are amplitude modulated in the overlapping region giving rise to the cross term introduced above. Due to the amplitude modulations we refer to the spectrally modulated pulses as quasi-chirped.

For this study, we use an angular carrier frequency of  $\omega_0 = 0.570$  a.u. (15.5 eV) and different pulse intensities, represented by the electric field amplitudes  $\mathcal{E}_0 = 1.69 \times 10^{-2}$ ,  $1.69 \times 10^{-1}$ , and  $1.69$  a.u. (corresponding to intensities of  $I = 10^{13}$ ,  $10^{15}$ , and  $10^{17}$  W cm $^{-2}$ , respectively). If not stated otherwise, the intermediate value of  $\mathcal{E}_0 = 1.69 \times 10^{-1}$  a.u. is employed. Different FWHM pulse lengths  $\tau$  between 140 as and 10 fs, and different CEP values,  $\phi_{\text{CE}} \in \{-\frac{\pi}{2}, 0, \frac{\pi}{2}, \pi\}$ , are considered as well. We investigate unchirped,  $\phi_2 = 0$ , and quasi-chirped,  $\phi_2 = -0.125$  fs $^2$ , pulses as displayed in figures 1 and 2. For the latter, the quasi-chirped vector field based on equation (8) is used:

$$\mathcal{A}_c(t) = -\frac{\tilde{\mathcal{E}}_0}{\sqrt{2}\omega_0} \left( \frac{i}{\sqrt{\beta_\omega + i\frac{\phi_2}{2}}} e^{-\beta_c t^2 + i(\omega_0 + 2\phi_2\beta_c\beta t)t + i\phi_{\text{CE}}} + \text{c.c.} \right). \quad (10)$$



**Figure 2.** Ultrashort, few-cycle XUV pulse with  $\tau = 140$  as and a quadratic spectral modulation of  $\phi_2 = -0.125$  fs<sup>2</sup> resulting in a temporal elongation to  $\tau_c = 5.0$  fs (left: a,b). Long XUV pulse with  $\tau = 5$  fs and a quadratic spectral modulation of  $\phi_2 = -90.0$  fs<sup>2</sup> resulting in a temporal elongation to  $\tau_c = 100.0$  fs (right: d,e). The temporal (first row: a,c) and spectral representations (second row: b,c) are shown. The different terms are explained in the text.

The full time-dependent Hamiltonian within the dipole approximation and employing the velocity gauge reads:

$$\mathcal{H}(t) = \frac{1}{2} (p + \mathcal{A}(t))^2 + V(x), \quad (11)$$

where  $p$  is the electronic momentum.

We numerically solve the time-dependent Schrödinger equation

$$i \frac{\partial}{\partial t} |\Psi(t)\rangle = \mathcal{H}(t) |\Psi(t)\rangle \quad (12)$$

for atomic systems in 3D using QPROP 3.2 [36] and in 1D using a screened one-dimensional atomic model system with the potential [37–40]

$$V(x) = -\frac{\text{erf}(|x|/a)}{|x|}. \quad (13)$$

Here,  $x$  is the electron coordinate, erf denotes the error function and  $a = 2.83$  a.u. is the truncation parameter, which results in an ionization potential of 0.320 a.u. (8.72 eV). Using a model system allows us to draw qualitative conclusions and compare to a variety of theory to draw intuitive pictures of the processes. It also reduces computational costs and numerical difficulties for the spectrally modulated pulses that are extremely broad in both time and energy. Thus, the results in the main text are obtained using aforementioned model system. Additionally, we compare and validate our findings to numerical solutions

of the TDSE of the 3D hydrogen atom expanded in spherical harmonics in the appendix A.

Atomic units (a.u.) are used throughout the manuscript if not specified otherwise. In the following, the terminology forward (backward) for  $x > 0$  ( $x < 0$ ) is used, in particular, to describe photoelectron emission directions and their asymmetries.

## 2.2. Level of theory

To disentangle first and higher-order effects, and to identify specific quantum effects, such as interference and transient processes, different levels of theory are applied. In the following, the direct numerical solution of the TDSE will be contrasted against a first-order PT and a semi-analytical approach based on PT and continuum plane waves (PTPW).

**2.2.1. Numerical details.** The time-dependent wave function  $|\Psi(t)\rangle$  is represented on a spatial grid of  $[-907, 907]$  a.u. with 2048 grid points. The direct propagation is carried out numerically employing the short-time propagator with a time step size of  $\Delta t = 1$  as by the symmetric split operator technique [41] in coordinate and momentum space and using the FFTW3 library [42] for Fourier transform. Time propagation starts at  $t_0 = -5\tau$ , if not indicated otherwise. Bound electronic eigenstates  $\{|\varphi_n\rangle\}$  are obtained via the relaxation method [43] with the time-independent, field-free Hamiltonian

$$\mathcal{H}_0 = V(x) + \frac{p^2}{2} \quad (14)$$

yielding 37 bound states  $\{|\varphi_n\rangle\}$ ,  $n \in \{0, \dots, 36\}$ , with negative eigenenergy  $E_n < 0$ . The electronic ground state is used as initial wave function,  $|\Psi(t_0)\rangle = |\varphi_0\rangle$ , in all propagation schemes.

To suppress reflection at the grid boundaries in forward (fwd) and backward (bwd) direction during propagation, cut-off functions are used in the asymptotic region of the atomic potential [44]

$$f_{\text{fwd}}(x) = [1 + e^{\zeta_1(x-\zeta_2)}]^{-1} \quad (15a)$$

$$f_{\text{bwd}}(x) = [1 + e^{\zeta_1(-x-\zeta_2)}]^{-1} \quad (15b)$$

with parameters  $\zeta_1 = 0.025$  a.u. and  $\zeta_2 = 983$  a.u. Parts of the wavefunction that reach the cut-off region,  $(1 - f_\nu(x))\langle x|\Psi(t)\rangle$ ,  $\nu \in \{\text{fwd}, \text{bwd}\}$ , are removed from  $|\Psi(t)\rangle$ , transformed into momentum space, and coherently added to  $\langle p|\tilde{\Psi}_{\text{out},\nu}(t)\rangle = \tilde{\Psi}_{\text{out},\nu}(p,t)$  over time, which yields the photoelectron spectrum (PES) at the end of the propagation [44]:

$$\tilde{\sigma}_\nu^{\text{TDSE}}(p) = \lim_{t \rightarrow \infty} \left| \tilde{\Psi}_{\text{out},\nu}(p,t) \right|^2, \quad (16)$$

where only components in the direction of emission, i.e.  $p > 0$  ( $p < 0$ ) for  $\nu = \text{fwd}$  ( $\text{bwd}$ ), are considered. In our calculations,  $t \rightarrow \infty$  is set to  $t = 500$  fs.

**2.2.2. First-order PT.** Within first-order PT, the time-dependent wavefunction reads:

$$|\Psi^{\text{PT}(1)}(t)\rangle = -i \int_{t_0}^t dt' e^{-i\mathcal{H}_0(t-t')} W(t') e^{-iE_0(t'-t_0)} |\varphi_0\rangle, \quad (17)$$

with the time-dependent perturbation for a negatively charged particle

$$W(t) = x\mathcal{E}(t). \quad (18)$$

The continuum propagation with the field-free Hamiltonian,  $\mathcal{H}_0$  (equation (14)) is carried out via the split operator method outlined above. This explicit propagation provides a description of the transition from the bound state to the continuum within first-order, i.e. without transient ionization, where the system does not necessarily remain ionized but may recombine within a very short time window [45–47]. The PES,  $\tilde{\sigma}_\nu^{\text{PT}}(p)$ , is obtained as in equation (16) replacing  $\tilde{\Psi}_{\text{out},\nu}(p,t)$  by its perturbative counterpart  $|\Psi^{\text{PT}(1)}(t)\rangle$ .

**2.2.3. Perturbation theory with plane waves approach (PTPW).** As additional level of approximation, we represent the continuum by plane waves (PTPW). Starting from the PT approach (equation (17)), we replace the field-free propagator by a propagator with a (discretized) plane-wave basis

$$e^{-i\mathcal{H}_0(t-t')} \rightarrow \int_{-\infty}^{\infty} dp e^{-i\tilde{E}_p(t-t')} |p\rangle\langle p| \quad (19)$$

and the eigenvalues  $\tilde{E}_p = p^2/2$ . We obtain

$$|\tilde{\Psi}^{\text{PTPW}(1)}(t)\rangle = -i \int_{t_0}^t dt' \int_{-\infty}^{\infty} dp e^{-i\tilde{E}_p(t-t')} |p\rangle \times \langle p|x\mathcal{E}(t')e^{-iE_0(t'-t_0)}|\varphi_0\rangle \quad (20a)$$

$$= -i \int_{-\infty}^{\infty} dp |p\rangle \langle p|x|\varphi_0\rangle e^{-i\tilde{E}_p t} e^{iE_0 t_0} \int_{t_0}^t dt' \mathcal{E}(t') e^{-i(E_0 - \tilde{E}_p)t'}. \quad (20b)$$

The time integral can be rewritten as

$$\int_{t_0}^t dt' \mathcal{E}(t') e^{+i(\tilde{E}_p - E_0)t'} \approx \int_{-\infty}^{\infty} dt' \mathcal{E}(t') e^{+i(\tilde{E}_p - E_0)t'} = FT^{-1}\{\mathcal{E}(t')\} = \tilde{\mathcal{E}}(\tilde{E}_p - E_0). \quad (21)$$

In the momentum integral the transition dipole moment to the continuum (ionization dipole moment) occurs:

$$\langle p|x|\varphi_0\rangle = \int_{-\infty}^{\infty} dx e^{-ipx} x\varphi_0(x) = FT\{x\varphi_0(x)\} = \mu(p). \quad (22)$$

In the femtosecond regime, the ionization transition dipole moment (equation (22)) is often assumed to be constant and set to one (Condon approximation) [48], which is a good approximation for the comparatively narrow spectral profile. However, in attosecond pulse interaction, the  $p$ -dependence becomes non-negligible. Thus, equation (20b) can be rewritten as:

$$|\tilde{\Psi}^{\text{PTPW}(1)}(t)\rangle = -i e^{iE_0 t_0} \int_{-\infty}^{\infty} dp |p\rangle e^{-i\tilde{E}_p t} \mu(p) \tilde{\mathcal{E}}(\tilde{E}_p - E_0) \quad (23)$$

yielding the intuitive expression for the PES for  $t \rightarrow \infty$  ('Fermi's Golden Rule')

$$\tilde{\sigma}_\nu^{\text{PTPW}}(p) = \left| \langle p|\tilde{\Psi}^{\text{PTPW}(1)}(t \rightarrow \infty)\rangle \right|^2 = |\mu(p)|^2 \left| \tilde{\mathcal{E}}(\tilde{E}_p - E_0) \right|^2, \quad (24)$$

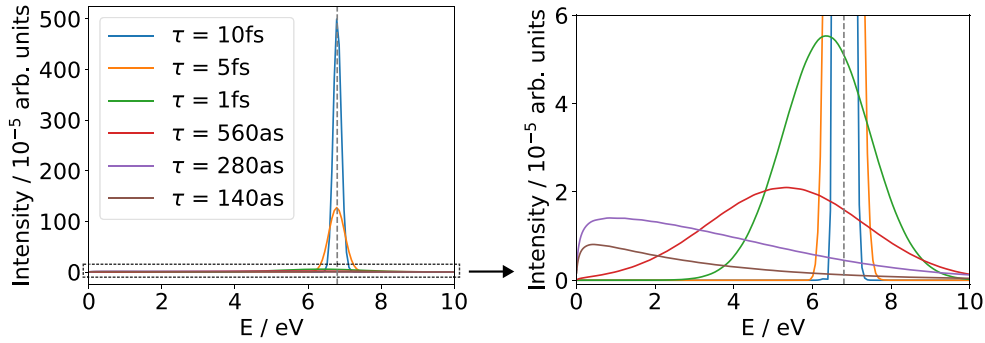
with  $\nu = \text{fwd}$  ( $\text{bwd}$ ) for  $p > 0$  ( $p < 0$ ), as a product of the modulus squared of the transition dipole moment and the electric field in the frequency domain, shifted by the ground state energy,  $E_0$ . The latter has been defined as the spectral intensity, see equation (9).

### 3. Results and discussion

#### 3.1. Pulse lengths dependence

In the long pulse limit, XUV ionization is intuitively described as a one photon process removing an electron from its bound state with energy  $E_0$  and placing it into the continuum, with an excess kinetic energy,  $E$ , given by energy conservation

$$E = \omega + E_0 \quad (25)$$



**Figure 3.** PES,  $\sigma_{\text{fwd}}^{\text{TDSE}}(E)$ , obtained by TDSE for different pulse lengths,  $\tau$ , intensity  $I = 10^{15} \text{ W cm}^{-2}$ , CEP of  $\phi_{\text{CE}} = 0$ ,  $\phi_2 = 0$ . The vertical dashed line represents the long pulse limit, equation (25)

( $E_0 = -I_p$ ). Recall, for long, spectrally narrow pulses, the carrier frequency  $\omega_0$  equals to the photon energy  $\omega$ . In our model system employed throughout this chapter, this corresponds to  $E = 15.5 \text{ eV} - 8.7 \text{ eV} = 6.8 \text{ eV}$ . This is demonstrated in figure 3 for unchirped ( $\phi_2 = 0$ ) pulses of different pulse lengths  $\tau$ . Apart from the obvious decrease in intensity due to the reduced total—i.e. time-integrated—pulse intensity, it is clear that equation (25) holds only for long XUV pulses comprised of many optical cycles. By reducing the pulse length, the PES not only broadens but substantially shifts its peak position towards lower kinetic energies, away from the expected one-photon long pulse limit (dashed vertical line).

This effect can be explained qualitatively by PTPW, which expresses the PES, equation (24), as the product of the transition dipole moment and the spectral intensity profile. Both quantities are shown in figure 4 panel (a) for three selected pulse lengths,  $\tau = 5 \text{ fs}$ ,  $560 \text{ as}$ , and  $140 \text{ as}$ . The transition dipole moment,  $|\mu(p)|^2$  (orange curve) is largest for low energies. The spectral intensity profile of the XUV pulses,  $\tilde{I}(\omega)$  (blue curves), does not only broaden with decreasing pulse duration, but also substantially blueshifts (vertical dotted lines), recall section 2.1. The overlap between  $\tilde{I}(\omega)$  and  $|\mu(p)|^2$  is largest in the region of low kinetic photoelectron energies, thereby shifting the PES towards lower kinetic energies [28]. The transition dipole moment becomes the limiting contribution and we observe a dipole-dependent reshaping and imprint of  $\mu(p)$  on the PES. In figure 4 panels (b)–(d), this effect is shown comparing results obtained by the TDSE, PT, and PTPW approach. All three levels of theory display the intensity shift towards low kinetic energies marking it as a linear property. While PT overall agrees well with the TDSE approach, the PTPW slightly underestimates the yield for low kinetic energies indicating the error induced by using plane waves in the latter. Not surprisingly, the deviations become larger, the smaller the kinetic energy of the emitted electron [49].

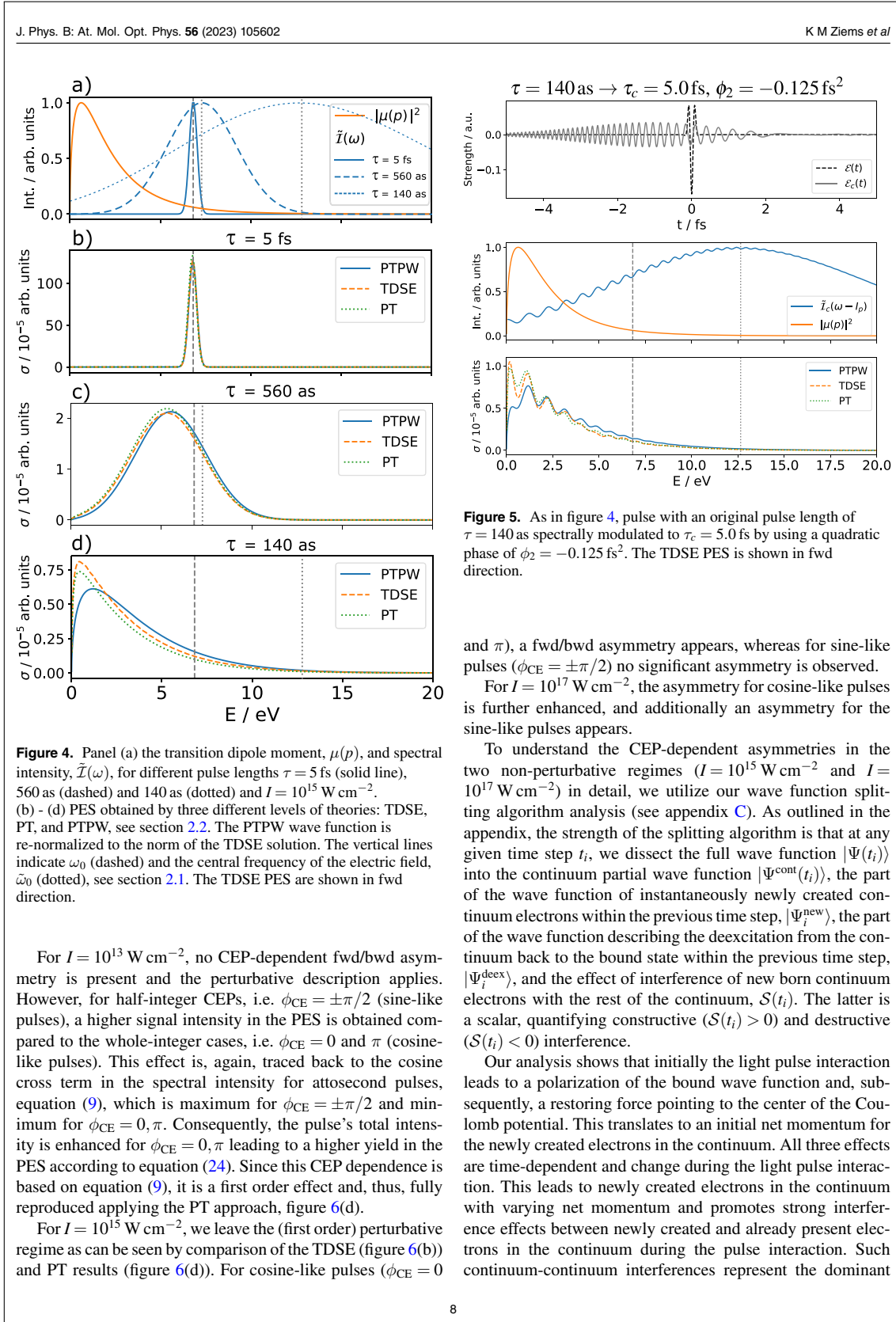
### 3.2. PES for a quasi-chirped pulse

Recent work on dynamic interference emphasizes the importance of the temporal envelope of pulses for XUV ionization

[50–52]. In order to disentangle effects originating due to the temporal envelope of the ultrashort attosecond pulse from those originating from the extreme broad spectral profile, we next investigate attosecond few-cycle pulses with a spectral modulation [53–55]. As a consequence, while the spectral width remains broad, the temporal profile stretches (recall section 2.1). We employ the same parameters as in the previous section: a few-cycle pulse with pulse length of  $\tau = 140 \text{ as}$  and a spectral phase of  $\phi_2 = -0.125 \text{ fs}^2$ , which linearly changes the instantaneous frequency and effectively elongates the pulse to  $\tau_c = 5.0 \text{ fs}$ . The same analysis as for the unchirped pulses in the previous section is performed and shown in figure 5. The overall shift of the PES towards low energies remains unaffected by the quasi-chirp. This is also reproduced by the PT approaches (PT, PTPW). As before, the PES shift originates from the spectral profile of a pulse and not its temporal envelope function. Second, an oscillation in the spectral intensity can be observed, which is imprinted in the PES. This is reminiscent of the cosine cross term,  $\tilde{I}^{\text{cross}}(\omega)$ , that becomes relevant for spectrally broad XUV pulses (recall equation (9) and figure 2(b)). The first-order PT approach with an exact continuum propagation is very similar to the TDSE results further underlining that higher order effects are negligible here and that we deal with the same linear effect as for unchirped pulses with the addition of oscillations due to the interplay of the spectral modulation with the broad spectrum of the attosecond pulse.

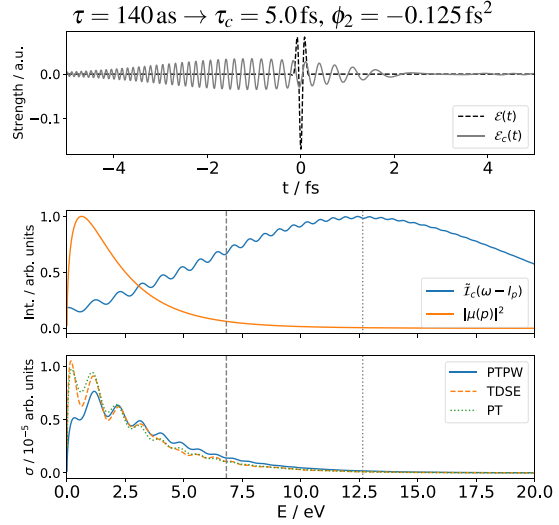
### 3.3. Intensity-dependent CEP effects

Results discussed above were obtained with a CEP of  $\phi_{\text{CE}} = 0$  simulating the PES in fwd ( $x > 0$ ) direction. For long and/or weak pulses, the CEP does not affect the PES. We now look into CEP effects of a few-cycle ( $\tau = 140 \text{ as}$ ) pulse and its effect on the PES in fwd/bwd direction with different intensities. In figures 6(a)–(c), the PES in fwd and bwd direction is shown for CEP values of  $\phi_{\text{CE}} \in \{-\pi/2, 0, \pi/2, \pi\}$  and for different intensities of the original few-cycle XUV pulse ( $\phi_2 = 0$ ). We can distinguish three different regimes with unique CEP-dependent asymmetries.



For  $I = 10^{13}$  W cm $^{-2}$ , no CEP-dependent fwd/bwd asymmetry is present and the perturbative description applies. However, for half-integer CEPs, i.e.  $\phi_{CE} = \pm\pi/2$  (sine-like pulses), a higher signal intensity in the PES is obtained compared to the whole-integer cases, i.e.  $\phi_{CE} = 0$  and  $\pi$  (cosine-like pulses). This effect is, again, traced back to the cosine cross term in the spectral intensity for attosecond pulses, equation (9), which is maximum for  $\phi_{CE} = \pm\pi/2$  and minimum for  $\phi_{CE} = 0, \pi$ . Consequently, the pulse's total intensity is enhanced for  $\phi_{CE} = 0, \pi$  leading to a higher yield in the PES according to equation (24). Since this CEP dependence is based on equation (9), it is a first order effect and, thus, fully reproduced applying the PT approach, figure 6(d).

For  $I = 10^{15}$  W cm $^{-2}$ , we leave the (first order) perturbative regime as can be seen by comparison of the TDSE (figure 6(b)) and PT results (figure 6(d)). For cosine-like pulses ( $\phi_{CE} = 0$



**Figure 5.** As in figure 4, pulse with an original pulse length of  $\tau = 140$  as spectrally modulated to  $\tau_c = 5.0$  fs by using a quadratic phase of  $\phi_2 = -0.125$  fs $^2$ . The TDSE PES is shown in fwd direction.

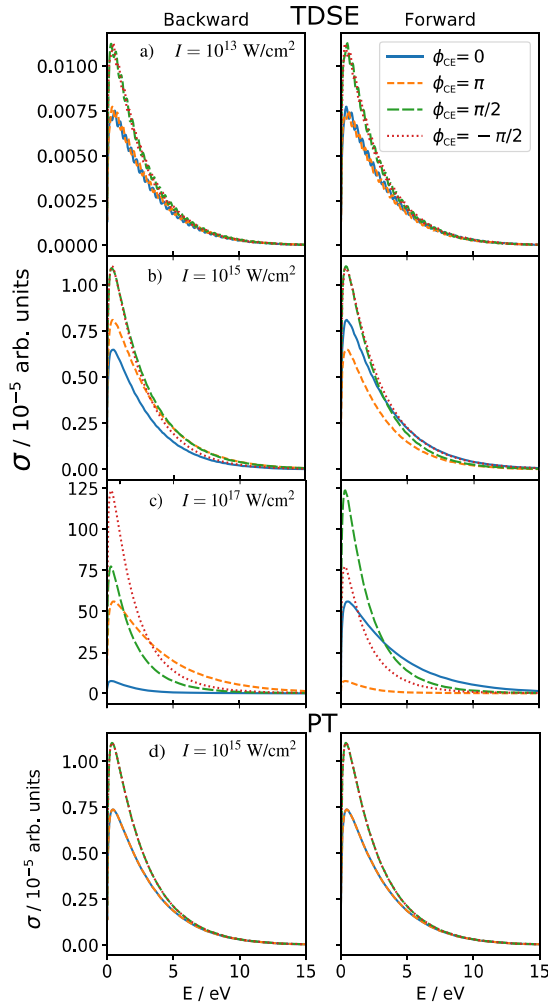
and  $\pi$ ), a fwd/bwd asymmetry appears, whereas for sine-like pulses ( $\phi_{CE} = \pm\pi/2$ ) no significant asymmetry is observed.

For  $I = 10^{17}$  W cm $^{-2}$ , the asymmetry for cosine-like pulses is further enhanced, and additionally an asymmetry for the sine-like pulses appears.

To understand the CEP-dependent asymmetries in the two non-perturbative regimes ( $I = 10^{15}$  W cm $^{-2}$  and  $I = 10^{17}$  W cm $^{-2}$ ) in detail, we utilize our wave function splitting algorithm analysis (see appendix C). As outlined in the appendix, the strength of the splitting algorithm is that at any given time step  $t_i$ , we dissect the full wave function  $|\Psi(t_i)\rangle$  into the continuum partial wave function  $|\Psi^{\text{cont}}(t_i)\rangle$ , the part of the wave function of instantaneously newly created continuum electrons within the previous time step,  $|\Psi_i^{\text{new}}\rangle$ , the part of the wave function describing the deexcitation from the continuum back to the bound state within the previous time step,  $|\Psi_i^{\text{dex}}\rangle$ , and the effect of interference of new born continuum electrons with the rest of the continuum,  $\mathcal{S}(t_i)$ . The latter is a scalar, quantifying constructive ( $\mathcal{S}(t_i) > 0$ ) and destructive ( $\mathcal{S}(t_i) < 0$ ) interference.

Our analysis shows that initially the light pulse interaction leads to a polarization of the bound wave function and, subsequently, a restoring force pointing to the center of the Coulomb potential. This translates to an initial net momentum for the newly created electrons in the continuum. All three effects are time-dependent and change during the light pulse interaction. This leads to newly created electrons in the continuum with varying net momentum and promotes strong interference effects between newly created and already present electrons in the continuum during the pulse interaction. Such continuum-continuum interferences represent the dominant





**Figure 6.** PES induced by a  $\tau = 140$  as XUV pulse in forward and backward direction for different CEP values,  $\phi_{\text{CE}} \in \{-\pi/2, 0, \pi/2, \pi\}$ , and different intensities: (a)  $I = 10^{13} \text{ W cm}^{-2}$ , (b)  $I = 10^{15} \text{ W cm}^{-2}$ , (c)  $I = 10^{17} \text{ W cm}^{-2}$ , obtained by numerically solving the TDSE. In (d) the PES for  $I = 10^{15} \text{ W cm}^{-2}$  is obtained by first-order PT.

part of the ionization process (see appendix C). The interference pattern in the continuum dictates the final emission asymmetry reported above. For  $I = 10^{15} \text{ W cm}^{-2}$ , we obtain a fwd (positive) asymmetry for  $\phi_{\text{CE}} = 0$ , while for  $\phi_{\text{CE}} = \frac{\pi}{2}$  the interference contributions cancel out. For  $I = 10^{17} \text{ W cm}^{-2}$  and  $\phi_{\text{CE}} = \frac{\pi}{2}$ , strong destructive interference of negative net momenta leads to the final fwd emission asymmetry.

For the quasi-chirped attosecond XUV pulse described in section 3.2, these non-perturbative CEP- and intensity-dependent effects are not present. This is because—unlike the redshift of the PES reported above—these asymmetries are

a temporal pulse effect originating from the time-dependent polarization and continuum-continuum interference. Since the quasi-chirped attosecond XUV pulse behaves in time like a femtosecond pulse, we do not observe these asymmetries.

Finally, we point out that for unchirped attosecond XUV pulses, no interference structure is found in the final PES neither for 1D (section 3.1) nor 3D appendix A simulations. We report—beyond the long pulse limit—a red-shift of the PES as a spectral effect, and a CEP- and intensity-dependent asymmetry as temporal interference effect. We did not find any indication for spatial or temporal interference leading to modulations/structures in the final PES for XUV ionization [25]. Modulations due to dynamic interference have been observed for longer high-frequency pulses [50–52] and such effects arise in our simulations only for a temporally elongated quasi-chirped attosecond XUV pulse with  $I = 10^{17} \text{ W cm}^{-2}$ .

#### 4. Summary

In this work, we have addressed systematically several quantum effects occurring in few-cycle XUV attosecond ionization. To this end, we thoroughly introduced the properties and modulations unique to attosecond, few-cycle XUV pulses beyond the SVEA.

Apart from the trivial effect of a broad spectral bandwidth, envelope-induced contributions lead to a temporal modulation. In the frequency realm this results in a strong blueshift and a cross term in the spectral intensity profile depending on the CEP and spectral modulations.

For weak to moderate intensities, the light–atom interaction can be well described within linear response: despite the blueshift of an attosecond XUV pulse, the resulting PES are shifted towards lower kinetic energies. This is reasoned by the two contributions, the  $p$ -dependence of the ionization matrix element, and the broad spectral profile of the pulse. Since this shift is a linear effect in the spectral domain, a quasi-chirped XUV attosecond pulse, which stretches the pulse in the time domain, while only marginally affecting its spectral intensity width, results in the same red shift.

These cross terms of the spectral intensity, that is unique to attosecond pulses beyond the SVEA, vary the total pulse intensity, rendering the PES sensitive to the CEP of an ultrashort pulse even within first-order effects. For half-integer CEPs, the yield in the PES is maximum, whereas for whole-integer CEPs, a minimum signal follows.

As a non-perturbative effect, we report on fwd/bwd asymmetries in the PES for unchirped few-cycle XUV pulses, which depend on the field strength and the CEP of the pulse. This effect is defined by the temporal property of the pulse and is not present for temporally elongated, quasi-chirped XUV pulses. By applying a wave function splitting algorithm, we traced the origin of the asymmetries back to an initial bound state polarization and CEP- and intensity-specific continuum–continuum interferences that drive the ionization process.

Future questions in this field could be investigating dynamical interference of strong, (un)chirped, few-cycle XUV pulses and hereby extending the works of long, high frequency pulses

[50–52]. It is yet to be addressed how temporal dynamic interference effects are present for these kind of pulses and have to be thoughtfully dissected from the CEP- and intensity-dependent effects unraveled in this work. Moreover, it has been shown recently that electronic and nuclear correlation lead to asymmetries in the PES during XUV ionization [56], therefore, the interplay with the asymmetry from attosecond pulses reported here would be of future interest.

#### Data availability statement

All data that support the findings of this study are included within the article and appendix.

#### Acknowledgments

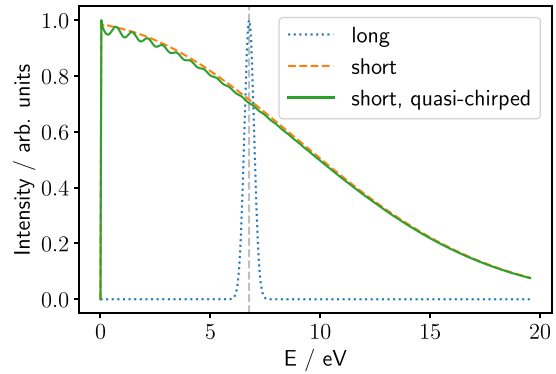
K M Z is grateful for fruitful discussions with Kevin Fiedlerling and Rešad Kahvedžić. K M Z and S G are part of the Max Planck School of Photonics supported by BMBF, Max Planck Society, and Fraunhofer Society. A S and S G acknowledge the ERC Consolidator Grant QUEM-CHEM (772676) and funding by the SFB NOA (Project Number 398816777), project A1.

#### Appendix A. Calculation on 3D hydrogen

In order to validate and quantify the results of the text, we performed TDSE calculations on the hydrogen atom in 3D using an expansion in spherical harmonics. To this end, we utilized QPROP 3.2 [36] modified to allow for our pulse definitions in section 2.1.

The electronic ground state was obtained by imaginary time propagation. The light pulse was linearly polarized and added in the dipole approximation using velocity gauge with the vector potentials shown in equation (1a) (unchirped) and equation (10) (quasi-chirped). The PES was calculated via t-SURFF [57] during the pulse interaction time, while the propagation of the wavefunction from the end of the pulse to infinity used i-SURFF [58]. For the expansion in spherical harmonics,  $L_{\max} = 15$  was used and  $m = m_0 = 0$  since the magnetic quantum number of the initial state is conserved. The grid, time propagation, and  $t/i$ -SURFF parameter had to be chosen carefully to encapsulate the high frequency, broad spectrum with very slow and fast electrons and (temporally elongated) time span of the (modulated) light pulses. We used a time step of  $\Delta t = 0.02$ , grid spacing of  $\Delta r = 0.2$ , and a grid size of  $R_{\text{grid}} = 1600$  with cut-off of the binding potential to a linear function becoming zero at the grid boundaries at  $R_{\text{CO}} = 400$ . The t-SURFF flux is collected at the grid boundary. The imaginary potential to suppress grid reflection used the parameters  $V_{\text{im,max}} = 100$  and  $W_{\text{im}} = 400$  with a factor of 10 for the i-SURFF propagation. For further detail on the implementation of the parameters, we refer to the original QPROP and  $t/i$ -SURFF publications [36, 57, 58].

In the simulations, we used  $\omega = 0.749$ ,  $E_0 = 0.0169$  and three pulses identical to the ones used in the text for the model



**Figure S1.** Normalized PES of hydrogen in 3D using an expansion in spherical harmonics and obtained by numerical solution to the TDSE. Calculations with the same properties as in the text were performed validating the model system approach. A long, femtosecond XUV pulse (blue dotted line) leads to a spectrum centered around the one-photon limit (vertical grey dashed line). The attosecond pulse (dashed orange line) exhibits a red shift. The quasi-chirp of the attosecond pulse (green line) leads to an imprint of the spectral modulation parameter due to the unique cross term for attosecond pulses discussed in the text.

system: (i) a long, femtosecond XUV pulse within the SVEA with  $\tau = 5$  fs (figure 1 right column), (ii) an attosecond XUV pulse with  $\tau = 140$  as (figure 1 left column), and (iii) a quasi-chirped, attosecond XUV pulse with  $\tau = 140$  as,  $\tau_c = 5.0$  fs, and a quadratic spectral modulation  $\phi'' = -0.125 \text{ fs}^2$  (figure 2 left column). The corresponding PES are shown in figure S1 and confirm the results of the text presented in figures 4 and 5.

#### Appendix B. Wave function splitting algorithm

In order to understand and quantify different effects contributing to attosecond pulse interaction, such as direct ionization, deexcitation and continuum interference, a wave function splitting algorithm is derived. To that end, a projector

$$\mathcal{P} = \sum_n |\varphi_n\rangle\langle\varphi_n| \quad (\text{B1})$$

and its complement  $\mathcal{Q} = \mathbb{1} - \mathcal{P}$  are introduced, dissecting a wavefunction into its ‘bound’ and ‘unbound’ component, respectively.

Applying the projectors to the full wave function,  $|\Psi(t_i)\rangle$ ,  $i \in [0, N_t]$ , at a certain point in time  $t_i$  yields two partial wave functions, indicating which components can be considered to be bound at time step  $t_i$  and which components are unbound, i.e. in a continuum state (cont):

$$|\Psi^{\text{bound}}(t_i)\rangle = \mathcal{P}|\Psi(t_i)\rangle \quad (\text{B2})$$

$$|\Psi^{\text{cont}}(t_i)\rangle = \mathcal{Q}|\Psi(t_i)\rangle. \quad (\text{B3})$$



Consequently, the instantaneous new creation of unbound continuum electrons from the bound components of the wavefunction during a single propagation time step  $\Delta t$  at time  $t_i$  can be obtained via

$$|\Psi_i^{\text{new}}\rangle = \mathcal{Q} \hat{U}(t_i, t_{i-1}) |\Psi^{\text{bound}}(t_{i-1})\rangle, \quad (\text{B4})$$

where  $\hat{U}(t_i, t_{i-1})$  is the short-time propagator with the full Hamiltonian and the wavefunction index  $i$  indicates the time of birth at timestep  $t_i$  of the newly created unbound electron.

Further propagation of the newly generated part of the continuum electron's wave function,  $|\Psi_i^{\text{new}}\rangle$ , from its time of birth  $t_i$  to a later time  $t_j, j \geq i$ , and again dissecting the wavefunction, allows monitoring the influence of the Coulomb potential and light field on the continuum electrons:

$$|\Psi_i^{\text{free}}(t_j)\rangle = \begin{cases} |\Psi_i^{\text{new}}\rangle & \text{for } j = i \\ \left( \prod_{m=i+1}^j \mathcal{Q} \hat{U}(t_m, t_{m-1}) \right) |\Psi_i^{\text{new}}\rangle & \text{for } j > i. \end{cases} \quad (\text{B5})$$

$|\Psi_i^{\text{free}}(t_j)\rangle$  represents those parts of the wave function that were entering the continuum at time  $t_i$  and are still found to be unbound at time  $t_j$ . This will be especially interesting for the final time step,  $j = N_t$ , i.e. when the light pulse is switched off. Note that the coherent sum of all continuum electrons born at different times  $t_i$  (and propagated to  $t_j$ ) yields the unbound part of the total wavefunction:

$$\sum_{i=1}^j |\Psi_i^{\text{free}}(t_j)\rangle = |\Psi^{\text{cont}}(t_j)\rangle. \quad (\text{B6})$$

Analogously to equation (B4), the deexcitation from the transiently populated continuum into the bound states within a single time step  $\Delta t$  is calculated as:

$$|\Psi_i^{\text{deex}}\rangle = \mathcal{P} \hat{U}(t_i, t_{i-1}) |\Psi^{\text{cont}}(t_{i-1})\rangle. \quad (\text{B7})$$

Moreover, the splitting approach allows to isolate the influence of interference between newly generated continuum electrons at time  $t_j$ ,  $|\Psi_j^{\text{new}}\rangle$ , and continuum electrons generated at earlier points in time  $\sum_{i < j} |\Psi_i^{\text{free}}(t_j)\rangle$  on the total amount of the photoionization probability. To this end, we start from equation (B6), write the last time step explicitly, and use the identities equations (B4) and (B7):

$$|\Psi^{\text{cont}}(t_j)\rangle = \sum_{i=1}^{j-1} |\Psi_i^{\text{free}}(t_j)\rangle + |\Psi_j^{\text{free}}(t_j)\rangle \quad (\text{B8a})$$

$$= \mathcal{Q} \hat{U}(t_j, t_{j-1}) \sum_{i=1}^{j-1} |\Psi_i^{\text{free}}(t_{j-1})\rangle + |\Psi_j^{\text{new}}\rangle \quad (\text{B8b})$$

$$= \hat{U}(t_j, t_{j-1}) |\Psi^{\text{cont}}(t_{j-1})\rangle + |\Psi_j^{\text{new}}\rangle - |\Psi_j^{\text{deex}}\rangle. \quad (\text{B8c})$$

This expression correspond to the coherently propagated wavefunction of the unbound electrons, which is extended by

the newly generated photoelectrons at time step  $t_j$  and reduced by the electrons that return into a bound state at the same time.

The total photoionization probability is therefore

$$\begin{aligned} \langle \Psi^{\text{cont}}(t_j) | \Psi^{\text{cont}}(t_j) \rangle &= \langle \Psi^{\text{cont}}(t_{j-1}) | \Psi^{\text{cont}}(t_{j-1}) \rangle \\ &+ \langle \Psi_j^{\text{new}} | \Psi_j^{\text{new}} \rangle + \langle \Psi_j^{\text{deex}} | \Psi_j^{\text{deex}} \rangle \\ &- 2\text{Re} \left\{ \langle \Psi_j^{\text{deex}} | \hat{U}(t_j, t_{j-1}) | \Psi^{\text{cont}}(t_{j-1}) \rangle \right\} \\ &+ 2\text{Re} \left\{ \langle \Psi_j^{\text{new}} | \hat{U}(t_j, t_{j-1}) | \Psi^{\text{cont}}(t_{j-1}) \rangle \right\}, \end{aligned} \quad (\text{B9})$$

where we used  $\langle \Psi_j^{\text{new}} | \Psi_j^{\text{deex}} \rangle = 0$ . Using equation (B7) and the projector identity  $\mathcal{P} = \mathcal{P}^2$ , the second to last term becomes  $-2\langle \Psi_j^{\text{deex}} | \Psi_j^{\text{deex}} \rangle$ . The last term in equation (B9) represents the interference  $\mathcal{S}(t_j)$  of newly generated photoelectrons at timestep  $t_j$  with previously generated photoelectrons, which can be positive, in case of constructive interference, or negative in case of destructive interference. Using equations (B4) and (B6), and  $\mathcal{Q} = \mathcal{Q}^2$ , it can be written as

$$\mathcal{S}(t_j) = 2\text{Re} \left\{ \langle \Psi_j^{\text{new}} | \hat{U}(t_j, t_{j-1}) | \Psi^{\text{cont}}(t_{j-1}) \rangle \right\} \quad (\text{B10a})$$

$$= 2\text{Re} \left\{ \langle \Psi_j^{\text{new}} | \mathcal{Q} \hat{U}(t_j, t_{j-1}) \left| \sum_{i=1}^{j-1} |\Psi_i^{\text{free}}(t_{j-1})\rangle \right. \right\} \quad (\text{B10b})$$

$$= 2 \sum_{i=1}^{j-1} \text{Re} \left\{ \langle \Psi_j^{\text{new}} | \Psi_i^{\text{free}}(t_j) \rangle \right\}. \quad (\text{B10c})$$

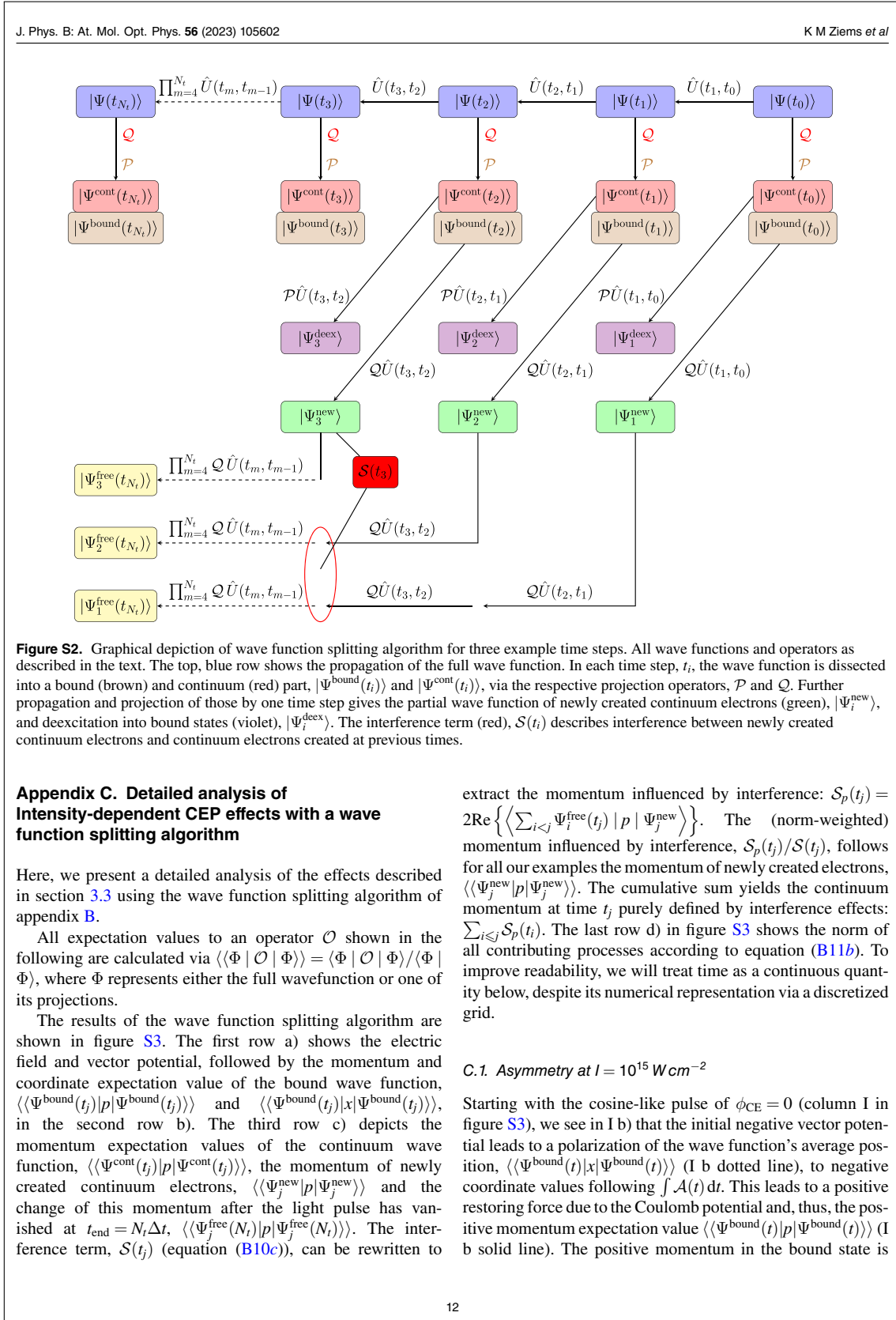
The total photoionization probability at time  $t_j$  is then given by:

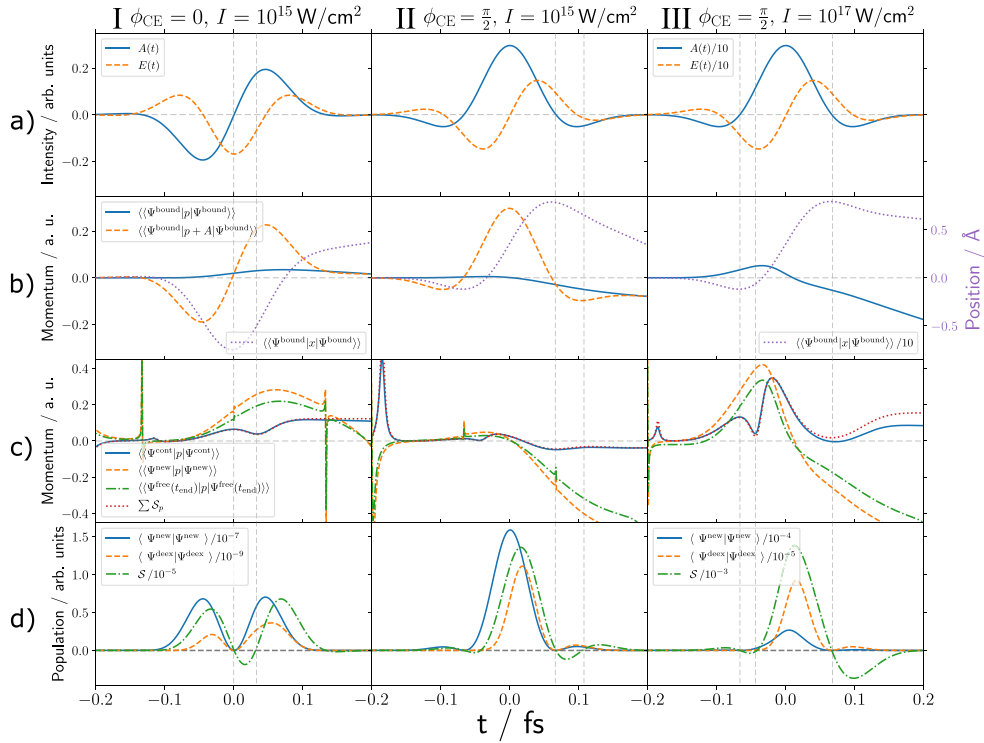
$$\begin{aligned} \langle \Psi^{\text{cont}}(t_j) | \Psi^{\text{cont}}(t_j) \rangle &= \langle \Psi^{\text{cont}}(t_{j-1}) | \Psi^{\text{cont}}(t_{j-1}) \rangle \\ &+ \langle \Psi_j^{\text{new}} | \Psi_j^{\text{new}} \rangle - \langle \Psi_j^{\text{deex}} | \Psi_j^{\text{deex}} \rangle \\ &+ \mathcal{S}(t_j) \end{aligned} \quad (\text{B11a})$$

$$= \sum_{i=1}^j \left\{ \langle \Psi_i^{\text{new}} | \Psi_i^{\text{new}} \rangle - \langle \Psi_i^{\text{deex}} | \Psi_i^{\text{deex}} \rangle + \mathcal{S}(t_i) \right\}, \quad (\text{B11b})$$

where we have applied the decomposition of  $|\Psi^{\text{cont}}(t_j)\rangle$  recursively to all previous time steps  $t_i$ . Thus, we interpret the total photoionization probability as the sum of all contributions being excited into the continuum states over all points in time minus the probability of its deexcitation back into a bound state plus the interference term, which is further examined in section 3.3.

Figure S2 visualizes the wave function splitting algorithm and its contributions outlined above for three explicit time steps. The wave function splitting algorithm is mathematically not depending on the dimensionality of the wave function and can be applied as long as the basis of the projection operators can be calculated. For higher dimensions, obtaining this basis is computationally demanding.





**Figure S3.** Results of the wave function splitting algorithm for column I:  $\phi_{CE} = 0$  and  $I = 10^{15} \text{ W cm}^{-2}$ , column II:  $\phi_{CE} = \frac{\pi}{2}$  and  $I = 10^{15} \text{ W cm}^{-2}$ , and column III:  $\phi_{CE} = \frac{\pi}{2}$  and  $I = 10^{17} \text{ W cm}^{-2}$ . For clarity, in a given row the legend is only shown in the first panel (column I). In column III, re-scaling of some data was performed and is indicated by a new legend. Row (a) shows the vector and electric field,  $A(t)$  (solid blue) and  $E(t)$  (dashed orange). Row (b) shows momentum and position behavior of the bound wave function,  $\langle\langle \Psi^{\text{bound}}(t)|p|\Psi^{\text{bound}}(t) \rangle\rangle$  (solid blue) and  $\langle\langle \Psi^{\text{bound}}(t)|x|\Psi^{\text{bound}}(t) \rangle\rangle$  (dotted purple). Row (c) depicts the momentum expectation values of the continuum wave function,  $\langle\langle \Psi^{\text{cont}}(t)|p|\Psi^{\text{cont}}(t) \rangle\rangle$  (solid blue), the momentum of newly created continuum electrons,  $\langle\langle \Psi_t^{\text{new}}|p|\Psi_t^{\text{new}} \rangle\rangle$  (dashed orange), the change of this momentum after the light pulse has vanished at  $t_{\text{end}} = N_r \Delta t$ ,  $\langle\langle \Psi_t^{\text{free}}(t_{\text{end}})|p|\Psi_t^{\text{free}}(t_{\text{end}}) \rangle\rangle$  (dashed-dotted green), and the continuum momentum at time  $t$  purely defined by interference effects:  $\sum_{i \leq t} S_p(i)$  (dotted purple). The last row (d) gives the norm of all contributing processes according to equation (B11b). The long vertical dashed lines indicate zero points in the interference term that are of interest and discussed in the text. These zero points lead to a modulation in the continuum momentum,  $\langle\langle \Psi^{\text{cont}}(t)|p|\Psi^{\text{cont}}(t) \rangle\rangle$ . Note the different order of magnitude indicated in the legend. The cusps in panel (c) are due to singularities in the norm of  $|\Psi_t^{\text{new}}\rangle$ .

qualitatively similar, but enhanced in the momentum of the newly born electrons into the continuum at each time step,  $\langle\langle \Psi_t^{\text{new}}|p|\Psi_t^{\text{new}} \rangle\rangle$  (I c dashed line).  $\langle\langle \Psi_t^{\text{free}}(t_{\text{end}})|p|\Psi_t^{\text{free}}(t_{\text{end}}) \rangle\rangle$  (I c dashed-dotted line) reveals that this initial momentum is only slightly altered by further propagation in the Coulomb and light field. The (accumulated) momentum in the continuum,  $\langle\langle \Psi^{\text{cont}}(t)|p|\Psi^{\text{cont}}(t) \rangle\rangle$  (I c solid line), differs from the momentum of the newly created continuum electrons and shows temporal modulations. A comparison with the momentum purely defined by interference,  $\sum_{t' \leq t} S_p(t')$  (I c dotted line), shows a perfect overlap indicating a fully interference-driven process of ionization. This is also evident by comparing the norms of the different contributing processes (I d). Interference (I d dashed-dotted line) is dominating by a factor of 100 over newly created continuum electrons (I d solid line), while deexcitation into the bound states is negligible (I d dashed line). The interference-driven modulations

in the continuum momentum,  $\langle\langle \Psi^{\text{cont}}(t)|p|\Psi^{\text{cont}}(t) \rangle\rangle$  (I c solid line), can also be reasoned by the interference term,  $S(t)$  (I d dashed-dotted line), directly: For  $t < 0.0$  fs the interference term is positive (constructive), in the interval  $t \in [0.00, 0.03]$  fs it is negative (destructive) and afterwards again positive (constructive). The destructive interference during  $t \in [0.00, 0.03]$  fs of positive momenta leads to the modulation seen in  $\langle\langle \Psi^{\text{cont}}(t)|p|\Psi^{\text{cont}}(t) \rangle\rangle$  (I c solid line).

For the sine-like pulse of  $\phi_{CE} = \frac{\pi}{2}$  (column II), we follow the same reasoning as above to explain the behavior of the continuum electron. The temporal momentum behavior can again be traced back to interference dominating the ionization and leading to modulation in the momentum,  $\langle\langle \Psi^{\text{cont}}(t)|p|\Psi^{\text{cont}}(t) \rangle\rangle$  (II c solid line) due to constructive and destructive interference (II d dashed-dotted line). The reason that no (substantial) asymmetry is observed is due to, firstly, bound state polarization in both directions (II b dotted line)

leading to a change in restoring force (II b solid line) imprinted on the continuum electrons (II c dashed line) and, secondly, an interference that compensates constructive and destructive parts after  $t > 0.07$  fs.

### C.2. Asymmetries at $I = 10^{17} \text{ W cm}^{-2}$

The latter point of constructive and destructive compensation in interference contribution is the essential change when going to  $I = 10^{17} \text{ W cm}^{-2}$  that leads to an asymmetry for  $\phi_{\text{CE}} = \frac{\pi}{2}$  (column III in figure S3): For the increased intensity, the bound state polarization (III b dotted line) scales by a factor of ten (proportional to the electric field strength) compared to  $I = 10^{15} \text{ W cm}^{-2}$ , which leads to larger restoring force (III b solid line) and, subsequently, momentum expectation values (III c). However, their qualitative behavior is identical for both intensities. The momentum modulation in the continuum,  $\langle \langle \Psi^{\text{cont}}(t) | p | \Psi^{\text{cont}}(t) \rangle \rangle$  (III c solid line), is again interference-driven and can be explained by the change in positive and negative values of  $S(t)$  (III d dashed-dotted line). Here lies the difference to the asymmetry-free sine-like pulse at  $I = 10^{15} \text{ W cm}^{-2}$ . After  $t > 0.07$  fs the interference,  $S(t)$ , is strictly negative for  $I = 10^{17} \text{ W cm}^{-2}$  (III d dashed-dotted line), while it is equally positive and negative for  $I = 10^{15} \text{ W cm}^{-2}$  (II d dashed-dotted line). This difference leads to a final positive asymmetry for  $I = 10^{17} \text{ W cm}^{-2}$ , that is absent for lower intensities. The negative (destructive) interference,  $S(t)$  (III d dashed-dotted line), of negative momentum components,  $\langle \langle \Psi_i^{\text{new}} | p | \Psi_i^{\text{new}} \rangle \rangle$  (III c dashed line), leads to a net positive momentum imprinted in the final continuum wave packet after ionization,  $\langle \langle \Psi^{\text{cont}}(t_{\text{end}}) | p | \Psi^{\text{cont}}(t_{\text{end}}) \rangle \rangle$  (III c solid line).

Moreover, row III d) shows a change in relative contribution of the different processes involved. The deexcitation term is increased compared to lower intensity, but still overall negligible (factor ten compared to contribution of newly created electrons). In general, the overall ionization magnitude and the norm of the processes involved follows the vector potential (row d), i.e. are zero if the vector potential is zero.

To summarize, while the polarization of the bound wave function is responsible for the initial momentum of newly created electrons in the continuum, the important term driving the ionization is interference of newly created continuum electrons with the already present continuum electrons (continuum-continuum interference). This term explains the temporal momentum modulations and is responsible for the final emission asymmetry. Moreover, the CEP- and intensity-dependent effect reported in this section is—unlike the redshift of the PES reported in section 3.1—a temporal pulse effect, which is not present in our simulations for a temporally elongated, quasi-chirped attosecond XUV pulse with a comparable spectral intensity.

We are confident that the wave function splitting algorithm can be applied to a plethora of problems and systems. In this first example, interference turned out to be the driving force, but for other setups deexcitation might become relevant and can be monitored in detail using this algorithm. We also want to point out that the partitioning by bound and continuum projection operators is just one example. In principle,

the algorithm can be applied to any kind of Hilbert space partitioning, as long as the eigenfunctions of the projection operators are computationally accessible.

### ORCID iDs

Karl Michael Ziems  <https://orcid.org/0000-0001-5369-7778>

Matthias Wollenhaupt  <https://orcid.org/0000-0002-0839-1494>

Stefanie Gräfe  <https://orcid.org/0000-0002-1747-5809>

Alexander Schubert  <https://orcid.org/0000-0002-8560-6436>

### References

- [1] Corkum P B and Krausz F 2007 Attosecond science *Nat. Phys.* **3** 381
- [2] Hentschel M, Kienberger R, Spielmann C, Reider G A, Milosevic N, Brabec T, Corkum P, Heinzmann U, Drescher M and Krausz F 2001 Attosecond metrology *Nature* **414** 509
- [3] Calegari F, Sansone G, Stagira S, Vozzi C and Nisoli M 2016a Advances in attosecond science *J. Phys. B: At. Mol. Opt. Phys.* **49** 062001
- [4] McNeil B W J and Thompson N R 2010 X-ray free-electron lasers *Nat. Photon.* **4** 814
- [5] Krausz F and Ivanov M 2009 Attosecond physics *Rev. Mod. Phys.* **81** 163
- [6] Baltuška A et al 2003 Attosecond control of electronic processes by intense light fields *Nature* **421** 611
- [7] Brabec T and Krausz F 2000 Intense few-cycle laser fields: frontiers of nonlinear optics *Rev. Mod. Phys.* **72** 545
- [8] Kienberger R et al 2004 Atomic transient recorder *Nature* **427** 817
- [9] Gaumnitz T, Jain A, Pertot Y, Huppert M, Jordan I, Ardana-Lamas F and Wörner H J 2017 Streaking of 43-attosecond soft-X-ray pulses generated by a passively CEP-stable mid-infrared driver *Opt. Express* **25** 27506
- [10] Sansone G et al 2006 Isolated single-cycle attosecond pulses *Science* **314** 443
- [11] Goulielmakis E et al 2008 Single-cycle nonlinear optics *Science* **320** 1614
- [12] Schötz J et al 2020 Phase-matching for generation of isolated attosecond XUV and soft-x-ray pulses with few-cycle drivers *Phys. Rev. X* **10** 041011
- [13] Tzallas P, Skantzakis E, Nikolopoulos L A, Tsakiris G D and Charalambidis D 2011 Extreme-ultraviolet pump-probe studies of one-femtosecond-scale electron dynamics *Nat. Phys.* **7** 781
- [14] Mikhailova J M, Fedorov M V, Karpowicz N, Gibbon P, Platonenko V T, Zheltikov A M and Krausz F 2012 Isolated attosecond pulses from laser-driven synchrotron radiation *Phys. Rev. Lett.* **109** 245005
- [15] Fröbel F G, Ziems K M, Peschel U, Gräfe S and Schubert A 2020 The impact of electron-electron correlation in ultrafast attosecond single ionization dynamics *J. Phys. B: At. Mol. Opt. Phys.* **53** 144005
- [16] Calegari F et al 2014 Ultrafast electron dynamics in phenylalanine initiated by attosecond pulses *Science* **346** 336
- [17] Remacle F and Levine R D 2006 An electronic time scale in chemistry *Proc. Natl Acad. Sci.* **103** 6793
- [18] Ossiander M et al 2017 Attosecond correlation dynamics *Nat. Phys.* **13** 280

- [19] Calegari F, Trabattoni A, Palacios A, Ayuso D, Castrovilli M C, Greenwood J B, Declava P, Martín F and Nisoli M 2016b Charge migration induced by attosecond pulses in bio-relevant molecules *J. Phys. B: At. Mol. Opt. Phys.* **49** 142001
- [20] Ngoko Djiojakap J M, Manakov N L, Meremianin A V and Starace A F 2013 Carrier-envelope-phase-induced asymmetries in double ionization of helium by an intense few-cycle XUV pulse *Phys. Rev. A* **88** 053411
- [21] Feist J, Nagele S, Pazourek R, Persson E, Schneider B I, Collins L A and Burgdörfer J 2009a Probing electron correlation via attosecond XUV pulses in the two-photon double ionization of helium *Phys. Rev. Lett.* **103** 063002
- [22] Feist J, Pazourek R, Nagele S, Persson E, Schneider B I, Collins L A and Burgdörfer J 2009b Ab initio calculations of two-electron emission by attosecond pulses *J. Phys.: Conf. Ser.* **194** 012010
- [23] Fomouo E, Hamido A, Antoine P, Piraux B, Bachau H and Shakeshaft R 2010 Time-dependent analysis of the mechanism for two-photon double escape in helium: from very long to attosecond time scales *J. Phys. B: At. Mol. Opt. Phys.* **43** 091001
- [24] Argenti L, Pazourek R, Feist J, Nagele S, Liertz M, Persson E, Burgdörfer J and Lindroth E 2013 Photoionization of helium by attosecond pulses: extraction of spectra from correlated wave functions *Phys. Rev. A* **87** 053405
- [25] Borbély S, Tóth A, Arbó D G, Tökési K and Nagy L 2019 Photoelectron holography of atomic targets *Phys. Rev. A* **99** 013413
- [26] Borbély S, Tóth A, Tökési K and Nagy L 2013 Spatial and temporal interference during the ionization of H by few-cycle XUV laser pulses *Phys. Rev. A* **87** 013405
- [27] Tóth A, Borbély S, Tökési K and Nagy L 2014 Ionization of atoms by few-cycle EUV laser pulses: carrier-envelope phase dependence of the intra-pulse interference effects *Eur. Phys. J. D* **68** 339
- [28] Yuan K-J and Bandrauk A D 2014 Molecular attosecond photoionization with few cycle XUV laser pulses *J. Phys.: Conf. Ser.* **497** 012014
- [29] Diels J-C and Rudolph W 2006 *Ultrashort Laser Pulse Phenomena* (Amsterdam: Elsevier)
- [30] Lin Q, Zheng J and Becker W 2006 Subcycle pulsed focused vector beams *Phys. Rev. Lett.* **97** 253902
- [31] Venzke J, Joyce T, Xue Z, Becker A and Jaron-Becker A 2018 Central frequency of few-cycle laser pulses in strong-field processes *Phys. Rev. A* **98** 063409
- [32] Rauch J and Mourou G 2006 The time integrated far field for Maxwell's and d'Alembert's equations *Proc. Am. Math. Soc.* **134** 851
- [33] Chelkowski S and Bandrauk A D 2005 Asymmetries in strong-field photoionization by few-cycle laser pulses: Kinetic-energy spectra and semiclassical explanation of the asymmetries of fast and slow electrons *Phys. Rev. A* **71** 053815
- [34] Milošević D, Paulus G, Bauer D and Becker W 2006 Above-threshold ionization by few-cycle pulses *J. Phys. B: At. Mol. Opt. Phys.* **39** R203
- [35] Wollenhaupt M, Assion A and Baumert T 2012 Short and ultrashort laser pulses *Springer Handbook of Lasers and Optics* (Berlin: Springer) pp 1047–94
- [36] Tulsy V and Bauer D 2020 Qprop with faster calculation of photoelectron spectra *Comput. Phys. Commun.* **251** 107098
- [37] Sprik M and Klein M L 1988 Optimization of a distributed gaussian basis set using simulated annealing: application to the adiabatic dynamics of the solvated electron *J. Chem. Phys.* **89** 1592
- [38] Shin S and Metiu H 1995 Nonadiabatic effects on the charge transfer rate constant: a numerical study of a simple model system *J. Chem. Phys.* **102** 9285
- [39] Erdmann M, Gross E and Engel V 2004 Time-dependent electron localization functions for coupled nuclear-electronic motion *J. Chem. Phys.* **121** 9666
- [40] Falge M, Engel V and Gräfe S 2011 Time-resolved photoelectron spectroscopy of coupled electron-nuclear motion *J. Chem. Phys.* **134** 184307
- [41] Feit M D, Fleck J A and Steiger A 1982 Solution of the Schrödinger equation by a spectral method *J. Comput. Phys.* **47** 412
- [42] Frigo M and Johnson S 1998 FFTW: an adaptive software architecture for the FFT *Proc. 1998 IEEE Int. Conf. on Acoustics, Speech and Signal Processing, ICASSP'98 (Cat.No.98CH36181)* vol 3 (Seattle, WA, USA: IEEE) pp 1381–4
- [43] Kosloff R and Tal-Ezer H 1986 A direct relaxation method for calculating eigenfunctions and eigenvalues of the Schrödinger equation on a grid *Chem. Phys. Lett.* **127** 223
- [44] Heather R and Metiu H 1987 An efficient procedure for calculating the evolution of the wave function by fast Fourier transform methods for systems with spatially extended wave function and localized potential *J. Chem. Phys.* **86** 5009
- [45] Ivanov M Y, Spanner M and Smirnova O 2005 Anatomy of strong field ionization *J. Mod. Opt.* **52** 165
- [46] Gräfe S, Doose J and Burgdörfer J 2012 Quantum phase-space analysis of electronic rescattering dynamics in intense few-cycle laser fields *J. Phys. B: At. Mol. Opt. Phys.* **45** 055002
- [47] Smirnova O, Spanner M and Ivanov M 2006 Coulomb and polarization effects in sub-cycle dynamics of strong-field ionization *J. Phys. B: At. Mol. Opt. Phys.* **39** S307
- [48] Seel M and Domcke W 1991 Femtosecond time-resolved ionization spectroscopy of ultrafast internal-conversion dynamics in polyatomic molecules: theory and computational studies *J. Chem. Phys.* **95** 7806
- [49] Yu C, Fu N, Zhang G and Yao J 2013 Dynamic stark effect on XUV-laser-generated photoelectron spectra: numerical experiment on atomic hydrogen *Phys. Rev. A* **87** 043405
- [50] Ning Q-C, Saalmann U and Rost J M 2018 Electron Dynamics Driven by Light-Pulse Derivatives *Phys. Rev. Lett.* **120** 033203
- [51] Shao H-C and Robicheaux F 2016 Photodetachment of  $h^-$  from intense, short, high-frequency pulses *Phys. Rev. A* **93** 053414
- [52] Toyota K, Tolstikhin O I, Morishita T and Watanabe S 2009 Slow electrons generated by intense high-frequency laser pulses *Phys. Rev. Lett.* **103** 153003
- [53] Yudin G L, Bandrauk A D and Corkum P B 2006 Chirped attosecond photoelectron spectroscopy *Phys. Rev. Lett.* **96** 063002
- [54] Barmaki S, Lanteigne P and Laulan S 2014 Control of two-photon double ionization of helium with intense chirped attosecond laser pulses *Phys. Rev. A* **89** 063406
- [55] Pronin E A, Starace A F and Peng L-Y 2011 Perturbation-theory analysis of ionization by a chirped few-cycle attosecond pulse *Phys. Rev. A* **84** 013417
- [56] Ziems K M, Bruhnke J, Engel V and Gräfe S Nuclear-electron correlation effects and their photoelectron imprint in molecular XUV ionisation *Frontiers Chem.* **821**
- [57] Tao L and Scrinzi A 2012 Photo-electron momentum spectra from minimal volumes: the time-dependent surface flux method *New J. Phys.* **14** 013021
- [58] Morales F, Bredtman T and Patchkovskii S 2016 iSURF: a family of infinite-time surface flux methods *J. Phys. B: At. Mol. Opt. Phys.* **49** 245001



1 **Non-Adiabatic Electronic and Vibrational Ring-Opening Dynamics**  
2 **Resolved with Attosecond Core-Level Spectroscopy**

3  
4 **S. Severino<sup>1,\*</sup>, K.M. Ziemis<sup>2,\*</sup>, M. Reduzzi<sup>1</sup>, A. Summers<sup>1</sup>, H.-W. Sun<sup>1</sup>, Y.-H. Chien<sup>1</sup>, S. Gräfe<sup>2,3,4</sup>, J.**  
5 **Biegert<sup>1,5,†</sup>**

6  
7 <sup>1</sup> *ICFO - Institut de Ciències Fotoniques, The Barcelona Institute of Science and Technology, 08860 Castelldefels (Barcelona),*  
8 *Spain*

9 <sup>2</sup> *Institute of Physical Chemistry and Max Planck School of Photonics, Friedrich-Schiller-Universität Jena, Germany*

10 <sup>3</sup> *Fraunhofer Institute for Applied Optics and Precision Engineering, Albert-Einstein-Str. 7, Jena, Germany*

11 <sup>4</sup> *Institute of Applied Physics and Abbe Center of Photonics, Friedrich-Schiller-Universität Jena, Germany*

12 <sup>5</sup> *ICREA, Pg. Lluís Companys 23, 08010 Barcelona, Spain*

13 <sup>†</sup> *Correspondence to: jens.biegert@icfo.eu*

14 <sup>\*</sup> *These authors contributed equally*

15

16 **Non-adiabatic dynamics and conical intersections play a central role in the chemistry of**  
17 **most polyatomic molecules, ranging from isomerization to heterocyclic ring opening and**  
18 **avoided photo-damage of DNA. Studying the underpinning correlated dynamics of**  
19 **electronic and nuclear wave packets is a major challenge in real-time and many times**  
20 **involves optically dark transient states. We show that attosecond core-level spectroscopy**  
21 **reveals the pathway dynamics of neutral furan across several conical intersections and**  
22 **resolves competitive relaxation pathways. Our method detects electronic-nuclear**  
23 **correlations, the dephasing of electronic coherence due to nuclear motion, and identifies**  
24 **the ring-opened isomer as the dominant product. These results demonstrate the efficacy**  
25 **of attosecond core level spectroscopy as a potent method to investigate the real-time**  
26 **dynamics of photochemical reaction pathways in complex molecular systems.**

27

28

29 Chemical reactions occur through the redistribution of valence electrons, which involves  
30 nuclear motion mediated by the Coulomb force. The coupling between electronic and  
31 nuclear degrees of freedom<sup>1</sup> can often be very strong, thus making the real-time  
32 investigation of electronic dynamics very challenging<sup>2</sup>. However, such non-adiabatic  
33 dynamics are essential to understand as they frequently occur in polyatomic molecular  
34 systems. Conical intersections<sup>3,4</sup> (CIs) provide fast and radiation-less energy relaxation  
35 between different potential energy surfaces (PESs), efficiently converting electronic  
36 excitation into vibrational excitation. Prominent examples are the retinal isomerization<sup>5</sup>  
37 of the vision process and the photo-stability of DNA bases<sup>6</sup>. Due to the importance of  
38 valence electron dynamics, many methods were developed; e.g., ultrafast two-  
39 dimensional spectroscopy<sup>7-11</sup>, attosecond transient absorption<sup>12-14</sup>, time-resolved  
40 photoelectron spectroscopy<sup>15-17</sup>, x-ray spectroscopy<sup>18,19</sup> and high harmonic  
41 spectroscopy<sup>20-25</sup>. Nevertheless, a tremendous challenge for existing methods is still the  
42 combined requirement for ultrafast time resolution<sup>26-28</sup>, the capability to disentangle time-  
43 overlapping electronic and nuclear dynamics<sup>29</sup>, and to follow radiation-less decay across  
44 transient and optical dark states<sup>30</sup>.

45

46 Here, we meet these combined challenges with attosecond core-level spectroscopy, which  
47 reveals the pathways and real-time conical intersection dynamics in photo-excited neutral  
48 furan and its electronic and vibrational dynamics on their native ultrafast time scale. The  
49 element and orbital selectivity of core-level spectroscopy, combined with attosecond  
50 temporal resolution, reveals the heterocyclic system's electronic and nuclear evolution  
51 predominantly into its ring-opening product. Moreover, we are able to resolve electronic  
52 and vibrational quantum beating during the pathway dynamics as inherent marker of the  
53 dynamic properties of the electronic and vibrational wave packets. We chose to



54 investigate furan ( $C_4H_4O$ ) since it serves as a prototypical system for heterocyclic organic  
55 rings<sup>31,32</sup>, which are essential building blocks of polymers, fuels, pharmaceuticals,  
56 atmospheric constituents, organic electronics and light-harvesting systems,  
57 agrochemicals, and more. Thus, their photochemical dynamics and relaxation processes  
58 are of great interest<sup>33</sup> for various applications. The results of our investigation  
59 demonstrate that the initially recognized potential of ultrafast x-ray absorption  
60 spectroscopy<sup>34-39</sup> is now matured with attosecond core-level spectroscopy<sup>14,34,35,40-42</sup> into  
61 a powerful analytical technique to elucidate complex chemical reaction dynamics.

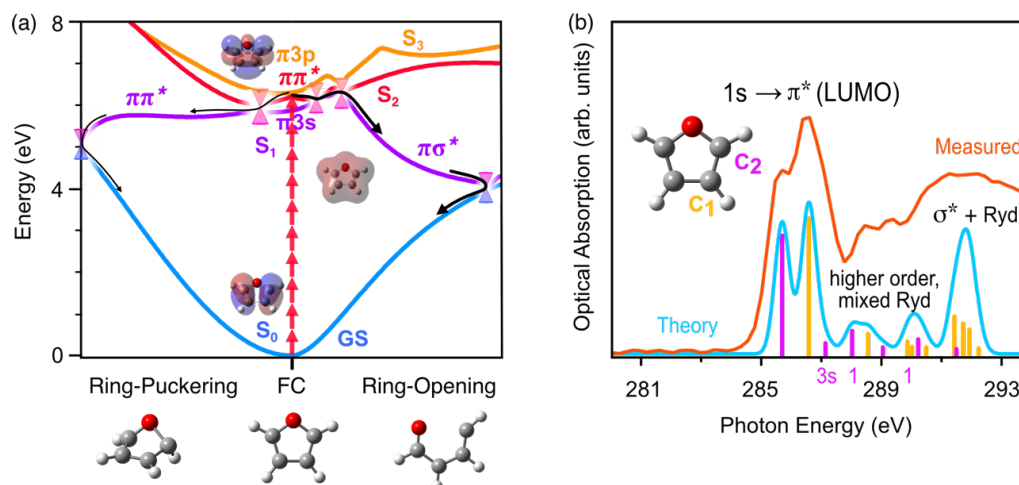
62

63 Attosecond core-level spectroscopy provides information on the unoccupied electronic  
64 density of states (UDOS) via dipole-allowed core-level K- or L-shell transitions; thus, the  
65 method is sensitive to optically dark states that cannot be detected with UV/VIS transient  
66 absorption methods, but that play a crucial role in many reaction pathways. We emphasize  
67 that core-level attosecond spectroscopy is distinct from general attosecond transient  
68 absorption spectroscopy (ATAS<sup>12,13,43</sup>) in that the absorption spectrum arises only due to  
69 transitions from the innermost core states, i.e., 1s (K) or 2s, 2p (L) states. The difference  
70 in binding energy between the core and valence states is sufficiently high such that  
71 screening ensures the valence UDOS to be probed is not significantly altered by removing  
72 a core electron. Shallow-bound semi-core or near-valence states, that are accessible with  
73 XUV radiation, may not have sufficient screening. Moreover, the absorption spectrum  
74 from shallow-bound semi-core to valence transitions incur multiplet effects<sup>44</sup>, i.e. a large  
75 number of transitions lead to the final state that have to be disentangled for a meaningful  
76 interpretation of the measured optical spectrum. For instance, ignoring spin, the 1s  
77 transition involves only one electron to the final state. In stark contrast, a 3p semi core  
78 hole ( $3p^5 3d^{N+1}$ ) would lead to 45 final states that determine the x-ray spectral shape

79

80 of the final state. Core-level transitions avoid such complications and are thus critical for  
 81 the unambiguous identification of electronic and nuclear effects<sup>45</sup>.

82



83

84 *Figure 1. (a) Potential energy surfaces showing the RO and RP pathways and the relevant electronic*  
 85 *states. Note that the excited states  $S_1$ ,  $S_2$ , and  $S_3$  refer to the adiabatic states, which change their electronic*  
 86 *configurations upon passage across the CIs. (b) Static (non-excited furan) carbon-edge XANES. The*  
 87 *measured absorption (red) and the calculated one (blue) are shown. Purple and yellow vertical lines*  
 88 *indicate spectral contributions from the two symmetry-distinguishable carbon atoms ( $C_1$  and  $C_2$ ). The*  
 89 *prominent peak at 286 eV originates from transitions from the two non-symmetry-equivalent carbon atoms*  
 90 *to the lowest unoccupied molecular orbital, LUMO ( $C(1s) \rightarrow \pi^*$ ). Further shown are contributions to higher*  
 91 *lying electronic states, such as Rydberg states, anti-bonding  $\sigma^*$ , and higher order  $\pi^*$  states (indicated as*  
 92 *1), see also SI S4.*

93

94 The relevant electronic states for photo-excited furan are shown in Fig. 1(a) Infrared  
 95 multi-photon absorption of 0.7 eV (1850 nm) photons excites the molecule from its  
 96 electronic ground state (GS) to the  $\pi\pi^*$  ( $S_2$ ) excited state. We note that the first excited  
 97 state, the  $\pi 3s$  ( $S_1$ ) Rydberg state, is optically dark in the Franck-Condon (FC) region while  
 98 the  $\pi 3p$  ( $S_3$ ) Rydberg state, which is energetically very close to the  $S_2$  state, possesses a

99 6x smaller oscillator strength (see SI S5.2). Theoretical investigations<sup>31,46–48</sup> have  
100 discussed two competitive pathways along which furan evolves after photo-excitation  
101 into the  $S_2$  state: (i) The molecule can evolve after  $\pi\pi^*$  excitation in the FC region via  
102 non-adiabatic passage through the  $S_2(\pi\pi^*)/S_1(3s)$  crossing and  $S_1(\pi\pi^*)/S_0$  conical  
103 intersections back to the initial GS ( $S_0$ ). This pathway leads to distortion of the nuclear  
104 framework out of the molecular plane, called ring-puckering (RP). (ii) Alternatively, RO  
105 occurs via 3 CIs.  $\pi\pi^*$  excitation in the FC region proceeds through a  $S_2(\pi\pi^*)/S_1(3s)$   
106 conical intersection and subsequently leads to a transient population of the optically dark  
107  $\pi\sigma^*$  state via non-adiabatic passage through the  $S_1(\pi\pi^*)/S_1(\pi\sigma^*)$  conical intersection. The  
108 anti-bonding  $\pi\sigma^*$  state is repulsive, thus leading to the fission of the C-O bond. At the  
109 ring-opened geometry, the system further relaxes through the  $S_1(\pi\sigma^*)/S_0$  conical  
110 intersection to the electronic ground state. This non-adiabatic pathway is called ring-  
111 opening (RO). Both pathways<sup>49</sup> lead to strong vibrational excitation.

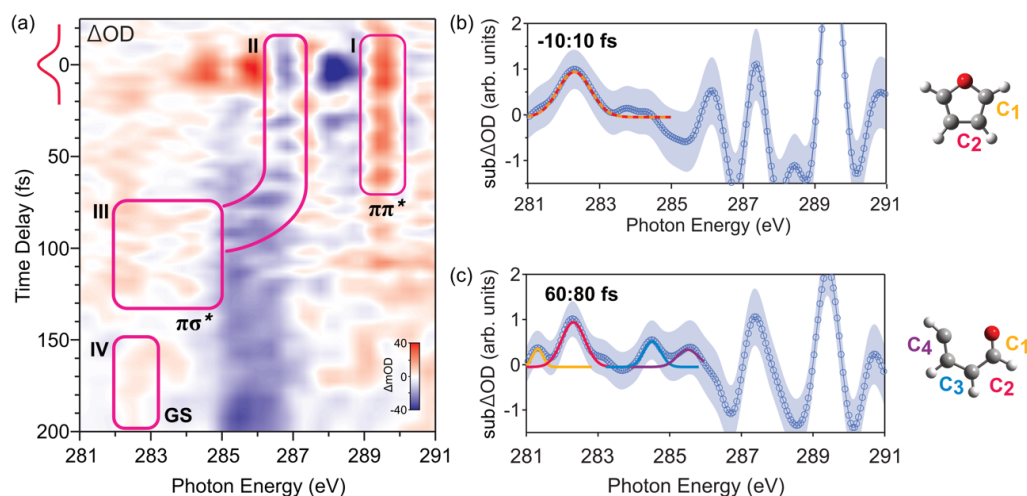
112 Previous experimental studies employed single- and strong-field excitation to identify  
113 these pathways. For instance, photoemission experiments successfully identified, yet with  
114 contradicting outcome, the photoproducts of RP<sup>50,51</sup> or RO<sup>52</sup> and inferred branching  
115 ratios<sup>53</sup> and diabatic passage<sup>42</sup> through a CI, but with insufficient resolution to identify  
116 and track the predicted electronic dynamics. A recent investigation with ultrafast electron  
117 diffraction on cyclohexadiene<sup>54</sup> has directly revealed the end product of conformational  
118 change. Femtosecond x-ray absorption spectroscopy on furfural<sup>55</sup> identified the chemical  
119 shift and population of PES, but it could not resolve electronic coherences or vibrational  
120 excitations upon diabatic passage. Thus far, despite encouraging progress<sup>55,56</sup>, identifying  
121 the non-adiabatic pathways with their expected electronic and vibrational coherences has  
122 been obscured by the challenge of temporally resolving and directly spectrally identifying

123 them<sup>19,57</sup>. Even more so, the evolution of the coupling of electronic and vibrational  
124 dynamics in real time has been largely elusive.

125 Here, we meet this challenge with IR-pump, core-level x-ray absorption near-edge  
126 spectroscopy (XANES) probe measurements with an attosecond soft x-ray beamline on  
127 gas-phase furan. We photo-excite furan inside a 4-mm-long effusive cell with 400-micron  
128 entrance and exit holes for pump and probe beams by multi-photon absorption of 17-fs-  
129 duration, carrier-envelope phase (CEP) stable pulses at 1850 nm (0.7 eV) with intensity  
130 up to 47 TW/cm<sup>2</sup> on target. This intensity yields photo-excited neutral states with an  
131 estimated negligible fraction of ionization of up to 2.5%. The attosecond soft-x-ray (SXR)  
132 pulse interrogates photo-excited furan in transmission by measuring the XANES with a  
133 homebuilt SXR spectrometer with 1/1000 resolution at the carbon K-edge at 284 eV. See  
134 the SI for experimental details.

135 Before detailing the temporal reaction dynamics, we highlight the sensitivity of XANES  
136 to orbital symmetries. For instance, in the GS, the molecule exhibits C<sub>2v</sub> symmetry, i.e.,  
137 only 2 of the 4 carbon atoms are distinct. This symmetry arises from the different binding  
138 of the two sets of carbon atoms (C<sub>1</sub> and C<sub>2</sub>) and sensitively registers as two energetically  
139 shifted core transitions C<sub>1,2</sub>(1s)→π\* in the x-ray absorption spectrum. Figure 1(b) shows  
140 the measured static (un-pumped) XANES, in which the two distinct carbon atoms are  
141 visible as double peaks around 285.6 eV and 286.5 eV. Further visible in the edge region,  
142 above the two LUMO peaks, are contributions from transitions into the Rydberg and σ\*  
143 states and higher order and mixed π\* states.

144



145

146

147 *Figure 2. (a) Differential attosecond-resolved XANES measurement. Indicated is the 17-fs pump pulse,*  
 148 *whose envelope is centered at “0” delay time. Further shown are areas “I”-“IV,” which facilitate*  
 149 *discussion of different spectral contributions in the text. Substantial changes in absorption around zero*  
 150 *delay time are observed, followed by various modulations to varying frequencies due to electronic and*  
 151 *vibrational coherences. (b). Time-integrated lineouts of the Sub $\Delta$ OD trace (see SI S3) across the energy*  
 152 *range of (a) during the pump pulse and (c) after relaxation to the  $\pi\sigma^*$  state along the RO pathway. This*  
 153 *corresponds to lineouts of the differential attosecond-resolved XANES measurement from which we*  
 154 *subtracted the overlap and long-lasting features that obscure the dynamics. A singly occupied molecular*  
 155 *orbital (SOMO) peak (b) in the pre-edge region, below 285 eV, indicates a  $\pi\pi^*$  excitation. Carbon-*  
 156 *heteroatom bond fission (RO) breaks the  $C_{2v}$  symmetry and, consequently, the excitation across 4 distinct*  
 157 *carbon atoms ( $C_1$ - $C_4$ ) registers as splitting of the singly-occupied molecular orbital (SOMO) peak into 4*  
 158 *absorption peaks (c). See text and SI for details.*

159

160 We now turn to investigate the dynamics of photo-excited furan and will follow its time  
 161 evolution. Figure 2(a) shows the measured differential absorption spectrum, which  
 162 displays the changes in the XANES relative to un-excited (ground-state) furan. In the  
 163 following, we will use the combination of experiment and theory to elucidate the entire  
 164 non-adiabatic evolution of the furan system. We focus on the temporal features and pre-  
 165 edge spectral region, while providing a full spectral analysis in SI S6. Our theoretical

166 methods include coupled cluster singles and doubles calculations<sup>58</sup> to calculate the XAS  
167 spectra, and for the excited-state dynamics, semi-classical ab-initio on-the-fly surface-  
168 hopping dynamics including non-adiabatic and laser couplings<sup>59</sup>; see the SI S8 for  
169 detailed information.

170

171 **Early times – coherent electronic wave packet dynamics induced at the 1<sup>st</sup> conical**  
172 **intersection  $S_2(\pi\pi^*)/S_1(\pi 3s)$**

173

174 Figure 2a shows that very early delay times feature rich dynamics. We attribute the initial  
175 pump pulse interaction to an excitation into the  $\pi\pi^*$  ( $S_2$ ) state of neutral furan by  
176 comparison of the spectral data to various theoretical simulations (see supplement S5 and  
177 figures therein). Optical excitation of one electron from the highest occupied molecular  
178 orbital (HOMO) into the lowest unoccupied molecular orbital (LUMO) by the pump  
179 pulse creates singly occupied molecular orbitals (SOMO). It registers as a new absorption  
180 peak in the differential absorption spectrum: the appearance of the single SOMO peak in  
181 the pre-edge region (below 285 eV), shown as a line out in Fig. 2(b), is due to electronic  
182 excitation of the  $\pi\pi^*$  ( $S_2$ ) state in the FC region and core excitation of  $C_{1,2}(1s)$  into the  
183 hole created in the  $\pi$  orbital. Subsequently, analysis of the time evolution of different  
184 energetic signatures above the edge region provides insight into the electronic coupling  
185 and dynamics. Immediately apparent in Fig. 2(a) at early delay times are strong  
186 modulations in the differential absorption spectrum, both positive (red) and negative  
187 (blue), and across the entire shown photon energy range. The strong modulations in the  
188 differential absorption spectrum are especially pronounced at 287 eV and 289.4 eV  
189 (signal region “I” and “II”), shown as a line-out of in Fig. 3(a). The two differential  
190 absorption curves reveal rapid modulations at a frequency of  $63 \pm 9$  THz, corresponding

191 to a period of 16 fs; see inset in Fig. 3(a). Interestingly, these modulations are out-of-  
192 phase to each other and reduce in depth after about 80 fs.

193

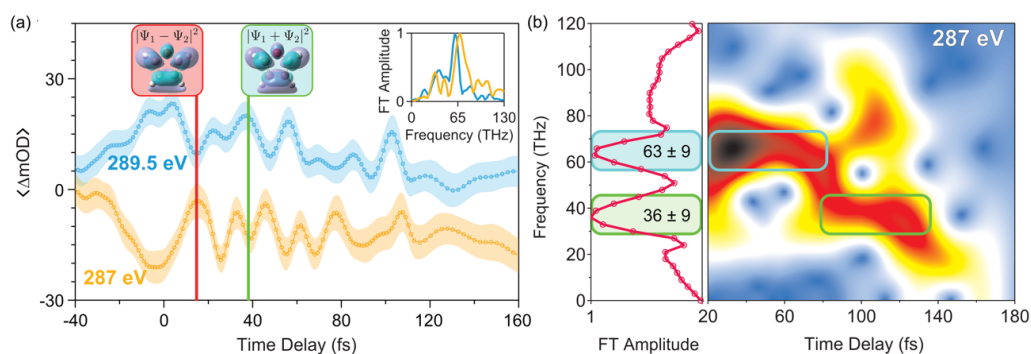
194 To elucidate the origin of this behavior, Fig. 4(a) shows the calculated population  
195 dynamics within the first electronic excited states. The remarkable agreement with the  
196 measurement allows us to explain the observed behavior: we find from the semi-classical  
197 dynamics that already after 12 fs  $\pi\pi^*$  population traverses the  $S_2(\pi\pi^*)/S_1(\pi3s)$  conical  
198 intersection. Passage through the conical intersection simultaneously populates the first  
199 ( $S_1$ ) and the second ( $S_2$ ) excited states. Splitting of the electronic wavepacket upon  
200 crossing of the CI thus establishes a fixed phase relation between the two evolving  
201 populations which manifests itself in quantum beats due to the intrinsic electronic  
202 coherence (see S7 of SI for more details). The measured beat frequency of  $63 \pm 9$  THz is  
203 in excellent agreement with theory, which predicts frequencies of  $60 \pm 6$  THz for RO and  
204  $62 \pm 9$  THz for RP; see Fig. 4(c). Simulations confirm the dephasing of the coherence  
205 around 60 fs due to the different dispersion of PES, in good agreement with the  
206 measurement.

207

208 Further, the coherent electronic motion of charge density across the two distinct carbon  
209 atoms of furan exhibits a  $\pi$ -phase shift between the spatially separate nuclear sites, shown  
210 as red and green insets in Fig. 3(a) and SI Fig. S18. Such out-of-phase oscillations of  
211 electronic quantum beats have been theoretically predicted<sup>60</sup> but not experimentally  
212 detected in x-ray absorption. They register via the complex transition dipole matrix  
213 element of the core-transition to the common final (valence) state as anti-phase evolution  
214 of quantum beats at the two energies that are distinct for the two carbon sites. The  
215 detection of the beating signifies that the measurement provides site-specific tracking of

216 the coherent wave-packet evolution across the molecule's nuclear structure and clocking  
 217 electronic coherence between different states. The electronic quantum beating is  
 218 predominant in spectral regions "I" and "II" as in these spectral areas, the two involved  
 219 valence states  $S_1$  and  $S_2$  have a common final state in the x-ray absorption (for a more  
 220 detailed discussion see SI S7).

221



222

223

224 *Figure 3. (a) Lineout data from the differential XANES (Fig. 2(a)) at two distinct energies (negative and*  
 225 *positive differences), regions I and II). After the buildup of the negative (yellow) and positive (blue)*  
 226 *absorption signals, pronounced oscillations with a frequency of 63 THz are observed. This is due to*  
 227 *coherent electronic wave packet dynamics of states  $S_1$  and  $S_2$ , across the molecule's nuclear structure with*  
 228 *two distinct carbon sites, leading to quantum beating in anti-phase. The relevant wave packet*  
 229 *superpositions are shown inside the red and green panels above the curves. (b) A windowed Fourier*  
 230 *analysis of the 287-eV curve in (a) reveals the time evolution of frequencies. The persistence of a frequency*  
 231 *over a time range reveals coherence. In the case of furan, we find that the electronic coherence, with  $63$*   
 232  *$\pm 9$  THz beat frequency, dephases due to the buildup of coherent vibrational excitation at a lower frequency*  
 233 *of  $36 \pm 9$  THz.*

234

235 **Vibrational dynamics in the excited electronic state – 2<sup>nd</sup> conical intersection**

236  **$S_1(\pi\pi^*)/S_1(\pi\sigma^*)$**

237



238 Following the dynamic evolution of the coherent mode at 63 THz, we observe switchover  
239 around 80 fs to a lower-frequency mode at  $36 \pm 9$  THz (Fig. 3b). This mode decays after  
240 140 fs. Our combined experimental and theoretical analysis shows in the following that  
241 this switchover is a direct real time observation of electron-nuclear correlation around a  
242 conical intersection manifested as a change in quantum beating: the semi-classical  
243 dynamics shows that for the RO pathway the nuclear wave packet passes through another  
244 conical intersection,  $S_1(\pi\pi^*)/S_1(\pi\sigma^*)$ , after around 58 fs. This passage results in a change  
245 of the  $S_1$  state's electronic character to the optically dark dissociative  $\pi\sigma^*$  state (see SI  
246 S6). The appearance of the  $36 \pm 9$  THz frequency mode originates from coherent  
247 vibrational motion along this dissociative state as vibrational quantum beating. A normal  
248 mode analysis on the ensemble of trajectories allows us to identify a 37 THz mode as  
249 being unique to the RO pathway (see Fig. 4(d), SI S11) and resembling the C-O bond  
250 fission. This nuclear wave packet motion is accompanied by the dephasing of the coherent  
251 electronic wave-packet motion due to the rapidly increasing energy separation of  
252 electronic states along the RO pathway (Fig. 4(b)). The stretching of the nuclear  
253 framework destabilizes the  $S_2$  and  $S_3$  PES, while it stabilizes  $S_1$  (see Fig. 1(a)). Thus, we  
254 clearly see the interplay of nuclear and electronic wave packet as change in the frequency  
255 of the quantum beating from 63 THz to 36 THz around the  $S_1(\pi\pi^*)/S_1(\pi\sigma^*)$  conical  
256 intersection. The experimentally retrieved time scales of this coupled nuclear and  
257 electronic dynamics are in excellent agreement with the results of the simulations.

258 In addition, the increasing PES gradient of the RO trajectory results in strong deformation  
259 of the nuclear framework and coherent vibrational excitation. This is visible as a large  
260 chemical shift from 286.5 to 284 eV in the differential absorption spectrum; see Fig. 2(a)  
261 area "II"-"III". The accompanying observed splitting of the single SOMO peak (Fig. 2(c))  
262 into 4 peaks after about 80 fs is the unmistakable signature of ring scission due to the

263 breakage of  $C_{2v}$  molecular symmetry and of presence of electronic population in the  $\pi\sigma^*$   
264 dark state (see also SI S6 and S12).

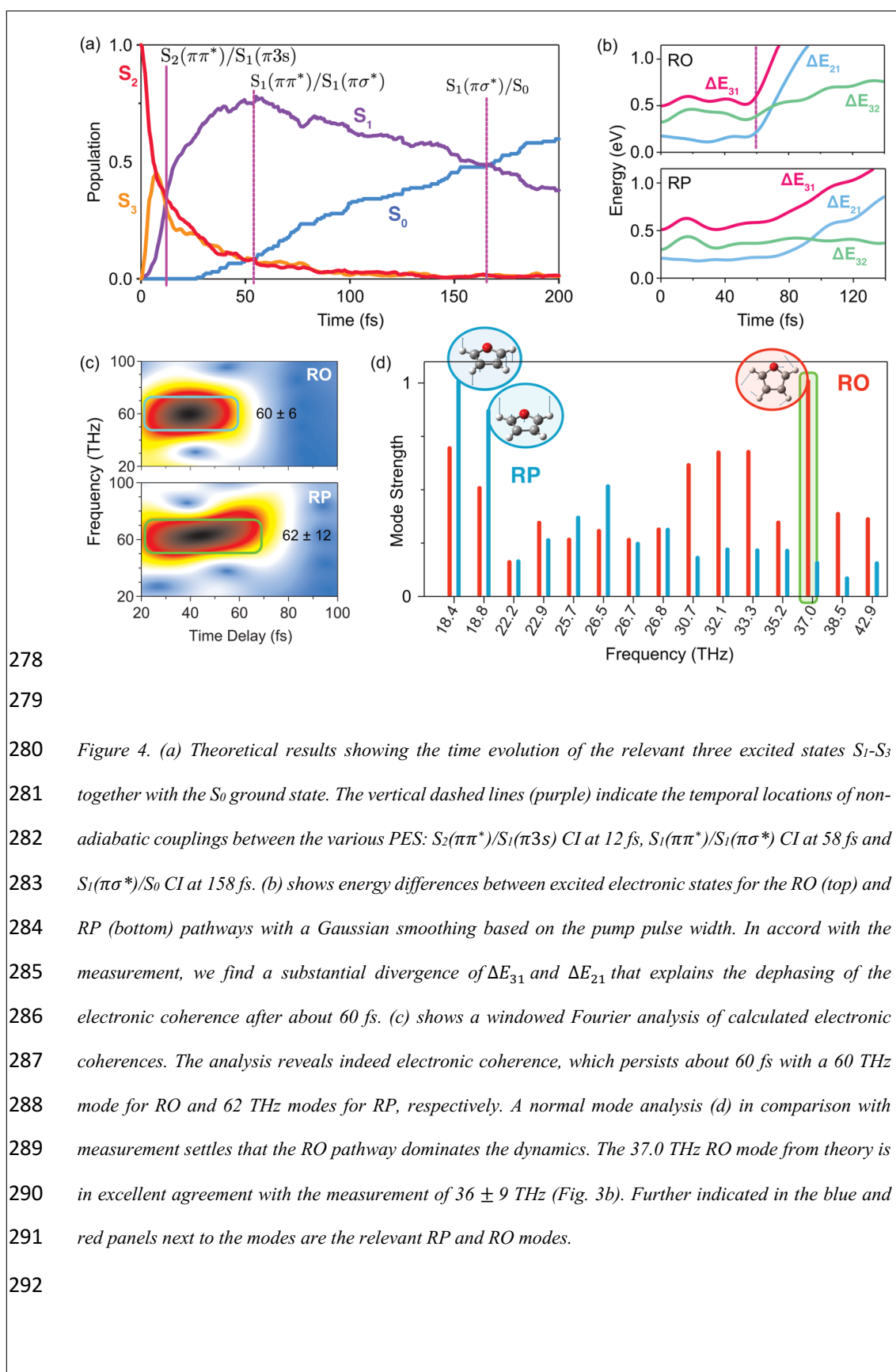
265

266 **Later times, ring-opening to the GS – the 3<sup>rd</sup> conical intersection  $S_1(\pi\sigma^*)/S_0$**

267

268 Lastly, we find that the vibrational coherence and the spectral features of the  $\pi\sigma^*$  state  
269 vanish after 140 fs (Fig. 3 and SI S6). This is in excellent agreement with the theory which  
270 predicts passage along the RO trajectory through the  $S_1(\pi\sigma^*)/S_0$  conical intersection after  
271 158 fs that manifest as a long-lasting signal around 282 eV unique to RO (Fig. 2(a), area  
272 “IV”, see also SI S6). This, combined with the observation of the SOMO peak splitting  
273 (Fig. 2(c)), and the measured vibrational coherence with a frequency of  $36 \pm 9$  THz (c.f.  
274 Fig. 3(b) and Fig. 4(d)) are clear evidence of the system’s evolution towards RO. Theory  
275 predicts a probability of 76% for the observed relaxation channel along the RO  
276 coordinate. This is in excellent agreement with the measurement.

277



278

279

280 *Figure 4. (a) Theoretical results showing the time evolution of the relevant three excited states  $S_1$ - $S_3$* 281 *together with the  $S_0$  ground state. The vertical dashed lines (purple) indicate the temporal locations of non-*282 *adiabatic couplings between the various PES:  $S_2(\pi\pi^*)/S_1(\pi 3s)$  CI at 12 fs,  $S_1(\pi\pi^*)/S_1(\pi\sigma^*)$  CI at 58 fs and*283  *$S_1(\pi\sigma^*)/S_0$  CI at 158 fs. (b) shows energy differences between excited electronic states for the RO (top) and*284 *RP (bottom) pathways with a Gaussian smoothing based on the pump pulse width. In accord with the*285 *measurement, we find a substantial divergence of  $\Delta E_{31}$  and  $\Delta E_{21}$  that explains the dephasing of the*286 *electronic coherence after about 60 fs. (c) shows a windowed Fourier analysis of calculated electronic*287 *coherences. The analysis reveals indeed electronic coherence, which persists about 60 fs with a 60 THz*288 *mode for RO and 62 THz modes for RP, respectively. A normal mode analysis (d) in comparison with*289 *measurement settles that the RO pathway dominates the dynamics. The 37.0 THz RO mode from theory is*290 *in excellent agreement with the measurement of  $36 \pm 9$  THz (Fig. 3b). Further indicated in the blue and*291 *red panels next to the modes are the relevant RP and RO modes.*

292

293 We have shown that attosecond core-level spectroscopy is a potent method to reveal  
294 correlated multi-body dynamics in a complex molecular system on its native ultrafast  
295 timescale. We demonstrate the technique provides several different observables that  
296 allow us to disentangle the entire time-evolution of complex-coupled molecular  
297 electronic and vibrational dynamics after photo-excitation. The method's particular  
298 sensitivity to electronic coherences, phases, optically dark states, and vibrational  
299 dynamics allows to resolve and identify non-adiabatic passages, changes in a system's  
300 electronic character, and quantum beats. Further, core-level spectroscopy is state and  
301 element-specific, permitting spatially resolving electronic wave-packet dynamics across  
302 the molecular framework. This study on furan disentangles the system's whole non-  
303 adiabatic passage across three conical intersections and reveals the entire buildup of CI-  
304 mediated electronic coherences with their dephasing induced by a coupled vibrational  
305 cooling to the ring-opening ground state. Such combined energy and time resolution of  
306 attosecond core-level spectroscopy reveals hitherto inaccessible insight into molecular  
307 systems' real-time electronic and nuclear dynamics. Armed with intricate knowledge of a  
308 molecular system's different couplings and phase evolution, this may provide a decisive  
309 new basis for an engineered approach to quantum control. Insight into vibronic couplings  
310 may allow arresting dephasing of electronic excitations to facilitate efficient molecular  
311 reaction dynamics, to study the correlated multi-body dynamics leading to isomerization  
312 (Azo and retinal), or to understand energy relaxation dynamics in DNA.

313

#### 314 Methods

315 In our experiment, a 1.8  $\mu\text{m}$  CEP-stable 17 fs strong-field pump with estimated on-target  
316 peak intensity of  $4.7 \times 10^{13}$  W/cm<sup>2</sup> excites the furan molecule. A time-delayed, isolated  
317 attosecond probe pulse allows following the excited-state dynamics. This pulse is

318 obtained through high harmonics generation by tightly focusing a portion of the sub-2  
319 cycle 1.8  $\mu\text{m}$  pulse in a gas cell filled with helium at high pressure and has a retrieved  
320 temporal duration of 165 as. Both pump and probe beams are focused collinearly into a  
321 sample cell with 400  $\mu\text{m}$  entrance and exit apertures, where the furan vapor is delivered.  
322 The experimental results were accompanied by an advanced combination of state-of-the-  
323 art theoretical methods: the nonadiabatic excited-state dynamics is simulated via ab  
324 initio on-the-fly surface hopping including non-adiabatic and laser coupling<sup>59</sup>. This  
325 enables us to sample all possible excited-state relaxation pathways without presuming  
326 reaction modes while incorporating all relevant quantum and strong-field effects. For  
327 selected structures along the trajectories, x-ray absorption spectra were calculated using  
328 the core-valence-separation scheme in the frozen-core equation of motion model for  
329 electronically excited states on the coupled cluster singles and doubles level of theory (fc-  
330 CVS-EOM-EE-CCSD)<sup>58</sup>.  
331 More detailed information, figures and references can be found in the supporting  
332 information.

333

### 334 Data availability

335 All data that support the plots within this paper and other findings of this study are  
336 available from the corresponding authors upon reasonable request.

337

### 338 Acknowledgment

339 J.B. acknowledges financial support from the European Research Council for ERC  
340 Advanced Grant “TRANSFORMER” (788218), ERC Proof of Concept Grant “miniX”  
341 (840010), FET-OPEN “PETACom” (829153), FET-OPEN “OPTologic” (899794),  
342 FET-OPEN “TwistedNano” (101046424), Laserlab-Europe (871124), Marie

343 Skłodowska-Curie ITN “smart-X” (860553), MINECO for Plan Nacional PID2020–  
344 112664 GB-I00; AGAUR for 2017 SGR 1639, MINECO for “Severo Ochoa” (CEX2019-  
345 000910-S), Fundació Cellex Barcelona, the CERCA Programme/Generalitat de  
346 Catalunya, and the Alexander von Humboldt Foundation for the Friedrich Wilhelm  
347 Bessel Prize. S.S. acknowledges Marie Skłodowska-Curie Grant Agreement No. 713729  
348 (COFUND). M.R. and A.S. acknowledge Marie Skłodowska-Curie Grant Agreement No.  
349 754510 (PROBIST). K.M.Z. and S.G. are part of the Max Planck School of Photonics  
350 supported by BMBF, Max Planck Society, and Fraunhofer Society. S.G. highly  
351 acknowledges support from the European Research Council via the Consolidator Grant  
352 QUEM-CHEM (772676) and the CRC 1375 NOA –“Nonlinear Optics down to Atomic  
353 scales”. K.M.Z. acknowledges fruitful discussions with Martin Richter. We thank J.  
354 Menino and C. Dengra for their technical support.

355

#### 356 Authors’ contribution

357 J.B. supervised the project. S.S. and M.R. performed the experiments with support from  
358 J.B., A.S., H-W S. and Y-H C.; S.S. analyzed experimental data with support from M.R.,  
359 J.B. and K.M.Z.; K.M.Z. performed the quantum chemical and semi-classical dynamics  
360 calculations with support of S.G.; K.M.Z. and S.G. analyzed theory data; J.B. wrote the  
361 manuscript with help from S.S., K.M.Z. and S.G.

362

#### 363 Competing interest declaration

364 The authors declare no competing financial interests.

365

#### 366 Additional information

367 Supplementary Information is available for this paper.

368 Correspondence and requests for materials should be addressed to J.B.

369 Reprints and permissions information is available at [www.nature.com/reprints](http://www.nature.com/reprints)

370

### 371 Bibliography

- 372 1. Schmidtke, H.-H. I. B. Bersuker, V. Z. Polinger: *Vibronic Interactions in Molecules*  
373 *and Crystals*, Vol. 49 aus: Springer Series in Chemical Physics. Springer-Verlag  
374 Berlin, Heidelberg, New York, London, Paris, Tokyo 1989. 422 Seiten, Preis: DM  
375 178,—. *Berichte der Bunsengesellschaft für physikalische Chemie* **94**, 896–897  
376 (1990).
- 377 2. Domcke, W. & Stock, G. Theory of ultrafast nonadiabatic excited-state processes  
378 and their spectroscopic detection in real time. *Advances in Chemical Physics* **100**,  
379 15 (1997).
- 380 3. Worth, G. A. & Cederbaum, L. S. BEYOND BORN-OPPENHEIMER: Molecular  
381 Dynamics Through a Conical Intersection. *Annu. Rev. Phys. Chem.* **55**, 127–158  
382 (2004).
- 383 4. Yarkony, D. R. Diabolical conical intersections. *Rev. Mod. Phys.* **68**, 985–1013  
384 (1996).
- 385 5. Polli, D. *et al.* Conical intersection dynamics of the primary photoisomerization  
386 event in vision. *Nature* **467**, 440–443 (2010).
- 387 6. Crespo-Hernández, C. E., Cohen, B., Hare, P. M. & Kohler, B. Ultrafast excited-state  
388 dynamics in nucleic acids. *Chemical reviews* **104**, 1977–2020 (2004).

- 389 7. Sommer, E., Sio, A. D., Mena-Osteritz, E., Bäuerle, P. & Lienau, C. Two-dimensional  
390 electronic spectroscopy reveals ultrafast dynamics at a conical intersection in an  
391 organic photovoltaic material. *EPJ Web Conf.* **205**, 06014 (2019).
- 392 8. Borrego-Varillas, R. *et al.* Two-dimensional UV spectroscopy: a new insight into the  
393 structure and dynamics of biomolecules. *Chemical Science* **10**, 9907–9921 (2019).
- 394 9. Hamm, P. & Zanni, M. *Concepts and methods of 2D infrared spectroscopy*.  
395 (Cambridge University Press, 2011).
- 396 10. Jonas, D. M. Two-dimensional femtosecond spectroscopy. *Annual review of*  
397 *physical chemistry* **54**, 425 (2003).
- 398 11. Cho, M., Brixner, T., Stiopkin, I., Vaswani, H. & Fleming, G. R. Two dimensional  
399 electronic spectroscopy of molecular complexes. *Journal of the Chinese Chemical*  
400 *Society* **53**, 15–24 (2006).
- 401 12. Warrick, E. R., Cao, W., Neumark, D. M. & Leone, S. R. Probing the dynamics of  
402 Rydberg and valence states of molecular nitrogen with attosecond transient  
403 absorption spectroscopy. *The Journal of Physical Chemistry A* **120**, 3165–3174  
404 (2016).
- 405 13. Lucchini, M. *et al.* Attosecond dynamical Franz-Keldysh effect in polycrystalline  
406 diamond. *Science* **353**, 916–919 (2016).
- 407 14. Schultze, M. *et al.* Attosecond band-gap dynamics in silicon. *Science* **346**, 1348–  
408 1352 (2014).
- 409 15. Liu, Y., Knopp, G., Qin, C. & Gerber, T. Tracking ultrafast relaxation dynamics of  
410 furan by femtosecond photoelectron imaging. *Chemical Physics* **446**, 142–147  
411 (2015).



- 412 16. Fuji, T. *et al.* Ultrafast photodynamics of furan. *The Journal of Chemical Physics*  
413 **133**, 234303 (2010).
- 414 17. Filatov, M., Lee, S., Nakata, H. & Choi, C.-H. Signatures of Conical Intersection  
415 Dynamics in the Time-Resolved Photoelectron Spectrum of Furan: Theoretical  
416 Modeling with an Ensemble Density Functional Theory Method. *IJMS* **22**, 4276  
417 (2021).
- 418 18. Neville, S. P., Chergui, M., Stolow, A. & Schuurman, M. S. Ultrafast X-ray  
419 spectroscopy of conical intersections. *Phys. Rev. Lett.* **120**, 243001 (2018).
- 420 19. Hua, W. *et al.* Monitoring conical intersections in the ring opening of furan by  
421 attosecond stimulated X-ray Raman spectroscopy. *Struct. Dyn.* **3**, 023601 (2016).
- 422 20. Baker, S. *et al.* Probing proton dynamics in molecules on an attosecond time scale.  
423 *Science* **312**, 424–427 (2006).
- 424 21. Haessler, S. *et al.* Attosecond imaging of molecular electronic wavepackets. *Nature*  
425 *Physics* **6**, 200–206 (2010).
- 426 22. Li, W. *et al.* Time-resolved dynamics in N<sub>2</sub>O<sub>4</sub> probed using high harmonic  
427 generation. *Science* **322**, 1207–1211 (2008).
- 428 23. Torres, R. *et al.* Probing orbital structure of polyatomic molecules by high-order  
429 harmonic generation. *Physical review letters* **98**, 203007 (2007).
- 430 24. Wörner, H. J., Bertrand, J. B., Kartashov, D. V., Corkum, P. B. & Villeneuve, D. M.  
431 Following a chemical reaction using high-harmonic interferometry. *Nature* **466**,  
432 604–607 (2010).
- 433 25. Smirnova, O. *et al.* High harmonic interferometry of multi-electron dynamics in  
434 molecules. *Nature* **460**, 972–977 (2009).

- 435 26. Robinson, M. S. *et al.* Ultrafast Photo-ion Probing of the Ring-Opening Process in  
436 Trans-Stilbene Oxide. *Chemistry – A European Journal* **27**, 11418–11427 (2021).
- 437 27. Weinkauff, R., Lehr, L., Schlag, E. W., Salzmann, S. & Marian, C. M. Ultrafast  
438 dynamics in thiophene investigated by femtosecond pump probe photoelectron  
439 spectroscopy and theory. *Physical Chemistry Chemical Physics* **10**, 393–404 (2008).
- 440 28. Wolf, T. J. A. *et al.* The photochemical ring-opening of 1,3-cyclohexadiene imaged  
441 by ultrafast electron diffraction. *Nat. Chem.* **11**, 504–509 (2019).
- 442 29. Ruckenbauer, M., Mai, S., Marquetand, P. & González, L. Revealing Deactivation  
443 Pathways Hidden in Time-Resolved Photoelectron Spectra. *Sci Rep* **6**, 35522 (2016).
- 444 30. Srinivasan, R., Feenstra, J. S., Park, S. T., Xu, S. & Zewail, A. H. Dark structures in  
445 molecular radiationless transitions determined by ultrafast diffraction. *Science* **307**,  
446 558–563 (2005).
- 447 31. Gromov, E. V., Trofimov, A. B., Gatti, F. & Köppel, H. Theoretical study of  
448 photoinduced ring-opening in furan. *The Journal of Chemical Physics* **133**, 164309  
449 (2010).
- 450 32. Gavrilov, N., Salzmann, S. & Marian, C. M. Deactivation via ring opening: A  
451 quantum chemical study of the excited states of furan and comparison to  
452 thiophene. *Chemical Physics* **349**, 269–277 (2008).
- 453 33. Ashfold, M. N. *et al.* Exploring the dynamics of the photoinduced ring-opening of  
454 heterocyclic molecules. *The journal of physical chemistry letters* **8**, 3440–3451  
455 (2017).
- 456 34. Cousin, S. L. *et al.* High-flux table-top soft x-ray source driven by sub-2-cycle, CEP  
457 stable, 1.85- $\mu\text{m}$  1-kHz pulses for carbon K-edge spectroscopy. *Opt. Lett., OL*  
458 **39**, 5383–5386 (2014).

- 459 35. Saito, N. *et al.* Real-time observation of electronic, vibrational, and rotational  
460 dynamics in nitric oxide with attosecond soft x-ray pulses at 400 eV. *Optica* **6**,  
461 1542–1546 (2019).
- 462 36. Kraus, P. M., Zürch, M., Cushing, S. K., Neumark, D. M. & Leone, S. R. The ultrafast  
463 X-ray spectroscopic revolution in chemical dynamics. *Nature Reviews Chemistry* **2**,  
464 82–94 (2018).
- 465 37. Chen, M. & Lopata, K. First-principles simulations of X-ray transient absorption for  
466 probing attosecond electron dynamics. *Journal of chemical theory and*  
467 *computation* **16**, 4470–4478 (2020).
- 468 38. Kleine, C. *et al.* Soft X-ray Absorption Spectroscopy of Aqueous Solutions Using a  
469 Table-Top Femtosecond Soft X-ray Source. *J. Phys. Chem. Lett.* **10**, 52–58 (2019).
- 470 39. Liao, C.-T. & Sandhu, A. XUV Transient Absorption Spectroscopy: Probing Laser-  
471 Perturbed Dipole Polarization in Single Atom, Macroscopic, and Molecular  
472 Regimes. *Photonics* **4**, 17 (2017).
- 473 40. Buades, B. *et al.* Attosecond state-resolved carrier motion in quantum materials  
474 probed by soft x-ray XANES. *Applied Physics Reviews* **8**, 011408 (2021).
- 475 41. Moulet, A. *et al.* Soft x-ray excitonics. *Science* **357**, 1134–1138 (2017).
- 476 42. Zinchenko, K. S. *et al.* Sub-7-femtosecond conical-intersection dynamics probed at  
477 the carbon K-edge. *Science* **371**, 489–494 (2021).
- 478 43. Wang, H. *et al.* Attosecond time-resolved autoionization of argon. *Physical review*  
479 *letters* **105**, 143002 (2010).
- 480 44. De Groot, F. Multiplet effects in X-ray spectroscopy. *Coordination Chemistry*  
481 *Reviews* **249**, 31–63 (2005).

- 482 45. Sidiropoulos, T. P. H. *et al.* Probing the Energy Conversion Pathways between Light,  
483 Carriers, and Lattice in Real Time with Attosecond Core-Level Spectroscopy. *Phys.*  
484 *Rev. X* **11**, 041060 (2021).
- 485 46. Gromov, E. V., Trofimov, A. B., Vitkovskaya, N. M., Schirmer, J. & Köppel, H.  
486 Theoretical study of the low-lying excited singlet states of furan. *The Journal of*  
487 *Chemical Physics* **119**, 737–753 (2003).
- 488 47. Gromov, E. V. *et al.* Theoretical study of excitations in furan: Spectra and molecular  
489 dynamics. *The Journal of Chemical Physics* **121**, 4585–4598 (2004).
- 490 48. Stenrup, M. & Larson, Å. A computational study of radiationless deactivation  
491 mechanisms of furan. *Chemical Physics* **379**, 6–12 (2011).
- 492 49. Schalk, O. *et al.* Competition between ring-puckering and ring-opening excited  
493 state reactions exemplified on 5H-furan-2-one and derivatives. *J. Chem. Phys.* **152**,  
494 064301 (2020).
- 495 50. Adachi, S., Schatteburg, T., Humeniuk, A., Mitrić, R. & Suzuki, T. Probing ultrafast  
496 dynamics during and after passing through conical intersections. *Phys. Chem.*  
497 *Chem. Phys.* **21**, 13902–13905 (2019).
- 498 51. Spesyvtsev, R., Horio, T., Suzuki, Y.-I. & Suzuki, T. Excited-state dynamics of furan  
499 studied by sub-20-fs time-resolved photoelectron imaging using 159-nm pulses. *J.*  
500 *Chem. Phys.* **143**, 014302 (2015).
- 501 52. Urness, K. N. *et al.* Pyrolysis of furan in a microreactor. *J. Chem. Phys.* **139**, 124305  
502 (2013).
- 503 53. Gromov, E. V., Lévêque, C., Gatti, F., Burghardt, I. & Köppel, H. *Ab initio* quantum  
504 dynamical study of photoinduced ring opening in furan. *The Journal of Chemical*  
505 *Physics* **135**, 164305 (2011).

- 506 54. Wolf, T. J. A. *et al.* Imaging the ring opening reaction of 1,3-cyclohexadiene with  
507 MeV ultrafast electron diffraction. *EPJ Web Conf.* **205**, 07006 (2019).
- 508 55. Bhattacharjee, A. *et al.* Photoinduced Heterocyclic Ring Opening of Furfural:  
509 Distinct Open-Chain Product Identification by Ultrafast X-ray Transient Absorption  
510 Spectroscopy. *J. Am. Chem. Soc.* **140**, 12538–12544 (2018).
- 511 56. Zinchenko, K. S., Ardana-Lamas, F., Seidu, I. & Neville, S. P. Sub-7-femtosecond  
512 conical-intersection dynamics probed at the carbon K-edge. *6* (2021).
- 513 57. Maiuri, M., Garavelli, M. & Cerullo, G. Ultrafast Spectroscopy: State of the Art and  
514 Open Challenges. *J. Am. Chem. Soc.* **142**, 3–15 (2020).
- 515 58. Vidal, M. L., Feng, X., Epifanovsky, E., Krylov, A. I. & Coriani, S. New and Efficient  
516 Equation-of-Motion Coupled-Cluster Framework for Core-Excited and Core-Ionized  
517 States. *J. Chem. Theory Comput.* **15**, 3117–3133 (2019).
- 518 59. Richter, M., Marquetand, P., González-Vázquez, J., Sola, I. & González, L. SHARC: ab  
519 Initio Molecular Dynamics with Surface Hopping in the Adiabatic Representation  
520 Including Arbitrary Couplings. *J. Chem. Theory Comput.* **7**, 1253–1258 (2011).
- 521 60. Kobayashi, Y., Neumark, D. M. & Leone, S. R. Theoretical analysis of the role of  
522 complex transition dipole phase in XUV transient-absorption probing of charge  
523 migration. *Opt. Express* **30**, 5673 (2022).
- 524

## Supplementary Information

## Non-Adiabatic Electronic and Vibrational Ring-Opening Dynamics Resolved with Attosecond Core-Level Spectroscopy

S. Severino<sup>1,\*</sup>, K.M. Ziems<sup>2,\*</sup>, M. Reduzzi<sup>1</sup>, A. Summers<sup>1</sup>, H.-W. Sun<sup>1</sup>, Y.-H. Chien<sup>1</sup>,  
S. Gräfe<sup>2,3,4</sup>, J. Biegert<sup>1,5,†</sup>

<sup>1</sup> ICFO - Institut de Ciències Fòniques, The Barcelona Institute of Science and Technology, 08860 Castelldefels (Barcelona), Spain

<sup>2</sup> Institute of Physical Chemistry and Max Planck School of Photonics, Friedrich-Schiller-Universität Jena, Germany

<sup>3</sup> Fraunhofer Institute for Applied Optics and Precision Engineering, Albert-Einstein-Str. 7, Jena, Germany

<sup>4</sup> Institute of Applied Physics and Abbe Center of Photonics, Friedrich-Schiller-Universität Jena, Germany

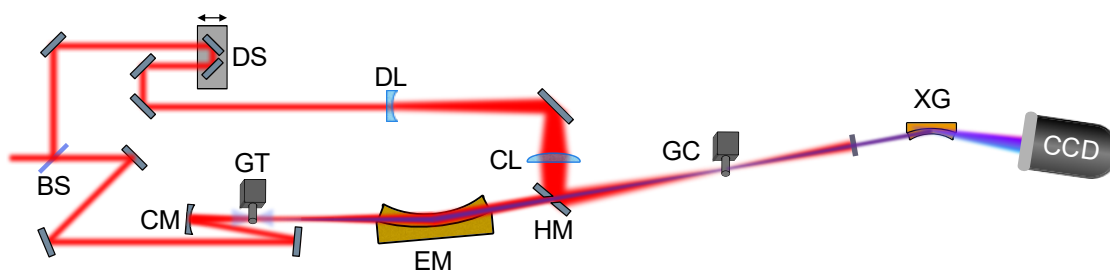
<sup>5</sup> ICREA, Pg. Lluís Companys 23, 08010 Barcelona, Spain

<sup>†</sup>Correspondence to: jens.biegert@icfo.eu

\*These authors contributed equally

### S1 Experimental Setup

X-ray absorption near-edge fine structure (XANES) spectroscopy was performed in a home-built soft X-ray (SXR) beamline in which a Mach-Zehnder interferometer permits attosecond-resolved pump-probe experiments; Fig. S1 shows a sketch of the setup. A 380- $\mu$ J, 1850-nm (0.7 eV), sub-2-cycle, CEP-stable pulse from a home-built 1-kHz laser system<sup>1</sup> is sent into the beamline. This pulse is split by 70/30 beam splitter (BS) and the low energy portion is directed as pump to the target. The high-energy part is focused into a high-pressure gas target (GT)<sup>2-4</sup>, with backing pressures up to 12 bar in Helium.



*Figure S1. Sketch of the pump-probe scheme in the Attosecond Beamline to study ultrafast carrier and lattice dynamics in graphite. The output of the laser system is separated by a beam-splitter (BS) into a pump and high-harmonic driver with a ratio 30/70. The transmitted beam is focused (CM) into a gas target (GT) filled with Helium to produce isolated attosecond soft X-ray pulses via high harmonic generation which constitute the probe of the experiment. The X-ray are focused by an ellipsoidal mirror (EM) onto the gas cell (GC), being transmitted through a holey mirror (HM). The transmitted X-rays is then dispersed by an X-ray grating (XG) and detected by an X-ray camera (CCD). The reflection of the beam-splitter constitutes the pump arm, synchronized with the probe with a delay stage (DS). The beam is first expanded (DL), then focused with a calcium fluoride lens (CL) onto the GC, where the beam is overlapped in space and time with the probe. The remaining pump light is then blocked by a movable slit (MS) and a second metallic filter (MF) to reduce stray light on the camera.*

The conditions for the present experiment were identical to the ones in Ref.<sup>4</sup> for producing an isolated 165-as pulse in the SXR water window with a spectrum from 250 to 500 eV (see Figure S2 a). The emerging SXR pulse is focused onto target with a SXR ellipsoidal mirror (EM) (Carl Zeiss AG) to a focal spot of  $15 \pm 5 \mu\text{m}$  FWHM. The target is a gas sample cell (GC) (4mm long) with 400 $\mu\text{m}$  holes to pass the laser beams and through which the vapors of furan (Sigma-Aldrich, concentration >95%) at room temperature exit. After the target, a 100 nm Sn filter (MF) is used to reject the pump light before the SXR radiation is dispersed with a home-built SXR spectrograph, which consists of a flat-field aberration-corrected and reflecting concave grating (2400 lines/mm; Hitachi High Technologies America, Inc.) and a cooled, back-illuminated CCD (PIXIS-XO; Princeton Instruments); the resolution of the spectrograph is 0.3 eV at the Carbon K-edge at 284 eV. The pump-probe delay is controlled via a closed-loop delay stage (Smaract GmbH) and the pump beam is recombined with the SXR one with a holey mirror (HM) before the target. In order to achieve high intensity, the pump beam is focused with a combination of a diverging ( $f = -300$  mm) and a focusing ( $f = 300$  mm) lenses, respectively DL and FL, at a relative distance of 40 cm. This ensures a large beam size on the holey mirror that allows to reduce losses and a focal waist of  $48 \pm 1 \mu\text{m}$ . This is almost three times larger than the probe spot size, which ensures probing a homogeneously pumped region of the sample by the much smaller SXR beam. A pump pulse duration of 17 fs was retrieved from a second-order-harmonic frequency-resolved optical gating (FROG) measurement (see Figure S2 c). This would lead to a peak pump intensity of  $6.4 \pm 2 \times 10^{13}$  W/cm<sup>2</sup>. However, considering the temporal profile of the pump, the useful area under the

temporal peak corresponds to an applicable peak intensity of  $4.7 \pm 2 \times 10^{13}$  W/cm<sup>2</sup> at the molecular target.

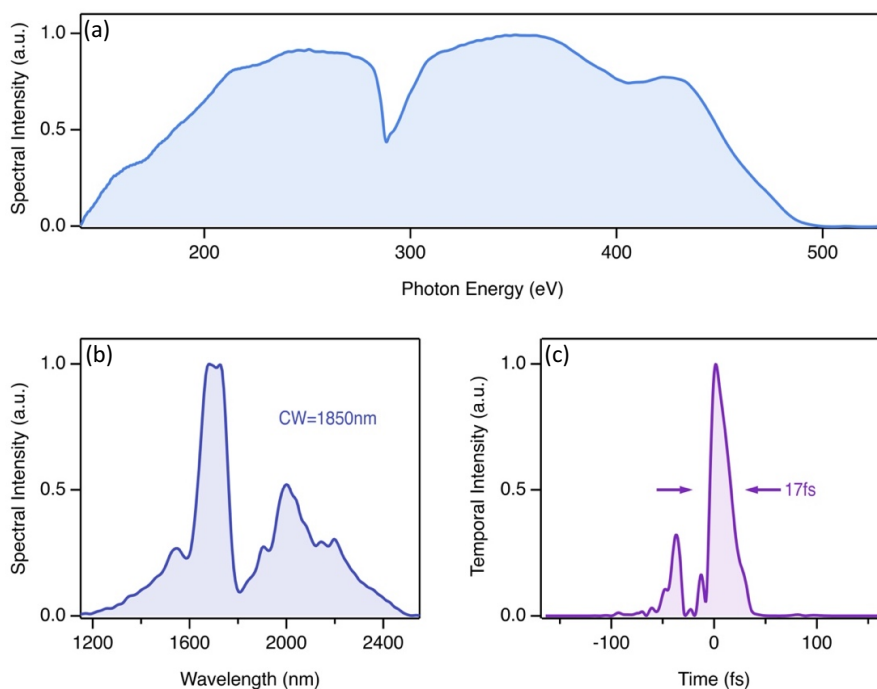


Figure S2. Spectral and temporal characterization of the pump and probe pulses. (a) the spectrally resolved SXR attosecond pulse. (b): measured spectral profile of the 1.85  $\mu$ m pump. (c) Reconstructed temporal profiles from second-harmonic frequency resolved optical gating (SH-FROG) measurements of the 1.85  $\mu$ m pump.

## S2 Data acquisition

The data acquisition protocol consists of a collection of series of spectra with different combinations of pump and probe beams on the sample. Shutters along the probe and the pump paths are synchronized with the CCD camera and were used to alternate in a sequence of 55 spectra of 15 seconds integration for the pump plus probe ( $I_{pp}$ ), 55 spectra of 15 s integration for the probe ( $I_0$ ) and 10 spectra of 15 s for the pump ( $I_p$ ) case. This scheme allows to minimize the shot-to-shot noise of the SXR beam; the pump-only acquisition enables the correct background subtraction of the  $I_{pp}$  spectra. Each delay step resulted in 35 min of measurement time. To account for possible slow drifts in the SXR flux, we normalize each background corrected pump plus probe spectrum to the corresponding  $I_0$  on two energy regions, one



before the carbon K-edge (260 to 280 eV) and one after (300 to 320 eV), both being far enough from the edge such that no pump induced effect are present. Finally, the contributions of each delay step are summed together and the resulting spectra,  $\overline{I_{pp}}$  and  $\overline{I_0}$ , are then used to build the differential absorption as  $\Delta OD = -\ln\left(\frac{\overline{I_{pp}}}{\overline{I_0}}\right)$ .

In the first part of the measurement (-45 fs to 115 fs), we used a pump-probe delay step size of 2.5 fs to catch all the details of the first part of the dynamic; afterwards the step size has been increased first to 5 fs (115 fs to 180 fs) and then to 20 fs (180 fs to 380 fs) in order to capture the long timescales dynamics.

In Fig. S3 we show the complete data set.

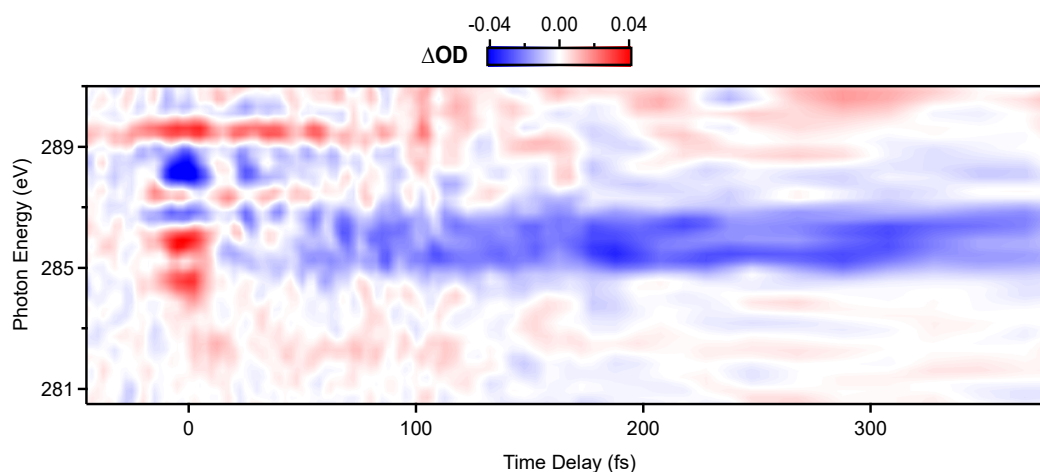


Figure S3. Time-dependent attosecond XANES measurement in furan. Experimentally retrieved OD trace. Positive delay indicates that pump pulse proceeded the probe one.

The error on each pixel in energy and time,  $\sigma_{\overline{\Delta OD}}$ , is estimated as the standard deviation of the average  $\overline{\Delta OD}$ , calculated from the standard deviation of the 55 repetitions of the  $\Delta OD$  trace. Figure S4 shows the maximum error at a few instances in energy and time range maximally to 7 mOD while they are typically below 4-5 mOD across the entire measures time-energy spectrum.

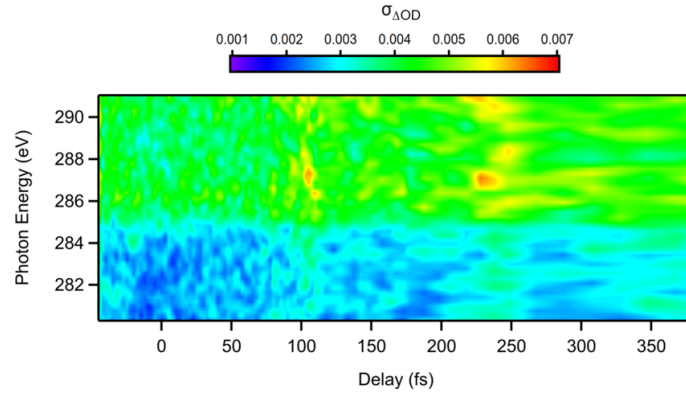


Figure S4. Analysis of the variance. The 2D map shows the standard deviation of the measured 55 absorption measurements across the time – energy trace.

### S3 Global Fit

The differential attosecond-resolved XANES measurement can be modelled to extract the rich dynamics in more details according to the following:

$$\overline{\Delta OD}(E, \tau) = \sum_{i=1}^3 OD_i(E) f_i(\tau).$$

Where  $f_i(\tau)$  is the convolution between a Gaussian and an exponential decay function:

$$f_i(\tau) = \frac{1}{\gamma_i \sqrt{2\pi}} e^{-\frac{1}{2} \left( \frac{\tau - \tau_{0i}}{\gamma_i} \right)^2} * e^{-\frac{\tau - \tau_{0i}}{\tau_i}}.$$

The number of independent spectral amplitudes was set to three to differentiate features of the overlap region, rich dynamics, and long-lasting contributions. The free parameters used in the fit are  $OD_i(E)$ , along with the width,  $\gamma_i$ , and the center,  $\tau_i^0$ , of the Gaussian function and the characteristic exponential decay time,  $\tau_i$ . In Fig. S5 and Tab. S1, we show the results of the fit done following a least square fitting procedure. We can see how they reproduce the main characteristics of the data. The three independent components have very distinct temporal behavior:  $f_1$  is present just at the pump-probe overlap, it is symmetric in its rise and decay and it has a FWHM that is comparable with the one of the pump pulse

(see Figure S2c); its spectral amplitude,  $OD_1$ , has strong positive contribution at 284.5 eV and 286 eV.  $f_2$  lasts till roughly 100 fs. Finally,  $f_3$  peaks at later times but does not decay and its amplitude has strong negative contribution between 285 eV and 287 eV and a positive contribution at 282.5 eV. In Fig. S6 we show the comparison between the  $\Delta OD$  trace and the one obtained as  $\text{sub}\Delta OD = \Delta OD - (A_1 f_1 + A_3 f_3)$ , which we will refer to as  $\text{sub}\Delta OD$ . This corresponds to the differential attosecond-resolved XANES measurement subtracted by the overlap and long-lasting features that can obscure the extracting of the rich dynamics. Thus, in the  $\text{sub}\Delta OD$  the fast dynamics around the pump-probe overlap and the long-lasting signal are not present, while the dynamics between 15 fs and 150 fs are highlighted, such as the oscillations and energy shifts.

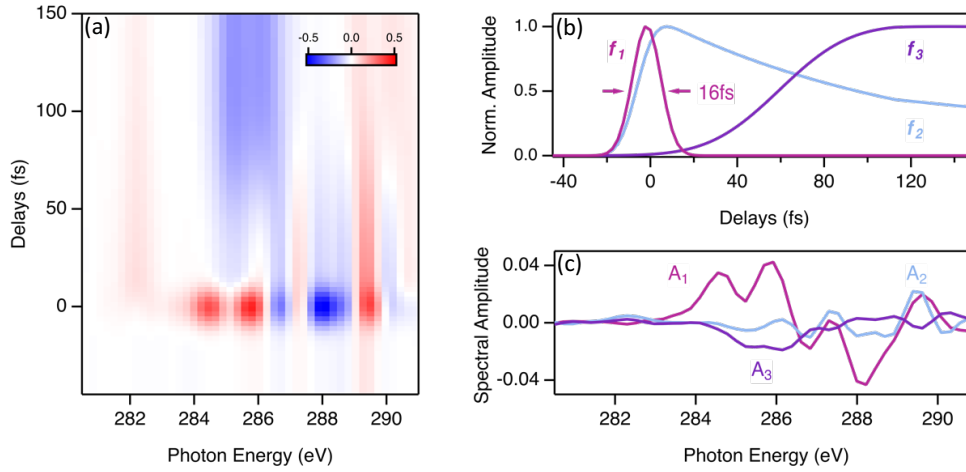


Figure S5: Results of the global fit described in the text. (a): the 2D fit result; (b): time dependence of the  $f_i$ ; (c): spectral amplitude  $A_i$ .

	$\tau_{0i}$ (fs)	$\gamma_i$ (fs)	$\tau_i$ (fs)
$i = 1$	-1.7	6.7	0.1
$i = 2$	-3.2	25.1	69.9
$i = 3$	52.2	10	6165697

Table S1: parameters obtained from the global fit described in the text.

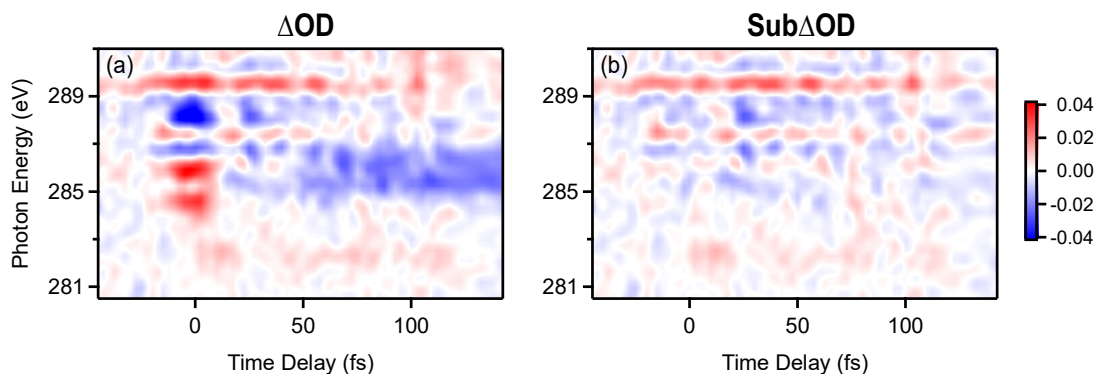


Figure S6: Comparison between the  $\Delta OD$  (a) and the sub $\Delta OD$  (b) traces. The sub $\Delta OD$  has been obtained removing  $(A_{1f_i})$  and  $(A_{3,f_3})$  from  $\Delta OD$ .

#### S4 Static Absorption of Furan

Despite many previous studies, a complete and consistent characterization of the XANES spectrum of furan has remained elusive. Here, through a combination of experiment and theory, we provide an exhaustive interpretation of its main features at the carbon K-edge. Figure S7 shows the measured ground state absorption spectrum of furan and its comparison with simulations. The comparison between the measured and simulated ground state absorption spectrum of furan at the carbon K-edge allows us to provide an assignment of its main spectroscopic features. At the ground state equilibrium, furan has a planar geometry with a  $C_{2v}$  symmetry (see inset of Fig. S7), with two identical carbon atoms bonded to each other,  $C_1$ , and two bonded to the oxygen,  $C_2$ . XANES calculations show that  $C_1$  and  $C_2$  generate distinct contributions to the XANES. The first two features of the GS spectrum correspond to the transitions to the Lowest Unoccupied Molecular Orbital (LUMO) with  $\pi^*$  electronic configuration from, respectively,  $C_1$  and  $C_2$  1s core orbital,  $1s_{C_1} \rightarrow \pi^*(LUMO)$  and  $1s_{C_2} \rightarrow \pi^*(LUMO)$ . The shoulder peak at 287.2 eV is assigned a  $1s_{C_1} \rightarrow 3s$  Rydberg state excitation. The higher energy features at 288.0 eV and 289.3 eV are primarily comprised of  $1s \rightarrow \pi^*$  (higher order) transitions, respectively from  $C_1$  and  $C_2$ , mixed with excitations to Rydberg states. Finally, the feature at 292 eV is largely  $1s_{C_1}$  excitation into different  $\sigma^*$  orbitals.

Interestingly, our XANES calculations allow us to attribute the presence of a resonance to a Rydberg state at 287.2 eV from  $C_1$  that has never been identified before. The assignment of this feature has been

a primary area of ambiguity to date. In fact, while Newbury et al. did not resolve it<sup>5</sup>, E.E. Rennie et al. show it but did not interpret it<sup>6</sup>.

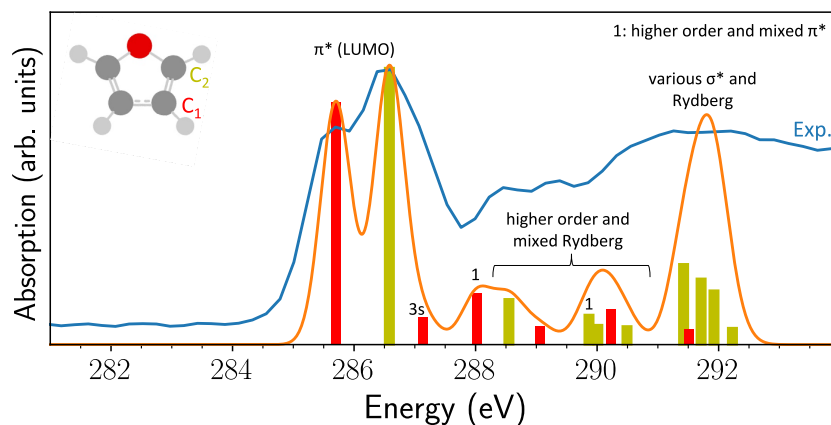


Figure S7: Calculated and experimental static XANES of furan in the electronic GS ( $S_0$ ) at the FC region: Excitation bars, Gaussian-smoothed spectra (orange line), and experimental comparison (blue line). Excitations from different carbons are color-coded and indicated in the inset on the top left.

## S5 Initial pump excitation and the role of ionization

We apply several theoretical approaches to confirm the assignment of the initial pump excitation in the text. Firstly, in S5.1. we show real-time time-dependent density functional theory simulations that confirm a very low ionization yield. Secondly, in S5.2 and S5.3 we discuss excitation in the neutral Furan framework. We show how the theoretical calculations of spectra and dynamics match the experimental data in energy and temporal domain for an initial excitation into the  $\pi\pi^*$  state of neutral Furan in the Frank-Condon region. Thirdly, potential additional excitation channels are discussed in S5.4

### S5.1 Assessing the contribution to ionization (real-time TDDFT simulations)

We have performed real-time time-dependent density functional theory (rtTDDFT) simulations using the Octopus program package<sup>31,32</sup> in order to assess the strong field-induced electron dynamics. Herein, the electron density is propagated on a spatial grid with explicit pump pulse interaction within the frozen nuclei approximation, see computational details below, S8.4. We first investigate the configuration and

parameters for which ionization is expected to be maximum: thus, we define the laser polarization to lie along the molecular dipole, with a peak intensity of  $6.4 \times 10^{13}$  W/cm<sup>2</sup>. The time-dependent ionization yield induced by the intense pump pulse is shown in Figure S8 a), defined as the part of electron density leaving the computational grid. For an intensity of  $6.4 \times 10^{13}$  W/cm<sup>2</sup>, the maximum ionization yield for this relative orientation is 0.086 electrons. We emphasize that this yield of 0.086 is obtained assuming “perfect conditions” without any loss due to the experimental setup and without focal averaging. However, the effective intensity of the pulse would be much lower. In this respect, the calculation with an intensity of  $6.4 \times 10^{13}$  W/cm<sup>2</sup> constitutes the “worst case” scenario. Therefore, in addition, we also performed simulations with the realistic and applied lower peak intensity of  $4.7 \times 10^{13}$  W/cm<sup>2</sup>, which gives an ionization yield of 0.028 electrons. Please note that this still constitutes the relative geometry where ionization is expected to give the largest impact (laser polarization parallel to the molecular dipole). Still, an overall single ionization of 8% (and 2% for the realistic intensity) is non-negligible, and we further investigated the strong-field dynamics. For this, every 3000-time steps, we calculated the projection of the time-dependent density on the initial field-free (static) Kohn-Sham orbitals to estimate the time-dependent population of the occupied molecular orbitals, Fig. S8 b). It shows the ionization occurs with almost equal weight from the highest four occupied molecular orbitals. This indicates that the cation would not only be in its electronic ground state (removal of 0.02 or 0.005 (realistic intensity) electron from the  $3\pi$  electronic state, HOMO) but also in excited electronic states (removal of 0.02 or 0.005 (realistic intensity) electron from the  $2\pi$ ,  $10\sigma$ , and  $9\sigma$  electronic state, HOMO-1, -2 and -3, respectively). The relevant molecular field-free Kohn-Sham orbitals are shown in Tab. S2 below. This means that the system would be in *several* cationic states, each (including the electronic ground state of the cation) with a very low weight of about maximum 2% at “perfect conditions” (0.5% at realistic intensity). (We note that within rtTDDFT, we cannot reliably access excited electronic states originating from transitions towards previously unoccupied orbitals (LUMO+n).) Despite the very low ionization of max. 2% into cationic excited states, we considered the possibility of a cationic dynamics in furan further. However, as we will show below, in particular, the ring-opened structure of the cation gives rise to a very different XANES spectrum, which does not reflect the experimentally recorded spectra, Fig. S12. Most prominently, this would be indicated by a new peak occurring around 281 eV, which is

experimentally not seen. Thus, we conclude that while ionization may occur, it will not be the dominant contribution to the observed dynamics.

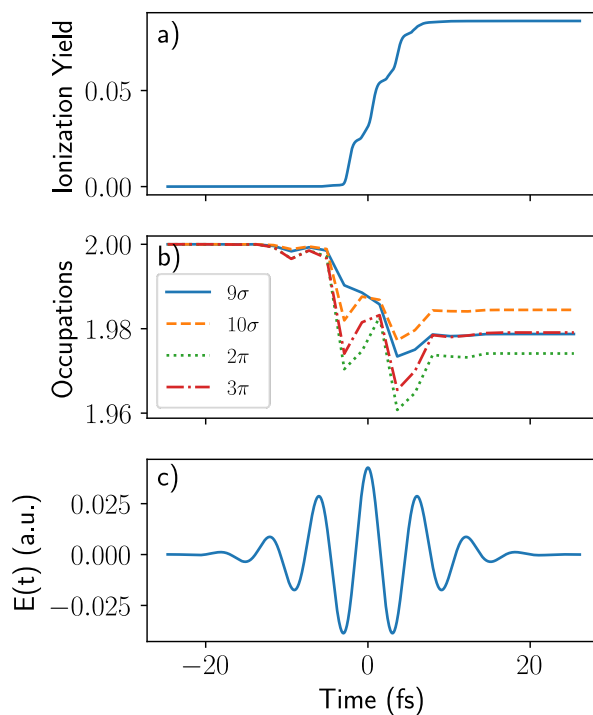
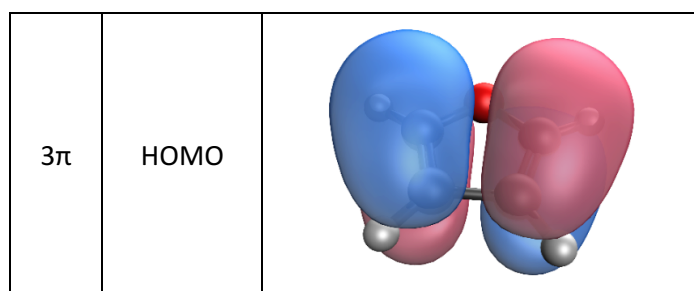


Figure S8: Time-dependent ionization yield during real-time TDDFT simulation for the pump pulse interaction with worst case peak intensity at focal position of  $6.4 \times 10^{13} \text{ W/cm}^2$ : a) ionization yield in electrons, b) occupation number of highest four occupied molecular orbitals (orbital pictures below), c) electric field of pump pulse. The relative geometry is such that the laser polarization is parallel to the molecular dipole termed “perfect condition” for ionization.



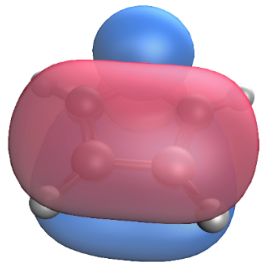
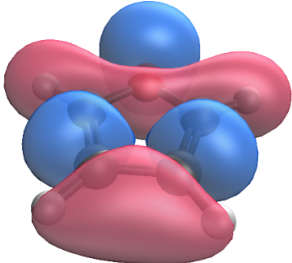
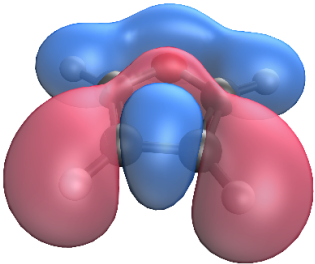
2π	HOMO-1	
10σ	HOMO-2	
9σ	HOMO-3	

Table S2: Relevant Kohn-Sham molecular orbitals obtained by a static real-time TDDFT calculation

### S5.2 Franck-Condon excitations

The calculated energy level of the first excited states of furan and their corresponding oscillator strengths at the FC region allows us to judge the valence electronic transitions relevant for the strong-field pump in the neutral furan and assign the XANES feature at the time-overlap (delay time around time “zero”, see Tab. S3). The lowest state,  $S_1$ , corresponds to a Rydberg state with  $\pi 3s$  electronic configuration, and is optically dark.  $S_2$  ( $\pi \rightarrow \pi^*$  excitation) and  $S_3$  ( $\pi \rightarrow 3p_x$  excitation) are energetically very close and have both non-zero probability to be optically excited, with a clear preference for a  $S_2$  excitation. The RO relevant  $\pi\sigma^*$  state is optically and energetically inaccessible at the FC region<sup>7</sup>. We will discuss the alternative excitation into  $S_3$  in S5.4. While there is a manifold of higher excited electronic states, these are energetically higher, and have, moreover, often low oscillator strengths. The next bright excited state of neutral furan lies about 2 eV higher in energy ( $S_{13}$ , around 8.15 eV), and, thus, close to the ionization threshold (at around 8.9 eV). While we generally cannot neglect possible excitation to higher lying



electronic states beyond the herein discussed electronic states  $S_1$ - $S_3$ , their relative contribution is expected to be small, as: i) excitation of many electronic states with a long-wavelength driver is less probable in the tunneling regime compared to the multi-photon case; ii) even if high-lying excited states close to the ionization threshold become populated, upon interaction with the falling slope of the pump, they will be efficiently depleted. Thus, we will continue to focus on the main excitation path into the  $S_2$  ( $\pi\pi^*$ ) electronic state.

	Transition	$\Delta E$ (eV)	$f$
$S_1$	$3\pi \rightarrow 3s$	5.87	0.00
$S_2$	$3\pi \rightarrow 4\pi^*$	6.2	0.17
$S_3$	$3\pi \rightarrow 3p_x$	6.37	0.03
$S_8$	$2\pi \rightarrow 3s$	7.30	0.02
$S_{13}$	$2\pi \rightarrow 4\pi^*$ and $3\pi \rightarrow 5\pi^*$	8.15	0.40
$S_{18}$	$2\pi \rightarrow 5\pi^*$	8.76	0.14
$S_{20}$	$2\pi \rightarrow 3p_z + 4\pi^*$	8.84	0.02

Table S3: Calculated electronic transitions, vertical excitation energies ( $\Delta E$ ) and oscillator strengths ( $f$ ) of the first bright excited electronic states of furan at the FC region up to the ionization threshold. Other states are dark.

### S5.3 Rise and decay of the $\pi\pi^*$ signature

According to the simulations, during the first 60 fs of the relaxation dynamics, the  $\pi\pi^*$  electronic state ( $S_2$ ) is expected to be the most populated one before passing a CI that leads to population of the  $\pi\sigma^*$  state (cf. Fig. 4 (a), manuscript). This is confirmed in the experimental data: Fig. S9b shows that both the  $\Delta OD$  and the sub $\Delta OD$  match with the simulated  $\pi\pi^*$   $\Delta OD$  spectrum (obtained as difference of el. GS and  $\pi\pi^*$  XANES, see computational details in S6.2) in the temporal region (15 fs to 60 fs). At the overlap (-15 fs to 15 fs),  $\Delta OD$  deviates from simulated spectra because of strong-field effects (Fig. S9a). This overlap feature can be removed using our global fit approach discussed in appendix S3 and shows perfect agreement within the (15 fs to 60 fs) region. This confirms the theoretical prediction of  $S_2$  ( $\pi\pi^*$ ) population within the first 60 fs due to the diabatic transition when passing the first CI  $S_2(\pi\pi^*)/S_1(\pi 3s)$  that maintains the  $\pi\pi^*$  character of the wavefunction. Fitting the temporal evolution of the characteristic XANES features of this state, we find further experimental confirmation: Figure S10 shows the peak at 289.5 eV as function of pump-probe delay, superimposed to the fit result obtained using the convolution

of a Gaussian and a decay exponential function. The free parameters used are the width,  $\gamma$ , the center of the Gaussian function,  $\tau_0$ , and the characteristic exponential decay time,  $\tau$ . It reaches its maximum value at zero delay and decays in  $65 \pm 10$  fs, in good accordance with the theory predictions.

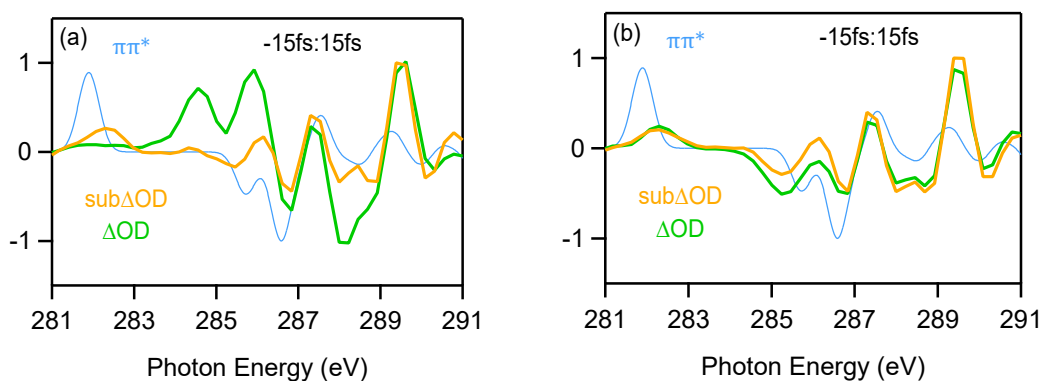


Figure S9: Comparison of the  $\Delta OD$  and the sub $\Delta OD$  with the simulated  $\pi\pi^*$   $\Delta O$  spectrum in the time window -15 to 15 fs (a) and 15 to 60 fs (b). The comparison shows that within the first 60 fs, the dynamics is dominated by the  $\pi\pi^*$  electronic state.

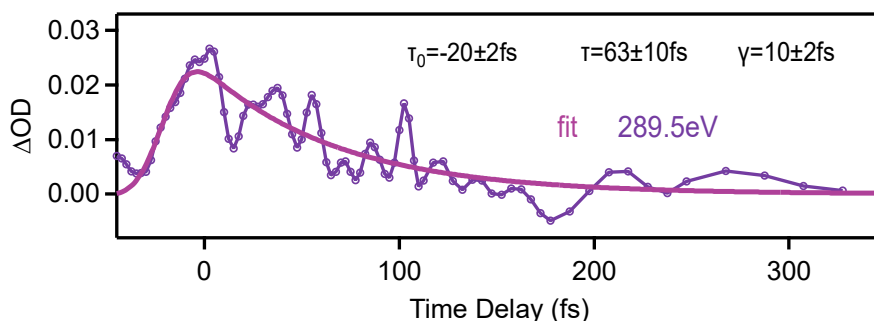


Figure S10: Temporal behavior of the energy pixel at 289.5 eV and its fitting result.

#### S5.4 Comparison to alternative excitation/ionization channels

In section S5.1, we have seen that the ionization yield is very low; section S5.3 shows very good agreement in spectral and time domain for an initial  $\pi\pi^*$  excitation in the neutral furan. For completeness we also discuss here alternative excitation channels and show by means of theoretical spectra how they would manifest in the initial absorption signal. Figure S11 is analogous to Fig. S9, but here we compare a possible initial excitation into the cation or neutral S3 ( $\pi 3p$ ) state. The region at 285 eV and 289.5 eV

shows poor agreement between theory and experiment compared to an initial excitation into  $S_2$  ( $\pi\pi^*$ ) as shown in Fig. S9.

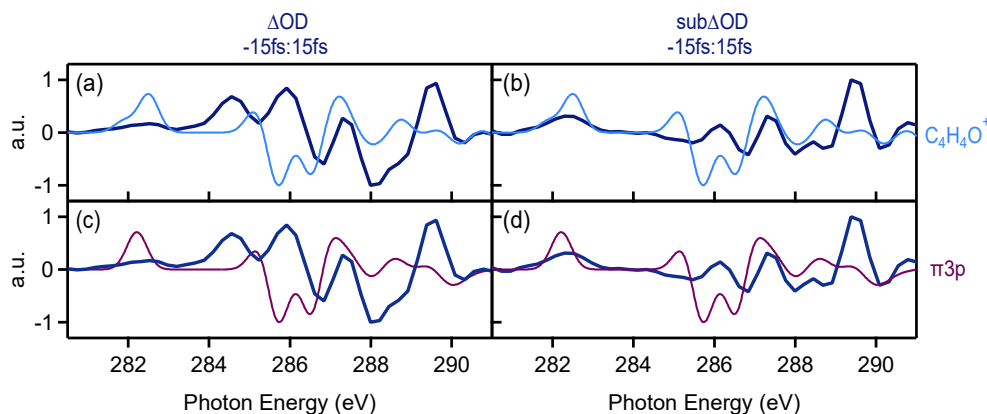


Figure S11: Comparison between the simulated differential XANES spectra and the measured (bold line)  $\Delta OD$  ((a) and (c)) and sub  $\Delta OD$  ((b) and (d)) time averaged between -15 fs and 15 fs. In (a) and (b) these are compared with the **cation** ( $C_4H_4O^+$ ) (light blue), in (c) and (d) with neutral  $S_3$  state ( $\pi 3p$ ) (magenta).

Still, even though there is a very low ionization yield, assuming the cationic state ultimately leads to a ring-opening, we would obtain the calculated XANES shown in Fig. S12, green line. Herein, we compare theoretically the structure at the ROCI for neutral (orange) and cation (green) furan in their respective electronic GS. From the experiment, we conclude relaxation back to the electronic GS to occur after 150 fs, see chapter SI S6, specifically in Figs. S14 a) and d). The characteristic experimental feature (apart from a GS bleach) is a **positive** signal in the range of 282 eV - 282.9 eV, area highlighted in red in Fig. S12. It only fits the calculated signal of the neutral furan; the cation would have additional XANES features at lower energies (281.5 eV) and at 283.2 eV, 285 eV whereas in the experiment, no such positive signal can be observed. This is another indication for RO in neutral furan.

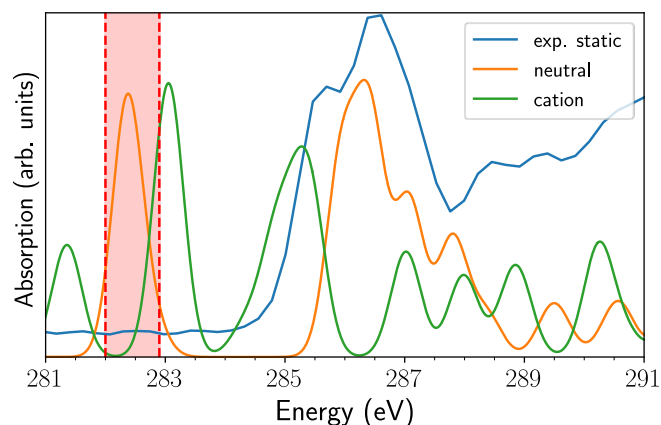


Figure S12: Theoretical XANES at ROCI geometry for electronic GS of neutral (orange) and cation (green) furan. For comparison, the static experimental furan XANES is shown in blue. The experiment (see SI section S6) shows only one single positive peak at around 282.5 eV (red area) after relaxation in the GS (and GS bleach). This fits only the neutral furan.

In S5.2 we showed that excitation in the  $S_3$  ( $\pi 3p$ ) state is energetically accessible but has a much lower oscillation strength compared to the  $S_2$  ( $\pi\pi^*$ ) excitation discussed in the manuscript. Figure S13 displays the semi-classical surface hopping dynamics for initial excitation into  $S_2$  (left panel, as presented in the text) and comparison the initial excitation into  $S_3$  (right panel). The differences are insignificant due to a strong coupling / population exchange between  $S_2$  and  $S_3$ .

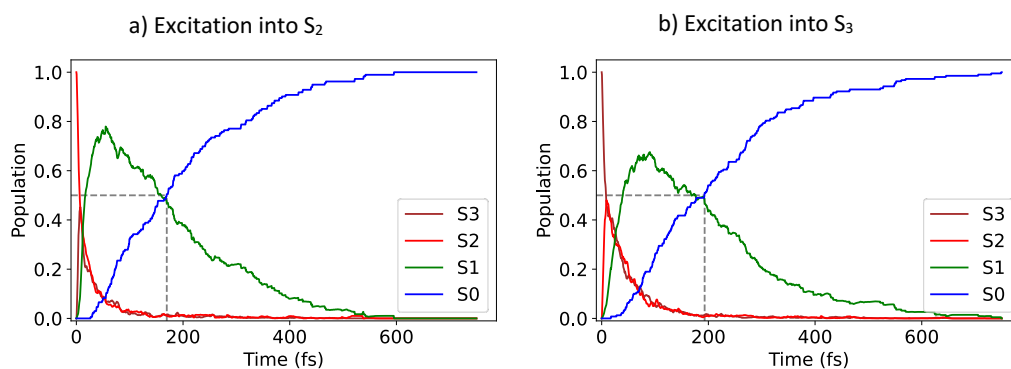


Figure S13: Semi-classical dynamics starting 200 trajectories in  $S_2$  (a) and  $S_3$  (b).

## S6 Absorption spectra comparison of theory and experiment

Figure S14a displays the difference between the furan XANES spectra with and without the pump excitation,  $\Delta OD$  as function of the probe photon energy and pump-probe delay in the ultrafast time range

between -40 to 200 fs (for the full dataset up to 380 fs, see SI S2). The differential absorption spectrum features rich dynamics in the energy region between 282 eV and 290 eV in the first 150 fs, which is consistent with the expected timescale for the propagation up to the CIs to the GS provided by the semi-classical dynamics. In order to retrieve more details of the molecular dynamics and elucidate comparison with simulations, we subtract two dominant contributions (overlap region and long-lasting component) from the experimentally measured time-resolved differential absorption, obtaining a sub $\Delta$ OD (recall SI S3). In what follows, we will discuss several characteristic features of both  $\Delta$ OD and sub $\Delta$ OD traces.

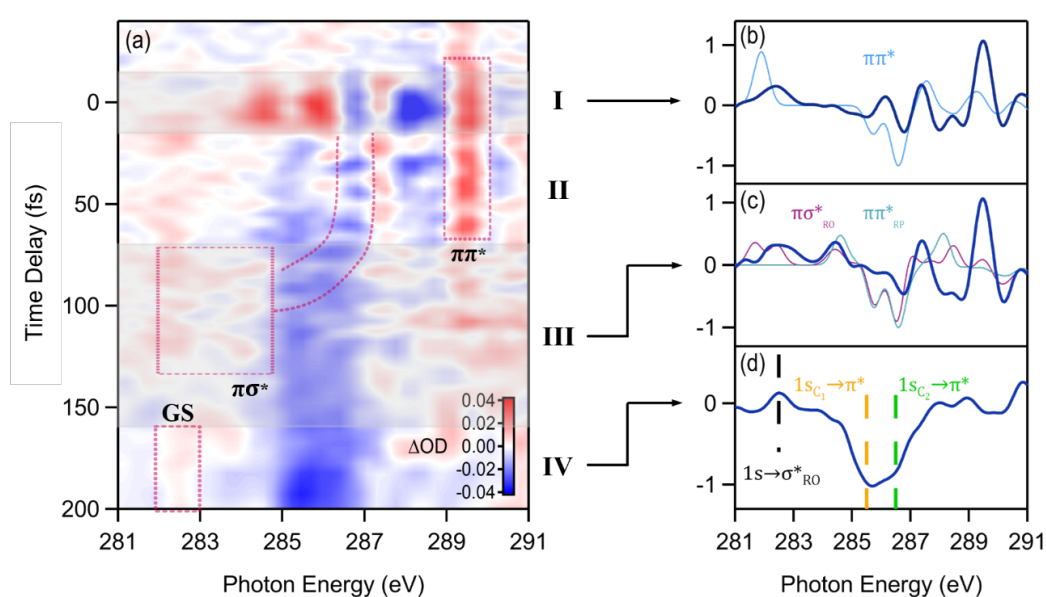


Figure S14: Time-resolved attosecond XANES measurement. (a): Experimentally retrieved  $\Delta$ OD trace; Positive delay indicates that pump pulse preceded the x-ray probe. The relevant features discussed in text are marked in red; the different time regions that show different characteristic features are highlighted by the shaded areas: I: -15 to 15 fs, overlap region; II: 15 to 60 fs; III: 60 to 150 fs; IV: 160 to 200 fs (b): time-averaged sub $\Delta$ OD between -15 fs and 15 fs (area I) (bold dark blue line) compared with the simulated  $\pi\pi^*$   $\Delta$ OD spectrum at the GS equilibrium geometry (thin light blue line). Both the  $\Delta$ OD and sub $\Delta$ OD signals time-averaged between 15 fs and 60 fs (area II) are spectrally consistent with the thick dark blue line in (b), recall SI S5.3. (c) sub $\Delta$ OD between 70 fs and 110 fs (area III) compared with the  $\Delta$ OD spectrum of the first excited states at the RO and RP geometrical structure of, respectively,  $\pi\sigma^*$  and  $\pi\pi^*$  electronic configuration (thin purple and cyan line). (d)  $\Delta$ OD trace between 160 fs and 200 fs (area IV); labeled are the energetic positions of relevant transitions of the electronic GS XANES spectrum at the RO structure (in black) and at the FC region (orange and green).

We first focus on the temporal region around zero delay time (area I in Fig. S14a), where strong-field excitation occurs. Figure S14b shows the sub $\Delta$ OD signal time-averaged between -15 fs and 15 fs (solid lines); for comparison, the calculated XANES differential spectra of the  $\pi\pi^*$  excited state at the equilibrium structure is displayed (light blue thin line). It shows the creation of photoexcited furan in the  $S_2$  ( $\pi\pi^*$ ) state (recall SI S5.3). Its most characteristic features are the positive signals at 282 eV, 287.5 eV and 289.5 eV, as well as a bleaching of the LUMO ( $\pi^*$ ) signatures (285 - 286 eV). The theoretical analysis allows us to assign the new absorption feature at 282 eV to  $C_1$  and  $C_2$  1s core electron transition to the singly occupied molecular orbital (SOMO) freed up by the pump-induced excitation from  $3\pi \rightarrow 4\pi^*$ , thus,  $C(1s) \rightarrow 3\pi$ . The  $\Delta A$  is strongly dominated by the peaks at 284.5 eV, 286 eV and 288.5 eV, which are temporally restricted to the pump-probe overlap and have been subtracted to obtain the sub $\Delta$ OD. In strong-field tr-AttoXANES, features like these are usually attributed to reshape of the X-ray absorption lines or light-induced states<sup>8</sup>. These components mask the weaker spectroscopic signatures of electronic excited states in the  $\Delta$ OD trace.

We next investigate the dynamics following the initial  $\pi\pi^*$  excitation, focusing first on the time window between 15 fs and 60 fs (area II in Fig. S14a). Both the  $\Delta$ OD and sub $\Delta$ OD signals time-averaged in this temporal region are spectrally consistent with the sub $\Delta$ OD in area I (recall SI S5.3), hence experimentally demonstrating that this time range is dominated by contributions from the  $\pi\pi^*$  state. As a further confirmation, the bleach of the characteristic XANES signal at 289.5 eV can be fitted with an exponential function with a decay time of  $65 \pm 10$  fs (see SI 5.3). The accompanying non-adiabatic trajectory calculations, manuscript Fig. 4 a, shows fast population dynamics involving the first three excited states in the first 60 fs upon excitation. After about 15 fs, we have electronic population changes from  $S_1$  to  $S_2$ . This is a diabatic crossing at the first CI, where the  $\pi\pi^*$  electronic state becoming the energetically lowest state maintaining its electronic character (recall manuscript Fig. 1a). This diabatic transfer is evident in the experiment as area I and II are identical and exhibit the same  $\pi\pi^*$  features.

Theoretically, a small contribution from the bright  $S_3$  Rydberg state is expected at very early times, which is, however, not visible in the experimental data as it is probably masked by the strong-field effects discussed above.

Following these early times, we focus on the next time window between 60 fs and 150 fs (area III in Fig. S14a). Experimentally, the time range is characterized by three contributions (see Fig. S14a): (a) the positive feature of  $\Delta OD$  around 289.5 eV decays to zero; (b) a prominent energetic shift of an absorption feature from 286.5 eV to down to 284 eV (the typical chemical shift caused by nuclear motion along a steep gradient of the potential energy surface<sup>9</sup>); (c) the rise, and then the decay, of a positive absorption feature at 284.5 eV. The theoretical calculations (manuscript Fig. 4a) show that for delay times larger than 60 fs,  $S_2$  and  $S_3$  are depopulated, and  $S_1$  becomes the only excited state with non-negligible population. Moreover,  $S_1$  diverges energetically from the other excited states, as the C-O bond elongates. This stretching destabilizes  $S_3$  and  $S_2$  energetically while it stabilizes  $S_1$  (manuscript Fig. 4b). As elucidated in the text this leads to the dephasing of the electronic coherence. For the (dominant) RO pathway, this time frame relates to the CI where  $S_1$  changes its electronic configuration from  $\pi\pi^*$  state to the dark dissociative  $\pi\sigma^*$  state, 2nd conical intersection  $S_1(\pi\pi^*)/S_1(\pi\sigma^*)$ . This passage explains the experimentally observed decay of the absorption peak at 289.5 eV (feature I), caused by the depopulation of the  $\pi\pi^*$  state, and the energetic shift from 286 eV to 284 eV (feature II), originating from the nuclear dynamics in this state.

Simultaneously with the decay of the  $\pi\pi^*$  feature, the data display the rise of a positive peak at 284.5 eV (feature III), as shown by the time-averaged  $\text{sub}\Delta OD(E,\tau)$  spectrum between 70 fs and 110 fs (Fig. S14c). This signal is assigned to the first excited state ( $S_1$ ) at both RO and RP geometrical structures and is identified as a  $1s \rightarrow \text{SOMO}$  transition into the valence  $\pi$  orbital freed up by the  $\pi \rightarrow \sigma^*$  (RO) and  $\pi \rightarrow \pi^*$  (RP) valence excitations. Moreover, this new feature is a direct experimental proof of symmetry breaking during the relaxation process and its impact on electronic features, i.e., the SOMO peak. While at the FC region, there are two symmetry equivalent carbon atoms leading to two transitions at 282 eV (see above), along the relaxation pathways, these transitions split into four contributions as symmetry breaks all four carbons become symmetrically non-equivalent. In the RO case, the four  $C(1s) \rightarrow \text{SOMO}$  transitions are found theoretically at 281.5 eV, 282.5 eV, 284.5 eV and 285.5 eV (see section S12) and are experimentally resolved (manuscript Fig. 2c). The occurrence of a positive peak at 282.5 eV in the experimental data, together with the one at 284.5 eV, (manuscript Fig. 2c) is a direct and unique signature of electronic population in the dark dissociative  $\pi\sigma^*$  state leading to RO and demonstrates the

sensitivity of the tr-AttoXANES method to trace transient signatures of competing photophysical pathways simultaneously.

Finally, the disappearance of the  $C(1s) \rightarrow \text{SOMO}$  transition at 284.5 eV after 160 fs is interpreted as the passage through the 3rd conical intersection  $S_1(\pi\sigma^*)/S_0$  that defines the complete relaxation of the system back to the electronic GS. At longer time delays (160 to 200 fs),  $\Delta\text{OD}$  is characterized by a strong depletion of the main XANES feature of the ground state,  $C_1(1s) \rightarrow \pi^*$  and  $C_2(1s) \rightarrow \pi^*$ , and a positive peak at 282.5 eV (Fig. S14(d)). This last signal confirms the identification of RO furan as the primary relaxation pathway, as it is found in the calculated electronic GS XANES spectrum at the RO structure and is assigned as a  $1s \rightarrow \sigma^*$  transition<sup>10</sup>. It is not present for RP as shown in Figure S15, thus, together with the vibrational frequency matching, and the  $\pi\sigma^*$  trace (recall Fig. S14 (c)), RO is clearly experimentally identified. The theoretical calculations show that 76% of the trajectories follow the RO relaxation pathways, with the remaining trajectories resulting in RP, which is in excellent agreement with the experimental observation.

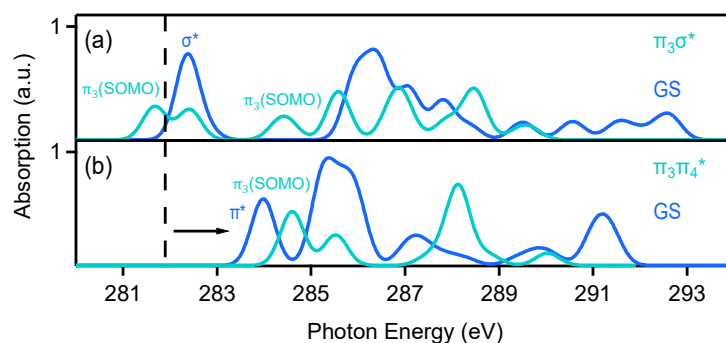


Figure S15: Theoretical  $\Delta\text{OD}$  spectrum at the ROCI (a) and RPCI (b) geometry. Electronic ground (dark blue) and first excited state (light blue, for RO:  $\pi\sigma^*$ , for RP:  $\pi\pi^*$ ). The vertical dashed line indicates long lasting experimental signal after 150 fs. Only RO has a signal in this area.

### S7 Origin of electronic coherence

The high frequency component (63 THz) is visible in the experiment in the time region between 20 fs and 80 fs. We recall that this interval is characterized by a coherent superposition of the electronic states  $S_2$  and  $S_1$  passing through the 1st conical intersection  $S_2(\pi\pi^*)/S_1(\pi 3s)$ . The quantum beating of such an



electronic wave packet leads to intensity modulations of the XANES signal with a frequency defined by the energy difference between the coherently populated electronic states,  $\Delta E_{21}(\mathbf{R}) = E[S_2(\mathbf{R})] - E[S_1(\mathbf{R})]$ . This beating would continue until dephasing or decoherence will become important. As the energies of the electronic potential surfaces depend strongly on the nuclear coordinates, also their difference,  $\Delta E_{21}(\mathbf{R})$  does. Peculiarly, the potential energy difference along both modes, RO and RP, is almost equidistant over a large range around the equilibrium structure,  $\Delta E_{21}(\mathbf{R}) \approx \Delta E_{21}(\mathbf{R}_{\text{eq}})$  (manuscript Fig. 4b). Dominant periodic components of  $60 \pm 6$  THz for the RO mode and  $62 \pm 12$  THz for the RP case are clearly visible, both decaying around 60 - 70 fs, when the potential surfaces deviate energetically (recall Fig. 1a and Fig. 4c) and the dependence on the nuclear degrees of freedom,  $\Delta E_{21}(\mathbf{R}(t))$ , leads to a dephasing. In the experiment, two spectral regions, one between 289 eV and 290 eV and a second one between 286.2 eV and 287.5 eV, feature the 63 THz frequency peak. The reason that the oscillations appear in these spectral areas is because there the valence states populated at the CI have a common final state in the XANES. Specifically, the valence excited  $\pi\pi^*$  state has a transition  $1s \rightarrow 3s$  while the valence excited  $\pi 3s$  state has a core transition  $1s \rightarrow \pi^*$ . Thus, there is a common final state with a hole in the  $1s$ ,  $\pi$ ,  $\pi^*$ , and  $3s$ , see Fig. S16. Moreover, the XANES transitions in the two spectral areas of 289 - 290 eV (violet) and 286.2 - 287.5 eV (light blue) originates from different carbon sites, i.e.,  $C_1$  (red bars) and  $C_2$  (green bars), which is shown theoretically in Fig. S17. This leads to the observed out-of-phase oscillatory behavior in the experiment (manuscript Figs. 3a and S18) and is based on the complex transition dipole moment as recently shown theoretically<sup>11</sup>.

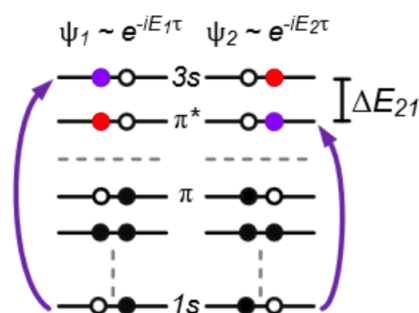


Figure S16: Schematic representation of the projection of the two coherently excited states to a common final doubly excited state via core excitation. The red dot indicates the electronic state created by passing through the first CI (left:  $\Psi_1$ :  $\pi\pi^*$ ; right:  $\Psi_2$ :  $\pi 3s$ ), and the purple dots and arrow indicate the probe pulse excitation needed to create two identical final states.

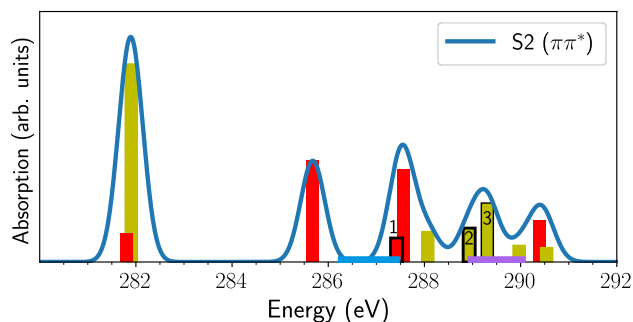


Figure S17: Calculated XANES at FC region for the electronic  $S_2$  ( $\pi\pi^*$ ) state. The red and green bars show the calculated XANES transitions originating from  $C_1$  or  $C_2$  ( $1s$ ) core orbitals, respectively (recall Fig. S7). The horizontal light blue and violet bars indicate the two areas of electronic coherence modulation in the experiment. The XANES transitions that lead to a common final state, i.e.,  $1s \rightarrow 3s$  for the here shown  $S_2$  ( $\pi\pi^*$ ) state, are indicated with a number and a black edge. It is evident that in the two areas of electronic coherence, the transitions leading to a common final state originate from different carbon sites. All XANES transitions are of mixed character where the  $1s \rightarrow 3s$  contribution is 87% (transition 1), 68% (transition 2), and 7% (transition 3).

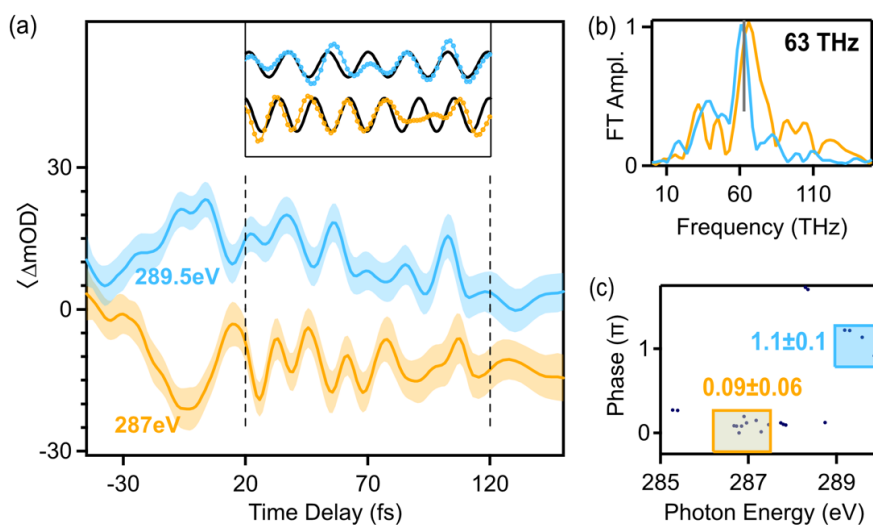


Figure S18: (a) Out-of-phase experimental modulations from  $\Delta OD$  at 286.2 eV - 287.5 eV (orange) and 289 eV - 290 eV (blue). The top inset shows the same oscillations with sloping background subtracted to highlight the modulations. Superimposed is a sin-wave fit with the initial phase adjusted to the data. (b) Fourier analysis of (a) revealing the two modal frequencies. (c) Analysis of the relative phase between the modulation of the sub $\Delta OD$  trace as function of photon energy. Marked in the colored boxes the spectral range of the lineouts in fig(a). The two curves from (a) oscillate in anti-phase.

This demonstrates that we cannot only probe the existence of an electronic wavepacket but also trace a  $\pi$ -phase difference back to the two sites of the molecule.

## S8 Computational Details

### S8.1 One-dimensional potential energy curves

The coordinates for the one-dimensional potential energy surfaces displayed in Fig. 1a of the main text were obtained by linear interpolation between the optimized nuclear ground state (GS) of furan and the optimized ring-opening conical intersection (ROCI) and ring-puckering conical interaction (RPCI), respectively. The structures were taken from Ref. 12, and the linear interpolation was done in internal redundant coordinates using the *pysisyphus* program suite<sup>13</sup>. The electronic ground- and excited-states calculations were performed with the *Gaussian 16* program<sup>14</sup> using (time-dependent) density functional theory (TD-DFT), the hybrid functional PBE0<sup>15,16</sup> and the valence triple-zeta basis set with diffuse and polarisation functions, 6-311++G(d,p)<sup>17,18</sup>. The obtained PES are in very good agreement with the PES by Stenrup and Larson<sup>12</sup> using CCSD/6-311+G\*+sp and MS-CASPT2(8,7)/6-311G\* level of theory and, thus, confirms the validity of our theory setup for use in the subsequent semi-classical dynamics.

### S8.2 X-ray absorption spectra

XANES were calculated at various nuclear geometries (FC, RPCI, ROCI taken from Ref. 12) and in different electronic states (GS, S<sub>1</sub>, S<sub>2</sub>). For calculations in the electronic GS, we employed equation-of-motion coupled cluster theory including singles and doubles (EOM-CCSD)<sup>19,20</sup> while for the calculations involving electronic excited states, we employed the core-valence-separation scheme<sup>21</sup> in the frozen-core equation of motion model for electronically excited states on the coupled cluster singles and doubles level of theory (fc-CVS-EOM-EE-CCSD)<sup>22,23</sup>. Both methods utilized the aug-cc-pVDZ basis set<sup>24,25</sup> and were performed with *QChem 5.3*<sup>26</sup>. Depending on convergence and symmetry of the structure, 50-120 roots were calculated.

### S8.3 Semi-classical dynamics

For the nonadiabatic excited-state dynamics, the semi-classical program package *SHARC 2.1*<sup>27,28</sup> was interfaced with *Gaussian* using the functional and basis set described above (PBE0/6-311++g(d,p)) to calculate solutions to the time-independent electronic Schrödinger equation on-the-fly.

The initial nuclear ground state equilibrium structure was obtained using the same quantum chemical method, and a subsequent vibrational analysis was carried out to verify that we obtained a minimum on the potential energy surface. To simulate the ground state nuclear wave packet, we applied a Wigner sampling at the Franck-Condon (FC) region using the harmonic GS frequencies Boltzmann weighted at 300 K<sup>29,30</sup>. Assuming a delta peak absorption, an initial set of 200 trajectories were started in the bright  $\pi\pi^*$  state ( $S_2$  in the FC region). The classic trajectories were propagated for 750 fs with a time step of 0.5 fs while the electronic states were treated in the diagonal representation with 25 steps for the electronic integration. Frustrated hops were reflected along the gradient difference vector, and an energy-based decoherence scheme was applied. Hops to the electronic GS were forced by energy difference, as explicit hops to the GS are not possible in a TD-DFT approach. The parameters of the semi-classical dynamics were studied thoroughly to ensure converged results. To this end, several calculations changing a single parameter were conducted, such as using a time step of 0.1 fs, no reflection of frustrated hops, augmented fewest-switching surface hopping decoherence, surface hopping in the molecular Coulomb Hamiltonian representation, and changing the TD-DFT parameters (B3LYP functional and aug-cc-pvdz basis set). None of these parameter changes exhibited significant changes in the dynamics presented in the manuscript. Moreover, the influence of the pump pulse on the dynamics was analyzed by means of including the pump pulse in various polarization directions as off-diagonal elements of the electronic Hamiltonian during propagation, see S10. No significant alternation of the RO dynamics was observed. Additionally, the pump pulse influence on the initial equilibrium wave packet was studied and did not lead to a significant alternation of the RO dynamics either.

#### **S8.4 Real-time TDDFT simulations**

The real-time TDDFT calculations were performed with the *Octopus* package<sup>31,32</sup>. All 26 valence electrons are included in the simulation. The time-dependent Kohn–Sham orbitals that construct the electron density are propagated numerically in real-time and real-space using finite element methods.

The numerical details include a spherical box with a radius of  $r = 15 \text{ \AA}$ , spacing of  $\Delta r = 0.16 \text{ \AA}$ , time step of  $0.03 \text{ a.u.}$ , and a mask function of width  $w = 4.0 \text{ a.u.}$  at the boundary. The simulations were tested for convergence in box radius, spacing, and time step. The pump pulse, parallel to the molecular dipole, was implemented with the parameters presented in S1. For the exchange-correlation potential, the local-density approximation (LDA) functional was utilized<sup>33–35</sup>.

### S9 Trajectory analysis

The trajectories were categorized as ring-opening (RO) and ring-puckering (RP) based on their geometry at the time of the electronic GS hop. For an initial set of 150 trajectories, we found 97 RO and 29 RP trajectories. RO and RP exhibit very similar time scales as shown in Fig. S19 if the pump pulse is not included in the dynamics. The combined dynamics are shown in the manuscript in Fig. 4a.

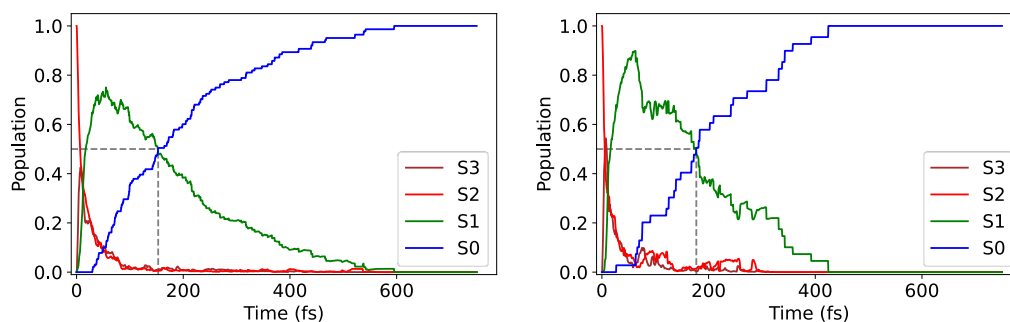


Figure S19: Population dynamics of RO (left) and RP (right) trajectories.

To obtain the average, time-resolved potential energy landscape during the non-adiabatic relaxation dynamics leading to either RO or RP, we construct the nuclear wave packet, or rather its time-dependent mean position, in the electronic excited state manifold for each of the two relaxation pathways. This is done as a post-processing of the semi-classical dynamics. To this end, we take, respectively, all RO and RP trajectories at a given time, average the structure over all trajectories, and calculate the time-resolved potential energy landscape using the quantum chemical method of the semi-classical dynamics. Note that to obtain the average structure along the RO or RP pathway at a given time, the individual structures of each trajectory have to be matched and aligned in coordinate space due to the symmetry of the

relaxation pathways, e.g., RO can occur by cleavage of either of the two symmetric CO bonds. This has been done using coordinate space analysis and the Hungarian method to align the molecules<sup>36,37</sup>. The time-dependent potential energy landscape along RO and RP pathway have been used to calculate the time-dependent energy gaps along either relaxation (see Figure 4b in the manuscript) and, subsequently, to estimate the electronic coherence as described in the manuscript. The vibrational dynamics are investigated via normal mode analysis. Here, the harmonic normal modes of the nuclear and electronic GS are used as basis for analyzing the structural dynamics of the excited state trajectories along the RO and RP relaxation pathway. The coherent motion in each mode is judged by means of the standard deviation over time of the average trajectory and is displayed in Fig. 4d<sup>38,39</sup>.

### **S10 Strong-field effect on the semi-classical dynamics**

The influence of the Wigner sampling on the semi-classical dynamics was compared at various temperature and including the strong-field pump as off-diagonal element in the Hamiltonian of the semi-classical dynamics (cf. section S8.3).

To understand the strong field effect in detail, we optimized the nuclear GS geometry including the peak field strength of the pump pulse, which lead to a change of C-O bond length of +0.05 Å (positive polarization along dipole) or -0.03 Å (negative polarization along dipole). Performing Wigner sampling and semi-classical dynamics from this new distorted geometry and including the strong field pump in the dynamics, leads to the population dynamics shown in Table S4. It shows that the ring opening dynamics does not change significantly when the laser pulse is incorporated explicitly while the ring puckering pathway is accelerated. The latter time scale does not fit the experiment and is another indication of a dominant ring-opening in the experiment.

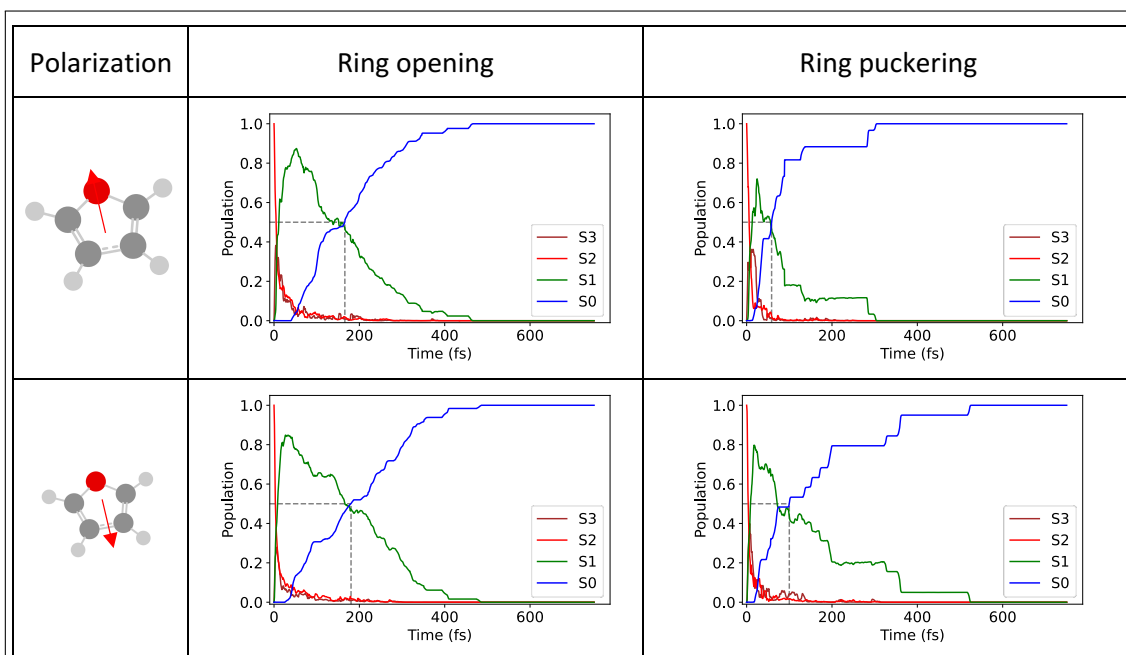


Table S4: Semi-classical dynamics including coupling with the strong-field pump

### S11 Fourier Transform analysis of vibrational dynamics

We confirmed the validity of the normal mode analysis by additional Fourier analysis of the semi-classical data. We analyzed the dynamics of all trajectories along all bonds in Fourier space and confirmed that the C-O and C-C bonds vibrate in the same frequency area as the RO normal mode analysis showed (manuscript Fig. 4d).

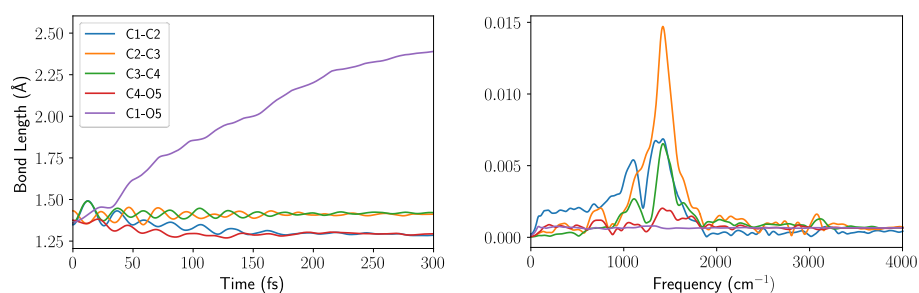


Figure S20: Fourier analysis of C-C and C-O bonds during the semi-classical dynamics without explicit pump pulse interaction

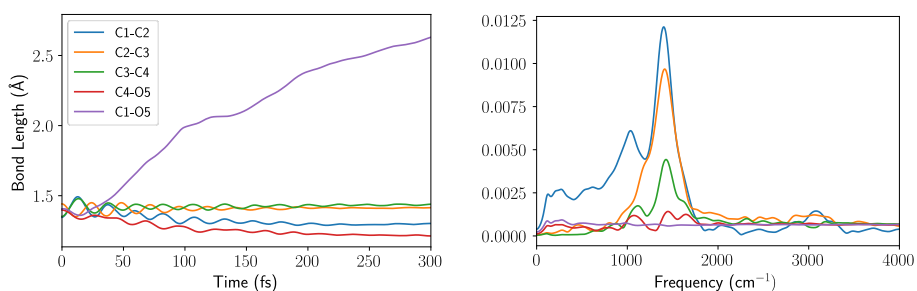


Figure S21: Fourier analysis of C-C and C-O bonds during the semi-classical dynamics with explicit pump pulse interaction, polarized along the permanent dipole of furan.

### S12 Symmetry breaking along ring-opening

Furan's structure is of  $C_{2v}$  symmetry at the FC region with two symmetry equivalent carbon atoms while it is of the lower  $C_s$  symmetry at the ROCI, with four distinct carbon atoms. Thus, going from the FC region to the ROCI during the RO pathway leads to a symmetry breaking. This is imprinted on the XANES by means of splitting of the SOMO peak. As discussed in the text, the SOMO peak at the FC region appears as the electronic state changes from the electronic ground to the  $\pi\pi^*$  state and constitutes two distinct transitions from the  $C_1$  and  $C_2$  1s core orbitals. The two different XANES at the FC region are shown in Fig. S22(a) in orange (GS) and green ( $\pi\pi^*$ ). The SOMO peak and its two transitions are indicated as a light green and red bar referring to a 1s core transition from  $C_2$  and  $C_1$ , respectively. The  $C_1$  and  $C_2$  is labelled on the right in the molecule inset. At the ROCI, all four carbon atoms are unique leading to a splitting of the SOMO in the electronic  $S_1$  state into four contributions as indicated in Figure S22(b) with the dashed arrows. The numbers below the peaks of the  $S_1$  ROCI XANES (purple) refer to the SOMO peak originating from the four different carbon atoms. The labelling is indicated in the ROCI structure on the right. The peak at 284.5 eV, i.e.,  $C_2$  1s  $\rightarrow$  SOMO( $\pi$ ), is a unique spectral feature in the experiment, not overlapping with any other XANES. For reference, in brown the electronic ground state XANES at ROCI is shown. The  $\pi$  orbital, i.e., the HOMO, is fully occupied and cannot be populated in the XANES anymore. The lowest transition corresponds to 1s  $\rightarrow$   $\sigma^*$ (LUMO). Due to symmetry, the four distinct SOMO peaks are not all bright in the el. GS at ROCI.



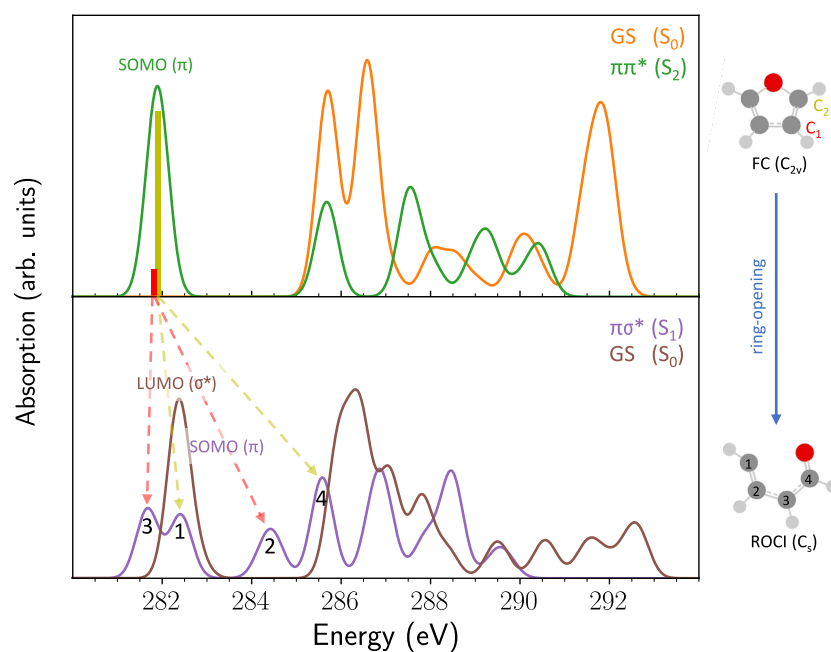


Figure S22: XANES for different electronic configurations at (a) FC region and (b) ROCI geometry. Arrows indicate how the SOMO peak splits due to symmetry breaking.

FC, $S_2(\pi\pi^*)$ $1s(C_2) \rightarrow \pi(SOMO)$		
FC, $S_2(\pi\pi^*)$ $1s(C_1) \rightarrow \pi(SOMO)$		
ROCI, $S_1(\pi\sigma^*)$ $1s(C_1) \rightarrow \pi(SOMO)$		

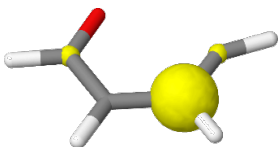

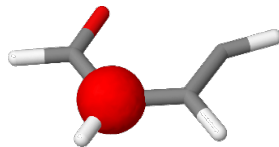
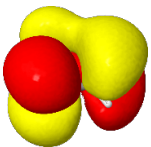
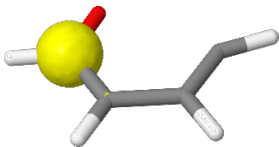
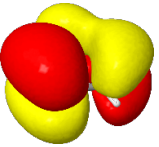
ROCl, $S_1$ ( $\pi\sigma^*$ ) $1s$ ( $C_2$ ) $\rightarrow$ $\pi$ (SOMO)		
ROCl, $S_1$ ( $\pi\sigma^*$ ) $1s$ ( $C_3$ ) $\rightarrow$ $\pi$ (SOMO)		
ROCl, $S_1$ ( $\pi\sigma^*$ ) $1s$ ( $C_4$ ) $\rightarrow$ $\pi$ (SOMO)		

Table S5: Natural transition orbitals for the SOMO transitions discussed in the text

## References

1. Cousin, S. L. *et al.* High-flux table-top soft x-ray source driven by sub-2-cycle, CEP stable, 1.85- $\mu\text{m}$  1-kHz pulses for carbon K-edge spectroscopy. *Opt. Lett.*, **OL 39**, 5383–5386 (2014).
2. Silva, F., Teichmann, S. M., Cousin, S. L., Hemmer, M. & Biegert, J. Spatiotemporal isolation of attosecond soft X-ray pulses in the water window. *Nat Commun* **6**, 6611 (2015).
3. Teichmann, S. M., Silva, F., Cousin, S. L., Hemmer, M. & Biegert, J. 0.5-keV Soft X-ray attosecond continua. *Nat Commun* **7**, 11493 (2016).
4. Cousin, S. L. *et al.* Attosecond Streaking in the Water Window: A New Regime of Attosecond Pulse Characterization. *Phys. Rev. X* **7**, 041030 (2017).
5. Newbury, D. C., Ishii, I. & Hitchcock, A. P. Inner shell electron-energy loss spectroscopy of some heterocyclic molecules. *Can. J. Chem.* **64**, 1145–1155 (1986).
6. Rennie, E. E. *et al.* A core-level photoionization study of furan. *The Journal of Chemical Physics* **117**, 6524–6532 (2002).

7. Gromov, E. V., Trofimov, A. B., Gatti, F. & Köppel, H. Theoretical study of photoinduced ring-opening in furan. *The Journal of Chemical Physics* **133**, 164309 (2010).
8. Wu, M., Chen, S., Camp, S., Schafer, K. J. & Gaarde, M. B. Theory of strong-field attosecond transient absorption. *J. Phys. B: At. Mol. Opt. Phys.* **49**, 062003 (2016).
9. Kobayashi, Y., Chang, K. F., Zeng, T., Neumark, D. M. & Leone, S. R. Direct mapping of curve-crossing dynamics in IBr by attosecond transient absorption spectroscopy. *Science* **365**, 79–83 (2019).
10. Bhattacharjee, A. *et al.* Photoinduced Heterocyclic Ring Opening of Furfural: Distinct Open-Chain Product Identification by Ultrafast X-ray Transient Absorption Spectroscopy. *J. Am. Chem. Soc.* **140**, 12538–12544 (2018).
11. Kobayashi, Y., Neumark, D. M. & Leone, S. R. Theoretical analysis of the role of complex transition dipole phase in XUV transient-absorption probing of charge migration. *Opt. Express* **30**, 5673 (2022).
12. Stenrup, M. & Larson, Å. A computational study of radiationless deactivation mechanisms of furan. *Chemical Physics* **379**, 6–12 (2011).
13. Steinmetzer, J., Kupfer, S. & Gräfe, S. pysisyphus: Exploring potential energy surfaces in ground and excited states. *International Journal of Quantum Chemistry* **121**, e26390 (2021).
14. Frisch, M. J. *et al.* Gaussian 16 Rev. C.01. (2016).
15. Adamo, C. & Barone, V. Toward reliable density functional methods without adjustable parameters: The PBE0 model. *J. Chem. Phys.* **110**, 6158–6170 (1999).
16. Ernzerhof, M. & Scuseria, G. E. Assessment of the Perdew–Burke–Ernzerhof exchange–correlation functional. *J. Chem. Phys.* **110**, 5029–5036 (1999).
17. Clark, T., Chandrasekhar, J., Spitznagel, G. W. & Schleyer, P. V. R. Efficient diffuse function-augmented basis sets for anion calculations. III. The 3-21+G basis set for first-row elements, Li–F. *Journal of Computational Chemistry* **4**, 294–301 (1983).
18. Krishnan, R., Binkley, J. S., Seeger, R. & Pople, J. A. Self-consistent molecular orbital methods. XX. A basis set for correlated wave functions. *J. Chem. Phys.* **72**, 650–654 (1980).

19. Purvis, G. D. & Bartlett, R. J. A full coupled-cluster singles and doubles model: The inclusion of disconnected triples. *J. Chem. Phys.* **76**, 1910–1918 (1982).
20. Stanton, J. F. & Bartlett, R. J. The equation of motion coupled-cluster method. A systematic biorthogonal approach to molecular excitation energies, transition probabilities, and excited state properties. *J. Chem. Phys.* **98**, 7029–7039 (1993).
21. Cederbaum, L. S., Domcke, W. & Schirmer, J. Many-body theory of core holes. *Phys. Rev. A* **22**, 206–222 (1980).
22. Vidal, M. L., Feng, X., Epifanovsky, E., Krylov, A. I. & Coriani, S. New and Efficient Equation-of-Motion Coupled-Cluster Framework for Core-Excited and Core-Ionized States. *J. Chem. Theory Comput.* **15**, 3117–3133 (2019).
23. Coriani, S. & Koch, H. Communication: X-ray absorption spectra and core-ionization potentials within a core-valence separated coupled cluster framework. *J. Chem. Phys.* **143**, 181103 (2015).
24. Dunning, T. H. Gaussian basis sets for use in correlated molecular calculations. I. The atoms boron through neon and hydrogen. *J. Chem. Phys.* **90**, 1007–1023 (1989).
25. Kendall, R. A., Dunning, T. H. & Harrison, R. J. Electron affinities of the first-row atoms revisited. Systematic basis sets and wave functions. *J. Chem. Phys.* **96**, 6796–6806 (1992).
26. Shao, Y. *et al.* Advances in molecular quantum chemistry contained in the Q-Chem 4 program package. *Molecular Physics* **113**, 184–215 (2015).
27. Richter, M., Marquetand, P., González-Vázquez, J., Sola, I. & González, L. SHARC: ab Initio Molecular Dynamics with Surface Hopping in the Adiabatic Representation Including Arbitrary Couplings. *J. Chem. Theory Comput.* **7**, 1253–1258 (2011).
28. Mai, S., Marquetand, P. & González, L. Nonadiabatic dynamics: The SHARC approach. *WIREs Computational Molecular Science* **8**, e1370 (2018).
29. Dahl, J. P. & Springborg, M. The Morse oscillator in position space, momentum space, and phase space. *J. Chem. Phys.* **88**, 4535–4547 (1988).
30. Schinke, R. *Photodissociation Dynamics: Spectroscopy and Fragmentation of Small Polyatomic Molecules*. (Cambridge University Press, 1993). doi:10.1017/CBO9780511586453.

31. Andrade, X. *et al.* Time-dependent density-functional theory in massively parallel computer architectures: the octopus project. *Journal of Physics: Condensed Matter* **24**, 233202 (2012).
32. Tancogne-Dejean, N. *et al.* Octopus, a computational framework for exploring light-driven phenomena and quantum dynamics in extended and finite systems. *J. Chem. Phys.* **152**, 124119 (2020).
33. Dirac, P. a. M. Note on Exchange Phenomena in the Thomas Atom. *Mathematical Proceedings of the Cambridge Philosophical Society* **26**, 376–385 (1930).
34. Perdew, J. P. & Zunger, A. Self-interaction correction to density-functional approximations for many-electron systems. *Phys. Rev. B* **23**, 5048–5079 (1981).
35. Bloch, F. Bemerkung zur Elektronentheorie des Ferromagnetismus und der elektrischen Leitfähigkeit. *Zeitschrift für Physik* **57**, 545–555 (1929).
36. Kuhn, H. W. The Hungarian Method for the Assignment Problem. in *50 Years of Integer Programming 1958-2008: From the Early Years to the State-of-the-Art* (eds. Jünger, M. et al.) 29–47 (Springer, 2010). doi:10.1007/978-3-540-68279-0\_2.
37. Ong, S. P. *et al.* Python Materials Genomics (pymatgen): A robust, open-source python library for materials analysis. *Computational Materials Science* **68**, 314–319 (2013).
38. Kurtz, L., Hofmann, A. & de Vivie-Riedle, R. Ground state normal mode analysis: Linking excited state dynamics and experimental observables. *J. Chem. Phys.* **114**, 6151–6159 (2001).
39. Plasser, F. Dynamics Simulation of Excited State Intramolecular Proton Transfer. 64.



# The contribution of Compton ionization to ultrafast x-ray scattering

Cite as: *J. Chem. Phys.* **159**, 044108 (2023); doi: 10.1063/5.0156363

Submitted: 28 April 2023 • Accepted: 3 July 2023 •

Published Online: 26 July 2023



View Online



Export Citation



CrossMark

Karl Michael Ziems,<sup>1,2</sup> Mats Simmermacher,<sup>3,a)</sup> Stefanie Gräfe,<sup>1,2</sup> and Adam Kirrander<sup>3,b)</sup>

## AFFILIATIONS

<sup>1</sup>Max Planck School of Photonics, 07745 Jena, Germany

<sup>2</sup>Institute of Physical Chemistry, Friedrich Schiller University Jena, 07743 Jena, Germany

<sup>3</sup>Department of Chemistry, University of Oxford, Oxford OX1 3QZ, United Kingdom

<sup>a)</sup>Author to whom correspondence should be addressed: [mats.simmermacher@chem.ox.ac.uk](mailto:mats.simmermacher@chem.ox.ac.uk)

<sup>b)</sup>Electronic mail: [adam.kirrander@chem.ox.ac.uk](mailto:adam.kirrander@chem.ox.ac.uk)

## ABSTRACT

We investigate the role of Compton ionization in ultrafast non-resonant x-ray scattering using a molecular model system, which includes the ionization continuum via an orthonormalized plane wave ansatz. Elastic and inelastic components of the scattering signal, as well as coherent-mixed scattering that arises from electron dynamics, are calculated. By virtue of a near-quantitative distinction between scattering related to electronic transitions into bound and continuum states, we demonstrate how Compton ionization contributes to the coherent-mixed component. Analogous to inelastic scattering, the contribution to the coherent-mixed signal is significant and particularly manifests at intermediate and high-momentum transfers. Strikingly, for molecules with inversion symmetry, the exclusion of bound or continuum transitions may lead to the prediction of spurious coherent-mixed signals. We conclude that qualitative and quantitative accuracies of predicted scattering signals on detectors without energy resolution require that elements of the two-electron density operator are used. This approach inherently accounts for all accessible electronic transitions, including ionization.

© 2023 Author(s). All article content, except where otherwise noted, is licensed under a Creative Commons Attribution (CC BY) license (<http://creativecommons.org/licenses/by/4.0/>). <https://doi.org/10.1063/5.0156363>

## I. INTRODUCTION

Over the last decade, novel light sources have revolutionized femtochemistry and femtophysics.<sup>1</sup> Recently constructed X-Ray Free-Electron Lasers (XFELs)<sup>2–4</sup> offer pulses of hard x-rays with unprecedented brightness and duration that permit gas-phase ultrafast non-resonant x-ray scattering experiments capable of tracking photochemical reactions on timescales of a few tens to hundreds of femtoseconds.<sup>5–7</sup> Such experiments are much aided by the high photon flux and repetition rate of XFELs, leading to vast reductions in data acquisition time and excellent signal-to-noise ratios.

The experimental ultrafast x-ray scattering (UXS) signal is dominated by scattering from core electrons, leading to a valuable sensitivity to nuclear structure. This physics underpins the independent atom model (IAM),<sup>8,9</sup> which approximates a molecule's elastic scattering cross-section by a coherent sum of pre-tabulated form factors of the constituent atoms.<sup>10,11</sup> Although this provides reasonable agreement with measured data, in particular, for molecules in their electronic ground states that are comprised of heavier elements, recent improvements in experimental capability as well as the

increasing focus on photoexcited systems demand a more accurate description based on electronic structure theory.<sup>12–17</sup>

These experimental and theoretical advances stand to allow subtle effects of electronic excitation, chemical bonding, or electronic correlation, previously hidden in the background of the data, to become visible.<sup>18</sup> Experiments have already demonstrated that excited electronic states,<sup>19</sup> charge transfer,<sup>20</sup> ionization,<sup>21</sup> and the orientation of transition dipole moments<sup>22</sup> can be identified in the scattering signals. Furthermore, the prospect of XFELs providing attosecond pulses in the hard x-ray regime<sup>23–30</sup> will eventually allow for the real-time observation of electron dynamics with UXS.<sup>20,31–41</sup> None of these effects can be accounted for by the IAM, and their emergence calls for further refinement of the theoretical framework.

The development of such a framework has received significant attention. It began with a semi-classical description of the time-resolved scattering cross-section,<sup>42,43</sup> continued with its rigorous derivation within non-relativistic quantum electrodynamics,<sup>31,37,44,45</sup> and culminated in the first proof-of-concept simulations of scattering from electronic wave packets.<sup>31,33,34,36,46</sup> Although these seminal simulations demonstrate

that UXS is capable of probing electron dynamics, they rely on the assumption of energy-resolving detectors or arbitrarily truncate the infinite sum over states, thereby excluding most inelastically scattered photons and their associated electronic transitions. Apart from general symmetry considerations,<sup>37,45,47</sup> it remains an open question of how these hitherto disregarded transitions, in particular, Compton ionization, affect the UXS signal of non-stationary electronic wave packets. We address this question using accurate simulations of x-ray scattering from a model system.

Model systems have a rich tradition in theoretical physics and chemistry and advance the qualitative understanding of fundamental processes. In strong field physics, for example, the classical recollision model<sup>48,49</sup> and reduced-dimensionality models<sup>50–55</sup> have been used to explain phenomena such as multiphoton ionization, above-threshold ionization, high-harmonic generation, laser-induced electron diffraction, and holography.<sup>56</sup> In the field of quantum molecular dynamics, models are used to understand coupled electron-nuclear dynamics<sup>57–61</sup> and their interplay with photoionization.<sup>62–66</sup> Here, we use a correlated two-electron molecular model system that allows us to obtain numerically exact solutions to all electronic states on a grid. This facilitates the explicit evaluation of all inelastic and coherent-mixed one-electron scattering matrix elements that contribute to the scattering signal.

We emphasize that performing such a calculation for a real molecule with reasonable accuracy is challenging or even impossible. To the best of our knowledge, the only attempt to compute the complete sum over all final states of a non-hydrogenic system explicitly was reported by Slowik *et al.* for static inelastic scattering from the carbon atom in its electronic ground state via a Hartree–Fock–Slater model.<sup>57,68</sup> Their approach, however, relied on the availability of accurate grid-based radial functions, and its extension to molecules is not straightforward. Once standard quantum-chemical basis sets are employed, results from a Hartree–Fock–Slater approach inevitably suffer from the limited size and flexibility of the basis set. With our molecular model system, we can account for electron correlation beyond a mean-field description, achieve complete convergence of the sum over states, and obtain quantitative accuracy of the scattering signals and their contributions.

At this point, it is worthwhile to distinguish the contribution of Compton ionization to non-resonant x-ray scattering, mediated by the  $\hat{A}^2$ -term of the interaction Hamiltonian, from the effect of other x-ray-driven processes that lead to ionization. Most notably, radiation damage incurred via photoionization, mediated by  $\hat{p} \cdot \hat{A}$ , is an important concern in serial femtosecond crystallography where highly intense pulses of hard x-rays are used.<sup>69–75</sup> This effect is particularly strong for targets that contain heavy elements with large photoionization cross-sections.<sup>74,75</sup> Gas-phase UXS experiments, in contrast, can be carried out at relatively low x-ray intensities, thanks to the large number of molecules in the interaction region, and the probability of sequential photoionization and scattering is usually negligible.<sup>6,19,21,76–84</sup> Focusing on UXS, this article, therefore, refrains from a further discussion of the impact of radiation damage on the scattering signal, and we refer to the previously mentioned work by Slowik *et al.* for a detailed theoretical analysis of that matter.<sup>68</sup> Finally, we note in passing that Compton ionization has also been exploited to measure the momentum distribution of bound electrons.<sup>85–87</sup>

The remainder of the paper is organized as follows: in the theory section, we introduce the model system, review the theory of UXS, and provide an orbital-based interpretation of the scattering signal to aid qualitative understanding. Special emphasis is placed on casting existing theory into a form appropriate for the model system as well as on the difference in calculating the scattering signal via elements of either the one- or the two-electron density operator. In the result section, we start with static scattering from a single electronic state and then turn to UXS of an electronic wave packet. Finally, we summarize our findings and provide a general perspective.

## II. THEORY

### A. Model system

We employ an electronic version of the one-dimensional-extended Shin–Metiu model<sup>61</sup> sketched in Fig. 1. The system is composed of three space-fixed nuclear point charges and two moving electrons with coordinates  $x$  and  $y$ , respectively. The two outer nuclei are fixed at  $\pm\zeta$ , whereas the position of the inner nucleus relative to the center of mass of the two outer nuclei is an adjustable parameter, given by the displacement coordinate  $R$ . The model's electronic Hamiltonian is

$$\mathcal{H}_0 = \frac{\hat{p}_x^2}{2} + \frac{\hat{p}_y^2}{2} + \hat{V}^{2e}(x, y; R), \quad (1)$$

where  $\hat{p}_x$  and  $\hat{p}_y$  are the momentum operators of the two electrons, and  $\hat{V}^{2e}(x, y; R)$  describes the Coulomb interaction between all particles, omitting the constant interaction of the fixed outer nuclei,

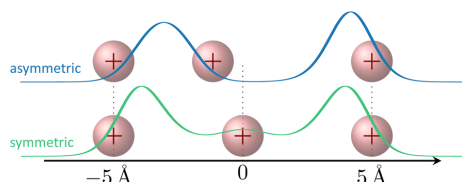
$$\begin{aligned} \hat{V}^{2e}(x, y; R) = & \frac{Z_1 Z}{|\zeta - R|} + \frac{Z_2 Z}{|\zeta + R|} + \frac{\text{erf}\left(\frac{|x-y|}{R_e}\right)}{|x-y|} \\ & - \frac{Z \text{erf}\left(\frac{|R-y|}{R_e}\right)}{|R-y|} - \frac{Z_1 \text{erf}\left(\frac{|\zeta-y|}{R_f}\right)}{|\zeta-y|} - \frac{Z_2 \text{erf}\left(\frac{|\zeta+y|}{R_f}\right)}{|\zeta+y|} \\ & - \frac{Z \text{erf}\left(\frac{|R-x|}{R_e}\right)}{|R-x|} - \frac{Z_1 \text{erf}\left(\frac{|\zeta-x|}{R_f}\right)}{|\zeta-x|} - \frac{Z_2 \text{erf}\left(\frac{|\zeta+x|}{R_f}\right)}{|\zeta+x|}. \end{aligned} \quad (2)$$

Here, soft Coulomb interactions are parameterized with error functions,  $\text{erf}(\dots)$ . Their screening parameters are set to  $R_e = R_f = R_e = 1.5 \text{ \AA}$ , the distance between the outer nuclei is  $2\zeta = 10.0 \text{ \AA}$ , and the nuclear charges are chosen to be  $Z_1 = Z_2 = Z = 1$ . In the following, we consider two values of the displacement coordinate  $R$  for the central nucleus. For  $R = 0 \text{ \AA}$ , the two electrons experience a symmetric Coulomb potential, whereas for  $R = -2.05 \text{ \AA}$ , the potential is asymmetric. The latter configuration is known to be the equilibrium geometry of the system.<sup>66</sup> Overall, this commonly employed set of parameters results in realistic internuclear distances and energetically well-separated eigenstates in the weak non-adiabatic coupling regime.<sup>64,66</sup>

With the two-electron Hamiltonian in Eq. (1), the time-independent electronic Schrödinger equation reads,

$$\left[ \frac{\hat{p}_x^2}{2} + \frac{\hat{p}_y^2}{2} + \hat{V}^{2e}(x, y; R) \right] \varphi_i^{2e}(x, y; R) = V_i^{2e}(R) \varphi_i^{2e}(x, y; R), \quad (3)$$





**FIG. 1.** Schematic representation of the symmetric ( $R = 0.00 \text{ \AA}$ , bottom) and asymmetric ( $R = -2.05 \text{ \AA}$ , top) model configurations. The colored solid lines show the one-electron density of the system in its electronic ground state,  $\rho_{00}(x)$ .

and yields the adiabatic two-electron eigenenergies,  $V_i^{2e}(R)$ , and eigenstates,  $\varphi_i^{2e}(x, y; R)$ . Although these eigenstates form a complete basis, it is computationally expensive to calculate all possible  $\mathcal{N}_x^2$  eigenstates on the Cartesian grid of  $\mathcal{N}_x$  points per dimension. We, therefore, use the exact two-electron eigenstates,  $\varphi_i^{2e}(x, y; R)$ , only to describe the manifold of  $\mathcal{N}_2$  bound states below the first ionization threshold and utilize a plane-wave approach to complete the basis. To this end, we define a cationic system that has the same nuclear configuration as the full two-electron system but contains only one electron. The time-independent electronic Schrödinger equation of this system is

$$\left[ \frac{\hat{p}_y^2}{2} + \hat{V}^{1e}(y; R) \right] \phi_i^{1e}(y; R) = V_i^{1e}(R) \phi_i^{1e}(y; R), \quad (4)$$

with the adiabatic one-electron eigenenergies,  $V_i^{1e}(R)$ , and eigenstates,  $\phi_i^{1e}(y; R)$ . The energy of the cationic ground state,  $V_0^{1e}(R)$ , defines the first ionization threshold employed to limit the number of exact two-electron states calculated with Eq. (3). Analogous to Eq. (2), the operator  $\hat{V}^{1e}(y; R)$  describes the Coulomb interactions of the one-electron system,

$$\hat{V}^{1e}(y; R) = \frac{Z_1 Z}{|\zeta - R|} + \frac{Z_2 Z}{|\zeta + R|} - \frac{Z \operatorname{erf}\left(\frac{|R-y|}{R_c}\right)}{|R-y|} - \frac{Z_1 \operatorname{erf}\left(\frac{|\zeta-y|}{R_c}\right)}{|\zeta-y|} - \frac{Z_2 \operatorname{erf}\left(\frac{|\zeta+y|}{R_c}\right)}{|\zeta+y|}. \quad (5)$$

Crucially, all bound and continuum solutions to the one-electron Schrödinger equation in Eq. (4) can be obtained numerically.

For brevity, we will now drop the parametric dependence of the eigenstates on the nuclear displacement coordinate  $R$  and introduce Dirac notation, i.e.,  $\varphi_i^{2e}(x, y; R) = \langle x, y | \varphi_i^{2e} \rangle$  and  $\phi_i^{1e}(y; R) = \langle y | \phi_i^{1e} \rangle$ . To complete the two-electron basis, the other electron not described by Eq. (4) is approximately mapped by a plane wave,  $\langle x | k \rangle = \exp[ikx]$ , where  $i$  is the imaginary unit and  $k$  a wave vector on the momentum grid. Starting from an initial singlet state with an antisymmetric spin function, each spatial two-electron basis function in the manifold of ionized or highly excited singlet states is then a symmetrized direct product,

$$\langle x, y | k, \phi_i^{1e} \rangle = \frac{1}{\sqrt{2}} \left( e^{ikx} \phi_i^{1e}(y) + \phi_i^{1e}(x) e^{iky} \right), \quad (6)$$

orthonormalized with respect to the subspace of bound states below the first ionization threshold,

$$|\phi_{i', \kappa}^{2e} \rangle = N_{i', \kappa} \left( |k, \phi_i^{1e} \rangle - \sum_{i=1}^{\mathcal{N}_2} |\varphi_i^{2e} \rangle \langle \varphi_i^{2e} | k, \phi_i^{1e} \rangle \right), \quad (7)$$

where  $\kappa$  is the index of  $k$  on the momentum grid,<sup>88</sup>  $\mathcal{N}_2$  is again the number of bound states below the first ionization threshold, and  $N_{i', \kappa}$  ensures normalization,

$$N_{i', \kappa} = \left( 1 + \left| \langle k | \phi_i^{1e} \rangle \right|^2 - \sum_{i=1}^{\mathcal{N}_2} \left| \langle \varphi_i^{2e} | k, \phi_i^{1e} \rangle \right|^2 \right)^{-1/2}. \quad (8)$$

We note that the direct-product ansatz in Eq. (7) cannot account for residual Coulomb interaction between the two electrons or between the plane-wave electron and the nuclei. However, the omission of this Coulomb interaction is of no concern here since we are not interested in particular eigenstates above the first ionization threshold but only seek to define a complete and orthonormal basis that explicitly includes the continuum.

To summarize, the two regimes of the model's two-electron basis in Eqs. (3) and (7) are

1. exact bound states,  $|\varphi_i^{2e} \rangle$ , with  $i \in [0, \mathcal{N}_2)$ , and
2. ionized and excited states above the first ionization threshold,  $|\phi_{i', \kappa}^{2e} \rangle$ , with  $i' \in [0, \mathcal{N}_x)$  and  $\kappa \in [0, \mathcal{N}_x)$ .

## B. Ultrafast x-ray scattering

The observable quantity in UXS is the time-dependent differential scattering cross-section,  $d\sigma/d\Omega$ . It is equal to the number of photons scattered into a given solid angle  $\Omega$  and can be derived within first-order time-dependent perturbation theory either based on semi-classical theory<sup>42,43</sup> or non-relativistic quantum electrodynamics.<sup>31,44</sup> For a coherent superposition of  $\mathcal{N}_s$  electronic eigenstates,

$$|\Psi(t)\rangle = \sum_{i=1}^{\mathcal{N}_s} c_i e^{-iE_i t/\hbar} |\varphi_i\rangle, \quad (9)$$

where  $t$  denotes the time,  $|c_i|^2$  is the population,  $\hbar$  is the reduced Planck constant,  $E_i = V_i^{2e}(R)$  is the electronic energy of state  $|\varphi_i\rangle = |\varphi_i^{2e}\rangle$ , and within the commonly applied Waller–Hartree approximation,<sup>89</sup> the scattering cross-section<sup>33,37</sup> for the model system can be written as

$$\frac{d\sigma}{d\Omega} = \left( \frac{d\sigma}{d\Omega} \right)_{\text{Th}} \sum_{i,j}^{\mathcal{N}_s} c_j^* c_i \Lambda_{ji}(q; R) \times \int_{-\infty}^{+\infty} I(t-\tau) e^{i\omega_{ji}t} dt. \quad (10)$$

In Eq. (10) above,  $(d\sigma/d\Omega)_{\text{Th}}$  is the Thomson scattering cross-section of a free electron,  $I(t-\tau)$  is the photon-number intensity of the x-ray pulse centered at time  $\tau$ , the angular frequency is  $\omega_{ji} = (E_j - E_i)/\hbar$ , and  $\Lambda_{ji}(q; R)$  is a two-electron scattering matrix element of the respective states,  $|\varphi_i\rangle$  and  $|\varphi_j\rangle$ , at momentum transfer coordinate  $q$ . Here,  $q$  is the component of the momentum transfer vector  $\mathbf{q}$  in the direction of the molecular axis. Because of the

model system's confinement to one dimension, components of  $q$  orthogonal to the molecular axis do not carry information about the target. Despite the one-dimensionality of the model system, however, the x-ray photon is still allowed to change its direction when scattered, such that values  $q > 0$  are possible. The scattering geometry is two-dimensional, and the solid angle  $\Omega$  reduces to the polar scattering angle  $\theta$ . For a given mean-photon energy of the incident x-ray pulse, and within the Waller–Hartree approximation,  $q$  can be bijectively mapped to  $\theta$ . The precise relationship between  $q$  and  $\theta$  also depends on the relative orientation of the molecular axis and the wave vector of the incoming photon. Since this mapping only leads to compression or stretch of the scattering signal and does not alter its information content [see Eq. (S1) and Fig. S1 of the supplementary material], we will not consider a specific orientation and discuss scattering signals of the model system as functions of  $q$  rather than  $\theta$ .

Turning back to Eq. (10) and dropping  $R$  again, the two-electron scattering matrix elements are<sup>37</sup>

$$\begin{aligned}\Lambda_{ji}(q) &= \langle \varphi_j | \hat{L}^\dagger(q) \hat{L}(q) | \varphi_i \rangle \\ &= \delta_{ij} N_e + 2 \iint e^{iq(x-y)} \Gamma_{ji}(x, y) dx dy.\end{aligned}\quad (11)$$

The operator  $\hat{L}(q)$  in the first line of Eq. (11) is the one-electron scattering operator. For the model system, it is  $\hat{L}(q) = \exp[iq\hat{x}] + \exp[iq\hat{y}]$ . Moreover,  $\delta_{ij}$  is the Kronecker delta,  $N_e = 2$  is the number of electrons, and  $\Gamma_{ji}(x, y)$  is the two-electron (transition) density,

$$\Gamma_{ji}(x, y) = \varphi_j^*(x, y) \varphi_i(x, y). \quad (12)$$

The two-electron scattering matrix element  $\Lambda_{ji}(q)$  can thus be obtained from the two-fold Fourier transform of the two-electron (transition) density. Its diagonal terms are equal to the total scattering probability of the respective electronic state.

The expression for the scattering cross-section in Eq. (10) above is valid for the most common case of energy-integrating detectors, i.e., under the condition that all scattered photons are detected irrespective of their individual energies. Nuclear dynamics and nuclear eigenstates are furthermore not considered in the model employed here.

### 1. Total and coherent-mixed scatterings

In the following, it is assumed that the x-ray pulse is much shorter than the period of the wave packet and that the corresponding photon-number intensity,  $I(t - \tau)$ , is normalized to unity. All scattering signals will be given in units of the Thomson scattering cross-section,  $(d\sigma/d\Omega)_{\text{Th}}$ , and are henceforth written as  $S(q, \tau)$ . With Eq. (10), we define the scattering signal of the model system as

$$S(q, \tau) = \sum_{ij} c_j^* c_i e^{i\omega_{ji}\tau} \Lambda_{ji}(q). \quad (13)$$

The static, diagonal, part of Eq. (13) with  $i = j$ ,

$$S_t(q) = \sum_i |c_i|^2 \Lambda_{ii}(q), \quad (14)$$

is known as *total scattering*. The time-dependent part with  $i \neq j$  is sometimes termed *coherent-mixed scattering*,<sup>36,37</sup>

$$S_{\text{cm}}(q, \tau) = 2 \sum_{i=1}^{N_e-1} \sum_{j>i}^{N_e} \text{Re}[c_j^* c_i e^{i\omega_{ji}\tau} \Lambda_{ji}(q)], \quad (15)$$

where the symmetry of the off-diagonal two-electron scattering matrix elements,  $\Lambda_{ij}(q) = \Lambda_{ji}^*(q)$ , is used to reduce the sum over  $j$  to  $j > i$ . As mentioned before, the coherent-mixed component can probe ultrafast electron dynamics in the target.

### 2. Scattering components

One can now dissect the total scattering signal,  $S_t(q)$ , in Eq. (14) into its constituent elastic and inelastic components.<sup>37,42,44,45</sup> The scattering is said to be elastic if no energy, only momentum, is interchanged between the x-ray photon and the molecule. Inelastic scattering, often referred to as Compton scattering,<sup>90</sup> in contrast, also implies an energy transfer to or from the photon. First, the identity,

$$1 = \sum_{f=1}^{\infty} |\varphi_f\rangle\langle\varphi_f|, \quad (16)$$

is introduced between the two scattering operators in Eq. (11), which yields

$$\Lambda_{ji}(q) = \sum_{f=1}^{\infty} L_{fj}^*(q) L_{fi}(q). \quad (17)$$

Here,  $L_{fi}(q)$  is a one-electron scattering matrix element (a state-specific scattering amplitude),

$$L_{fi}(q) = \langle \varphi_f | L(q) | \varphi_i \rangle = \int e^{iqx} \rho_{fi}(x) dx, \quad (18)$$

and  $\rho_{fi}(x)$  is the one-electron (transition) density,

$$\rho_{fi}(x) = 2 \int \varphi_f^*(x, y) \varphi_i(x, y) dy. \quad (19)$$

Using Eq. (17), we can now define the *elastic* component of the total scattering signal in Eq. (14) to be

$$S_{\text{el}}(q) = \sum_{i=1}^{N_e} |c_i|^2 |L_{ii}(q)|^2, \quad (20)$$

where all state indices in Eq. (17) are equal,  $i = j = f$ . Similarly, the *inelastic* component with  $i = j$  and  $f \neq i$  is

$$S_{\text{in}}(q) = \sum_{i=1}^{N_e} |c_i|^2 \sum_{f \neq i}^{\infty} |L_{fi}(q)|^2. \quad (21)$$

Here, the scattered photon leads to an electronic transition,  $f \leftarrow i$ , in the molecule. As an alternative to Eq. (21), the inelastic component can be defined without the infinite sum over  $f$  simply by subtraction of the elastic component, Eq. (20), from the total scattering, Eq. (14),

$$S_{\text{in}}(q) = S_t(q) - S_{\text{el}}(q). \quad (22)$$

Finally, one can also express the coherent-mixed scattering in Eq. (15) in terms of one-electron scattering matrix elements. Insertion of Eq. (17) leads to,

$$S_{\text{cm}}(q, \tau) = 2 \sum_{i=1}^{N_s-1} \sum_{j>i}^{N_s} \text{Re} \left[ c_j^* c_i e^{i\omega_{ji}\tau} \sum_{f=1}^{\infty} L_{fj}^*(q) L_{fi}(q) \right]. \quad (23)$$

### 3. Orbital-based interpretation of the scattering signal

In Sec. III, we will, among other things, compare the inelastic and coherent-mixed components calculated via Eqs. (21) and (22) and via Eqs. (15) and (23). Before we move to the results, though, the reader may wonder how the formal equivalence of Eqs. (21) and (22) can be understood physically. How is it possible that a calculation that explicitly includes all electronic transitions to bound and ionized states and a simulation that only involves the molecule's two-electron density yield, at least in principle, the same result? How is the two-electron density accounting for inelastic scattering? A qualitative answer is most easily given if the model system is in a single electronic singlet state, written approximately as an antisymmetrized Hartree product of real-valued spatial molecular orbitals,  $\phi_1(x)$  and  $\phi_2(y)$ ,<sup>90</sup>

$$\varphi_X(m_x, x, m_y, y) = \frac{1}{\sqrt{2}} (\phi_1(x) \alpha(m_x) \phi_2(y) \beta(m_y) - \phi_2(x) \beta(m_x) \phi_1(y) \alpha(m_y)), \quad (24)$$

where  $\alpha(m_x)$  and  $\beta(m_y)$  are orthonormal spin functions. Integrating over the spin coordinates,  $m_x$  and  $m_y$ , the respective one- and two-electron densities in Eqs. (12) and (19) are

$$\rho_{\text{XX}}(x) = |\phi_1(x)|^2 + |\phi_2(x)|^2, \quad (25)$$

and

$$\Gamma_{\text{XX}}(x, y) = \frac{1}{2} (|\phi_1(x)|^2 |\phi_2(y)|^2 + |\phi_2(x)|^2 |\phi_1(y)|^2). \quad (26)$$

Insertion of the one-electron density,  $\rho_{\text{XX}}(x)$ , into Eqs. (18) and (20) and the two-electron density,  $\Gamma_{\text{XX}}(x, y)$ , into Eqs. (11) and (14), yields the following expressions for the elastic and total scattering signals,

$$S_{\text{el}}(q) = |l_{11}(q)|^2 + |l_{22}(q)|^2 + 2 \text{Re}[l_{11}(q) l_{22}^*(q)], \quad (27)$$

and

$$S_{\text{i}}(q) = 2 + 2 \text{Re}[l_{11}(q) l_{22}^*(q)], \quad (28)$$

where the elements  $l_{mn}(q)$  are one-dimensional Fourier transforms of products of spatial orbitals,

$$l_{mn}(q) = \int \phi_m^*(x) e^{iqx} \phi_n(x) dx. \quad (29)$$

Comparing Eqs. (27) and (28), the inelastic component in Eq. (22) can now be identified as

$$S_{\text{in}}(q) = 2 - |l_{11}(q)|^2 - |l_{22}(q)|^2. \quad (30)$$

This expression only involves the two occupied orbitals,<sup>68</sup> yet completely describes the inelastic scattering of the wave function in Eq. (24). Thereby, it offers a physical explanation of the equivalence of Eqs. (21) and (22). Instead of explicitly adding the scattering probabilities of every electronic transition, the Fourier transform of the two-electron density accounts for inelastic scattering by subtraction of the elastic scattering probability of every bound electron from the total scattering probability of two free electrons. For a triplet state or a system with more than two electrons,  $S_{\text{in}}(q)$  would be further reduced by the sum of all off-diagonal elements that refer to Pauli-forbidden transitions between orbitals occupied by electrons with the same spin. Crucially, all required information is contained within the system's two-electron density.

A similar analysis can be made for the coherent-mixed component in Eqs. (15) and (23). Assuming coherence between the wave function in Eq. (24) and an electronically excited singlet state,  $\varphi_B$ , with  $\phi_3 \leftarrow \phi_2$ , the two-electron transition density in Eq. (12) is

$$\Gamma_{\text{BX}}(x, y) = \frac{1}{2} (|\phi_1(x)|^2 \phi_3^*(y) \phi_2(y) + \phi_3^*(x) \phi_2(x) |\phi_1(y)|^2). \quad (31)$$

Inserting  $\Gamma_{\text{BX}}(x, y)$  into Eq. (11), one obtains the off-diagonal two-electron scattering matrix element,

$$\Lambda_{\text{BX}}(q) = 2 \text{Re}[l_{11}(q) l_{23}^*(q)], \quad (32)$$

which leads to the coherent-mixed scattering signal defined in Eq. (15),

$$S_{\text{cm}}(q, \tau) = 4 \text{Re}[c_j^* c_i e^{i\omega_{ji}\tau}] \text{Re}[l_{11}(q) l_{23}^*(q)]. \quad (33)$$

The coherent-mixed component can thus be understood as an interference of the orbital-transition amplitude  $l_{23}^*(q)$  with the diagonal element  $l_{11}(q)$ . The former refers to the orbitals in which the two states differ, the latter, to the occupied orbitals the states share. We note that for a system containing more than two electrons, the transition amplitude would interfere with all diagonal elements of the other electrons and the signal would be furthermore reduced by all Pauli forbidden transitions into or out of the two orbitals that differ. That has an important consequence. Albeit being a relatively weak effect related to a single orbital transition, here  $\phi_3 \leftarrow \phi_2$ , the coherent mixed component is somewhat amplified by the diagonal elements of all other electrons.

We can now compare the coherent-mixed component in Eq. (33) with the expression obtained via the infinite sum over states in Eq. (23). For that, we define a basis of singlet states excited by  $\phi_r \leftarrow \phi_1$  and  $\phi_s \leftarrow \phi_2$  with respect to Eq. (24), where  $r$  and  $s$  may refer to all bound and virtual orbitals as well as to all one-electron continuum functions. With Eq. (19) and integration over the spin coordinates, we now obtain the relevant one-electron transition densities,

$$\rho_{fX} = \delta_{s2} \phi_r^*(x) \phi_1(x) + \delta_{r1} \phi_s^*(x) \phi_2(x), \quad (34)$$

$$\rho_{fB} = \delta_{s3} \phi_r^*(x) \phi_1(x) + \delta_{r1} \phi_s^*(x) \phi_3(x), \quad (35)$$

and with Eq. (18), the respective one-electron scattering matrix elements,

$$L_{fX}(q) = \delta_{s2} l_{r1}(q) + \delta_{r1} l_{s2}(q), \quad (36)$$

$$L_{fB}(q) = \delta_{s3} l_{r1}(q) + \delta_{r1} l_{s3}(q).$$

Following Eq. (17), the two-electron scattering matrix elements are, therefore,

$$\Lambda_{\text{BX}}(q) = \sum_{f=1}^{\infty} L_{f\text{B}}^*(q) L_{f\text{X}}(q) \\ = 2 \operatorname{Re} [l_{11}(q) l_{23}^*(q)] + \sum_{s=1}^{\infty} l_{22}(q) l_{33}^*(q). \quad (37)$$

Here, the sum over  $s$  runs over the entire basis of orbitals and continuum single-particle functions. If complete, this sum must vanish for Eq. (37) to match Eq. (32). This implies that any finite truncation of the infinite sum over states in Eq. (23) adds complex-valued terms to the coherent mixed component that are spurious as long as the truncation is not justified by the detector response. The common and most severe truncation that only includes the populated states, for example, yields

$$\Lambda_{\text{BX}}^{\text{min}}(q) = 2 \operatorname{Re} [l_{11}(q) l_{23}^*(q)] + l_{12}(q) l_{13}^*(q) \\ + l_{22}(q) l_{23}^*(q) + l_{23}(q) l_{33}^*(q). \quad (38)$$

Clearly, the three complex-valued terms at the right-hand side of Eq. (38) do not appear in Eq. (32) above and are a mere artifact of the truncation. However, we note that these terms may become valid and detectable in the future once detectors with sufficient energy resolution are available.

### C. Numerical methods

Equations (3) and (4) are solved numerically on a grid of dimensions  $[-60, 60 \text{ \AA}]$  with  $\mathcal{N}_x = 256$  grid points for each  $x$  and  $y$  using the relaxation method based on imaginary time propagation.<sup>91</sup> The integration in imaginary time is performed with a time step of 5 as by utilizing the split-operator method in second order<sup>92</sup> and the FFTW3 subroutine library for Fourier transforms.<sup>93</sup> The one- and two-electron scattering matrix elements, and thereby the scattering signals, are computed by direct numerical integration of Eqs. (11) and (18).

## III. RESULTS AND DISCUSSION

In the following, we investigate x-ray scattering from single electronic states as well as from coherent superpositions of electronic states for our model system and shed light on fundamental questions of x-ray scattering from molecules. Especially, we will address the questions of (i) how individual transitions add up to the inelastic and coherent-mixed scattering signals, (ii) what role ionization into continuum plays, and (iii) how the symmetry of the electronic wave function affects the scattering signal.

Since scattering signals are displayed as functions of  $q$  rather than  $\theta$ , no particular mean-photon energy of the incident x-ray pulse is assumed. However, 10 keV would be an appropriate choice for scattering angles  $\theta \leq 60^\circ$  (see Fig. S1 in the supplementary material). Following Eq. (13), it is furthermore assumed that the pulse duration is much shorter than the period of the electronic wave packet. For the two cases of coherent-mixed scattering considered, this implies pulses significantly shorter than 2 and 10 fs, respectively.

### A. Static scattering from a single electronic state

We start by investigating x-ray scattering from the electronic ground state,  $|\varphi_0^{2e}\rangle$ , for the asymmetric configuration with  $R = -2.05 \text{ \AA}$  and a first ionization threshold of  $-9.96 \text{ eV}$ . All  $\mathcal{N}_2 = 37$  bound states below this threshold are obtained from Eq. (3) and 65 536 orthonormalized product states, defined by Eq. (7), complete the two-electron basis.

The ground state's one- and two-electron densities,  $\rho_{00}(x)$  and  $\Gamma_{00}(x, y)$ , are shown in Figs. 2(a) and 2(b). The two-electron density is symmetric under reflection over the diagonal axis with  $x = y$  since two electrons are indistinguishable. Figure 2(c) also displays the electron-electron pair distribution function (PDF),  $g_{00}(x - y)$ , which is obtained from  $\Gamma_{00}(x, y)$  by the coordinate transform  $\{x, y\} \rightarrow \{\Delta r, \bar{r}\}$ , where  $\Delta r = x - y$  and  $\bar{r} = (x + y)/2$ , and subsequent integration over  $\bar{r}$ . It displays the distribution of distances between the two electrons and peaks at  $8.4 \text{ \AA}$ .

As discussed around Eqs. (14) and (20) before, the two-fold Fourier transform of the two-electron density yields the static total scattering signal,  $S_t(q)$ , whereas the Fourier transform of the one-electron density leads to the elastic scattering signal,  $S_{el}(q)$ . Total scattering can also be obtained from the Fourier transform of the PDF,

$$\Lambda_{00}(q) = 2 + 2 \int e^{iqx'} g_{00}(x') dx', \quad (39)$$

which follows from the application of the above-mentioned coordinate transform to the scattering matrix element in Eq. (11). This illustrates the well-known fact that the total scattering signal effectively probes the pairwise correlated distance of electrons.<sup>18,34,95</sup>

The resulting total scattering signal and its elastic and inelastic components are shown in Fig. 3. All three signals show the expected limiting behaviors at large and small momentum transfers. The total scattering signal is equal to  $N_e^2 = 4$  at  $q = 0$  and approaches  $N_e = 2$  as  $q \rightarrow \infty$ . The elastic and inelastic components are equal to  $N_e^2 = 4$  and 0 at  $q = 0$  and approach 0 and  $N_e = 2$  as  $q \rightarrow \infty$ , respectively. This is

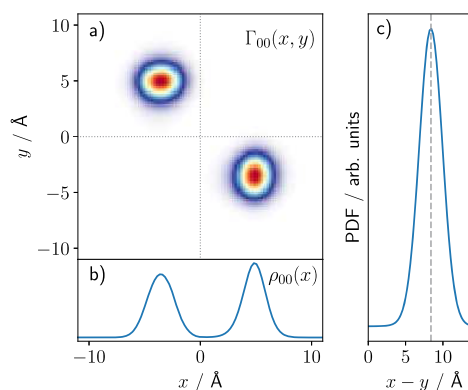
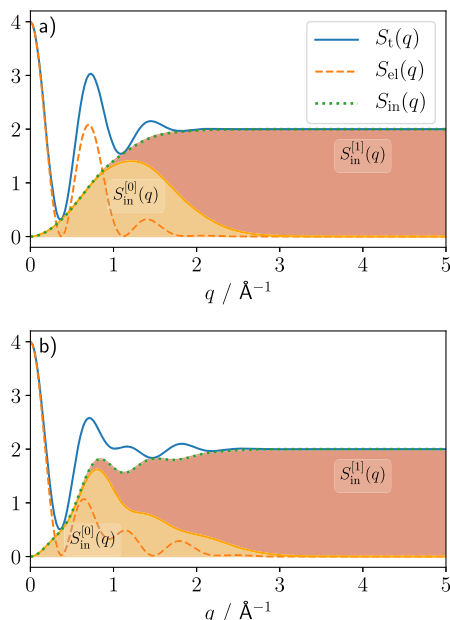


FIG. 2. Visualization of the electronic ground state of the model system in its asymmetric nuclear configuration with  $R = -2.05 \text{ \AA}$ . (a) Two-electron density,  $\Gamma_{00}(x, y)$ . (b) One-electron density,  $\rho_{00}(x)$ . (c) Pair distribution function (PDF),  $g_{00}(x - y)$ .



**FIG. 3.** Total x-ray scattering signal,  $S_t(q)$ , of the Shin–Metiu model system in its asymmetric nuclear configuration and its elastic and inelastic components,  $S_{el}(q)$  and  $S_{in}(q)$ . The colored areas display the decomposition of the inelastic signal into the contributions from bound-to-bound transitions (yellow) and single ionization (red). (a) The initial state is the electronic ground state. (b) The initial state is the second electronically excited state.

evident from the equations discussed in Sec. II B and conforms with the observation that x-ray scattering is predominantly elastic at small and inelastic at large values of  $q$ .

Following Eq. (22), the inelastic signal is calculated as the difference between the total and elastic signals. Moreover, it is also computed via the sum of all inelastic scattering matrix elements, Eq. (21), using the complete two-electron basis composed of both bound and continuum states. The latter approach permits the distinction of two contributions to the scattering signal that stem from different inelastic transitions:

1. bound-to-bound transitions into states below the first ionization threshold,  $|\varphi_f^{2e}\rangle \leftarrow |\varphi_0^{2e}\rangle$  with  $f \in [1, \mathcal{N}_2)$ , that lead to  $S_{in}^{[0]}(q)$ ,
2. single ionization,  $|\phi_{f',\kappa}^{2e}\rangle \leftarrow |\varphi_0^{2e}\rangle$  with  $f' \in [0, \mathcal{N}_x)$  and  $\kappa \in [0, \mathcal{N}_x)$ , that leads to  $S_{in}^{[1]}(q)$ .

The second contribution may also involve transitions into highly excited states above the first ionization threshold but is dominated by single ionization since the exact one-electron scattering operator in Eq. (18),  $L(q)$ , does not allow for direct double excitation of the electronic ground state. Figure 3(a) shows that these

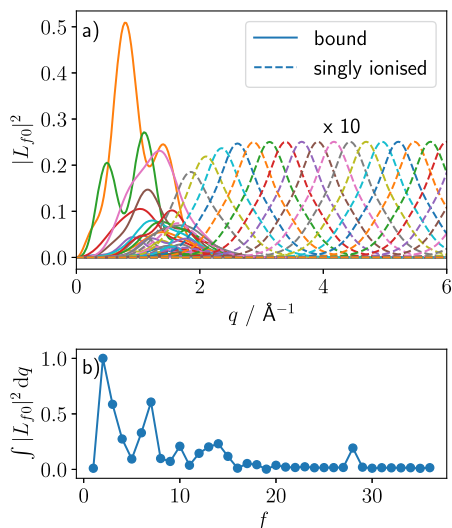
two contributions add up to the same inelastic signal as the calculation that utilizes the two-electron density and Eq. (22). The results illustrate the well-known fact that bound-to-bound transitions account for only a fraction of the inelastic signal and that transitions into the continuum have to be considered, in particular, at large values of  $q$ .<sup>86,87,90,96–99</sup> Although bound-to-bound transitions dominate the inelastic component up to around  $1.6 \text{ \AA}^{-1}$ , their contributions are negligible after  $\sim 3.0 \text{ \AA}^{-1}$ . Most photons that undergo a large momentum transfer thus ionize the model system. Considering all bound-to-bound contributions to the inelastic scattering cross-section calculated with Hartree–Fock–Slater, Slowik *et al.* reported similar findings at  $q \approx 5.0 \text{ \AA}^{-1}$  for the carbon atom in its electronic ground state.<sup>68</sup>

The same decomposition of the total scattering signal into its various contributions is shown for the second electronically excited state,  $|\varphi_2^{2e}\rangle$ , in Fig. 3(b). Overall, the general trends are the same as for the electronic ground state in Fig. 3(a). However, the signals deviate notably at intermediate momentum transfer, which is also the region of  $q$  where ionization begins to contribute significantly. Both the elastic and inelastic components clearly carry information about the state of the system,<sup>100</sup> although inelastic scattering is often considered to be incoherent and structureless. Similar findings have been reported for the isoelectric hydrogen molecule,<sup>36,37</sup> as well as for larger molecules.<sup>16,17</sup>

We note that these differences appear particularly strong here because the model system contains only two electrons. For atoms and molecules with a larger number of electrons, the relative effect of the electronic state on the scattering signal would be weaker. Nevertheless, the change in the total scattering signal on Rydberg excitation of a molecule with 44 electrons has been observed recently, demonstrating that such effects are indeed measurable.<sup>19</sup>

Next, we address the contributions of individual one-electron scattering matrix elements to the inelastic signal via their absolute squares according to Eq. (21). In Fig. 4(a), selected absolute-squared elements are shown. All elements that correspond to bound-to-bound transitions and every fifth element that relates to a single ionization is displayed. As already seen in Fig. 3(a), the bound-to-bound transitions contribute most at small values of  $q$ , whereas single ionization is prominent at larger momentum transfer. Intuitively, the larger the continuum quantum number  $\kappa$ , the higher the region of  $q$  where the corresponding element is found. For final states with a large value of  $k$ , the kinetic energy transfer  $\Delta E_{kin}$  of the inelastic transition roughly coincides with the mean momentum transfer  $\langle q \rangle$  of the respective absolute-squared element, i.e.,  $\Delta E_{kin} \approx (\hbar q)^2 / (2m_e)$  with  $m_e$  being the rest mass of the electron. This relation does, however, not hold for inelastic scattering within the manifold of completely bound states or for small values of  $k$ .

Unsurprisingly, the integrated weights of the bound-to-bound elements in Fig. 4(b) show that the elements tend to contribute less to the inelastic scattering the larger their respective transition is, i.e., the larger the index  $f$  of the final state. This overall trend follows the decreasing overlap between the ground state and excited states. Intriguingly, the inelastic element with  $f = 28$  somewhat breaks with this trend, being markedly stronger than all other elements above  $f = 14$ . This can be attributed to the characters of the final states: almost all states with  $f > 14$  display significant Rydberg character, whereas state 28 is a more localized excited state that interrupts the Rydberg series (see Figs. S2 and S3 in the supplementary material).



**FIG. 4.** (a) Individual absolute-squared inelastic one-electron scattering matrix elements for the electronic ground state of the asymmetric Shin–Metiu model system,  $|L_{f0}(q)|^2$ . The solid lines refer to all elements that correspond to bound-to-bound transitions, whereas the dashed lines depict every fifth element that describes a single ionization into  $|\varphi_{0\alpha}^{2e}\rangle$ . For better visibility, the latter elements are scaled by a factor of 10. (b) Integrated and normalized weights of different elements that imply a bound-to-bound transition into  $|\varphi_7^{2e}\rangle$ .

Hence, state 28 has a larger overlap with the electronic ground state and consequently contributes with a stronger inelastic element to the scattering signal.

### B. Scattering from an electronic wave packet

Next, we investigate UXS from a coherent superposition of electronic states. Such a superposition or wave packet can be created by, for instance, coherent broadband excitation of several electronic states or non-adiabatic coupling of two states at a conical intersection. Following Eq. (9), we consider the coherent superposition of the first and second electronically excited states of the Shin–Metiu model system in its asymmetric configuration,

$$|\Psi(t)\rangle = \frac{1}{\sqrt{2}} \left( e^{-iE_1 t/\hbar} |\varphi_1^{2e}\rangle + e^{-iE_2 t/\hbar} |\varphi_2^{2e}\rangle \right). \quad (40)$$

Here, both states contribute with equal weight. For this wave packet, the coherent-mixed component in Eq. (15) is

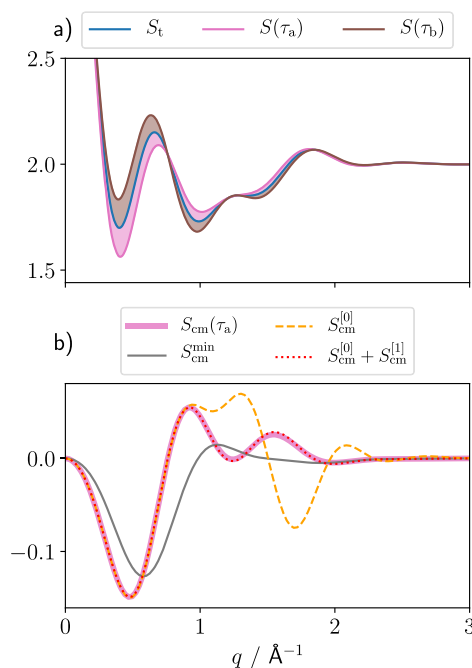
$$\begin{aligned} S_{\text{cm}}(q, \tau) &= \text{Re} \left[ e^{i\omega_{21}\tau} \Lambda_{21}(q) \right] \\ &= \cos[\omega_{21}\tau] \text{Re}[\Lambda_{21}(q)] - \sin[\omega_{21}\tau] \text{Im}[\Lambda_{21}(q)]. \end{aligned} \quad (41)$$

The numerical evaluation of the two-electron scattering matrix element reveals that  $\Lambda_{21}(q)$  is purely real-valued, which conforms qualitatively with the orbital-based analysis in Eq. (32). Hence, only the term proportional to  $\cos[\omega_{21}\tau]$  in Eq. (41) contributes to the

coherent-mixed scattering signal, whereas the term proportional to  $\sin[\omega_{21}\tau]$  vanishes. Since the two states in Eq. (40) differ in their energies by  $\Delta E_{21} \approx 1.785$  eV, the coherent-mixed signal in Eq. (41) oscillates with an angular frequency of  $\omega_{21} = \Delta E_{21}/\hbar \approx 2.712$  fs<sup>-1</sup>, which corresponds to a period of  $T_{21} \approx 2.317$  fs.

In the following, we will consider  $S_{\text{cm}}(q, \tau)$  at  $\tau_a = 0$  and  $\tau_b = 1/2 T_{21}$ . At these times, the coherent-mixed signal is the strongest.  $S_{\text{cm}}(q, \tau_a)$  and  $S_{\text{cm}}(q, \tau_b)$  have opposite signs but are otherwise equal. Figure 5(a) shows these signals on top of the static total scattering signal,  $S_t(q)$ . The coherent-mixed component modulates the magnitude of the scattering signal, and the curves at  $\tau_a$  and  $\tau_b$  show the two extremes between which the signal oscillates. Here,  $S_{\text{cm}}(q, \tau_a)$  and  $S_{\text{cm}}(q, \tau_b)$  are obtained via the two-fold Fourier transform of the two-electron transition density in Eq. (15).

Analogous to the analysis of the inelastic component in Sec. III A, we now dissect the coherent-mixed signal into its



**FIG. 5.** (a) Complete scattering signal,  $S(q, \tau)$ , of the asymmetric Shin–Metiu model system in a coherent superposition of its first and second electronically excited states. The complete signal contains the static total and non-stationary coherent-mixed components,  $S_t(q)$  and  $S_{\text{cm}}(q, \tau)$ , respectively. It is shown at times  $\tau_a = 0$  and  $\tau_b = 1/2 T_{21}$  with  $T_{21} \approx 2.317$  fs. The filled areas display how the coherent-mixed component modulates the scattering signal over the course of one period. (b) Decomposition of the coherent-mixed signal at  $\tau_a$  into its contributions from different electronic transitions.



contributions from different electronic transitions via the sum over states in Eq. (23). Equation (41) now becomes

$$\begin{aligned} S_{\text{cm}}(q, \tau) &= \text{Re} \left[ e^{i\omega_{21}\tau} \sum_{f=1}^{\infty} L_{f2}^*(q) L_{f1}(q) \right] \\ &= \cos[\omega_{21}\tau] \sum_{f=1}^{\infty} \text{Re}[L_{f2}^*(q) L_{f1}(q)] \\ &\quad - \sin[\omega_{21}\tau] \sum_{f=1}^{\infty} \text{Im}[L_{f2}^*(q) L_{f1}(q)]. \end{aligned} \quad (42)$$

Here, the coherent-mixed component is expressed in terms of its constituent one-electron scattering matrix elements,  $L_f(q)$ . Again, only the cosine term can contribute to the coherent-mixed scattering signal. The sum over the imaginary parts proportional to  $\sin[\omega_{21}\tau]$  must vanish in the limit  $f \rightarrow \infty$  to match the result obtained from the two-electron density, Eq. (41), and is always zero at times  $\tau_a$  and  $\tau_b$ . With the complete two-electron basis for the Shin–Metiu model system at hand, we can now, as before, distinguish between different contributions that arise from different electronic transitions:

1. transitions between the populated bound states only,  $|\varphi_f^{2e}\rangle \leftarrow |\varphi_f^{2e}\rangle$  and  $|\varphi_f^{2e}\rangle \leftarrow |\varphi_f^{2e}\rangle$  with  $f \in [1, 2]$ , which lead to  $S_{\text{cm}}^{\text{min}}(q, \tau)$ ,
2. all bound-to-bound transitions into states below the first ionization threshold,  $|\varphi_f^{2e}\rangle \leftarrow |\varphi_1^{2e}\rangle$  and  $|\varphi_f^{2e}\rangle \leftarrow |\varphi_2^{2e}\rangle$  with  $f \in [0, \mathcal{N}_2)$ , which lead to  $S_{\text{cm}}^{[0]}(q, \tau)$ , and
3. single ionization,  $|\varphi_{f',\kappa}^{2e}\rangle \leftarrow |\varphi_1^{2e}\rangle$  as well as  $|\varphi_{f',\kappa}^{2e}\rangle \leftarrow |\varphi_2^{2e}\rangle$  with  $f' \in [0, \mathcal{N}_x)$  and  $\kappa \in [0, \mathcal{N}_x)$ , which leads to  $S_{\text{cm}}^{[1]}(q, \tau)$ .

The third contribution may, again, involve transitions into highly excited states above the first ionization threshold but is dominated by single ionization.

In previous proof-of-concept simulations of coherent-mixed scattering, it was custom to consider either only the minimal contribution from the populated bound states or a truncated expansion somewhere in between contributions 1 and 2 since only a finite number of electronic states were available or energy-resolving detectors were assumed.<sup>20,31,33–36,38,40,101,102</sup> Such truncated simulations lack all contributions from ionization and even from most bound-to-bound transitions, potentially leading to strong discrepancy between the predicted coherent-mixed signal and the signal that would be measured on an energy-integrating detector.

Figure 5(b) shows that the contributions from all bound-to-bound transitions as well as single ionization add up to the same coherent-mixed scattering signal as obtained from the calculation via Eqs. (11) and (15). It is furthermore evident that the inclusion of more electronic transitions does not lead to a trend that is as clear and simple as for the inelastic scattering in Fig. 3 before. In the latter case, the one-electron scattering matrix elements of different electronic transitions added up incoherently and thus only increased the signal by specific  $q$ -dependent magnitudes. In coherent-mixed scattering, however, the individual amplitudes interfere both constructively and destructively and thus lead to a

more complex build-up of the signal that cannot be as easily anticipated from its constituent terms as for the inelastic component. Although the minimal contribution from the populated bound states roughly matches the full coherent-mixed component at low momentum transfer, it does not lead to the correct signal at intermediate values of  $q$ . Only the inclusion of all contributions, i.e., of all possible singly excited and singly ionized states, guarantees that the signal simulated via the sum over states in Eq. (42) is correct—at least as long as current energy-integrating detectors are employed. Clearly, such an infinite sum-over-states calculation would be infeasible for real molecules outside the realm of simple model systems. Future work on coherent-mixed scattering without energy resolution should, therefore, be based on the two-fold Fourier transform of the two-electron transition density rather than on a truncated sum over states.

Previous work has furthermore emphasized that the complete coherent-mixed signal vanishes for a superposition of electronic states that transform differently under inversion.<sup>37,45,47</sup> To further illustrate that we consider the symmetric Shin–Metiu model system with  $R = 0$  Å and a first ionization threshold of  $-9.10$  eV. All  $\mathcal{N}_2 = 48$  bound states below this threshold are obtained. Now, the system has a center of inversion at  $x = 0$  Å and  $y = 0$  Å, and the two superposed electronic states of the wave packet in Eq. (40) have different inversion symmetries, *gerade* and *ungerade*. The coherent-mixed scattering signal must, therefore, vanish in the limit  $f \rightarrow \infty$  now.

Figure 6, which displays the coherent-mixed scattering signal at  $\tau = 1/4 T_{21}$  with  $T_{21} \approx 10.12$  fs, shows that this is indeed the case. Again, the infinite sum over states and the two-fold Fourier transform of the two-electron transition density yield the same results, here zero. Any finite truncation of the sum in Eq. (42), however, retains non-vanishing terms proportional to  $\sin[\omega_{21}\tau]$  and thus leads to a spurious signal. Again, this conforms qualitatively with the orbital-based analysis in Eq. (37), which demonstrates that additional complex-valued terms may arise when the sum over states is truncated.

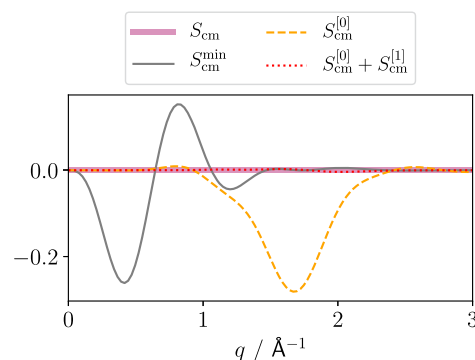


FIG. 6. Decomposition of the coherent-mixed signal,  $S_{\text{cm}}(q, \tau)$ , of the symmetric Shin–Metiu model system in a coherent superposition of the first and second electronically excited states. The signal and its contributions are shown at time  $\tau = 1/4 T_{21}$  with  $T_{21} \approx 10.12$  fs.

## IV. SUMMARY

In this work, we investigate how often disregarded electronic transitions affect the UXS signal, in particular, transitions into the continuum that lead to Compton ionization of the target. To this end, we employ a two-electron molecular model system, for which numerically exact solutions to the electronic Schrödinger equation and a complete continuum basis are obtained. For the latter, we use an orthonormalized plane-wave ansatz. Moreover, the theory of UXS is adapted to the model system, and an orbital-based interpretation of the x-ray scattering signal is provided.

The model system permits an accurate and direct calculation of the inelastic component of the total x-ray scattering signal via elements of the one-electron density operator and a formally infinite sum over all accessible electronic states, bound and continuum. Hence, a near-quantitative distinction between the contributions to inelastic scattering from bound-to-bound transitions and Compton ionization becomes possible. The well-known fact that bound-to-bound transitions dominate at low and single ionization at intermediate to high momentum transfer is thereby illustrated, and the capacity of the model to yield detailed information about the composition of the scattering signal is demonstrated.

For electron dynamics, i.e., when electronic states are superposed coherently and the duration of the x-ray pulse is sufficiently short, the UXS signal will contain an additional coherent-mixed component that appears alongside the more common and, in this context, static, elastic, and inelastic signals. Summing over the individual electronic transitions again, we also find a significant contribution of ionization to coherent-mixed scattering at intermediate-to-high momentum transfer. In contrast to the inelastic component, however, the scattering amplitudes from different electronic transitions interfere. We demonstrate that inaccurate or spurious UXS signals may be obtained if the continuum is not included in full. A strong recommendation that emerges from this result is that energy-integrated UXS signals for electronic wave packets should be calculated via elements of the two-electron density operator. Such an approach inherently and efficiently accounts for all electronic transitions mediated by the x-ray photon.

Future studies using this model could tackle the role of nuclear dynamics<sup>34–37,103</sup> and compare electron and x-ray scattering.<sup>104–106</sup> Overall, the presented work brings new physical insights into how electronic structure, excitation, and dynamics manifests in static and ultrafast x-ray scattering. Although the work employs a model system, the conceptual advances presented herein may guide prospective experiments with realistic and accurate simulations. With the current advances toward sub-fs pulses at XFELs,<sup>30,106</sup> measurements of electron dynamics using scattering are not far removed.

## SUPPLEMENTARY MATERIAL

The supplementary material contains a detailed discussion of the mapping of the momentum transfer component  $q$  to the scattering angle  $\theta$  for the parallel and perpendicular orientations of the incident photon's wave vector with respect to the molecular axis. Figure S1 displays the total, elastic, and inelastic scattering signals from Fig. 3(a) as functions of  $\theta$ . One-electron densities of the first 35 electronic states of the molecular model system in its asymmet-

ric nuclear configuration are presented in Figs. S2 and S3 shows the respective electronic states with  $i = 26–30$ .

## ACKNOWLEDGMENTS

K.M.Z. and S.G. were part of the Max Planck School of Photonics supported by the German Federal Ministry for Education and Research, the Max Planck Society, and the Fraunhofer Society. K.M.Z. gratefully acknowledges ScotCHEM and funding received from the Scottish Government under the SFC Saltire Emerging Researcher ScotCHEM European Exchanges Scheme. The work has been partially performed under the Project HPC-EUROPA3 (Grant No. INFRAIA-2016-1-730897), with the support of the EC Research Innovation Action under the H2020 Program; in particular, the authors acknowledge the computer resources and technical support provided by the EPCC. Furthermore, A.K. and M.S. gratefully acknowledge funding from the UK Engineering and Physical Sciences Research Council (EPSRC), Grant No. EP/V049240. A.K. also acknowledges the Leverhulme Trust (RPG-2020-208) and the Department of Energy, Office of Science, Basic Energy Sciences, under Award No. DE-SC0020276.

## AUTHOR DECLARATIONS

## Conflict of Interest

The authors have no conflicts to disclose.

## Author Contributions

**Karl Michael Ziems:** Conceptualization (equal); Data curation (lead); Formal analysis (equal); Funding acquisition (equal); Investigation (equal); Methodology (equal); Software (lead); Validation (equal); Visualization (lead); Writing – original draft (equal); Writing – review & editing (equal). **Mats Simmermacher:** Conceptualization (equal); Data curation (supporting); Formal analysis (equal); Funding acquisition (equal); Investigation (equal); Methodology (equal); Software (supporting); Supervision (lead); Validation (equal); Visualization (supporting); Writing – original draft (equal); Writing – review & editing (equal). **Stefanie Gräfe:** Funding acquisition (equal); Project administration (equal); Supervision (equal); Writing – review & editing (supporting). **Adam Kirrander:** Formal analysis (supporting); Funding acquisition (equal); Project administration (equal); Supervision (equal); Writing – review & editing (equal).

## DATA AVAILABILITY

The data that support the findings of this study are available from the corresponding author upon reasonable request.

## REFERENCES

- 1 L. Young, K. Ueda, M. Gühr, P. H. Bucksbaum, M. Simon, S. Mukamel, N. Rohringer, K. C. Prince, C. Masciovecchio *et al.*, *J. Phys. B: At., Mol. Opt. Phys.* **51**, 032003 (2018).
- 2 C. Bostedt, J. D. Bozek, P. H. Bucksbaum, R. N. Coffee, J. B. Hastings, Z. Huang, R. W. Lee, S. Schorb, J. N. Corlett *et al.*, *J. Phys. B: At., Mol. Opt. Phys.* **46**, 164003 (2013).



- <sup>3</sup>M. Yabashi, H. Tanaka, T. Tanaka, H. Tomizawa, T. Togashi, M. Nagasono, T. Ishikawa, J. R. Harries, Y. Hikosaka *et al.*, *J. Phys. B: At., Mol. Opt. Phys.* **46**, 164001 (2013).
- <sup>4</sup>J. Feldhaus, M. Krikunova, M. Meyer, T. Möller, R. Moshhammer, A. Rudenko, T. Tschentscher, and J. Ullrich, *J. Phys. B: At., Mol. Opt. Phys.* **46**, 164002 (2013).
- <sup>5</sup>J. M. Budarz, M. P. Miniti, D. V. Cofer-Shabica, B. Stankus, A. Kirrander, J. B. Hastings, and P. M. Weber, *J. Phys. B: At., Mol. Opt. Phys.* **49**, 034001 (2016).
- <sup>6</sup>B. Stankus, H. Yong, J. Ruddock, L. Ma, A. Carrascosa, N. Goff, S. Boutet, X. Xu, N. Zotev *et al.*, *J. Phys. B: At., Mol. Opt. Phys.* **53**, 234004 (2020).
- <sup>7</sup>A. Odate, A. Kirrander, P. M. Weber, and M. P. Miniti, *Adv. Phys.: X* **8**, 2126796 (2023).
- <sup>8</sup>P. Debye, *Phys. Z.* **31**, 419 (1930).
- <sup>9</sup>L. Bewilogua, *Phys. Z.* **33**, 688 (1932).
- <sup>10</sup>E. Prince, *International Tables for Crystallography, Volume C: Mathematical, Physical and Chemical Tables*, 3rd ed. (Wiley, New York, 2004), ISBN: 9780470710296.
- <sup>11</sup>R. Santra, *J. Phys. B: At., Mol. Opt. Phys.* **42**, 023001 (2008).
- <sup>12</sup>T. Northey, N. Zotev, and A. Kirrander, *J. Chem. Theory Comput.* **10**, 4911 (2014).
- <sup>13</sup>T. Northey, A. Moreno Carrascosa, S. Schäfer, and A. Kirrander, *J. Chem. Phys.* **145**, 154304 (2016).
- <sup>14</sup>A. Moreno Carrascosa and A. Kirrander, *Phys. Chem. Chem. Phys.* **19**, 19545 (2017).
- <sup>15</sup>T. Northey and A. Kirrander, *J. Phys. Chem. A* **123**, 3395 (2019).
- <sup>16</sup>A. Moreno Carrascosa, H. Yong, D. L. Crittenden, P. M. Weber, and A. Kirrander, *J. Chem. Theory Comput.* **15**, 2836 (2019).
- <sup>17</sup>N. Zotev, A. Moreno Carrascosa, M. Simmermacher, and A. Kirrander, *J. Chem. Theory Comput.* **16**, 2594 (2020).
- <sup>18</sup>A. Moreno Carrascosa, J. P. Coe, M. Simmermacher, M. J. Paterson, and A. Kirrander, *Phys. Chem. Chem. Phys.* **24**, 24542 (2022).
- <sup>19</sup>H. Yong, N. Zotev, J. M. Ruddock, B. Stankus, M. Simmermacher, A. Carrascosa, W. Du, N. Goff, Y. Chang *et al.*, *Nat. Commun.* **11**, 2157 (2020).
- <sup>20</sup>H. Yong, S. M. Cavaletto, and S. Mukamel, *J. Phys. Chem. Lett.* **12**, 9800 (2021).
- <sup>21</sup>J. M. Ruddock, N. Zotev, B. Stankus, H. Yong, D. Bellshaw, S. Boutet, T. J. Lane, M. Liang, S. Carbaljo *et al.*, *Angew. Chem., Int. Ed.* **58**, 6371 (2019).
- <sup>22</sup>H. Yong, N. Zotev, B. Stankus, J. M. Ruddock, D. Bellshaw, S. Boutet, T. J. Lane, M. Liang, S. Carbaljo *et al.*, *J. Phys. Chem. Lett.* **9**, 6556 (2018).
- <sup>23</sup>A. A. Zholents and W. M. Fawley, *Phys. Rev. Lett.* **92**, 224801 (2004).
- <sup>24</sup>E. Prat and S. Reiche, *Phys. Rev. Lett.* **114**, 244801 (2015).
- <sup>25</sup>N. Hartmann, G. Hartmann, R. Heider, M. S. Wagner, M. Ilchen, J. Buck, A. O. Lindahl, C. Benko, J. Grünert, J. Krzywinski, J. Liu *et al.*, *Nat. Photonics* **12**, 215 (2018).
- <sup>26</sup>A. Marinelli, J. MacArthur, P. Emma, M. Guetg, C. Field, D. Kharakh, A. A. Lutman, Y. Ding, and Z. Huang, *Appl. Phys. Lett.* **111**, 151101 (2017).
- <sup>27</sup>S. Huang, Y. Ding, Y. Feng, E. Hemsing, Z. Huang, J. Krzywinski, A. A. Lutman, A. Marinelli, T. J. Maxwell, and D. Zhu, *Phys. Rev. Lett.* **119**, 154801 (2017).
- <sup>28</sup>J. Duris, S. Li, T. Driver, E. G. Champenois, J. P. MacArthur, A. A. Lutman, Z. Zhang, P. Rosenberger, J. W. Aldrich *et al.*, *Nat. Photonics* **14**, 30 (2020).
- <sup>29</sup>A. Malyzhenkov, Y. P. Arbelo, P. Craievich, P. Dijkstra, E. Ferrari, S. Reiche, T. Schietinger, P. Juranic, and E. Prat, *Phys. Rev. Res.* **2**, 042018 (2020).
- <sup>30</sup>S. Li, T. Driver, P. Rosenberger, E. G. Champenois, J. Duris, A. Al-Haddad, V. Averbukh, J. C. T. Barnard, N. Berrah *et al.*, *Science* **375**, 285 (2022).
- <sup>31</sup>G. Dixit, O. Vendrell, and R. Santra, *Proc. Natl. Acad. Sci. U. S. A.* **109**, 11636 (2012).
- <sup>32</sup>G. Dixit, J. M. Slowik, and R. Santra, *Phys. Rev. A* **89**, 043409 (2014).
- <sup>33</sup>M. Simmermacher, N. E. Henriksen, and K. B. Møller, *Phys. Chem. Chem. Phys.* **19**, 19740 (2017).
- <sup>34</sup>M. Kowalewski, K. Bennett, and S. Mukamel, *Struct. Dyn.* **4**, 054101 (2017).
- <sup>35</sup>K. Bennett, M. Kowalewski, J. R. Rouxel, and S. Mukamel, *Proc. Natl. Acad. Sci. U. S. A.* **115**, 6538 (2018).
- <sup>36</sup>M. Simmermacher, N. E. Henriksen, K. B. Møller, A. Moreno Carrascosa, and A. Kirrander, *Phys. Rev. Lett.* **122**, 073003 (2019).
- <sup>37</sup>M. Simmermacher, A. Moreno Carrascosa, N. E. Henriksen, K. B. Møller, and A. Kirrander, *J. Chem. Phys.* **151**, 174302 (2019).
- <sup>38</sup>S. Giri, J. C. Tremblay, and G. Dixit, *Phys. Rev. A* **104**, 053115 (2021).
- <sup>39</sup>A. Moreno Carrascosa, M. Yang, H. Yong, L. Ma, A. Kirrander, P. M. Weber, and K. Lopata, *Faraday Discuss.* **228**, 60 (2021).
- <sup>40</sup>S. Giri, J. C. Tremblay, and G. Dixit, *Phys. Rev. A* **106**, 033120 (2022).
- <sup>41</sup>M. Zhang, Z. Guo, X. Mi, Z. Li, and Y. Liu, *J. Phys. Chem. Lett.* **13**, 1668 (2022).
- <sup>42</sup>J. Cao and K. R. Wilson, *J. Phys. Chem. A* **102**, 9523 (1998).
- <sup>43</sup>S. Bratos, F. Mirloup, R. Vuilleumier, and M. Wulff, *J. Chem. Phys.* **116**, 10615 (2002).
- <sup>44</sup>N. E. Henriksen and K. B. Møller, *J. Phys. Chem. B* **112**, 558 (2008).
- <sup>45</sup>U. Lorenz, K. B. Møller, and N. E. Henriksen, *Phys. Rev. A* **81**, 023422 (2010).
- <sup>46</sup>A. Venkatesh and F. Robicheaux, *Phys. Rev. A* **106**, 033125 (2022).
- <sup>47</sup>F. Allum, K. Amini, M. Ashfold, D. Bansal, R. J. F. Berger, M. Centurion, G. Dixit, D. Durham, E. Fasshauer, J. P. Figueira Nunes *et al.*, *Faraday Discuss.* **228**, 161 (2021).
- <sup>48</sup>P. B. Corkum, *Phys. Rev. Lett.* **71**, 1994 (1993).
- <sup>49</sup>M. Lewenstein, J. H. Eberly, M. Y. Ivanov, A. L'Huillier, and P. B. Corkum, *Phys. Rev. A* **49**, 2117 (1994).
- <sup>50</sup>Q. Su and J. H. Eberly, *Phys. Rev. A* **44**, 5997 (1991).
- <sup>51</sup>J. Javanainen, J. H. Eberly, and Q. Su, *Phys. Rev. A* **38**, 3430 (1988).
- <sup>52</sup>M. Lein, T. Kreibich, E. Gross, and V. Engel, *Phys. Rev. A* **65**, 033403 (2002).
- <sup>53</sup>S. Gräfe and M. Y. Ivanov, *Phys. Rev. Lett.* **99**, 163603 (2007).
- <sup>54</sup>U. Schwengelbeck and F. H. M. Faisal, *Phys. Rev. A* **50**, 632 (1994).
- <sup>55</sup>B. Belsa, K. Ziemis, A. Sanchez, K. Chirvi, X. Liu, S. Gräfe, and J. Biegert, *Phys. Rev. A* **106**, 043105 (2022).
- <sup>56</sup>B. Wolter, M. G. Pullen, M. Baudisch, M. Sclafani, M. Hemmer, A. Sentfleben, C. D. Schröter, J. Ullrich, R. Moshhammer, and J. Biegert, *Phys. Rev. X* **5**, 021034 (2015).
- <sup>57</sup>K. Hader, J. Albert, E. K. U. Gross, and V. Engel, *J. Chem. Phys.* **146**, 074304 (2017).
- <sup>58</sup>J. Albert, K. Hader, and V. Engel, *J. Chem. Phys.* **147**, 064302 (2017).
- <sup>59</sup>T. Schaupp and V. Engel, *J. Chem. Phys.* **151**, 084309 (2019).
- <sup>60</sup>T. Schaupp and V. Engel, *J. Chem. Phys.* **156**, 074302 (2022).
- <sup>61</sup>M. Erdmann, E. K. U. Gross, and V. Engel, *J. Chem. Phys.* **121**, 9666 (2004).
- <sup>62</sup>M. Falge, V. Engel, and S. Gräfe, *J. Chem. Phys.* **134**, 184307 (2011).
- <sup>63</sup>M. Falge, V. Engel, and S. Gräfe, *J. Phys. Chem. Lett.* **3**, 2617 (2012).
- <sup>64</sup>M. Falge, F. G. Fröbel, V. Engel, and S. Gräfe, *Phys. Chem. Chem. Phys.* **19**, 19683 (2017).
- <sup>65</sup>F. G. Fröbel, K. M. Ziemis, U. Peschel, S. Gräfe, and A. Schubert, *J. Phys. B: At., Mol. Opt. Phys.* **53**, 144005 (2020).
- <sup>66</sup>K. M. Ziemis, J. Bruhnke, V. Engel, and S. Gräfe, *Front. Chem.* **10**, 942633 (2022).
- <sup>67</sup>J. C. Slater, *Phys. Rev.* **81**, 385 (1951).
- <sup>68</sup>J. M. Slowik, S.-K. Son, G. Dixit, Z. Jurek, and R. Santra, *New J. Phys.* **16**, 073042 (2014).
- <sup>69</sup>R. Neutze, R. Wouts, D. van der Spoel, E. Weckert, and J. Hajdu, *Nature* **406**, 752 (2000).
- <sup>70</sup>A. Barty, C. Caleman, A. Aquila *et al.*, *Nat. Photonics* **6**, 35 (2012).
- <sup>71</sup>C. Yoon, M. Yurkov *et al.*, *Sci. Rep.* **6**, 24791 (2016).
- <sup>72</sup>C. Östlin, N. Timneanu, C. Caleman, and A. V. Martin, *Struct. Dyn.* **6**, 044103 (2019).
- <sup>73</sup>K. Nass, A. Gorel, M. M. Abdullah *et al.*, *Nat. Commun.* **11**, 1814 (2020).
- <sup>74</sup>B. Rudek, S.-K. Son, L. Foucar, S. W. Epp, B. Erk, R. Hartmann, M. Adolph, R. Andritschke, A. Aquila *et al.*, *Nat. Photonics* **6**, 858 (2012).
- <sup>75</sup>A. Rudenko, L. Inhester, K. Hanasaki, X. Li, S. J. Robatjazi, B. Erk, R. Boll, K. Toyota, Y. Hao *et al.*, *Nature* **546**, 129 (2017).
- <sup>76</sup>M. P. Miniti, J. M. Budarz, A. Kirrander, J. Robinson, T. J. Lane, D. Ratner, K. Saita, T. Northey, B. Stankus, V. Cofer-Shabica *et al.*, *Faraday Discuss.* **171**, 81 (2014).
- <sup>77</sup>J. Küpper, S. Stern, L. Holmegaard, F. Filsinger, A. Rouzée, A. Rudenko, P. Johnsson, A. V. Martin, M. Adolph, A. Aquila *et al.*, *Phys. Rev. Lett.* **112**, 083002 (2014).
- <sup>78</sup>B. Stankus, J. M. Budarz, A. Kirrander, D. Rogers, J. Robinson, T. J. Lane, D. Ratner, J. Hastings, M. P. Miniti, and P. M. Weber, *Faraday Discuss.* **194**, 525 (2016).

- <sup>79</sup>J. M. Glownia, A. Natan, J. P. Cryan, R. Hartsock, M. Kozina, M. P. Minitti, S. Nelson, J. Robinson, T. Sato, T. van Driel *et al.*, *Phys. Rev. Lett.* **117**, 153003 (2016).
- <sup>80</sup>B. Stankus, H. Yong, N. Zotev, J. M. Ruddock, D. Bellshaw, T. J. Lane, M. Liang, S. Boutet, S. Carbajo *et al.*, *Nat. Chem.* **11**, 716 (2019).
- <sup>81</sup>J. M. Ruddock, H. Yong, B. Stankus, W. Du, N. Goff, Y. Chang, A. Odate, A. M. Carrascosa, D. Bellshaw, N. Zotev *et al.*, *Sci. Adv.* **5**, eaax6625 (2019).
- <sup>82</sup>M. R. Ware, J. M. Glownia, N. Al-Sayyad, J. T. O'Neal, and P. H. Bucksbaum, *Phys. Rev. A* **100**, 033413 (2019).
- <sup>83</sup>T. Kierspel, A. Morgan, J. Wiese, T. Mullins, A. Aquila, A. Barty, R. Bean, R. Boll, S. Boutet, P. Bucksbaum *et al.*, *J. Chem. Phys.* **152**, 084307 (2020).
- <sup>84</sup>I. Gabalski, M. Sere, K. Acheson, F. Allum, S. Boutet, G. Dixit, R. Forbes, J. M. Glownia, N. Goff *et al.*, *J. Chem. Phys.* **157**, 164305 (2022).
- <sup>85</sup>S.-K. Son, O. Geffert, and R. Santra, *J. Phys. B: At., Mol. Opt. Phys.* **50**, 064003 (2017).
- <sup>86</sup>M. Kircher, F. Trinter, S. Grundmann, I. Vela-Perez, S. Brennecke, N. Eicke, J. Rist, S. Eckart, S. Houamer *et al.*, *Nat. Phys.* **16**, 756 (2020).
- <sup>87</sup>O. Chuluunbaatar, S. Houamer, Y. V. Popov, I. P. Volobuev, M. Kircher, and R. Dörner, *J. Quant. Spectrosc. Radiat. Transfer* **272**, 107820 (2021).
- <sup>88</sup>S. Reiter, D. Keefer, and R. de Vivie-Riedle, "Exact quantum dynamics (wave packets) in reduced dimensionality," in *Quantum Chemistry and Dynamics of Excited States* (John Wiley & Sons, Ltd., 2020), Chap. 11, pp. 355–381, ISBN: 9781119417774.
- <sup>89</sup>I. Waller and D. R. Hartree, *Proc. R. Soc. London, Ser. A* **124**, 119 (1929).
- <sup>90</sup>P. Eisenberger and P. M. Platzman, *Phys. Rev. A* **2**, 415 (1970).
- <sup>91</sup>R. Kosloff and H. Tal-Ezer, *Chem. Phys. Lett.* **127**, 223 (1986).
- <sup>92</sup>M. D. Feit, J. A. Fleck, and A. Steiger, *J. Comput. Phys.* **47**, 412 (1982).
- <sup>93</sup>M. Frigo and S. G. Johnson, in *Proceedings of the 1998 IEEE International Conference on Acoustics, Speech and Signal Processing, ICASSP'98 (Cat. No. 98CH36181)* (IEEE, Seattle, WA, 1998), Vol. 3, pp. 1381–1384, ISBN: 978-0-7803-4428-0.
- <sup>94</sup>L. S. Bartell and R. M. Gavin, *J. Am. Chem. Soc.* **86**, 3493 (1964).
- <sup>95</sup>L. S. Bartell and R. M. Gavin, *J. Chem. Phys.* **43**, 856 (1965).
- <sup>96</sup>L. R. Andersson and J. Burgdörfer, *Phys. Rev. Lett.* **71**, 50 (1993).
- <sup>97</sup>J. A. R. Samson, C. H. Greene, and R. J. Bartlett, *Phys. Rev. Lett.* **71**, 201 (1993).
- <sup>98</sup>J. A. R. Samson, Z. X. He, R. J. Bartlett, and M. Sagurton, *Phys. Rev. Lett.* **72**, 3329 (1994).
- <sup>99</sup>L. Spielberger, O. Jagutzki, R. Dörner, J. Ullrich, U. Meyer, V. Mergel, M. Unverzagt, M. Damrau, T. Vogt *et al.*, *Phys. Rev. Lett.* **74**, 4615 (1995).
- <sup>100</sup>J. Yang, X. Zhu, J. P. F. Nunes, J. K. Yu, R. M. Parrish, T. J. A. Wolf, M. Centurion, M. Gühr *et al.*, *Science* **368**, 885 (2020).
- <sup>101</sup>G. Hermann, V. Pohl, G. Dixit, and J. C. Tremblay, *Phys. Rev. Lett.* **124**, 013002 (2020).
- <sup>102</sup>H. Yong, J. R. Rouxel, D. Keefer, and S. Mukamel, *Phys. Rev. Lett.* **129**, 103001 (2022).
- <sup>103</sup>M. Simmermacher, A. Kirrander, and N. E. Henriksen, *Phys. Rev. A* **102**, 052825 (2020).
- <sup>104</sup>M. Stefanou, K. Saita, D. V. Shalashilin, and A. Kirrander, *Chem. Phys. Lett.* **683**, 300 (2017).
- <sup>105</sup>L. Ma, H. Yong, J. D. Geiser, A. M. Carrascosa, N. Goff, and P. M. Weber, *Struct. Dyn.* **7**, 034102 (2020).
- <sup>106</sup>H. Yong, D. Keefer, and S. Mukamel, *J. Am. Chem. Soc.* **144**, 7796 (2022).

**ELECTRONIC SUPPLEMENTARY INFORMATION**

for

*The Contribution of Compton Ionisation to Ultrafast X-Ray Scattering*

Karl Michael Ziems,<sup>1,2</sup> Mats Simmermacher,<sup>3,a)</sup> Stefanie Gräfe,<sup>1,2</sup> and Adam Kirrander<sup>3,b)</sup>

<sup>1)</sup>Max Planck School of Photonics, 07745 Jena, Germany.

<sup>2)</sup>Institute of Physical Chemistry, Friedrich Schiller University Jena, 07743 Jena, Germany.

<sup>3)</sup>Department of Chemistry, University of Oxford, Oxford OX1 3QZ, United Kingdom.

<sup>a)</sup>Electronic mail: mats.simmermacher@chem.ox.ac.uk

<sup>b)</sup>Electronic mail: adam.kirrander@chem.ox.ac.uk

## Mapping to Scattering Angle

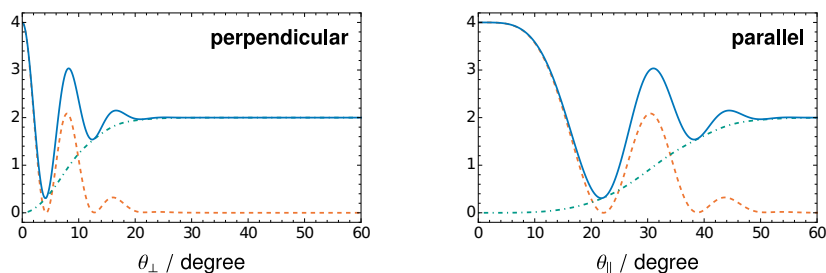
In main text of the article, x-ray scattering signals are displayed as functions of  $q$ , the component of the momentum transfer vector  $\mathbf{q}$  in direction of the model system's molecular axis. Here, the mapping of  $q$  to the polar scattering angle  $\theta$  and its impact on the scattering signals are discussed in greater detail.

For a particular orientation of the wave vector of the incident x-ray photon,  $\mathbf{k}_0$ , with respect to the molecular axis, and within the Waller-Hartree approximation,  $q$  bijectively maps to  $\theta$ . If  $\mathbf{k}_0$  is perpendicular or parallel to the molecular axis, the respective scattering angles in a two-dimensional scattering geometry are,<sup>a</sup>

$$\theta_{\perp} = \arcsin\left(\frac{q}{k_0}\right), \quad \theta_{\parallel} = \arcsin\left(\frac{\sqrt{q(2k_0 - q)}}{k_0}\right), \quad (\text{S1})$$

where  $k_0 = |\mathbf{k}_0| = E_0/(c\hbar)$  is a constant for a given mean-photon energy of the incident x-ray pulse,  $E_0$ .

To illustrate the effect of the direction of  $\mathbf{k}_0$ , the total, elastic, and inelastic scattering signals from Fig. 3 (a) of the manuscript are plotted against the angles  $\theta_{\perp}$  and  $\theta_{\parallel}$  in Fig. S1 below. For the perpendicular orientation, the scattering signals are visually indistinguishable from the signals shown in the manuscript because  $\arcsin(q/k_0)$  is essentially a linear function in range of  $q/k_0$  where the signals show structure. For the parallel orientation, the maxima and minima of the scattering signals are shifted towards higher angles, but apart from this stretch the curves are identical.



**Figure S1:** Total, elastic, and inelastic x-ray scattering signals of the asymmetric model system in its electronic ground state as functions of the scattering angles  $\theta_{\perp}$  and  $\theta_{\parallel}$  for the perpendicular and parallel orientations of  $\mathbf{k}_0$  relative to the molecular axis. A mean-photon energy of  $E_0 = 10$  keV is assumed.

We note that the outgoing, Compton ionised electron may also carry a component of momentum orthogonal to the molecular axis to ensure momentum conservation. Because the molecule's initial electronic state does not extend in this dimension, though, the orthogonal component of the electron momentum does not affect the simulated x-ray scattering signals. The respective integrals separate and solve to a factor of unity, *i.e.*,

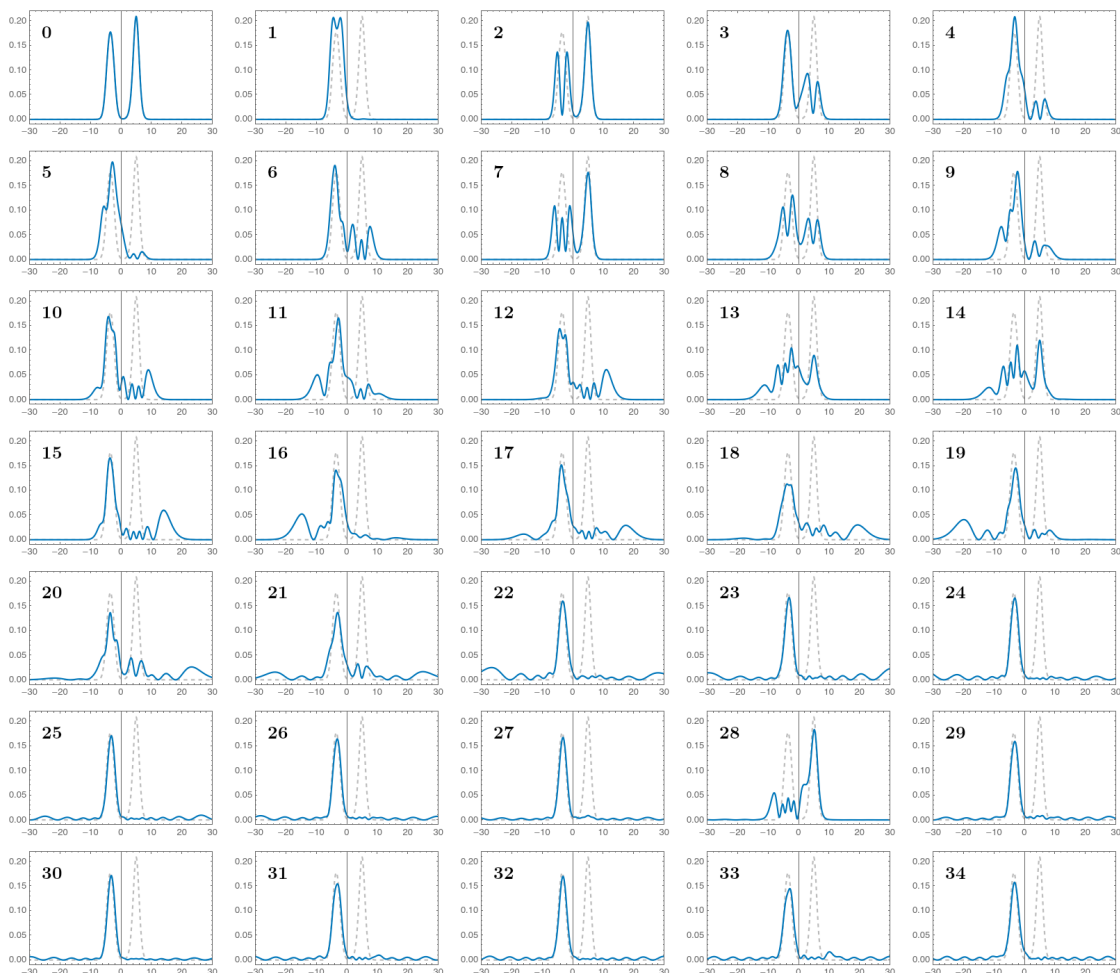
$$\int_{-\infty}^{+\infty} e^{-ik'z} e^{iq'z} \delta(z) dz = 1.$$

Here,  $z$  is an electronic coordinate orthogonal to either  $x$  or  $y$  and  $\delta(z)$  is the Dirac delta function that reflects that the initial, completely bound states of the molecular model system do not extend in  $z$ -direction. Moreover,  $k'$  and  $q'$  are components of the electron momentum and momentum transfer vector perpendicular to  $k$  and  $q$ , respectively. In addition, momentum is also conserved by the recoil of the molecule itself. The latter applies to all components of the scattering signal, also to those not related to Compton ionisation.

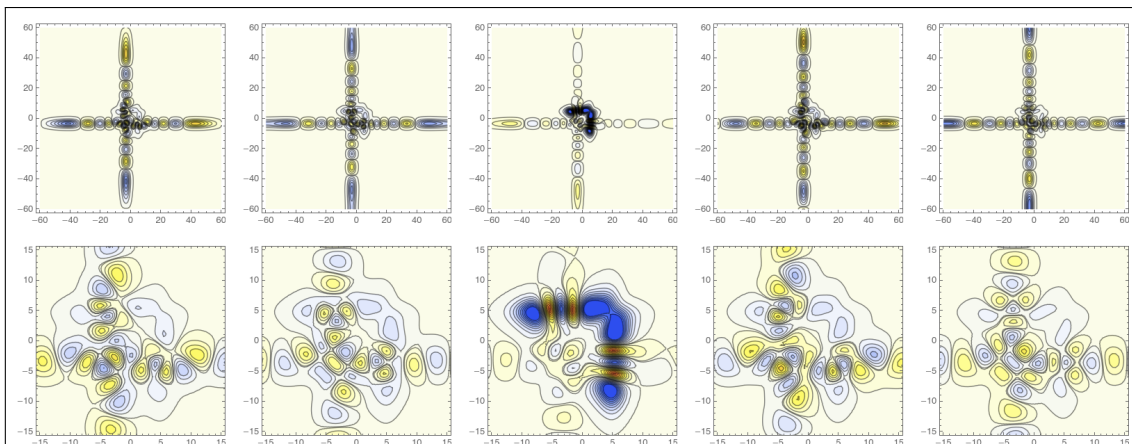
<sup>a</sup>The expressions can be derived from Eqs. (4.8) and (4.13) discussed on pp. 37–40 in [M. Simmermacher, *Theory and Simulations of Time-Resolved X-Ray Scattering*, Ph.D. Thesis, (Technical University of Denmark, Kongens Lyngby, Denmark, 2018)].

## Densities and States of the Molecular Model System

Here, a selection of one-electron densities and electronic eigenstates of the molecular model system are shown.



**Figure S2:** One-electron densities,  $\rho_{ii}(x)$ , of the first 35 electronic states of the two-electron model system in its asymmetric nuclear configuration with  $R = -2.05 \text{ \AA}$ . The  $x$ -axis refers to the electronic coordinate in Ångström. For states 1 to 34, the density of the electronic ground state is shown by a dashed gray line to facilitate comparison. All 35 states lie below the first ionisation threshold and are thus completely bound. Almost all states above  $i \approx 14$  display Rydberg character with relatively large density at large distances from the nuclei, extending even beyond the  $60\text{-\AA}$ -wide range of  $x$ -values shown here. For these states, the density in the vicinity of the two nuclei at  $R = -5.00 \text{ \AA}$  and  $R = -2.05 \text{ \AA}$  is very similar to the density of the electronic ground state, while the density close to the more distant nucleus at  $R = 5.00 \text{ \AA}$  is significantly depleted. Intriguingly, state 28 interrupts this Rydberg series. Its one-electron density is more localised and shows very little, if any, Rydberg character. Moreover, its density close to the nucleus at  $R = 5.00 \text{ \AA}$  is very similar to the density of the electronic ground state, while the density in the vicinity of the two nuclei at  $R = -5.00 \text{ \AA}$  and  $R = -2.05 \text{ \AA}$  has a more complex, more nodal, and slightly more diffuse, albeit still very localised structure.



**Figure S3:** Contour plots of the electronic states  $|\varphi_i^{2e}\rangle$  with  $i = 26$  to  $30$  (left to right) of the model system in its asymmetric nuclear configuration with  $R = -2.05$  Å. The  $x$ - and  $y$ -axes refer to the electronic coordinates in Ångström. The upper row shows the wave functions between  $-60$  Å and  $+60$  Å, the lower row between  $-15$  Å and  $+15$  Å. Blue colours depict negative and yellow to red colours positive amplitude of the wave function. The contours range from values smaller than  $-0.054$  to values larger than  $+0.054$  in increments of  $0.006$ . All five states shown lie below the first ionisation threshold and are thus completely bound. While states 26, 27, 29, and 30 display strong Rydberg character with relatively large amplitude at large distances from the nuclei, state 28 is significantly more localised.